# *Experimental constraints on the compositions and thermal regimes of terrestrial planetary interiors*

Doctoral Thesis

submitted to obtain the academic degree of Doctor of Natural Sciences
(Dr. rer. nat.)
of the Bayreuth Graduate School of Mathematical and Natural Sciences
(BayNAT)
of the University of Bayreuth

***Lianjie Man***
from *Weihai, China*
Bayreuth, 2024

This doctoral thesis was prepared at the Bayerisches Geoinstitut at the University of Bayreuth from December/2019 until December/2024 and was supervised by Prof. Dr. Daniel J. Frost.

This is a full reprint of the thesis submitted to obtain the academic degree of Doctor of Natural Sciences (Dr. rer. Nat.) and approved by the Bayreuth Graduate School of Mathematical and Natural Sciences (BayNAT) of the University of Bayreuth.

Form of the dissertation: Cumulative dissertation

Date of submission: 20.12.2024

Admission by the executive board: 09.01.2025

Date of defence: 05.05.2025

Acting director: Prof. Dr. Jürgen Köhler

Doctoral committee:

Prof. Dr. Daniel Frost (reviewer)
Prof. Dr. Tomoo Katsura (reviewer)
PD. Dr. Gerd Steinle-Neumann (chair)
Prof. Dr. Leonid Dubrovinsky

## Summary

Information on the structure and thermal regimes within the interiors of the terrestrial planets is crucial for understanding their formation, differentiation and internal dynamic processes. This can only be achieved, however, by interpreting geophysical and geochemical observations using experimental studies of planetary materials under the relevant conditions. In this thesis constraints are placed on the compositions and conditions within planetary interiors through the use of several novel high-pressure and temperature experimental approaches.

The first part of this work examines the solubility of $Al_2O_3$ in ferropericlase, a mineral found as an inclusion in sub-lithospheric diamonds, and explores whether the resulting relationship can be used to interpret the temperatures and pressures at which such diamonds form. A series of high-pressure multi-anvil experiments were conducted in the MgO-FeO-$Al_2O_3$ system at pressures between 15 and 50 GPa and temperatures up to 2623 K. The results reveal that $Al_2O_3$ solubility in periclase is strongly temperature-dependent, decreases with increasing pressure within the investigated conditions, and is only minimally affected by FeO incorporation. Thermodynamic modeling, using data from this study and the literature, indicates that mantle ferropericlase $Al_2O_3$-contents cannot be greater than 0.5 mol.% under present day adiabatic mantle temperatures and will also go through a minimum at mantle transition zone conditions. These findings exclude a number of Al-rich ferropericlase inclusions found in natural diamonds from being formed in the transition zone, unless mantle temperatures were super-adiabatic. This subset of inclusions likely formed either at the base of the upper mantle or the top of the lower mantle, but must have formed at near adiabatic temperatures. The majority of ferropericlase inclusions have $Al_2O_3$ contents that would be consistent with formation in the transition zone at near slab temperatures, but could still have been formed at higher temperatures if $Al_2O_3$ activities were low.

Chapter 5 is an experimental investigation performed to interpret seismic data from the

InSight mission on Mars in terms of the concentration of light alloying element in the Martian core. Understanding the influence of light elements on the elastic properties of liquid iron under high pressure and temperature conditions is crucial for characterizing the composition of planetary cores, which is the key to understanding how they were formed. In this subproject, a series of P-wave velocity and density measurements on Fe and Fe-S liquids were conducted at pressures up to 17.8 GPa and temperatures up to 2273 K, using ultrasonic interferometry, the Beer-Lambert method, and a combination of angular and energy-dispersive X-ray diffraction techniques. The melting curve of Fe and the density of solid FeS were also experimentally constrained to facilitate thermodynamic modeling. By integrating these results with literature data on thermodynamic properties at ambient pressure and the melting curves of Fe and FeS, a self-consistent thermodynamic model for the Fe-FeS system was developed under conditions relevant to the Martian core. The results indicate that sulfur lowers both the density and P-wave velocity of liquid Fe under Martian core conditions. To account for the observed density deficit in the Martian core, at least 20 wt.% sulfur would be required. However, such high sulfur concentrations would lower the P-wave velocity of liquid Fe, most significantly at the top of the Martian core, which conflicts with seismic observations from the InSight mission. This indicates that significant proportions of other light elements, such as carbon or hydrogen, are most likely required alongside sulfur to explain the large density deficit while maintaining the apparent high P-wave velocity in the Martian core.

The last part of this work presents the first crystal structure refinement of a high-pressure sulfide phase with the formula $Fe_{4+x}S_3$, which is potentially stable under Martian inner core conditions. As $Fe_{4+x}S_3$ is unstable at ambient conditions, the crystal structure was solved using *in situ* high-pressure single-crystal X-ray diffraction. The structure, with space group Pnma, comprises four edge-sharing Fe-S square pyramids and one semi-occupied interstitial Fe site, which allows the stoichiometry to vary from x=0 to 1. Measurements of volumes and chemical compositions confirm that the iron content in $Fe_{4+x}S_3$ increases with temperature, approaching the stoichiometry of $Fe_5S_3$ under conditions compatible with those of the Martian inner core. Further measurements confirm that $Fe_{4+x}S_3$ has a higher density than the liquid Martian core and its formation is consistent with estimates for the core's sulfur concentration. Although a Maritain inner core has so far not been detected, it can be shown that a $Fe_{4+x}S_3$ inner core would crystalize if temperatures fall below 1960 (±105) K, at the center of Mars, which is still within the range of estimates for the temperature at these conditions.

## Zusammenfassung

Informationen über die Struktur und die thermischen Verhältnisse im Inneren der terrestrischen Planeten sind entscheidend für das Verständnis ihrer Entstehung, Differenzierung und internen dynamischen Prozesse. Dies kann jedoch nur erreicht werden, indem geophysikalische und geochemische Beobachtungen durch experimentelle Untersuchungen von planetarischen Materialien unter den entsprechenden Bedingungen interpretiert werden. In dieser Arbeit werden die Zusammensetzung und die Bedingungen im Inneren von Planeten durch den Einsatz mehrerer neuartiger experimenteller Hochdruck- und Temperaturmethoden untersucht.

Im ersten Teil dieser Arbeit wird die Löslichkeit von $Al_2O_3$ in Ferroperiklas untersucht, einem Mineral, das als Einschluss in sublithosphärischen Diamanten vorkommt, und es wird untersucht, ob die sich daraus ergebende Beziehung zur Interpretation der Temperaturen und Drücke, bei denen sich solche Diamanten bilden, verwendet werden kann. Eine Serie von Hochdruck-Multi-Anvil-Experimenten wurde im MgO-FeO-$Al_2O_3$-System bei Drücken zwischen 15 und 50 GPa und Temperaturen bis zu 2623 K durchgeführt. Die Ergebnisse zeigen, dass die $Al_2O_3$-Löslichkeit in Periklas stark temperaturabhängig ist, mit zunehmendem Druck innerhalb der untersuchten Bedingungen abnimmt und nur geringfügig durch Zugabe von FeO beeinflusst wird. Thermodynamische Modellierungen unter Verwendung von Daten aus dieser Studie und der Literatur zeigen, dass der $Al_2O_3$-Gehalt von Ferroperiklas im Erdmantel bei den heutigen adiabatischen Manteltemperaturen nicht höher als 0,5 Mol-% sein kann und dass bei den Bedingungen in der Mantelübergangszone ebenfalls ein Minimum erreicht wird. Diese Erkenntnisse schließen aus, dass eine Reihe von Al-reichen Ferroperiklas-Einschlüssen, die in natürlichen Diamanten gefunden wurden, in der Übergangszone entstanden sind, es sei denn, die Temperaturen im Mantel waren superadiabatisch. Diese Untergruppe von Einschlüssen bildete sich wahrscheinlich entweder an der Basis des oberen Mantels oder an der Obergrenze des unteren Mantels, muss sich aber bei nahezu adiabatischen

Temperaturen gebildet haben. Die meisten Ferroperiklas-Einschlüsse weisen $Al_2O_3$-Gehalte auf, die mit einer Bildung in der Übergangszone bei Temperaturen übereinstimmen, die dort innerhalb einer subduzierten Platte herrschen, könnten aber auch bei höheren Temperaturen gebildet worden sein, wenn die $Al_2O_3$-Aktivitäten gering waren.

Kapitel 5 ist eine experimentelle Untersuchung zur Interpretation seismischer Daten der InSight-Mission auf dem Mars im Hinblick auf die Konzentration leichter Legierungselemente im Marskern. Das Verständnis des Einflusses leichter Elemente auf die elastischen Eigenschaften von flüssigem Eisen unter hohen Druck- und Temperaturbedingungen ist von entscheidender Bedeutung für die Charakterisierung der Zusammensetzung planetarer Kerne, die der Schlüssel zum Verständnis ihrer Entstehung ist. In diesem Teilprojekt wurde eine Reihe von P-Wellen-Geschwindigkeits- und Dichtemessungen an Fe- und Fe-S-Schmelzen bei Drücken bis zu 17,8 GPa und Temperaturen bis zu 2273 K durchgeführt, wobei Ultraschall-Interferometrie, die Beer-Lambert-Methode und eine Kombination von Winkel- und Energie-dispersiven Röntgenbeugungstechniken eingesetzt wurden. Die Schmelzkurve von Fe und die Dichte von festem FeS wurden ebenfalls experimentell bestimmt, um die thermodynamische Modellierung zu erleichtern. Durch die Integration dieser Ergebnisse mit Literaturdaten zu thermodynamischen Eigenschaften bei Umgebungsdruck und den Schmelzkurven von Fe und FeS wurde ein selbstkonsistentes thermodynamisches Modell für das Fe-FeS-System unter den für den Marskern relevanten Bedingungen entwickelt. Die Ergebnisse zeigen, dass Schwefel sowohl die Dichte als auch die P-Wellengeschwindigkeit von flüssigem Fe unter den Bedingungen des Marskerns verringert. Um das beobachtete Dichtedefizit im Marskern zu erklären, wären mindestens 20 Gew.-% Schwefel erforderlich. Solch hohe Schwefelkonzentrationen würden jedoch die P-Wellen-Geschwindigkeit von flüssigem Fe stark verringern, vor allem im oberen Teil des Marskerns, was im Widerspruch zu den seismischen Beobachtungen der InSight-Mission steht. Dies deutet darauf hin, dass neben Schwefel höchstwahrscheinlich erhebliche Anteile anderer leichter Elemente wie Kohlenstoff oder Wasserstoff erforderlich sind, um das große Dichtedefizit auszugleichen und gleichzeitig die scheinbar hohe P-Wellen-Geschwindigkeit im Marskern aufrechtzuerhalten.

Im letzten Teil dieser Arbeit wird die erste Kristallstrukturverfeinerung einer Hochdruck-Sulfidphase mit der Formel $Fe_{4+x}S_3$ vorgestellt, die unter den Bedingungen des inneren Marskerns potenziell stabil ist. Da $Fe_{4+x}S_3$ bei Umgebungsbedingungen instabil ist, wurde die Kristallstruktur mit Hilfe der In-situ-Hochdruck-Einzelkristall-Röntgenbeugung gelöst. Die Struktur mit der Raumgruppe Pnma umfasst vier über die Kanten verbundene Fe-S-Quadratpyramiden und einen halbbesetzten Fe-Zwischengitterplatz, wodurch die Stöchiometrie von x=0 bis 1 variieren kann. Messungen des Volumens und der chemischen Zusammensetzung bestätigen, dass der Eisengehalt in $Fe_{4+x}S_3$ mit der Temperatur zunimmt und sich der Stöchiometrie von $Fe_5S_3$ unter Bedingungen nähert, die mit denen des inneren Marskerns kompatibel sind. Weitere Messungen bestätigen, dass $Fe_{4+x}S_3$ eine höhere Dichte hat als der flüssige Marskern, und seine Bildung stimmt mit den Schätzungen für die Schwefelkonzentration des Kerns überein. Obwohl ein innerer Marskern bisher nicht nachgewiesen werden konnte, lässt sich zeigen, dass ein innerer $Fe_{4+x}S_3$-Kern kristallisieren würde, wenn die Temperaturen im Zentrum des Mars unter 1960 (±105) K fallen, was noch im Bereich der Abschätzungen für die Temperatur unter diesen Bedingungen liegt.

**Acknowledgment**

I would like to express my deepest appreciation to my supervisor, Prof. Dr. Dan Frost, for his invaluable support throughout my doctoral studies over the past five years. Pursuing my doctoral studies under Dan's guidance at BGI has been one of the best decisions I have ever made. I am also deeply grateful to Dr. Tiziana Boffa Ballaran, Prof. Dr. Leonid Dubrovinsky, and Dr. Nobuyoshi Miyajima for their dedicated mentorship and invaluable guidance throughout my research. Additionally, I would like to extend my sincere thanks to Dr. Tony Withers, Dr. Catherine McCammon, Dr. Andreas Audétat, Prof. Dr. Tomo Katsura, and Dr. Florian Heidelbach for their careful instruction during experiments and for the insightful scientific discussions.

I would also like to express my heartfelt gratitude to my collaborators at BGI, including Dr. Adrien Néri, Dr. Jonathan Dolinschi, Dr. Hongzhan Fei, Dr. Wenju Zhou, Dr. Eun Jeong Kim, Dr. Longjian Xie, Dr. Liang Yuan, Dr. Hu Tang, Dr. Fei Wang, Dr. Rémy Pierru, Dr. Alexander Kurnosov, Dr. Lin Wang, Dr. Amrita Chakraborti, Dr. Kui Han, Dr. Jia Chang, Cheng Qian, and Dr. Edith Kubik. Their collaboration greatly contributed to the success of the research, and I have gained invaluable research experience and learned so much from their scientific attitudes and expertise. I am also deeply appreciative of Raphael Njul, Sven Linhardt, Heinz Fischer, Dorothea Wiesner, Detlef Krauße, Alexander Rother, Gerald Bauer, Ulrike Trenz, Stefan Übelhack, Erik Konrad, Rebecka Matthäus, and Anke Potzel for their professional technical support. The technician team at BGI is truly exceptional. In addition to those mentioned above, I extend my deepest thanks to all my friends at BGI and to BGI as a whole. It has always been a pleasure to work in such a collaborative and inspiring environment, and I am proud to be a part of this incredible institution.

I sincerely appreciate the expertise and contributions of my external collaborators, including Dr. Xiang Li from Münster, Dr. Julien Chantel from Lille, Prof. Olivier Namur from Leuven, Dr. Hongsheng Yuan from Shanghai, and Guoliang Niu from Beijing.

The collaborations have been smooth, productive, and truly enjoyable. I would also like to express my deep appreciation to the beamline staff, including Dr. Robert Farla, Dr. Xiaokang Feng, Stefan Sonntag, Dr. Shrikant Bhat, and Dr. Shuailing Ma at PETRA III; Dr. Nicolas Guignot, Dr. Laura Henry, and Dr. Andrew King at SOLEIL; Prof. Yanbin Wang, Dr. Tony Yu, and Dr. Man Xu at APS; and Dr. Ilya Kupenko, Dr. Georgios Aprilis, Dr. Alexander Chumakov, and Dr. Michael Hanfland at ESRF. The success of the experiments in this work would not have been possible without the exceptional and unparalleled synchrotron beamlines they have constructed and maintained. I am especially grateful for their outstanding support and expertise during the experiments.

Last but not least, I would like to express my heartfelt gratitude to my parents for their unconditional trust and support, and to Ruotong for her invaluable love and companionship. Their presence and understanding have given me the strength to overcome all the challenges I encountered. Life has been truly happy and colorful with them by my side.

# CONTENTS

# 1 Introduction

The terrestrial planets (Mercury, Venus, Earth, and Mars) are rocky bodies that formed in the inner part of the solar nebula. While they share broadly similar rock and iron metal dominated compositions (e.g., McDonough and Yoshizaki, 2021), in detail their structures and chemistries exhibit notable variations, particularly when compared to the Earth (Fig. 1.1). Understanding the formation and characteristics of the terrestrial planets is fundamental to unraveling the origin and evolution of the Solar System (Morbidelli et al., 2012; Righter and O'Brien, 2011). The study of terrestrial planets typically requires a multidisciplinary approach, encompassing geophysical observations and modeling, geochemical and cosmochemical analyses of materials from planets, asteroids, and meteorites, as well as experimental and theoretical investigations on the nature of these planetary materials under the relevant conditions.

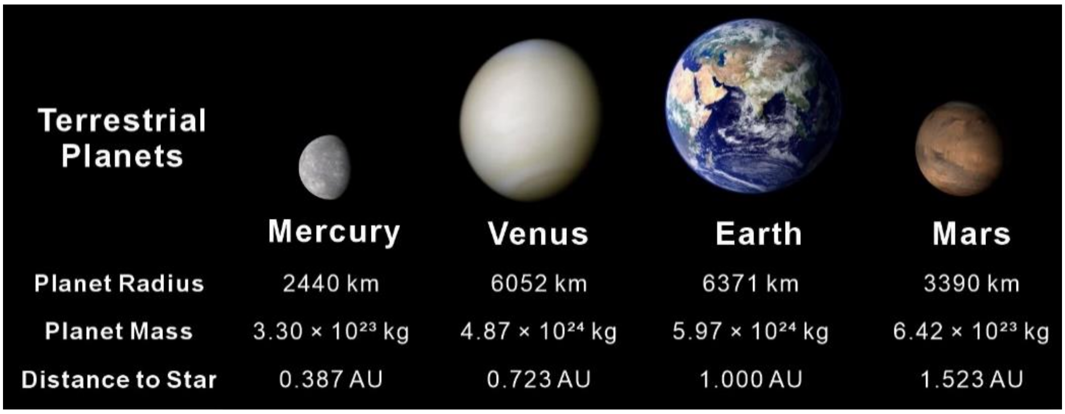

**Figure 1.1.** Characteristics of terrestrial planets in the Solar System. Pictures of planets courtesy of NASA/JPL-Caltech.

## 1.1 Formation of Terrestrial Planets in the Solar System

Planets form within protoplanetary disks, composed of gas and dust, surrounding young stars (Williams and Cieza, 2011; Morbidelli et al., 2012). While only remnants of this process remain in the Solar System, increasingly detailed astronomical observations of circumstellar disks have significantly advanced our understanding of planet formation (Andrew et al., 2018; Andrew, 2000; Drążkowska et al., 2022), as exemplified by images released within the last 6 years from the Atacama Large Millimeter/submillimeter Array (ALMA). The ALMA images show protoplanetary disks formed around very young stars that often show substructures comprised of concentric rings separated by gaps with lower densities. They provide evidence for very rapid organization of dust, as some of the observations are for stars that are only 1 million years old (Andrew et al., 2020).

Inside the protoplanetary disk, millimeter- to centimeter-sized dust aggregates, or "pebbles", can grow from micrometer-sized dust and ice particles via intermolecular forces and migrate toward the central star due to gas drag (Weidenschilling, 1977). Alternatively, turbulence within the disk can lead to the rapid formation of planetesimals larger than 100 km through the collective gravitational effects of dense swarms of small particles concentrated in localized regions, a process known as the gravoturbulent model (e.g., Johansen et al., 2007).

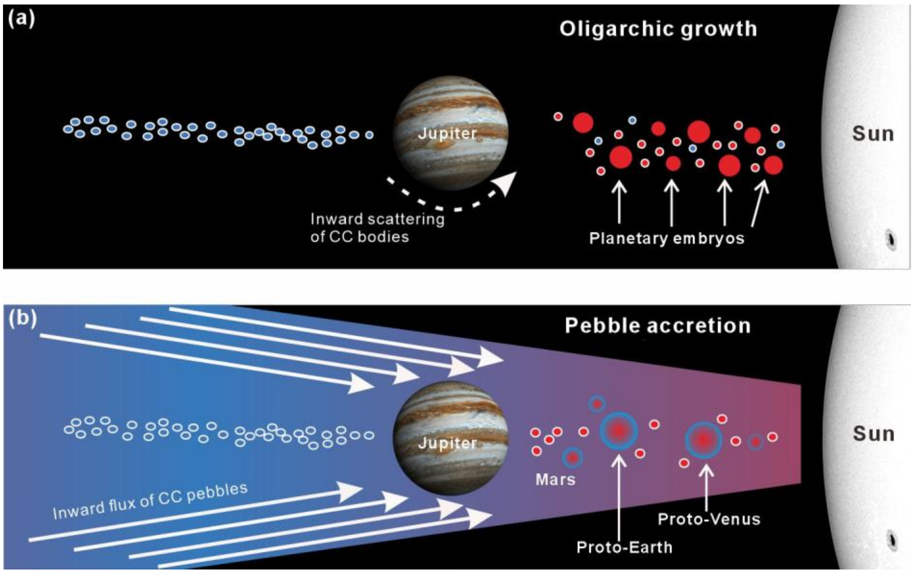

**Figure 1.2.** Terrestrial planets growth through the models of oligarchic growth (a) and pebble accretion (b). "CC" indicates carbonaceous. (Modified from Burkhardt et al, 2021)

In classical models of planet formation, once the protoplanetary disk develops a substantial population of planetesimals, the processes of "runaway growth" (Ida and Makino, 1993) and subsequent "oligarchic growth" (Kokubo and Ida, 1998, 2000) are triggered. During these stages, accretion is dominated by gravitational interactions between pairs of planetesimals, leading to the formation of Moon- to Mars-sized planetary embryos (Fig. 1.2a). In the final stage of planet formation, as the nebular gas dissipates from the protoplanetary disk, the eccentricities of planetary embryos grow rapidly, resulting in intersecting orbits and frequent collisions (Chambers and Wetherill, 1998). This chaotic phase, lasting tens of millions of years, is characterized by violent impacts between protoplanetary bodies, such as the Moon-forming giant impact, ultimately forming a small number of terrestrial planets with masses comparable to Earth (Morbidelli et al., 2012, and references therein).

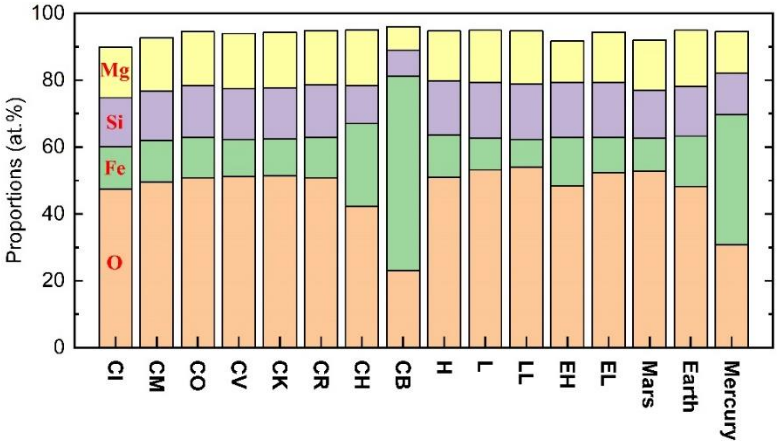

**Figure 1.3.** Major elements abundances of chondritic meteorites and terrestrial planets in the Solar System. Venus is excluded due to insufficient available data. The figure is modified from McDonough and Yoshizaki (2021) and references can be found in the original publication.

More recently, the "pebble accretion" scenario (Fig. 1.2b) has been proposed as an alternative model for planet formation, wherein planetary embryos grow to planets by accreting sunward-drifting pebbles from the outer disk under the influence of gas drag (Ormel and Klahr, 2010; Lambrechts and Johansen, 2012). Pebble accretion is significantly faster than planetesimal accretion and may explain the rapid formation of giant planet cores (e.g., Lambrechts and Johansen, 2012; Levison et al., 2015a). While numerical models suggest that terrestrial planets could also form through pebble accretion (Levison et al., 2015b; Johansen et al., 2021), this theory remains debated from geochemical and cosmochemical perspectives (e.g., Burkhardt et al., 2021; Olson et al., 2024; Morbidelli et al., 2025).

It is widely accepted that terrestrial planets may accrete from materials with compositions similar to chondritic meteorites—primitive and undifferentiated materials formed during the earliest stages of the Solar System (McDonough and Sun, 1995; Palme and O'Neill, 2014; Frost and Myhill, 2016). This is supported by the fact that the major element composition of chondritic meteorites (Wasson and Kallemeyn, 1988), while not identical to any known extant meteorite type (see Fig. 1.3), closely resembles both the solar photosphere's composition and the terrestrial planets (O'Neill and Palme, 1998; McDonough and Sun, 1995). The diversity in the compositions of terrestrial planets may result from variations in their building blocks, accretion histories, and post-accretion processes, such as collisional erosion (e.g., O'Neill and Palme, 2008)

## 1.2 Composition and Temperature of Earth's mantle

The composition of the bulk silicate Earth (BSE) has been constrained using petrological methods. A representative example is the pyrolitic model proposed by Ringwood (1975), which, based on petrological constraints, provides a composition that aligns well with geophysical observations (Dziewonski and Anderson, 1981) of the upper mantle and, to some extent, the upper part of the lower mantle (Ricolleau et al., 2009; Irifune et al., 2010). However, as Earth is differentiated into distinct layers (Fig. 1.4), whether the chemical composition of the lower mantle is consistent with that of the upper mantle—i.e., is aligned with the classic pyrolitic model—remains a subject of active debate (e.g., Irifune et al., 2010; Murakami et al., 2012; Kurnosov et al., 2017; Murakami et al., 2024). In addition to the pyrolitic model, alternative models proposing an Mg/Si ratio in the lower mantle of ~1.0—significantly lower than the pyrolitic model's ratio of ~1.2 and consistent with a chondritic BSE composition—have also been suggested. These chondritic models are supported by some studies of the elastic properties of lower mantle minerals, which indicate they may provide a better fit to observed seismic profiles of the lower mantle (Murakami et al., 2012; Mashino et al., 2020). This controversy stems primarily from the lack of sufficient direct measurements of acoustic velocities in mantle minerals under simultaneous high-pressure and high-temperature (P-T) conditions, as well as across the compositional ranges plausible for the mantle. Resolving this question requires further extensive experimental studies on the elastic properties of lower mantle minerals.

As illustrated in Fig. 1.4, the pyrolitic model suggests that Earth's upper mantle consists of ~50%–60% $(Mg,Fe)_2SiO_4$ olivine and its high-pressure polymorphs, which evolve with depth. The remaining composition primarily consists of clinopyroxene (cpx), orthopyroxene (opx), and garnet, with the majoritic component in garnet progressively increasing with depth until all pyroxenes are fully incorporated into the garnet structure (Ringwood, 1991). The $(Mg,Fe)_2SiO_4$ ringwoodite breaks down to bridgmanite and ferropericlase at approximately 23 GPa, corresponding to the 660 km seismic discontinuity (Ito and Takahashi, 1989; Ishii et al., 2019). This is accompanied by a gradual transformation of garnet into bridgmanite up to ~26 GPa (Irifune et al., 1996; Ishii et al., 2023). The lower mantle is primarily composed of ~75% Fe- and Al-bearing $MgSiO_3$ bridgmanite, ~20% (Fe,Mg)O ferropericlase, and ~5% Al- and Ti-bearing $CaSiO_3$ perovskite (Davemaoite). In the lowermost lower mantle, bridgmanite may transform into the post-perovskite phase, which has been proposed to explain the D” discontinuity (Murakami et al., 2004; Oganov and Ono, 2004; Shim et al., 2004). Recent studies also suggest that the $CaSiO_3$ solubility in bridgmanite increases with pressure, potentially eliminating the Davemaoite in the deep lower mantle (Ko et al., 2022). If the lower mantle has a chondritic composition (Murakami et al., 2012), with a smaller Mg/Si ratio than that of the pyrolitic model, the proportion of ferropericlase would be reduced to only 5–10%, and the lower mantle would be primarily dominated by bridgmanite (Murakami et al., 2024).

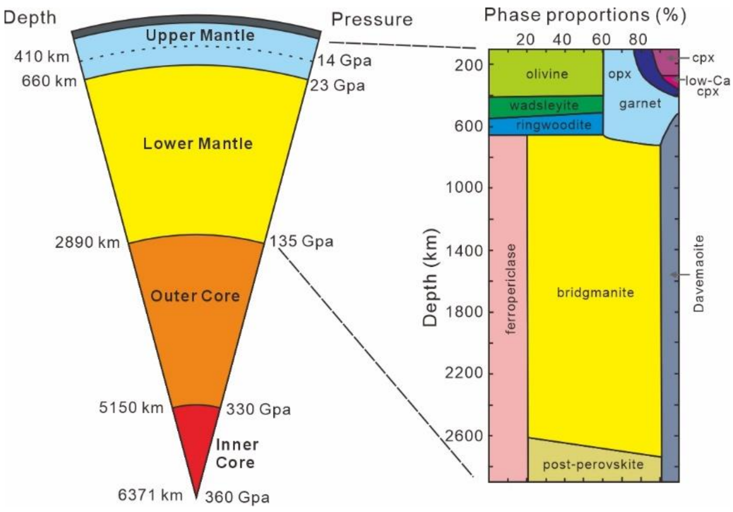

**Figure 1.4.** The structure and mineral assemblages of Earth’s interior. The mineral assemblages are based on the pyrolitic compositional model. Illustration of mineral assemblages modified from Irifune and Tsuchiya (2007).

The chemical composition of the BSE remains a topic of debate, and similarly, the temperature within Earth’s interior is also highly uncertain. Since direct measurement of Earth’s deep interior temperature is not possible, it can only be estimated using indirect methods. One of the most effective methods to estimate the mantle’s temperature is to determine the adiabatic temperature profile using the thermodynamic properties of its constituent minerals (Katsura et al., 2010; Katsura, 2022). The adiabatic temperature gradient with depth can be expressed as:

$$\left(\frac{dT}{dz}\right)_S = \frac{\alpha g T}{C_P} \tag{1.1}$$

where $\alpha$ is thermal expansivity, $g$ is the gravitational acceleration, T is temperature, and $C_P$ is the isobaric heat capacity of the mineral assemblage. The values of $\alpha$ and $C_P$ for each constituent mineral can be determined by fitting the data from calorimetry measurements and high-pressure and high-temperature (HP-HT) experiments into a self-consistent thermodynamic model (Stixrude and Lithgow-Bertelloni, 2022). Once the temperature at a fixed depth is established, the mantle's adiabatic temperature profile can be derived.

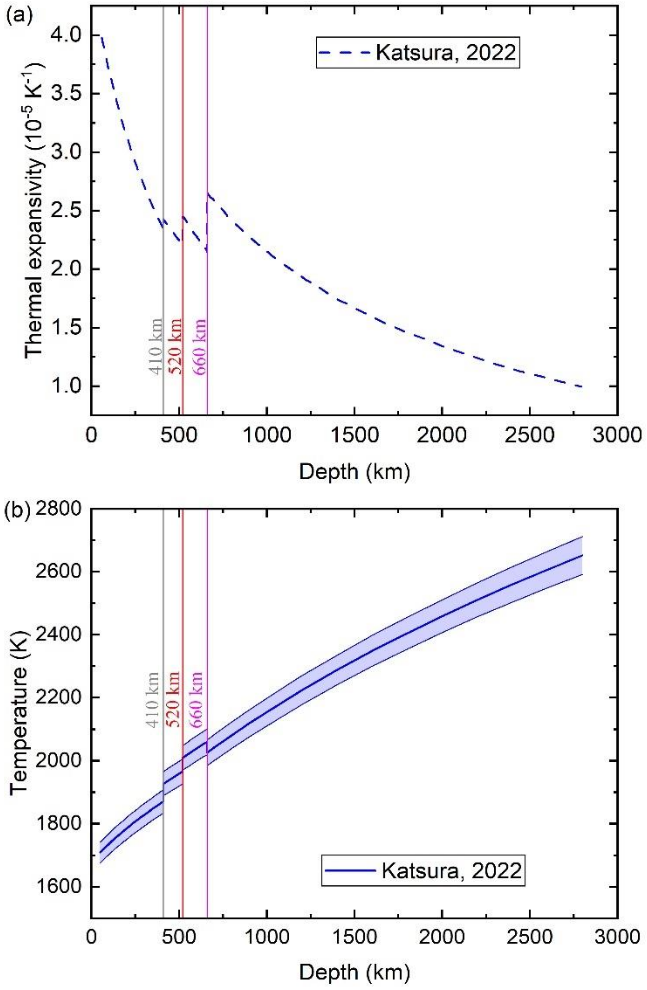

**Figure 1.5.** Thermal expansivity (a) and the adiabatic temperature profile (b) in the mantle, as determined by Katsura (2022).

Katsura et al. (2010) and Katsura (2022) estimated the temperature of the 410 km seismic discontinuity (D410) as a fixed reference point for the adiabatic temperature profile. D410 is widely accepted to result from the olivine-wadsleyite phase transition. Since the pressure at D410 is known, the temperature at this depth can be calculated using experimentally determined phase diagrams (Katsura et al., 2004). The thermal expansivity and the adiabatic temperature gradient of the mantle, as determined by Katsura (2022), are illustrated in Fig. 1.5.

While the adiabatic temperature profile provides insights into the average temperature at a given depth, inclusions in natural diamonds can offer valuable information about localized temperature conditions in the deep mantle. For instance, thermobarometry-thermometry methods, which involve measuring residual pressures of inclusions still trapped in diamonds, can help evaluate the pressure-temperature trajectory along which entrapment likely occurred (Angel et al., 2022). Moreover, the presence of minor elements in natural ferropericlase inclusions—the most common type of inclusion found in proposed sublithospheric diamonds (Walter et al., 2022)—may reveal critical insights into the pressure and temperature conditions of equilibrium. The mantle's temperature distribution is nonuniform, often influenced by cold subduction slabs (van Keken and Wilson, 2023) or hot mantle plumes (Koppers et al., 2021), and diamond inclusions could provide unique constraints on these localized environments.

## 1.3 Recent Advances in Understandings the Interior of Mars

Following Earth, Mars is the second most extensively explored planet in our Solar System, owing to the achievements of numerous Mars exploration missions since the 1960s, which continue to advance our understanding today (e.g., Banerdt et al., 2020; Farley et al., 2020; Tian et al, 2021). Complementing these space missions, systematic studies of Martian meteorites—shergottites, nakhlites, and chassignites (collectively known as SNC meteorites)—have provided valuable constraints on Mars' composition and evolution (e.g., Wänke and Dreibus, 1994; Sanloup et al., 1999; Taylor, 2013; Yoshizaki and McDonough, 2020; Khan et al., 2022). Mars differs from Earth in size, formation timing (Dauphas and Pourmand, 2011), and chemical and isotopic composition (e.g., Yoshizaki and McDonough, 2020), suggesting that it accreted from a distinct population of planetesimals and/or pebbles and underwent a unique evolutionary path. Comparative studies of Earth and Mars, therefore, offer valuable insights into the compositions and evolutionary processes of the terrestrial planets and the broader inner Solar System.

During the period of this thesis work, the seismic observations from NASA's InSight mission have significantly enhanced our understanding of the interior structure of Mars. Based on the seismic constraints, the thickness of the Martian crust has been determined to be at the range between 24 and 72 km (Knapmeyer-Endrun et al., 2021). The data have also revealed a very thick lithosphere (~500 km) and low S-wave velocities in the upper mantle, indicating a distinct thermal and compositional structure (Khan et al., 2021).

Furthermore, seismic measurements have determined the size and P-wave velocity of the Martian core (Stähler et al., 2021; Irving et al., 2023), suggesting significant enrichment in light elements (Fig. 1.6). Models assuming a homogeneous Martian mantle (Fig. 1.7a) indicate the light-element content of the core to be as high as ~30% (Stähler et al., 2021; Irving et al., 2023; Samuel et al., 2023). When a basal magma layer (BML) is incorporated into the models (Samuel et al., 2023; Khan et al., 2023), as shown in Fig. 1.7b, the resulting density deficit is smaller but still approximately ~20%, significantly higher than the ~5–10% estimated for Earth's core (e.g., Hirose et al., 2013).

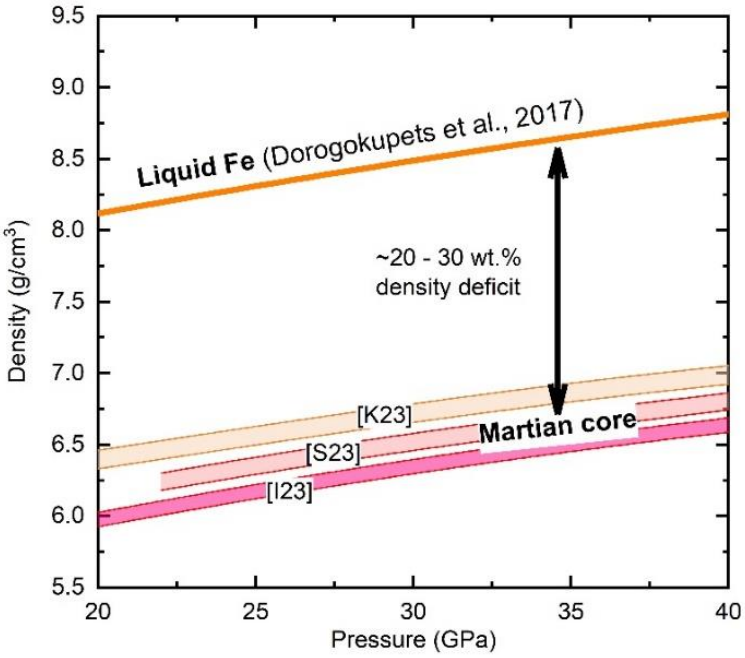

**Figure 1.6.** Comparison of the density models of Martian core with the density of liquid Fe under the relevant pressures. (I23: Irving et al., 2023; S23: Samuel et al., 2023; K23: Khan et al., 2023).

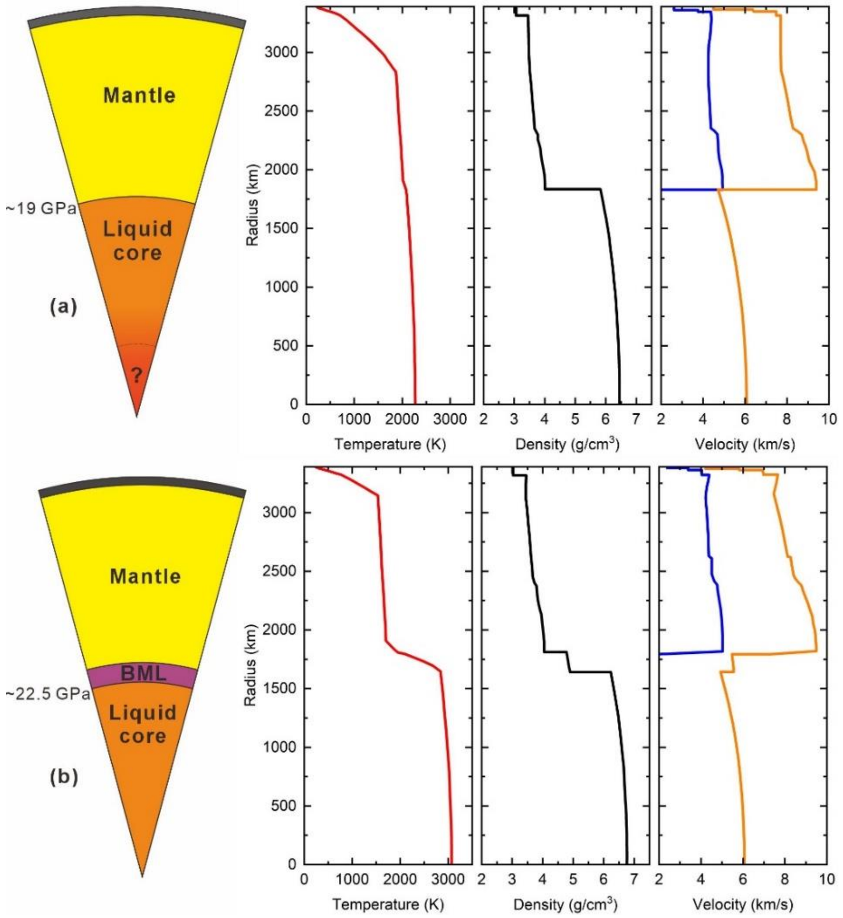

**Figure 1.7.** Internal structure and physical properties (temperature, density, and seismic velocity) of the Martian interior. (a) Model without a basal magma layer (BML). (b) Model incorporating a BML. Data adapted from Samuel et al. (2023).

From cosmochemical and geochemical perspectives, S is often considered the primary light element in the Martian core, alongside other potential candidates such as O, C, and H (e.g., Wänke and Dreibus, 1994; Sanloup et al., 1999; Taylor, 2013; Yoshizaki and McDonough, 2020; Khan et al., 2022). The enrichment of S in the Martian core is primarily supported by the observation of sulfur depletion in the Martian mantle, the fact that Mars appears more enriched in moderately volatile elements compared to Earth (e.g., Wänke and Dreibus, 1994), and sulfur's highly siderophile behavior at the moderate high pressure and temperature conditions likely to have prevailed during core-mantle differentiation of Mars (e.g., Rose-Weston et al., 2009; Suer et al., 2017; Steenstra and van Westrenen, 2018). If the effects of light elements on the density and P-wave velocity of liquid iron under HP-HT conditions are systematically constrained through experimental and theoretical studies, the composition of light elements in the Martian core could be determined in greater detail. However, experimental measurements of liquids under such conditions remain highly challenging, with significant uncertainties and notable discrepancies in the literature. Additionally, while theoretical calculations often show good agreement with experimental observations under the HP-HT conditions relevant to Earth's core, they face challenges when modeling liquid Fe alloys at the lower P-T conditions pertinent to the Martian core (e.g., Dewaele et al., 2008; Wagle and Steinle-Neumann, 2019). These challenges complicate the interpretation of seismic data, emphasizing the need for further studies to better constrain the elastic properties of Fe-rich liquid alloys under HP-HT conditions.

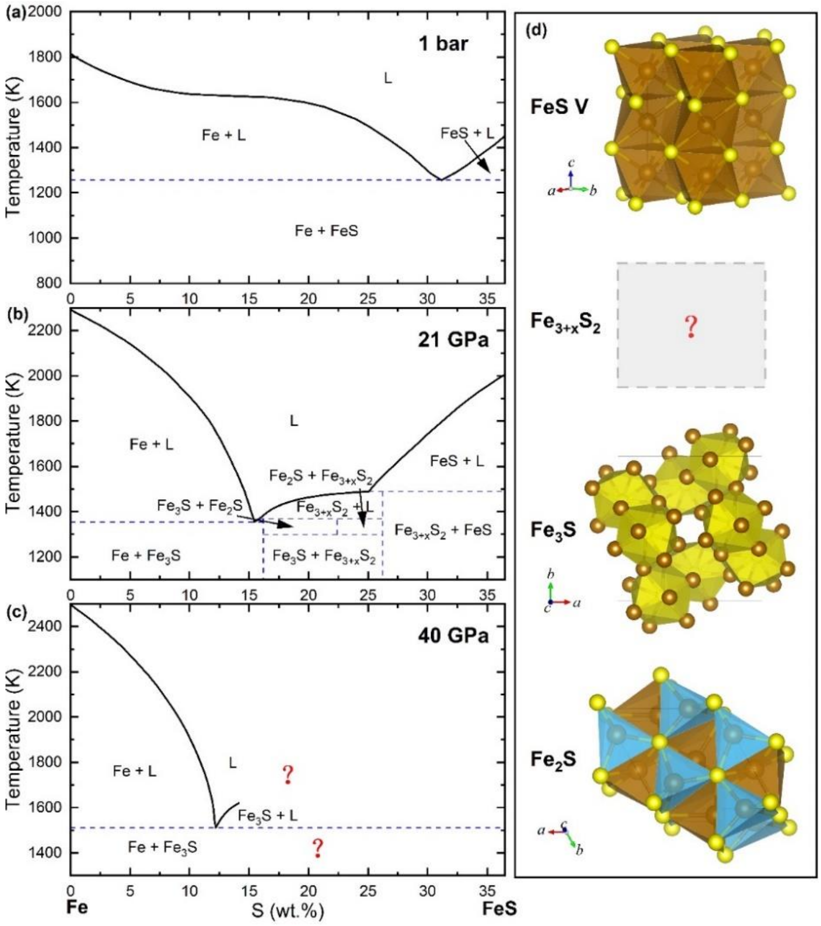

**Figure 1.8.** Phase diagrams and stable sulfide structures in the Fe-FeS system. (a) Fe-FeS phase diagram at 1 bar, modified from Waldner and Pelton (2005). (b) Fe-FeS phase diagram at 21 GPa, modified from Fei et al. (2000). (c) Fe-FeS phase diagram at 40 GPa, modified from Stewart et al. (2007). (d) Crystal structure models of FeS V (Fei et al., 1998), $Fe_3S$ (Koch-Müller et al., 2002), and $Fe_2S$ (Koch-Müller et al., 2002). The crystal structure of $Fe_{3+x}S_2$ remains unknown. "L" indicates liquid in (a-c). Brown and yellow spheres in (d) represent Fe and S atoms, respectively.

Another unresolved question in Martian core science is the potential existence of an inner core. While no direct geophysical evidence has confirmed or refuted the presence of a solid Martian inner core, the possibility of an inner core and the core crystallization regimes can be evaluated using the melting phase diagrams of Fe-rich alloys. Assuming S is the primary light element in the Martian core, Fe-FeS melting phase diagrams (Fig. 1.8) provide a framework for simulating Martian core crystallization (e.g., Fei et al., 2000; Stewart et al., 2007). The potentially high S content in the Martian core suggests that Fe sulfide phases could crystallize. However, the S-rich side of the Fe-FeS melting phase diagram remains incomplete under Martian core conditions. While melting phase relations in the S-rich region have been studied near the top of the Martian core (Fei et al., 2000), the deep-core conditions remain unexplored. Furthermore, the liquidus phase $Fe_{3+x}S_2$ (Fei et al., 1997), stable above ~14 GPa, lacks a resolved crystal structure. These gaps hinder precise modeling of Martian core crystallization, emphasizing the need for further experimental research.

This thesis aims to provide new constraints on the compositions and conditions of terrestrial planetary interiors using multiple experimental approaches. First, it seeks to constrain the temperature of Earth's mantle by applying experimental results on the MgO-FeO-$Al_2O_3$ system under high pressures to analyze ferropericlase inclusions found in natural diamonds that are proposed to originate from the deep mantle. Additionally, it integrates results from various HP-HT experimental methods, with a particular focus on the Martian core's composition and structure by comparing experimental results in Fe-S system with recent geophysical observations from NASA's InSight mission.

# 2 Method

The large volume press (LVP) and diamond anvil cell (DAC) are widely used tools for generating static high-pressure conditions that simulate the environments within planetary interiors (Ito et al., 2007; Bassett, 2009). The LVP can provide a well characterized and shallow thermal gradient over a relatively large sample volume, typically around cubic millimeters in size. Importantly, it also enables a thermodynamically closed system with an appropriate experimental assembly design. However, the pressure generation capability of the LVP is somewhat limited, reaching approximately 25 GPa with traditional multi-anvil techniques (Keppler and Frost, 2005). Recent advancements using binder-free tungsten carbide (WC) anvils with optimized geometry have increased this capacity to around 65 GPa (Kunimoto et al., 2016; Ishii et al., 2019), while pressures exceeding 100 GPa have been achieved using ultrahard, albeit costly, sintered polycrystalline diamond (PCD) anvils (Yamazaki et al., 2018). Despite these advancements, high absorption of electromagnetic waves by the LVP's ceramic pressure media and the limited angular access, restrict spectroscopic characterization methods. Consequently, powder X-ray diffraction (XRD) and X-ray radiography, typically using synchrotron-source white or high-energy monochromatic X-ray beams, remain the primary X-ray-based methods for characterizing samples in the LVP. (Shen and Wang, 2014)

In contrast, the DAC can generate pressures up to 1 TPa (Dubrovinskaia et al., 2016; Dubrovinsky et al., 2022), encompassing the pressure range of Earth's entire interior and simulating conditions found within giant planets and exoplanets. The transparency of diamond anvils across a broad spectrum—from infrared to visible light and X-ray—enables the DAC to support multiple in-situ high-pressure characterization techniques (Shen and Mao, 2016). Notably, recent advancements in high-pressure single crystal X-ray diffraction (SC-XRD) using DACs have made this technique even more powerful for characterizing material structures under extreme conditions (Dubrovinskaia and Dubrovinsky, 2018). However, although temperatures up to 7000 K can be achieved through laser heating in the DAC (Dewaele et al., 1998), samples typically experience significant temperature gradients in a laser-heated diamond anvil cell (LH-DAC). This gradient can lead to substantial compositional variations across the sample (Sinmyo and Hirose, 2010), complicating the attainment of thermodynamic equilibrium.

In this study, a complementary approach was applied, leveraging multiple techniques to analyze the same system from different perspectives. Both conventional and advanced multi-anvil techniques were employed to investigate equilibrium phase relations in materials under conditions analogous to Earth's mantle and the Martian core. Additionally, in-situ synchrotron-based multi-anvil techniques in conjunction with ultrasonic interferometry, Beer-Lambert X-ray absorption, and the CAESAR method—combining angle- and energy-dispersive structural analysis and refinement—were utilized to examine the elasticity of Fe-rich liquids under planetary core conditions. Furthermore, high-pressure single crystal XRD measurements in a DAC were conducted following *in-situ* sample synthesis via laser heating.

## 2.1 High Pressure and High Temperature Experiments in a Multi-anvil Press

### *2.1.1 In situ Multi-anvil Experiments at Synchrotron Beamlines*

Synchrotron radiation generates extremely bright electromagnetic waves with a wide energy range and sharp directivity (Schwinger, 1949). This occurs when relativistic electrons are accelerated along a curved path by magnetic fields. Synchrotron radiation facilities can produce high-brilliance hard X-ray beams that penetrate sample assemblies in multi-anvil experiments, enabling in-situ monitoring of sample conditions—including pressure, temperature, phase assemblages, and sample dimensions—under high-pressure and high-temperature conditions.

Although both energy-dispersive X-ray diffraction (ED-XRD) and angle-dispersive X-ray diffraction (AD-XRD) can be applied in in-situ multi-anvil experiments, ED-XRD is the primary technique used (Ito et al., 2007; Shen and Wang, 2014). A schematic of in-situ multi-anvil experiments is shown in Fig. 2.1. The advantages of ED-XRD over AD-XRD in conventional synchrotron multi-anvil experiments include: (1) ED-XRD provides information across a wider range of d-spacings compared to AD-XRD, which is constrained by the limited opening angle due to the use of X-ray-opaque tungsten carbide anvils; (2) the photon flux of the white beam used for ED-XRD is much greater than that of the monochromatic beam required for AD-XRD, resulting in higher intensity; and (3) ED-XRD provides a cleaner sample signal and clearer background from the multi-anvil assembly, as the measurement area can be limited to the sample region through the use of a collimator and receiving slits which reduce contaminating signals from the surrounding pressure medium (Fig. 2.1c).

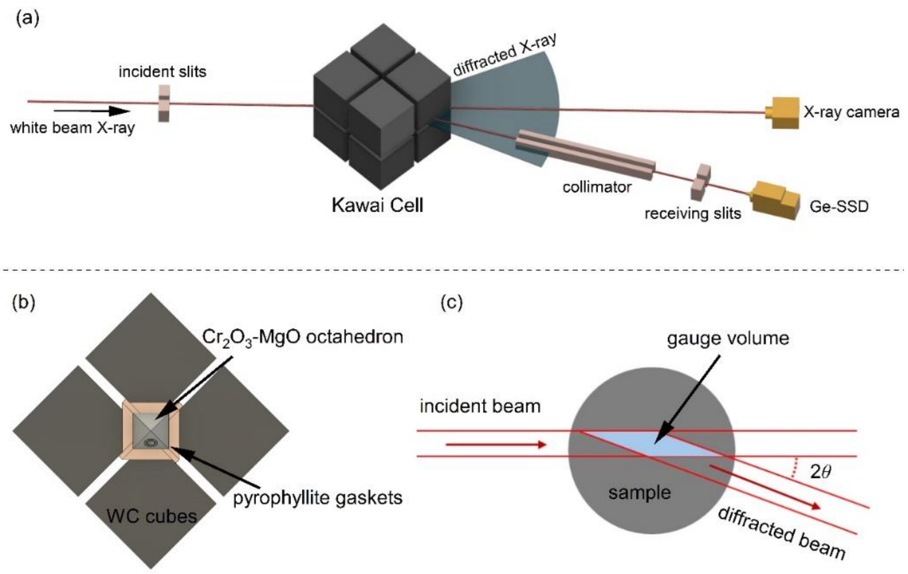

**Figure 2.1.** Schematic representation of in-situ multi-anvil experiments conducted at a synchrotron beamline. (a) Experimental setup for in-situ XRD and X-ray radiographic imaging at high pressures and temperatures. Note: the sketch is not to scale, and the multi-anvil press is omitted for clarity. (b) Configuration of the Kawai cell used in the experiments. (c) Gauge volume for ED-XRD measurements.

In the present study, in-situ multi-anvil experiments using synchrotron-based X-ray techniques were conducted at beamline P61B at PETRA III (Farla et al., 2022), beamline PSICHE at SOLEIL (Henry et al., 2022), and beamline 13IDD at the APS (Wang et al., 2009). The multi-anvil press at P61B is a 6-axis press (Aster-15), with six independently controlled rams used to compress a cubic space (Manthilake et al., 2012; Farla et al., 2022). The presses at PSICHE and 13IDD are uniaxial presses featuring Osugi-type (DIA-type) and split-sphere-type guide blocks, respectively (King et al., 2022; Wang et al., 2009). In all experiments, hydraulic forces were applied to the sample assemblies via Kawai cells, which consist of eight tungsten carbide cubes with truncated corners directed toward the sample assemblies (Fig. 2.1). For further details on the descriptions and classifications of multi-anvil facilities, refer to Ito et al. (2007) and Keppler and Frost (2005).

Sample temperatures were monitored using the electromotive force (EMF) of a type-D thermocouple. When the thermocouple failed, temperatures were estimated based on power-temperature relations determined from similar experiments. Sample pressures were assessed by comparing the unit-cell volumes of pressure standards, measured via ED-XRD, with the equations of state (EOSs) of standard materials found in the literature. Sample positioning in directions perpendicular to the beam was tracked through X-ray imaging, based on absorption contrast. To optimize positioning along the beam direction, the press was scanned along the beam to locate the point where the diffraction signal from the sample was strongest and interference from regions outside the sample was minimized. Taking into account factors such as temperature gradients within the sample, temperature fluctuations during experiments, fitting errors in the unit cell volume of pressure markers, and the accuracy of pressure markers, the experimental uncertainties in temperature and pressure were estimated to be approximately 50 K and 0.5 GPa, respectively.

### *2.1.2 In house Multi-anvil Experiments*

Complementary to the in-situ synchrotron multi-anvil experiments, in-house multi-anvil facilities offer easier access for conducting time-consuming experiments, as synchrotron beamtime is generally limited and highly competitive. In this study, multi-anvil presses at the Bayerisches Geoinstitut (BGI), University of Bayreuth, were utilized for in-house runs. Pressures during these experiments were determined using pre-calibrated press load–pressure relationships, based on the detection of pressure-induced phase transitions or changes in mixing behavior under applied loads. Additionally, these calibrations were complemented by comparisons with press load–pressure relationships established during synchrotron multi-anvil experiments conducted with the same type of multi-anvil press and guide blocks.

For multi-anvil experiments at pressures up to 23 GPa, we used multi-anvil presses equipped with split-sphere guide blocks (Hymag and Sumitomo), with pressure calibrations described by Keppler and Frost (2005) as illustrated in Fig. 2.2. In these experiments, a $Cr_2O_3$-doped MgO octahedral pressure medium with a 10 mm edge length (OEL = 10 mm) was compressed using eight tungsten carbide cubic anvils (Ha06 cubes from Hawedia) with truncation edge lengths (TEL) of 4 mm or 5 mm, depending on the pressure requirements. For higher pressures, ranging from 27 GPa to 50 GPa, we used the IRIS-15 press equipped with an Osugi-type guide block (Ishii et al., 2016). Cell assemblies with OEL/TEL ratios of 7 mm/3 mm and 5.7 mm/1.5 mm (F05 cubes from Fuji Die Co. Ltd.) were employed for experiments at 27 GPa and 33 GPa, respectively

(Ishii et al., 2016; Liu et al., 2017). For the experiment at 50 GPa, a 5.7 mm/1.5 mm cell assembly was used in conjunction with eight ultrahard 1°-tapered TJS01 tungsten carbide anvils (Fuji Die Co. Ltd.), calibrated according to Ishii et al. (2019). The pressure calibrations used for the IRIS-15 press are summarized in Fig. 2.3.

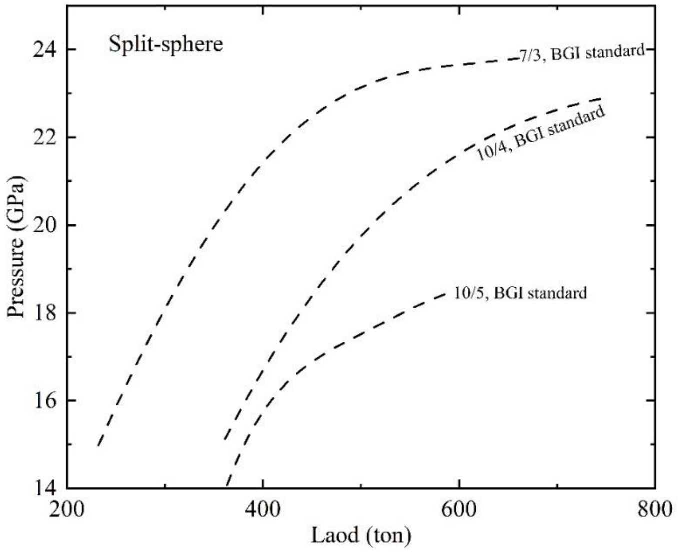

**Figure 2.2.** Pressure calibrations for experiments conducted in multi-anvil presses equipped with split-sphere modules at BGI. Adapted from Keppler and Frost (2005).

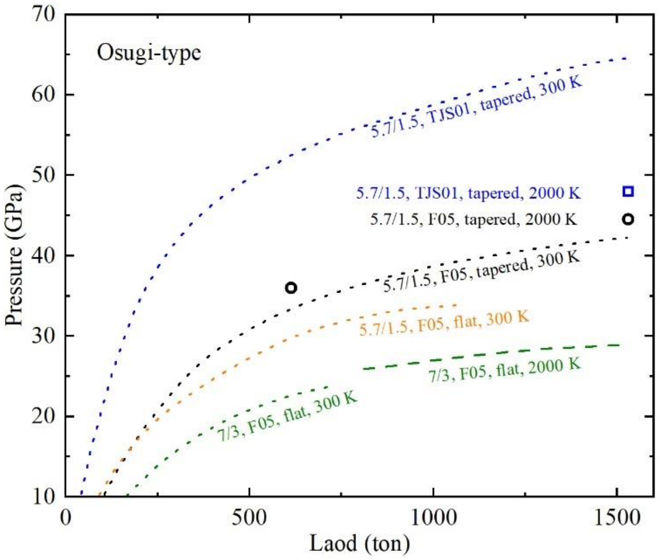

**Figure 2.3.** Pressure calibrations for experiments conducted in a multi-anvil press with an Osugi-type module (IRIS-15) at BGI (Ishii et al., 2016; Ishii et al., 2017; Liu et al., 2017).

## 2.2 Determination of Elastic Properties of Liquids under High Pressure

Due to the lack of long-range order in liquid structures, densities cannot be directly determined by measuring lattice parameters as is the case for solids. Experimental challenges in measuring the elastic properties of liquids have led to significant uncertainties and notable discrepancies in the literature. To better constrain the elastic properties of Fe metal-rich liquids, this work employed multiple in-situ methods independently and simultaneously at synchrotron multi-anvil beamlines. P-wave velocities under high-pressure and high-temperature conditions were measured using the ultrasonic interferometry method, while liquid densities were evaluated using the Beer-Lambert method and X-ray diffraction.

### *2.2.1 P-wave Velocity of Liquids measured by ultrasonic Interferometry*

There are two main methods for performing ultrasonic wave velocity measurements: the phase comparison method (Rigden et al., 1988) and the pulse-echo overlap method (Papadakis et al., 1974). Due to the simplicity of data analysis and the system required (Jing et al., 2020; Néri et al., 2024), the pulse-echo overlap method was employed in this study to perform ultrasonic measurements.

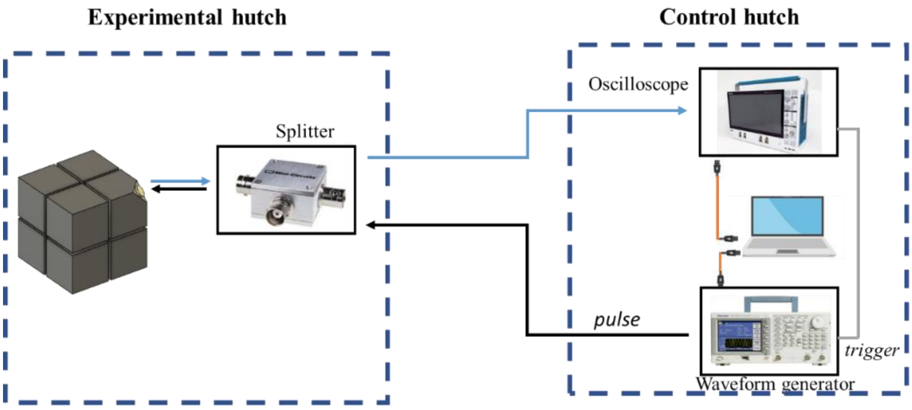

**Figure 2.4.** Schematic illustration of the ultrasonic interferometry system used at the synchrotron beamline.

Fig. 2.4 illustrates the ultrasonic interferometry system installed as a permanent setup at beamline P61B, PETRA III (Néri et al., 2024), which was used for our measurements. A similar ultrasonic interferometry system is also employed at BGI as an in-house facility and was temporarily installed at beamline PSICHE, SOLEIL during our beamtime there. The ultrasonic interferometry system consists of a $LiNbO_3$ piezoelectric crystal, an arbitrary waveform generator, and a digital oscilloscope, all connected via coaxial cables. Additional details about the ultrasonic system used at 13IDD, APS can be found in the review by Jing et al. (2020).

During measurements, the arbitrary waveform generator sends bursts of sinusoidal AC pulses of a fixed frequency to the transducer. The transducer then vibrates and generates compressional and/or shear waves, which are transmitted to the sample through the WC anvil and the buffer rod (BR). Reflections of the acoustic waves at various interfaces—including the BR-sample interface and the sample-backing plate (BP) interface—were recorded by the digital oscilloscope (Fig. 2.5).

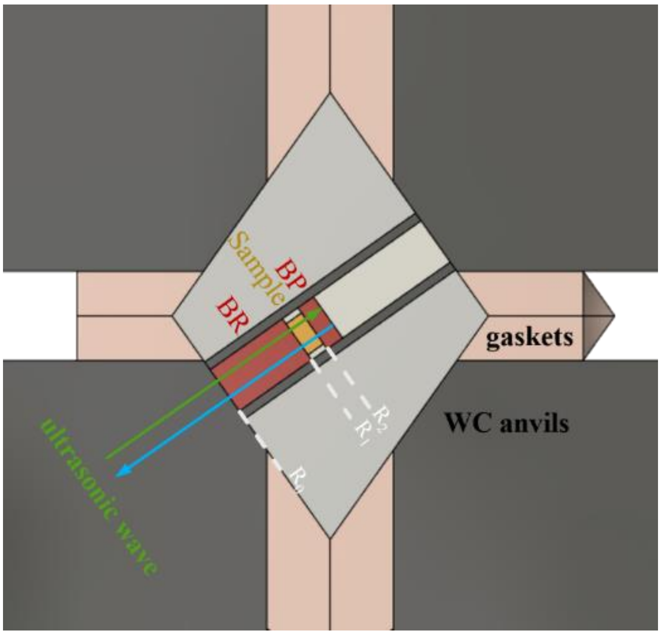

**Figure 2.5.** Schematic illustration of ultrasonic wave propagation through the high-pressure assembly during ultrasonic interferometry measurement. BR denotes the buffer rod, and BP indicates the back plates. $R_0$, $R_1$, and $R_2$ represent the interfaces of the anvil-BR, BR-sample, and sample-BP, respectively, where the ultrasonic wave is reflected due to acoustic impedance contrasts.

The arbitrary waveform generators used at BGI, P61B, and 13IDD were the Keysight Trueform 33622A, Tektronix AFG3152C, and Tektronix AFG3252C models, respectively. The digital oscilloscopes used at these facilities were the Keysight DSOS054A at BGI, Tektronix MSO64 at P61B, and Tektronix MSO54 at 13IDD. To generate longitudinal waves along the height of the cylindrical samples, 36°-Y cut $LiNbO_3$

transducers were attached to the backside of the WC anvils. These transducers had been fabricated into 2.5 mm or 3 mm diameter disks from 3-inch diameter, 60 μm thick $LiNbO_3$ wafers (Yamaju Ceramics) using a picosecond pulsed laser cutter. The transducers used at this study have a relatively wide bandwidth, with good performance at frequencies between 45 MHz to 75 MHz.

The travel times through the samples at each frequency were analyzed using the Echofinder software (Néri et al., 2024), allowing the calculation of sound velocities with the known sample lengths. During the experiments, the sample lengths were monitored *in situ* using X-ray radiography, which relied on the absorption contrast between the Fe-rich samples and the backing plate (BP) and buffer rod (BR).

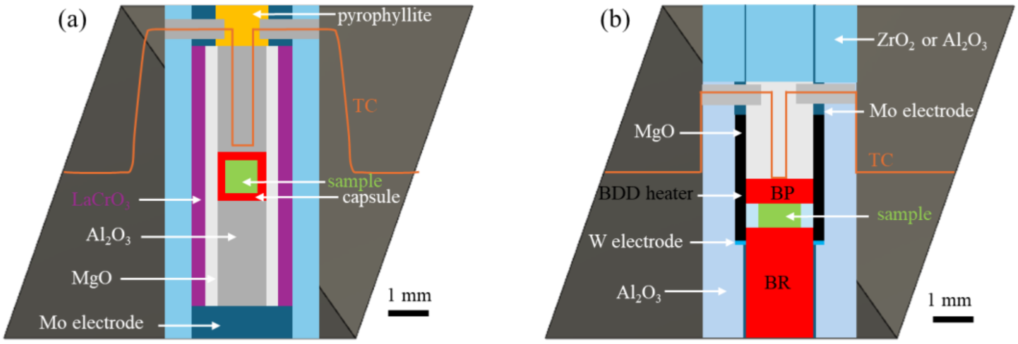

**Figure 2.6.** Assemblies for multi-anvil experiments using $LaCrO_3$ and BDD furnaces. (a) Standard 10-mm assembly with a $LaCrO_3$ furnace used for in-house experiments. (b) 10-mm assembly with a BDD furnace, developed in this study for synchrotron ultrasonic interferometry experiments.

Maintaining liquids within the capsule under high-pressure and high-temperature conditions, while preserving a regular shape with parallel surfaces presents a significant challenge in P-wave velocity measurements of liquids. To address this, we designed a novel assembly for ultrasonic interferometry measurements. As shown in Fig. 2.6, a boron-doped diamond (BDD) furnace was used in place of the conventionally employed $LaCrO_3$ heating elements employed for in-house experiments. The BDD furnaces utilized in this study were commercially available BDD tubes synthesized via chemical vapor deposition (CVD) methods (Changsha 3-Better Ultra-Hard Materials Co., Ltd). The use of CVD-BDD furnaces provided a stable thermal field for the samples under high pressures and facilitated synchrotron X-ray measurements due to the high X-ray transparency of BDD (Shatskiy et al., 2009; Xie et al., 2020). Additionally, the rigid structure of the BDD furnace minimized irregular deformation of the samples, thereby improving the precision of sample length measurements.

To further minimize sample deformation during compression, pre-processed samples were used to reduce the porosity of the starting materials as much as possible. For pure Fe samples, 1 mm diameter Fe wires with 99.99% purity were cut and subsequently double-side polished into the desired cylindrical shape. For S-bearing samples, Fe-FeS blocks were synthesized at 0.5–0.7 GPa and 1000 K using a piston-cylinder press and then machined into the desired cylindrical form.

### *2.2.2 Beer-Lambert Method*

The Beer-Lambert method is a widely used technique for determining the density of disordered samples under high pressure, based on measuring the relative change in X-ray attenuation upon melting (Katayama et al., 1993; Sanloup et al., 2000; Wang and Shen, 2014; Sakamaki, 2017; Henry et al., 2022). During a measurement, the sample with a nearly ideal cylindrical shape was scanned by X-ray beam along the radial direction (Fig. 2.7). Based on the Beer-Lambert Law, the density can be fitted from the absorption profile:

$$I(x) = I_0 \exp[-\mu_s \rho_s l_s(x) - \mu_{en} \rho_{en} l_{en}(x)] \tag{2.1}$$

where $x$ is the position along the absorption profile, $I_0$ and $I$ are the incident and transmitted beam intensities, respectively, $\mu$ is the mass absorption coefficient, $\rho$ is the density, and $l$ is the length of the beam path. The subscript $s$ and $en$ correspond to the sample and the surrounding assembly environment, respectively. As illustrated in Fig 2.7b., the length of the beam path can be expressed as:

$$l_s(x) = 2\sqrt{r^2 - (x - x_0)^2} \tag{2.2}$$

where $r$ is the radius of the sample, and $x_0$ is the center of an absorption profile.

In the conventional application of the Beer-Lambert law under high pressure, a monochromatic X-ray beam is typically used. The mass absorption coefficient, $\mu$, of the sample can either be calibrated by measuring the X-ray absorption of the sample in its solid state, where the density is known, or determined using theoretical values. However, as discussed in Chapter 2.11, the use of a white beam may offer significant advantages over a monochromatic beam for most multi-anvil experiments.

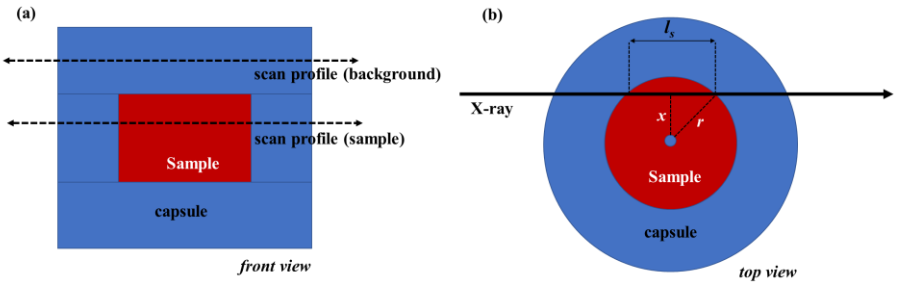

**Figure 2.7.** Schematic of the sample geometry for density measurements using the Beer-Lambert law, showing (a) the front view and (b) the top view. Here, $x$ denotes the position along the scan profile relative to the center of the capsule, $r$ is the sample radius, and $l_s$ indicates the sample thickness along the beam path.

In this study, we employed a recently developed method by Henry et al. (2022), which utilizes a polychromator placed in the beam path after the sample. The principle of this method involves measuring the ED-XRD pattern of the polychromator material (e.g., periclase or rutile) using a Ge detector, while scanning the sample with a white beam. At a specific position in the scanning profile, the intensity of the diffraction peaks at each energy is proportional to the intensity of the incident beam on the polychromator at the same energy, which corresponds to the transmitted beam intensity after being absorbed by the sample. As the Ge detector can simultaneously record a series of diffraction peaks from the polychromator, this setup enables the collection of multiple absorption profiles spanning energies from 20 keV to 80 keV using a white beam source at the beamline PSICHE.

This method offers several advantages. First, it is compatible with other X-ray techniques that rely on a white beam, such as the CAESAR method (see Chapter 2.3), allowing multiple measurements to be performed on the same molten sample. Additionally, the simultaneous collection of multiple absorption profiles provides a redundant dataset, which can reduce analytical uncertainties in density determination. For density measurements in this study, we used a newly designed high-pressure assembly (Fig. 2.8) with a CVD-BDD furnace and sintered samples, incorporating the same considerations as those applied for ultrasonic assemblies.

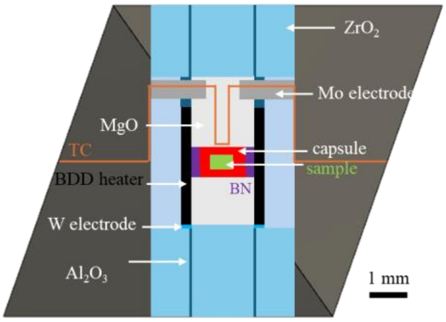

**Figure 2.8.** 10-mm assembly with a BDD furnace, designed in this study for in-situ density measurements using the Beer-Lambert method.

### *2.2.3 X-ray Diffraction on Liquids*

Although liquids lack long-range order, different liquids possess distinct local structures due to chemical bonding constraints, which are reflected in the diffuse scattering signals of their XRD patterns. By quantitatively analyzing the diffuse scattering signals, both structural information and densities of the liquids can be extracted from the XRD measurements. Using various static and dynamic compression techniques, the structure and density of liquids have been measured up to the megabar pressure range (Eggert et al., 2002; Morard et al., 2014; Drewitt, 2021; Morard et al., 2020; Singh et al., 2022), offering crucial insights into the physical properties of liquids and fluids in planetary interiors.

In this study, XRD measurements of Fe-S liquids were performed simultaneously with some of the ultrasonic interferometry and Beer-Lambert measurements at the PSICHE beamline, utilizing the combined angular and energy dispersive structural analysis and refinement (CAESAR) technique (Wang et al., 2005; King et al., 2022). During a CAESAR acquisition, a series of ED-XRD spectra are collected at varying 2θ angles with fine increments (typically less than 0.5°), achieved by adjusting the position of the Ge detector mounted on a rotation stage. As the Ge detector moves, the incident and diffracted beams remained aligned at a fixed point on the sample, while the slits are continuously adjusted to maintain an optimized gauge volume. A two-dimensional Energy-Angle-Intensity dataset was generated from each CAESAR acquisition, where the data at each 2θ angle corresponded to an ED-XRD spectrum, and each detector channel effectively served as an individual AD-XRD spectrum (Fig. 2.9).

The CAESAR data collection covers the maximum accessible range of the opening angle of a multi-anvil press, enabling the acquisition of XRD data over the widest possible range of the scattering vector $Q$ ($Q = 4\pi \sin(\theta)/\lambda$) (see Fig. 2.10). Compared to conventional multi-angle ED-XRD methods, which collect spectra at only a few 2θ angles, the CAESAR method generates a highly redundant dataset. This redundancy facilitates efficient background subtraction and data reduction (Wang et al., 2005; King et al., 2022). By applying the data treatment strategy outlined by King et al. (2022), a diffuse scattering profile with normalized intensity can be obtained directly from the CAESAR dataset without requiring additional empirical normalization factors.

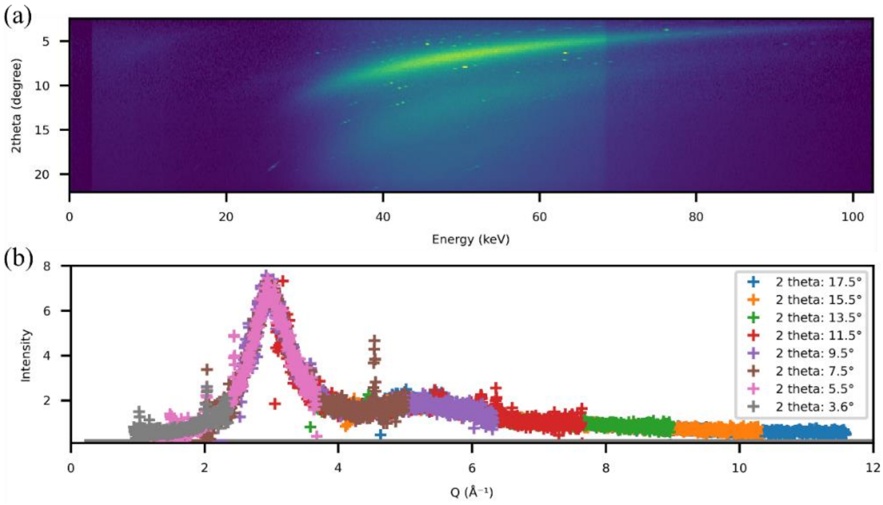

**Figure 2.9.** Example of XRD measurement results on a liquid sample. (a) A CAESAR scan of Fe-S liquid at 4.8 GPa and 1873 K. (b) Normalized scattering intensity as a function of $Q$. Markers in different colors indicate data collected at various $2\theta$ angles, demonstrating consistency in diffraction intensity.

An iterative analytical procedure is then employed to extract structural information from the diffuse scattering data (Kaplow et al., 1965; Eggert et al., 2002; Morard et al., 2014), enabling the determination of the structure factor $S(Q)$ and the radial distribution function $g(r)$. Based on the Krogh-Moe-Norman normalization (Krogh-Moe, 1956; Norman, 1957), the structure factor is defined as

$$S(Q) = \frac{[\alpha I_S(Q) - \sum I_{Incoh}(Q)] + (\langle f \rangle^2 - \langle f^2 \rangle)}{\langle f \rangle^2} \tag{2.3}$$

where $f$ is the atomic form factor of constituent elements, $\langle f^2 \rangle = \sum_n X_n f_n^2(Q)$, $\langle f \rangle^2 = \sum_n \sum_m X_n f_n(Q) X_m f_m(Q)$, $X_n$ is the atomic ratio of nth element, $I_S$ is the scattering signal from the sample and $\sum I_{Incoh}(Q)$ is the sum of the incoherent scattering signals from the sample.

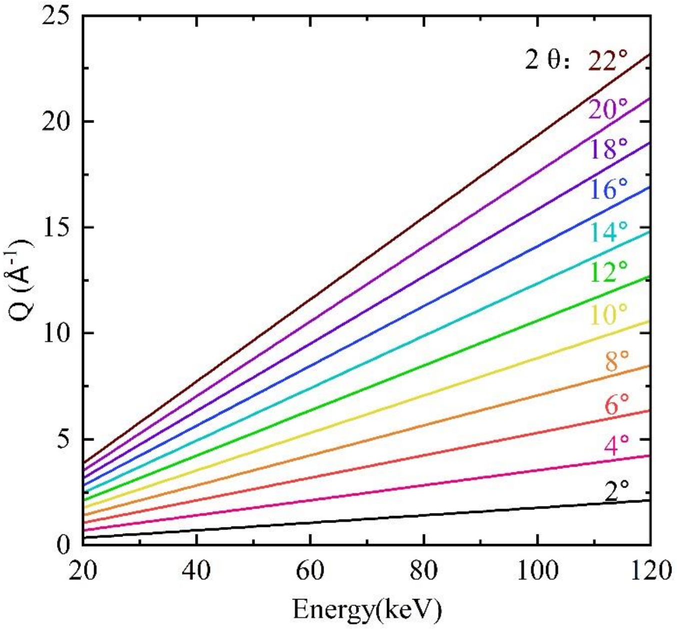

**Figure 2.10.** Scattering vector $Q$ as a function of energy with the Ge detector placed at various $2\theta$ angles. The values of $2\theta$ angles are indicated above each solid line.

The parameter $\alpha$ can be expressed as

$$\alpha = \frac{-2\pi^2\rho_0 + \int_0^{Q_{max}} \frac{\sum I_{Incoh}(Q) + \langle f^2 \rangle}{\langle f^2 \rangle} Q^2 dQ}{\int_0^{Q_{max}} \frac{I_S(Q)}{\langle f^2 \rangle} Q^2 dQ} \tag{2.4}$$

Where $\rho_0$ is the average density, and the $Q_{max}$ is the maximum value of the scattering vector. The distribution function $F(r)$ and the radial distribution function $g(r)$ can be defined by a Fourier transform of $S(Q)$:

$$F(r) = \frac{2}{\pi}\int_0^{Q_{max}} Q(S(Q)-1)\sin(Qr)\, dQ = 4\pi r[\rho(r) - \rho_0] \tag{2.5}$$

$$g(r) = \frac{F(r) + 4\pi r\rho_0}{4\pi r\rho_0} = \frac{\rho(r)}{\rho_0} \tag{2.6}$$

where $r$ is distance from the origin atom and $\rho(r)$ is the is the atomic density as a function of $r$.

It is assumed that no atoms are located at distances shorter than the first coordination shell. For $0 < r < r_{min}$, where $r_{min}$ is the minimum distance from the origin atom:

$$F(r) = -4\pi r \rho_0 \tag{2.7}$$

and

$$g(r) = 0 \tag{2.8}$$

An iterative procedure is employed to determine $S(Q)$, $F(r)$, $g(r)$, and $\rho_0$, ensuring that $F(r)$ exhibits minimal oscillations in the low-$r$ region. The iteration process concludes when the following $\chi^2$ function is minimized:

$$\chi^2(\rho_0) = \int_0^{r_{min}} [-F_i(r) - 4\pi r \rho_0]^2 dr \tag{2.9}$$

where $F_i$ is the distribution function after $i$-th iterations.

In the present study, the software Amorpheus (Boccato et al., 2022) was used to process the $I_S(Q)$ data of Fe-rich liquids. Following the estimation from Morard et al. (2014), the uncertainty of the density determined using this method is approximately 3 atom/nm$^3$, which corresponds to 0.3 g/cm$^3$.

## 2.3 Single Crystal Structure Determination in a Diamond Anvil Cell after Laser-Heating

Recent advancements in high-pressure single-crystal X-ray diffraction techniques (Dubrovinskaia and Dubrovinsky, 2018) have made it routine to study *in-situ* the crystal structures of µm- to sub-µm-sized grains synthesized in a laser-heated diamond anvil cell (LH-DAC) at high-pressure conditions. This technique has become a crucial tool for investigating materials under the extreme conditions of planetary interiors, particularly for synthetic phases whose crystal structures cannot be preserved at ambient pressure. In this study, we used high-pressure single-crystal X-ray diffraction to analyze the crystal structure of a novel high-pressure iron sulfide phase, synthesized *in situ* under high-pressure and high-temperature conditions in a DAC, as its structure cannot be retained upon decompression to ambient conditions.

### *2.3.1 In situ sample synthesis using Laser-heated Diamond Anvil Cell*

Gem-quality diamond anvils are transparent to a wide range of electromagnetic wavelengths, enabling interactions between the compressed sample in a DAC and various types of light. By absorbing the energy of lasers that pass through the diamonds and are focused on the sample (Fig 2.11), sample temperatures of the order of thousands of Kelvins can be reached (Ming and Bassett, 1974; Bassett, 2009).

Depending on the sample's absorption properties for laser light, either a near-infrared (IR) laser (wavelength = 1.064 μm) or a $CO_2$ laser (wavelength = 10.6 μm) can be selected for heating (Salamat et al., 2014; Anzellini and Boccato et al., 2020). In practice, a near-IR laser is commonly used to heat metallic phases and Fe-bearing opaque or semi-transparent minerals, while a $CO_2$ laser is preferred for heating optically transparent minerals. Consequently, in this study, a near-IR laser-heating systems was utilized to heat iron sulfide samples in DACs. The near-IR laser can be focused to a spot size ranging from a few micrometers to tens of micrometers on the sample surface (Anzellini and Boccato et al., 2020), making it advantageous for applications requiring a small heating area. This is particularly beneficial for laser-heating experiments at multi-megabar pressures, where the sample size is extremely small (Dubrovinsky et al., 2022). However, the small laser spot size can lead to steep temperature gradients, reaching up to hundreds of kelvins per micrometer in both radial and axial directions (Kavner and Nugent, 2008; Du et al., 2013; Geballe et al., 2012). The introduction of double-sided laser heating and the optimization of energy distribution within the laser spot help to reduce temperature gradients in LH-DAC experiments (Errandonea, 2006; Prakapenka et al., 2008).

In this study, the portable laser-heating system at the ID14 beamline at ESRF (Kupenko et al., 2012; Aprilis et al., 2017) and an in-house laser-heating system at BGI (Fedotenko et al., 2019), were used for LH-DAC experiments. We used a BX90-type diamond anvil cell (DAC) (Kantor et al., 2012) equipped with a pair of diamond anvils, each with a culet diameter of 250 μm. The diamonds were mounted on Boehler-type tungsten carbide seats (Boehler et al., 2004) to provide a relatively large optical opening angle. Back-transformed poorly crystalline iron sulfide crystals, synthesized in a multi-anvil press, were used as the starting material. The use of a pre-synthesized material with the desired composition ensures the correct chemical composition and homogeneity of the material within the minute laser-heated areas, which is critical for achieving reproducible experimental results. The samples were pre-compressed into pellets with a thickness of approximately 10 μm before being loaded into the sample chamber of the pre-indented Re gasket. KCl or helium were used as the pressure medium and thermal insulation layer, as illustrated in Fig. 2.11.

The samples were heated to temperatures above or near their solidus at the target pressures to promote crystal grain growth. Temperatures were estimated by fitting the sample's thermal radiation to a grey-body approximation. Once the target temperatures were reached, the samples were maintained at those conditions for 5 to 10 seconds before being quenched to room temperature.

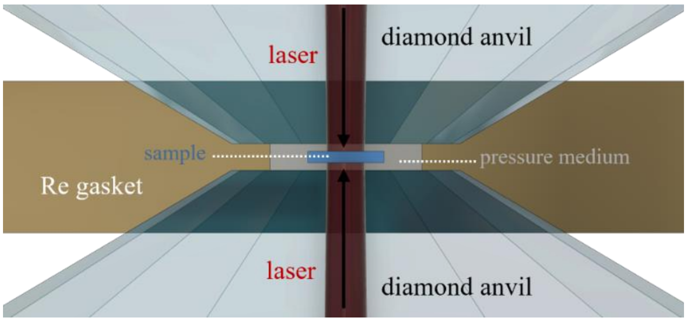

**Figure 2.11.** Schematic of the sample configuration in a laser-heated DAC experiment.

### 2.3.2 *Single Crystal Data Collection under High Pressure conditions*

The wavelength of X-rays is comparable to the interatomic distances within the lattice of a crystalline solid. When an incident X-ray beam interacts with the three-dimensional periodic structure of a single crystal, the crystal produces a series of distinct diffraction spots. These spots result from constructive interference of the scattered X-rays, governed by Bragg's law (eqn. 2.10), with each spot corresponding to a specific set of crystal planes.

$$2dsin\theta = n\lambda \tag{2.10}$$

where $d$ is the distance between crystal planes, $\theta$ is the angle between the incident X-rays and the crystal planes, $\lambda$ is the wavelength of the beam, and $n$ is any integer number.

Typical mineral structures produce hundreds to thousands of unique reflections, collectively forming a diffraction pattern. Each reflection is assigned Miller indices (*hkl*) that indicate its position within the pattern. This diffraction pattern exhibits a reciprocal Fourier transform relationship to the crystal lattice and the unit cell in real space. Consequently, by correctly fitting the Miller indices and the intensities of the diffraction spots, the crystal structure can be determined.

Although data collection and processing are significantly more complex, single-crystal XRD has more advantages with respect to powder XRD because it measures individual reflections from specific crystallographic planes, providing a three-dimensional diffraction pattern which allows to a more accurate and precise atomic arrangement determination. In contrast, powder XRD patterns consist of all equivalent reflections overlapping at given d-spacing values, which can cause ambiguities in indexing and challenges in resolving complex structures.

The limited opening angle in a DAC often causes the incident and diffracted beams to be obstructed by the WC seat or the DAC body, while the crystals synthesized in an LH-DAC are typically µm- to sub-µm-sized. These factors make single-crystal studies on such samples using an in-house X-ray source nearly impossible. However, the highly brilliant and low divergence X-ray beams from third- and fourth-generation synchrotron facilities offer significant advantages for these measurements. Firstly, the high-energy X-ray beams available at synchrotron facilities enable broader coverage of the reciprocal space and minimum absorption from the diamonds. More importantly, synchrotron X-ray beams can be focused to an area of a few µm² to sub-µm², comparable in size to the studied samples, which minimizes diffraction from the environment around the crystallite of interest (i.e. diffraction from the gasket material) and allows precise structural analysis of these tiny crystals

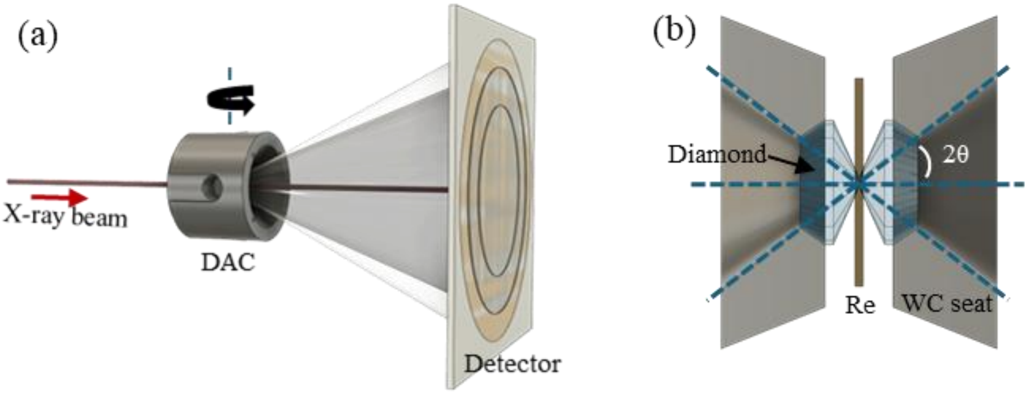

**Figure 2.12.** SC-XRD experiment in a DAC. (a) Schematic drawing of data collection regime. (b) Opening angle in a DAC, which is limited by the dimensions of the diamond anvil and the geometry of the WC seat in DAC.

In this thesis, single-crystal XRD experiments were performed at the Extreme Conditions X-ray Diffraction and Imaging beamline ID15B (Garbarino et al., 2024) at the ESRF. The measurements used an X-ray wavelength of 0.4100 Å and a beam size of approximately 1 × 1 μm. Initially, a 2D powder XRD map was constructed with a step size of 2 μm by scanning the sample stage (Hrubiak et al., 2019). This mapping process was performed to locate phases of interest within the samples. Once these phases were identified, SC-XRD data collection was carried out over the maximum available angular range (-30° to +30° or -34° to +34°, depending on the DAC's opening angle). The DAC was mounted on a motorized goniometer and rotated around the ω axis with an increment step of 0.5° for data acquisition. The single crystal XRD data collection process is illustrated in Fig. 2.12.

### *2.3.3 Data Reduction and Single Crystal Structure Refinement*

Depending on the grain size of the samples, a complete SC-XRD dataset collected from the laser-heated samples may contain up to hundreds of individual domains, as shown in Fig. 2.13, effectively forming a multi-grain system (Sørensen et al., 2012). To perform single-crystal structure analysis, it is essential to isolate the target domains from the full dataset.

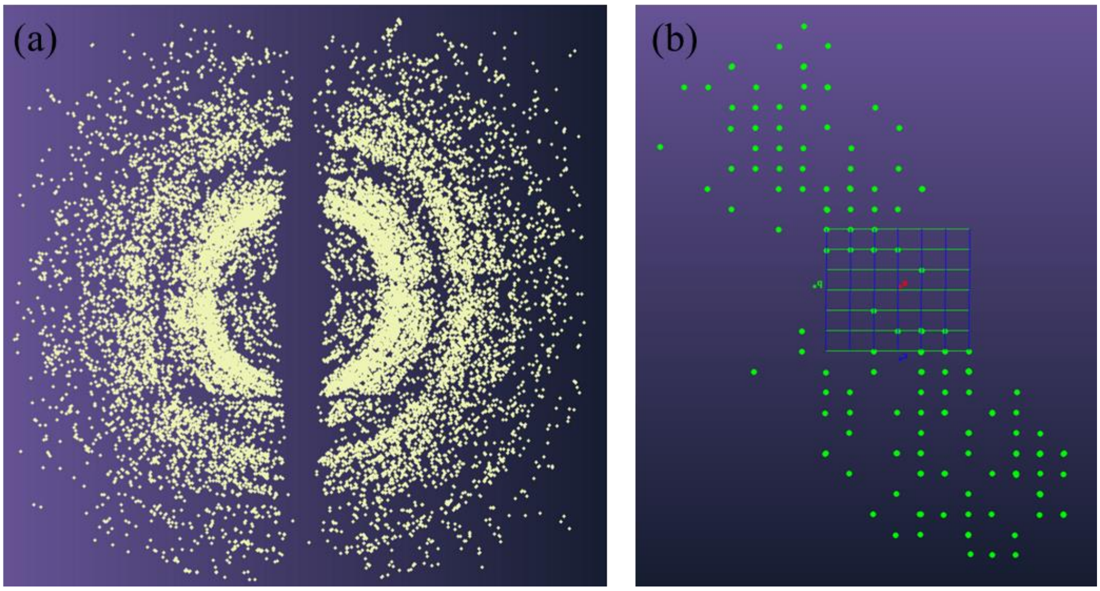

**Figure 2.13.** Example of SC-XRD data for Fe sulfide in a DAC after laser heating. (a) All reflections shown in reciprocal space. (b) A domain of a novel Fe sulfide ($Fe_{4+x}S_3$) indexed using the DAFi program (Aslandukov et al., 2022). Data visualized with CrysAlisPro software.

Several crystallographic software applications are available for processing multi-grain data, including GrainSpotter (Schmidt, 2014), ImageD11 (Sørensen et al., 2012), and DAFi (Aslandukov et al., 2022), all of which can sort reflections from individual domains. Unlike GrainSpotter and ImageD11, which require prior knowledge of possible lattice parameters, DAFi can perform domain searches without any pre-existing information about the crystal structure. This makes DAFi particularly useful when dealing with completely unknown phases or unfamiliar crystal chemistries. In this study, DAFi was chosen to process the data for separating the desired domain, as it is more compatible with the single-crystal data reduction software that has been used previously at the BGI (CrysAlis Pro). More details about the data reduction procedures can be found in Bykova (2015).

After data reduction of the selected domains, we used the Olex2 software package (Dolomanov et al., 2009) to solve and refine the single-crystal data. Despite the different orientations and reflection coverage of grains from the same sample, the solved structures showed strong consistency with each other. This consistency confirmed the reliability of the structural solution and refinement.

# 3 Synopsis

This chapter summarizes the results and implications of this thesis, which are detailed in Chapters 4 to 6. Chapter 4 presents systematic findings on the solubility of $Al_2O_3$ in ferropericlase under conditions corresponding to Earth's deep mantle. Parameterized through a thermodynamic model, these results were applied to constrain the origins of ferropericlase inclusions found in diamonds. The methodology described can also be used to determine temperatures and temperature gradients in high-pressure experiments. Chapter 5 focuses on the elastic properties of Fe-FeS liquids under high pressure and high temperature (HP-HT). The results reveal that sulfur reduces both the density and P-wave velocity of liquid Fe under Martian core conditions, indicating that Fe-S liquids alone cannot account for seismic observations of the Martian core. Chapter 6 presents the first crystal structure refinement of a high-pressure sulfide phase, $Fe_{4+x}S_3$, and explores the potential crystallization regime of the Martian core based on these experimental findings.

## 3.1 List of manuscripts and statement of authors' contribution

(1) **Lianjie Man***, Hongzhan Fei, Eun Jeong Kim, Adrien Néri, Longjian Xie, Daniel J. Frost. "Alumina solubility in periclase determined to lower mantle conditions and implications for ferropericlase inclusions in diamonds" **Published** in **Geochimica et Cosmochimica Acta**, 375 (2024). DOI: https://doi.org/10.1016/j.gca.2024.05.002

Lianjie Man: Writing – original draft, Visualization, Methodology, Investigation, Formal analysis, Data curation, Conceptualization. Hongzhan Fei: Writing – review & editing, Investigation, Conceptualization. Eun Jeong Kim: Writing – review & editing, Investigation. Adrien Néri: Writing – review & editing, Investigation. Longjian Xie: Writing – review & editing, Investigation. Daniel J. Frost: Writing – review & editing, Visualization, Methodology, Funding acquisition, Formal analysis, Conceptualization.

(2) **Lianjie Man***, Adrien Néri, Julien Chantel, Tiziana Boffa Ballaran, Robert Farla, Liang Yuan, Nicolas Guignot, Laura Henry, Jonathan Dolinschi1, Fei Wang, Rémy Pierru, Hu Tang, Andrew King, Tony Yu, Man Xu, Yanbin Wang, Daniel J. Frost. "*The Influence of Sulfur on the Elastic Properties of the Martian Core*" **Submitted** to ***Earth and Planetary Science Letters***.

Lianjie Man: Conceptualization, Data curation, Formal analysis, Investigation, Methodology, Validation, Visualization, and Writing – original draft. Adrien Néri: Conceptualization, Investigation, Methodology, Validation, and Writing – review and editing. Julien Chantel: Investigation, Methodology, Validation, and Writing – review and editing. Tiziana Boffa Ballaran: Data curation, Formal analysis, Investigation, Methodology, Validation, and Writing – review and editing. Robert Farla: Investigation, Methodology, Validation, and Writing – review and editing. Liang Yuan: Investigation, and Methodology, Validation. Nicolas Guignot: Investigation, Methodology, and Writing – review and editing. Laura Henry: Investigation, Methodology, and Writing – review and editing. Jonathan Dolinschi: Investigation, Methodology. Fei Wang: Investigation. Rémy Pierru: Investigation, Methodology. Hu Tang: Investigation. Andrew King: Methodology and Software. Tony Yu: Investigation, Methodology, and Writing – review and editing. Man Xu: Investigation, Methodology, and Writing – review and editing. Yanbin Wang: Investigation, Methodology, and Writing – review and editing. Daniel J. Frost: Conceptualization, Formal analysis, Investigation, Methodology, Validation, and Writing – review and editing.

(3) **Lianjie Man***, Xiang Li, Tiziana Boffa Ballaran1, Wenju Zhou, Julien Chantel, Adrien Néri, Ilya Kupenko, Georgios Aprilis, Alexander Kurnosov, Olivier Namur, Michael Hanfland, Nicolas Guignot, Laura Henry, Leonid Dubrovinsky, Daniel. J. Frost. "*The structure and stability of* $Fe_{4+x}S_3$ *and its potential to form a Martian inner core*" **Published** in **Nature Communications**, 16 (2025)**.**
DOI: https://doi.org/10.1038/s41467-025-56220-2

Lianjie Man conceived and designed this project. Lianjie Man, Xiang Li, Tiziana Boffa Ballaran, Leonid Dubrovinsky, Wenju Zhou, Julien Chantel, Adrien Néri, Ilya Kupenko, Georgios Aprilis, Alexander Kurnosov, Michael Hanfland, Nicolas Guignot, Laura Henry, and Daniel. J. Frost performed the experiments. Wenju Zhou, Tiziana Boffa Ballaran, Leonid Dubrovinsky, Xiang Li, and Lianjie Man analyzed the single-crystal X-ray diffraction data. Lianjie Man, Daniel. J. Frost, Xiang Li, Adrien Néri, Olivier Namur, Ilya Kupenko, and Leonid Dubrovinsky contributed to the interpretation of the results. Lianjie Man and Daniel. J. Frost wrote the paper with contributions from all the authors.

Note: * indicate correspondent author.

## 3.2 Alumina in ferropericlase in Earth's mantle

The majority of natural diamonds appear to have formed in the sub-cratonic lithospheric mantle, however, a rare subset of are considered to have formed at much deeper conditions in the sublithospheric mantle (Walter et al., 2022). This subset is characterized by the mineral inclusions found in these diamonds, with the main indicators for a sublithospheric origin being the minerals majoritic garnet and ferropericlase. The inclusions can potentially provide unique evidence for the conditions of temperature and composition within the deep mantle. To extract this information from inclusions in sublithospheric diamonds, however, studies need to be performed to determine temperature and pressure dependent element partitioning. A further problem is that because only a single mineral is generally preserved in the diamond, information is lacking on element activity as the inclusion formed or last equilibrated. If we study major elements that are likely to have high activities in the mantle, however, we can start by placing constraints on the solubility of the element within the phase in question and then consider how the activity my change from this upper limiting value for different assemblages. In this way it is still possible to interpret element concentrations in the inclusions in order to exclude certain sets of formation conditions.

In this study, we conducted a series of high-pressure multi-anvil experiments in the MgO-$Al_2O_3$ system between 15 and 50 GPa and at temperatures up to 2623 K, to determine the solubility of $Al_2O_3$ in periclase in the stability fields of coexisting spinel (Sp), corundum (Cor), the $Mg_2Al_2O_5$ modified ludwigite (Ldw) phase, $MgAl_2O_4$ calcium ferrite (CF) phase, and the $MgAl_2O_4$ calcium titanate (CT) phase. The results show that the $Al_2O_3$ solubility in periclase is strongly temperature-dependent over the conditions investigated, being, for example, < 0.5 mol.% at 1923 K but up to 6.8 mol.% at 2623 K at 23 GPa (see Fig. 3.1). Conversely, periclase $Al_2O_3$ solubility exhibits a negative relationship with pressure. Experiments in the MgO-FeO-$Al_2O_3$ system show that FeO has a negligible effect on the $Al_2O_3$ solubility in ferropericlase.

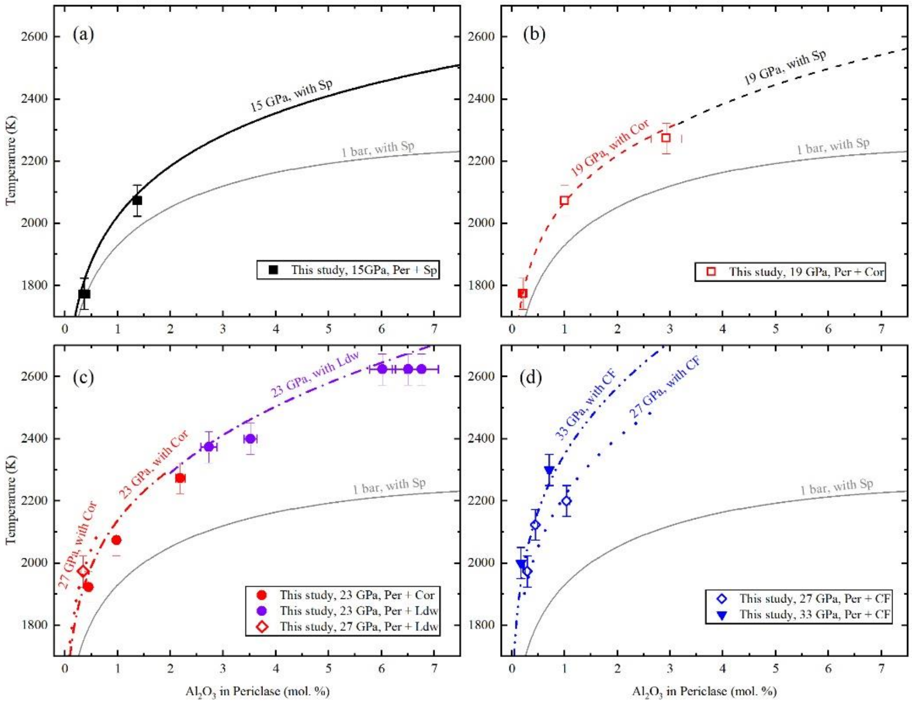

**Figure 3.1.** The solubility of $Al_2O_3$ in periclase as a function of pressure and temperature. Experimental results at 15 GPa (a), 19 GPa (b), 23 to 27 GPa (c), and 27 to 33 GPa are compared with the thermodynamic model established in this study. All curves are calculated considering the indicated coexisting phases at the denoted pressures using the thermodynamic model derived in this study.

Based on these experimental results, we built a thermodynamic model to describe periclase $Al_2O_3$ solubility in the $MgO$-$Al_2O_3$ and $MgO$-$SiO_2$-$Al_2O_3$ system up to 40 GPa. This model is used to investigate the $Al_2O_3$ contents of ferropericlase inclusions observed in natural diamonds, which vary up to 0.35 mol. %. Pressure-temperature curves along which particular inclusions formed can be produced if equilibrium can be assumed with Al-bearing minerals found in the same diamond. Alternatively, the maximum possible $Al_2O_3$ content in ferropericlase can be determined for a certain pressure-temperature profile and inclusions with $Al_2O_3$ contents that exceed this curve can be excluded from those conditions. To obtain such solubility curves, calculations are performed for periclase coexisting with the Al-rich phases spinel, garnet and bridgmanite (Fig. 3.2). The calculations indicate that ferropericlase $Al_2O_3$-contents cannot be greater than 0.5 mol.% under present day adiabatic mantle temperatures and go through a minimum at mantle transition zone conditions. This excludes a number of Al-rich ferropericlase inclusions found in natural diamonds (Walter et al., 2022), from being formed in the transition zone, unless temperatures were super-adiabatic. This subset of inclusions likely formed either at the base of the upper mantle or the top of the lower mantle, but must have formed at near adiabatic temperatures. The majority of ferropericlase inclusions, have $Al_2O_3$ contents that are consistent with formation in the transition zone at near slab temperatures, but could still have been formed at higher temperatures if $Al_2O_3$ activities were low.

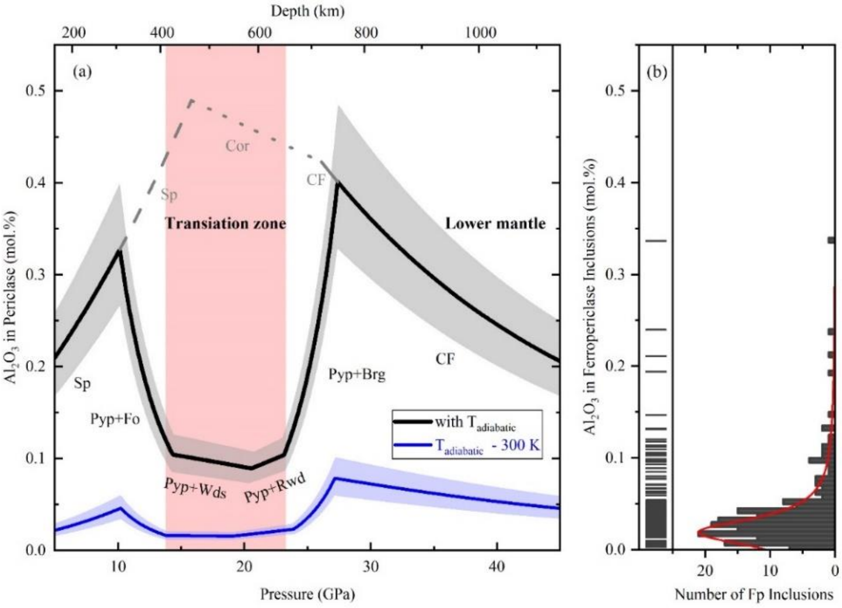

**Figure 3.2.** (a) $Al_2O_3$ solubility in periclase in the MgO-$SiO_2$-$Al_2O_3$ and MgO-$Al_2O_3$ systems calculated from the thermodynamic model. The black solid curve shows the calculated periclase $Al_2O_3$ concentration in the MgO-$SiO_2$-$Al_2O_3$ system coexisting with most Al-abundant mineral stable in the mantle at different depths, i.e., spinel (Sp), pyrope (Pyp), or $MgAl_2O_4$ CF phase, along a typical adiabatic mantle temperature. (b) The distribution in $Al_2O_3$ concentration in naturally formed ferropericlase inclusions found in diamonds.

## 3.3 Influence of Sulfur on the Elastic Characteristics of Martian Core

Recent geophysical observations, particularly seismic data from the InSight mission, have revealed the size of the Martian core (Stähler et al., 2021) and provided direct constraints on the P-wave velocity at the top part of the liquid core (Irving et al., 2023). Geophysical models based on seismic observations indicate that the density of the Martian core is significantly lower than that of pure liquid Fe under the same pressure and temperature conditions (Stähler et al., 2021; Irving et al., 2023; Samuel et al., 2023; Khan et al., 2023). However, the constrained P-wave velocity at the top of the Martian core remains comparable to that of pure liquid Fe (Irving et al., 2023; Samuel et al., 2023; Khan et al., 2023). If the effects of light elements, including sulfur, on the density and P-wave velocity of liquid iron under high pressures and temperatures are systematically constrained by experimental and theoretical studies, seismic observations of the Martian core can provide strong evidence for the core's composition, and for Mars' early differentiation and evolution processes.

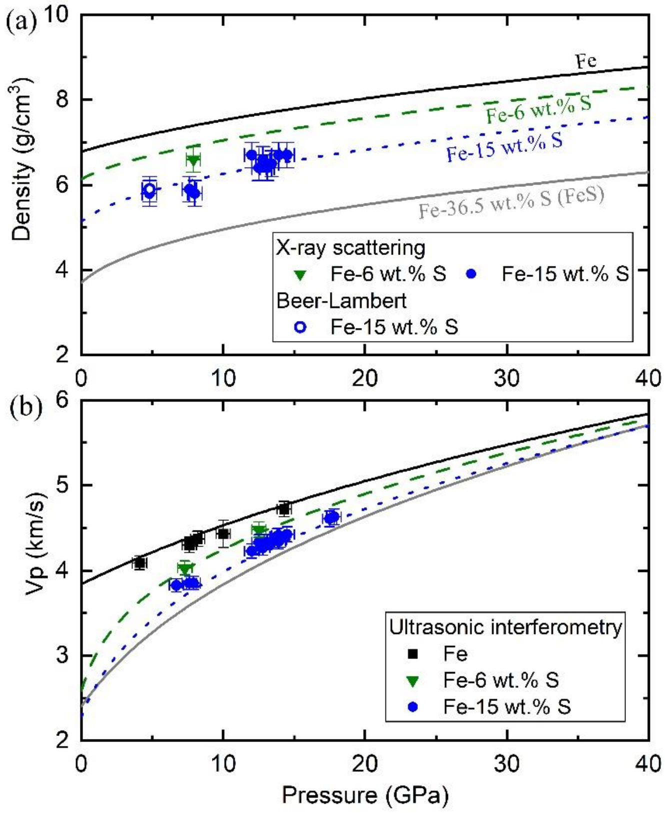

**Figure. 3.3.** Densities (a) and P-wave velocities (b) of liquid Fe-FeS solutions. The black squares, green inverted triangles, and blue circles indicate experimental data from this study for Fe (1873–2273 K), Fe-6 wt.% S (1690–1873 K), and Fe-15 wt.% S (1473–2073 K), respectively. The curves in the figure are derived from the thermodynamic model determined in this study, plotted at 2150 K for Fe (black solid curves) and 1750 K for Fe-6 wt.% S (green dashed curves), Fe-15 wt.% S (blue dotted curves), and FeS (grey solid curves), respectively.

In this study, we have used ultrasonic interferometry and several *in situ* X-ray methods, independently and simultaneously, to determine the elastic properties of pure Fe and Fe-S liquids under HP-HT, including density and P-wave velocity ($V_P$). By combining experimental constraints on solid phase density and melting curves, along with end-member thermodynamic data at ambient pressure and melting curves from the literature, we have developed a new self-consistent thermodynamic model for the Fe-FeS system applicable to the conditions of the Martian core. Models that are fit in this way to the widest possible number of experimental constraints are essential due to the large uncertainties inherent in liquid property measurements.

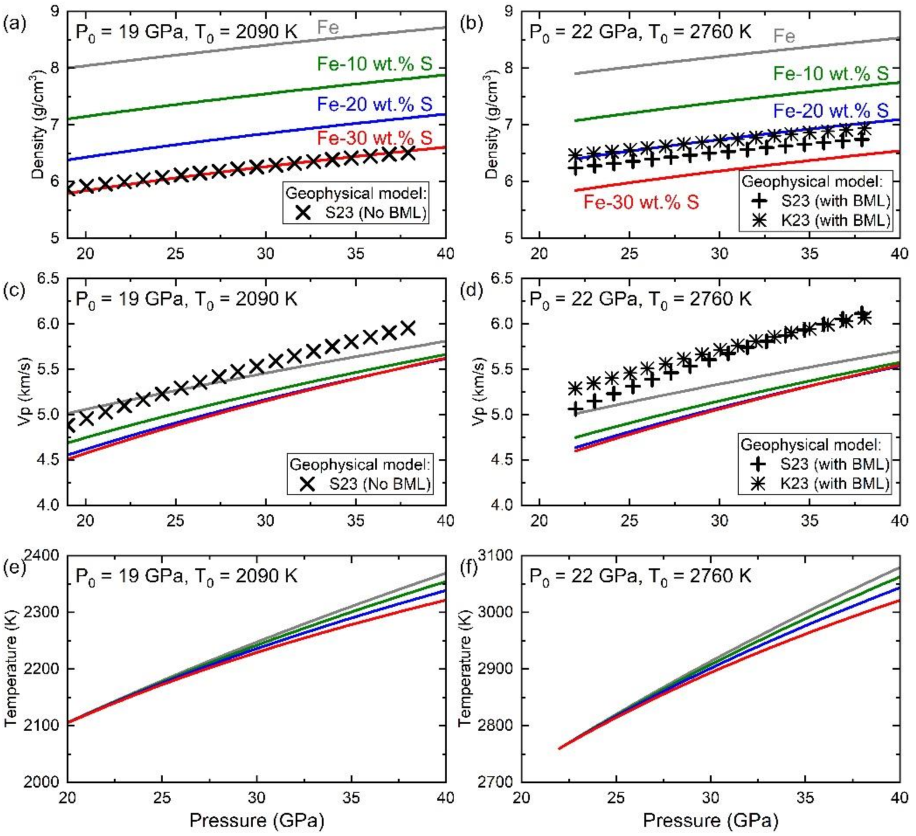

**Figure. 3.4.** Comparison between the adiabatic properties of Fe-S liquids calculated from the thermodynamic model developed in this study (solid curves), with models for Martian core properties that are based on InSight measurements. Panels (a), (c), and (e) show density, longitudinal velocity, and temperature profiles calculated using a reference CMB temperature (T0) of 2090 K at 19 GPa (P0), compared with profiles that employ InSight measurements but assume no basal magma layer (BML) at the Martian core-mantle boundary (S23: Samuel et al., 2023). Panels (b), (d), and (f) are calculated at a reference CMB temperature of 2760 K at 22 GPa and are compared with profiles based on InSight measurements that assume the existence of a BML at the CMB of Mars (S23: Samuel et al., 2023; K23: Khan et al., 2023). The grey, green, blue, and red curves indicate compositions of pure Fe, Fe with 10 wt.% S, Fe with 20 wt.% S, and Fe with 30 wt.% S, respectively.

Our results indicate that sulfur lowers both the density and P wave velocity of liquid Fe under Martian core conditions (Fig. 3.3). To account for the observed density deficit in the Martian core, at least 20 wt.% sulfur would be required. However, such high sulfur concentrations would lower the P-wave velocity of liquid Fe, most significantly at the top of the Martian core, which conflicts with seismic observations from the InSight mission (Fig. 3.4). This indicates that significant proportions of other light elements, most likely carbon or hydrogen, are required alongside sulfur to explain the large density deficit while maintaining the apparent high longitudinal wave velocity in the Martian core.

## 3.4 Crystal structure of $Fe_{4+x}S_3$ and its stability in Martian Core

Due to the similarity between estimates of the core's sulfur content and the iron - iron sulfide eutectic composition at core conditions, it has been concluded that temperatures are too high for Mars to have an inner core. Recent low-density estimates for the core, however, appear consistent with sulfur contents that are higher than the eutectic composition, leading to the possibility that an inner core could form from a high-pressure iron sulfide phase. Below pressures of around 14 GPa, the Fe-FeS system is a simple binary eutectic system, and FeS V is the only sulfide phase stable as a liquid phase on the S-rich side. Beyond 14 GPa, however, the melting phase diagram of the Fe-FeS system becomes more complex, and a range of intermediate iron sulfide phases emerge, including $Fe_{3+x}S_2$, $Fe_2S$, $Fe_{12}S_7$, and $Fe_5S_2$, each appearing under specific pressure-temperature-composition conditions (Fei et al., 2000; Zurkowski et al., 2022a, 2022b). Understanding the crystal structures and densities of these high-pressure sulfide phases is critical for understanding the status and evolution of Martian core.

In this study, we conducted a series of HP-HT experiments, employing multiple in-situ and ex-situ characterization techniques to investigate the crystal chemistry and melting phase relations in the Fe-FeS system. Using high-pressure single-crystal X-ray diffraction (SC-XRD) following in-situ synthesis via laser heating in a diamond anvil cell at 15-20 GPa, we identified a new Fe-sulfide structure, which based on its distribution of crystallographic sites, is best described as $Fe_{4+x}S_3$. This structure, with space group Pnma, consists of four edge-sharing Fe-S square pyramids and one partially occupied interstitial Fe site (see Fig. 3.5), which allows the stoichiometry to vary from $x = 0$ to 1. Phases previously synthesized under similar conditions, such as $Fe_3S_2$ and $Fe_{3+x}S_2$ (with an undetermined crystal structures), are likely to share this same structure. In-situ HP-HT powder X-ray diffraction measurements at a synchrotron multi-anvil beamline (Fig. 3.6) confirmed that $Fe_{4+x}S_3$ is the thermodynamically stable phase in the Fe-FeS system. Although a Martian inner core has not yet been detected, our modeled melting phase relations for the Fe-FeS system indicate that an $Fe_{4+x}S_3$ inner core could crystallize if temperatures at Mars's center drop below 1960 (±105) K. This temperature remains within the estimated range of current conditions for the Martian core.

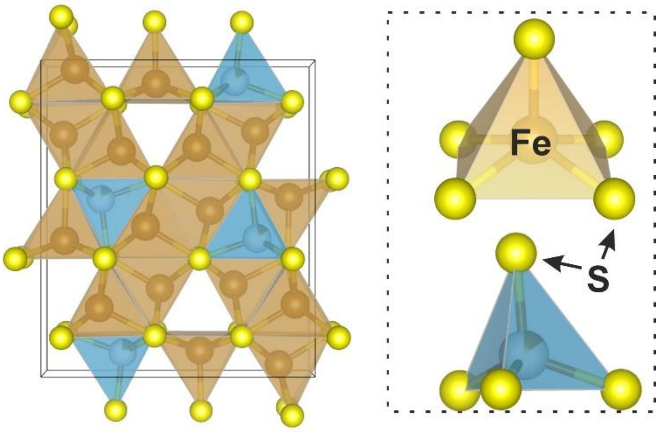

**Figure 3.5.** The structural model of $Fe_{4+x}S_3$ as determined by SC-XRD. The building blocks of $Fe_{4+x}S_3$ consist of four Fe-S pyramids and one semi-occupied Fe-S tetrahedron.

The crystallization of a sulfide inner core is consistent with the absence of an active dynamo, as the residual liquid would be richer in Fe and would, therefore, remain at the base of the outer core, inhibiting chemical convection The detection of a Martian inner core through further geophysical observations, along with an estimate of its density, would provide critical constraints on the chemical composition and temperature of the Martian core. Moreover, the existence of a Martian inner core would imply a relatively cool Martian interior, which would be incompatible with the presence of a basal magma layer on top of the CMB. Conversely, if an inner core is confirmed to be absent, the $Fe_{4+x}S_3$ melting temperature would provide a lower limit for the temperature at the center of Mars.

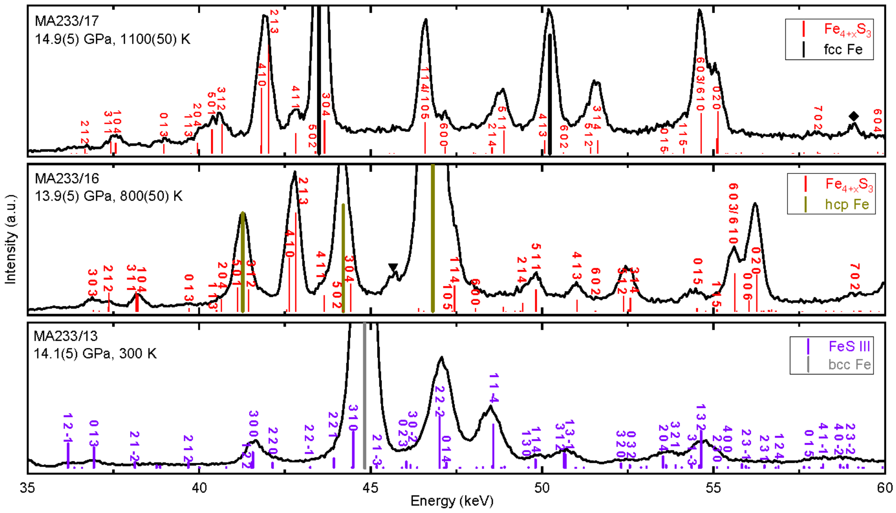

**Figure 3.6.** *In situ* ED-XRD patterns collected in a synchrotron MA experiment using an Fe85S15 starting material conducted at approximately 14 GPa and at the temperatures indicated. The grey, dark yellow, black, violet, and red sticks indicate bcc Fe, hcp Fe, fcc Fe, FeS III, and $Fe_{4+x}S_3$ reflections, respectively. The minor peaks marked with black reversed triangles appear to be residual from FeS IV and those marked by diamonds are from FeO.

# References (Chapter 1-3)

Andrews, S.M., Huang, J., Pérez, L.M., Isella, A., Dullemond, C.P., Kurtovic, N.T., Guzmán, V.V., Carpenter, J.M., Wilner, D.J., Zhang, S. and Zhu, Z., 2018. The disk substructures at high angular resolution project (DSHARP). I. Motivation, sample, calibration, and overview. The Astrophysical Journal Letters, 869(2), p.L41.

Andrews, S.M., 2020. Observations of protoplanetary disk structures. Annual Review of Astronomy and Astrophysics, 58(1), pp.483-528.

Angel, R.J., Alvaro, M. and Nestola, F., 2022. Crystallographic methods for non-destructive characterization of mineral inclusions in diamonds. Reviews in Mineralogy and Geochemistry, 88(1), pp.257-305.

Anzellini, S., & Boccato, S., 2020. A practical review of the laser-heated diamond anvil cell for university laboratories and synchrotron applications. Crystals, 10(6), 459.

Aprilis, G., Strohm, C., Kupenko, I., Linhardt, S., Laskin, A., Vasiukov, D. M., ... & Dubrovinsky, L., 2017. Portable double-sided pulsed laser heating system for time-resolved geoscience and materials science applications. Review of Scientific Instruments, 88(8).

Aslandukov, A., Aslandukov, M., Dubrovinskaia, N., & Dubrovinsky, L., 2022. Domain Auto Finder (DAFi) program: the analysis of single-crystal X-ray diffraction data from polycrystalline samples. Journal of applied crystallography, 55(5), 1383-1391.

Banerdt, W.B., Smrekar, S.E., Banfield, D., Giardini, D., Golombek, M., Johnson, C.L., Lognonné, P., Spiga, A., Spohn, T., Perrin, C. and Stähler, S.C., 2020. Initial results from the InSight mission on Mars. Nature Geoscience, 13(3), pp.183-189.

Bassett, W. A., 2009. Diamond anvil cell, 50th birthday. High Pressure Research, 29(2), 163-186.

Boccato, S., Garino, Y., Morard, G., Zhao, B., Xu, F., Sanloup, C., ... & Antonangeli, D., 2022. Amorpheus: a Python-based software for the treatment of X-ray scattering data of amorphous and liquid systems. High Pressure Research, 42(1), 69-93.

Boehler, R., & De Hantsetters, K., 2004. New anvil designs in diamond-cells. High

Pressure Research, 24(3), 391-396.

Burkhardt, C., Spitzer, F., Morbidelli, A., Budde, G., Render, J.H., Kruijer, T.S. and Kleine, T., 2021. Terrestrial planet formation from lost inner solar system material. Science advances, 7(52), p.eabj7601.

Bykova, E., 2015. Single-crystal X-ray diffraction at extreme conditions in mineral physics and material sciences. Universitaet Bayreuth (Germany).

Chambers, J.E. and Wetherill, G.W., 1998. Making the terrestrial planets: N-body integrations of planetary embryos in three dimensions. Icarus, 136(2), pp.304-327.

Dauphas, N. and Pourmand, A., 2011. Hf–W–Th evidence for rapid growth of Mars and its status as a planetary embryo. Nature, 473(7348), pp.489-492.

Dewaele, A., Fiquet, G., & Gillet, P., 1998. Temperature and pressure distribution in the laser-heated diamond–anvil cell. Review of scientific instruments, 69(6), 2421-2426.

Dewaele, A., Torrent, M., Loubeyre, P. and Mezouar, M., 2008. Compression curves of transition metals in the Mbar range: Experiments and projector augmented-wave calculations. Physical Review B—Condensed Matter and Materials Physics, 78(10), p.104102.

Dolomanov, O. V., Bourhis, L. J., Gildea, R. J., Howard, J. A., & Puschmann, H., 2009. OLEX2: a complete structure solution, refinement and analysis program. Journal of applied crystallography, 42(2), 339-341.

Drazkowska, J., Bitsch, B., Lambrechts, M., Mulders, G.D., Harsono, D., Vazan, A., Liu, B., Ormel, C.W., Kretke, K. and Morbidelli, A., 2022. Planet formation theory in the era of ALMA and Kepler: from pebbles to exoplanets. arXiv preprint arXiv:2203.09759.

Drewitt, J. W., 2021. Liquid structure under extreme conditions: high-pressure x-ray diffraction studies. Journal of Physics: Condensed Matter, 33(50), 503004.

Du, Z., Amulele, G., Robin Benedetti, L., & Lee, K. K., 2013. Mapping temperatures and temperature gradients during flash heating in a diamond-anvil cell. Review of Scientific Instruments, 84(7).

Dubrovinskaia, N., & Dubrovinsky, L., 2018. Crystallography taken to the extreme. Physica Scripta, 93(6), 062501.

Dubrovinskaia, N., Dubrovinsky, L., Solopova, N. A., Abakumov, A., Turner, S., Hanfland, M., ... & Snigirev, A., 2016. Terapascal static pressure generation with ultra-high yield strength nanodiamond. Science advances, 2(7), e1600341.

Dubrovinsky, L., Khandarkhaeva, S., Fedotenko, T., Laniel, D., Bykov, M., Giacobbe, C., ... & Dubrovinskaia, N., 2022. Materials synthesis at terapascal static pressures. Nature, 605(7909), 274-278.

Dziewonski, A.M. and Anderson, D.L., 1981. Preliminary reference Earth model. Physics of the earth and planetary interiors, 25(4), pp.297-356.

Eggert, J. H., Weck, G., Loubeyre, P., & Mezouar, M., 2002. Quantitative structure factor and density measurements of high-pressure fluids in diamond anvil cells by x-ray diffraction: Argon and water. Physical Review B, 65(17), 174105.

Errandonea, D., 2006. Phase behavior of metals at very high P–T conditions: A review of recent experimental studies. Journal of Physics and Chemistry of Solids, 67(9-10), 2017-2026.

Farla, R., Bhat, S., Sonntag, S., Chanyshev, A., Ma, S., Ishii, T., ... & Katsura, T., 2022. Extreme conditions research using the large-volume press at the P61B endstation, PETRA III. Journal of synchrotron radiation, 29(2), 409-423.

Farley, K.A., Williford, K.H., Stack, K.M., Bhartia, R., Chen, A., de la Torre, M., Hand, K., Goreva, Y., Herd, C.D., Hueso, R. and Liu, Y., 2020. Mars 2020 mission overview. Space Science Reviews, 216, pp.1-41.

Fedotenko, T., Dubrovinsky, L., Aprilis, G., Koemets, E., Snigirev, A., Snigireva, I., ... & Dubrovinskaia, N., 2019. Laser heating setup for diamond anvil cells for in situ synchrotron and in house high and ultra-high pressure studies. Review of Scientific Instruments, 90(10).

Fei, Y., Bertka, C.M. and Finger, L.W., 1997. High-pressure iron-sulfur compound, $Fe_3S_2$, and melting relations in the Fe-FeS system. Science, 275(5306), pp.1621-1623.

Fei, Y., Li, J., Bertka, C.M. and Prewitt, C.T., 2000. Structure type and bulk modulus of Fe3S, a new iron-sulfur compound. American Mineralogist, 85(11-12), pp.1830-1833.

Fei, Y., Prewitt C.T., Frost. D.J., Parise J.B., and Brister, K., 1998. Structures of FeS polymorphs at high pressure and temperature. The review of high pressure science and technology, 7, pp.55-58.

Frost, D.J. and Myhill, R., 2016. Chemistry of the lower mantle. Deep Earth: Physics and Chemistry of the Lower Mantle and Core, pp.225-240.

Garbarino, G., Hanfland, M. E., Gallego-Parra, S., Rosa, A. D., Mezouar, M., Duran, D., ... & Jacobs, J., 2024. Extreme conditions x-ray diffraction and imaging beamline id15b on the esrf extremely brilliant source. High Pressure Research, 44(3), 199-216.

Geballe, Z. M., & Jeanloz, R., 2012. Origin of temperature plateaus in laser-heated diamond anvil cell experiments. Journal of applied physics, 111(12).

Henry, L., Guignot, N., King, A., Giovenco, E., Deslandes, J. P., & Itié, J. P., 2022. In situ characterization of liquids at high pressure combining X-ray tomography, X-ray diffraction and X-ray absorption using the white beam station at PSICHE. Journal of Synchrotron Radiation, 29(3), 853-861.

Hirose, K., Labrosse, S. and Hernlund, J., 2013. Composition and state of the core. Annual Review of Earth and Planetary Sciences, 41(1), pp.657-691.

Hrubiak, R., Smith, J. S., & Shen, G., 2019. Multimode scanning X-ray diffraction microscopy for diamond anvil cell experiments. Review of Scientific Instruments, 90(2).

Ida, S. and Makino, J., 1993. Scattering of planetesimals by a protoplanet: Slowing down of runaway growth. Icarus, 106(1), pp.210-227.

Irifune, T. and Tsuchiya, T., 2007. Mineralogy of the Earth-Phase transitions and mineralogy of the lower mantle. Mineral physics, 2, pp.33-62.

Irifune, T., Koizumi, T. and Ando, J.I., 1996. An experimental study of the garnet-perovskite transformation in the system $MgSiO_3$-$Mg_3Al_2Si_3O_{12}$. Physics of the Earth and Planetary Interiors, 96(2-3), pp.147-157.

Irifune, T., Shinmei, T., McCammon, C.A., Miyajima, N., Rubie, D.C. and Frost, D.J.,

2010. Iron partitioning and density changes of pyrolite in Earth's lower mantle. Science, 327(5962), pp.193-195.

Irving, J.C., Lekić, V., Durán, C., Drilleau, M., Kim, D., Rivoldini, A., Khan, A., Samuel, H., Antonangeli, D., Banerdt, W.B. and Beghein, C., 2023. First observations of core-transiting seismic phases on Mars. Proceedings of the National Academy of Sciences, 120(18), p.e2217090120.

Ishii, T., Frost, D.J., Kim, E.J., Chanyshev, A., Nishida, K., Wang, B., Ban, R., Xu, J., Liu, J., Su, X. and Higo, Y., 2023. Buoyancy of slabs and plumes enhanced by curved post-garnet phase boundary. Nature Geoscience, 16(9), pp.828-832.

Ishii, T., Huang, R., Myhill, R., Fei, H., Koemets, I., Liu, Z., Maeda, F., Yuan, L., Wang, L., Druzhbin, D. and Yamamoto, T., 2019. Sharp 660-km discontinuity controlled by extremely narrow binary post-spinel transition. Nature Geoscience, 12(10), pp.869-872.

Ishii, T., Liu, Z., & Katsura, T., 2019. A breakthrough in pressure generation by a Kawai-type multi-anvil apparatus with tungsten carbide anvils. Engineering, 5(3), 434-440.

Ishii, T., Shi, L., Huang, R., Tsujino, N., Druzhbin, D., Myhill, R., ... & Katsura, T., 2016. Generation of pressures over 40 GPa using Kawai-type multi-anvil press with tungsten carbide anvils. Review of Scientific Instruments, 87(2).

Ito, E. and Takahashi, E., 1989. Postspinel transformations in the system $Mg_2SiO_4$-$Fe_2SiO_4$ and some geophysical implications. Journal of Geophysical Research: Solid Earth, 94(B8), pp.10637-10646.

Ito, E., Price, G.D. and Schubert, G., 2007. Theory and practice—multianvil cells and high-pressure experimental methods. Treatise on geophysics, 2, pp.197-230.

Jing, Z., Yu, T., Xu, M., Chantel, J., & Wang, Y., 2020. High-pressure sound velocity measurements of liquids using in situ ultrasonic techniques in a multianvil apparatus. Minerals, 10(2), 126.

Johansen, A., Oishi, J.S., Low, M.M.M., Klahr, H., Henning, T. and Youdin, A., 2007. Rapid planetesimal formation in turbulent circumstellar disks. Nature, 448(7157), pp.1022-1025.

Johansen, A., Ronnet, T., Bizzarro, M., Schiller, M., Lambrechts, M., Nordlund, Å. and Lammer, H., 2021. A pebble accretion model for the formation of the terrestrial planets in the Solar System. Science advances, 7(8), p.eabc0444.

Kantor, I., Prakapenka, V., Kantor, A., Dera, P., Kurnosov, A., Sinogeikin, S., ... & Dubrovinsky, L., 2012. BX90: A new diamond anvil cell design for X-ray diffraction and optical measurements. Review of Scientific Instruments, 83(12).

Kaplow, R., Strong, S. L., & Averbach, B. L., 1965. Radial density functions for liquid mercury and lead. Physical Review, 138(5A), A1336.

Katayama, Y., Tsuji, K., Chen, J. Q., Koyama, N., Kikegawa, T., Yaoita, K., & Shimomura, O., 1993. Density of liquid tellurium under high pressure. Journal of non-crystalline solids, 156, 687-690.

Katsura, T., 2022. A revised adiabatic temperature profile for the mantle. Journal of Geophysical Research: Solid Earth, 127(2), p.e2021JB023562.

Katsura, T., Yamada, H., Nishikawa, O., Song, M., Kubo, A., Shinmei, T., Yokoshi, S., Aizawa, Y., Yoshino, T., Walter, M.J. and Ito, E., 2004. Olivine-wadsleyite transition in the system (Mg, Fe)$_2$SiO$_4$. Journal of Geophysical Research: Solid Earth, 109(B2).

Katsura, T., Yoneda, A., Yamazaki, D., Yoshino, T. and Ito, E., 2010. Adiabatic temperature profile in the mantle. Physics of the Earth and Planetary Interiors, 183(1-2), pp.212-218.

Kavner, A., & Nugent, C., 2008. Precise measurements of radial temperature gradients in the laser-heated diamond anvil cell. Review of Scientific Instruments, 79(2).

Keppler, H., & Frost, D. J., 2005. Introduction to minerals under extreme conditions.

Khan, A., Ceylan, S., van Driel, M., Giardini, D., Lognonné, P., Samuel, H., Schmerr, N.C., Stähler, S.C., Duran, A.C., Huang, Q. and Kim, D., 2021. Upper mantle structure of Mars from InSight seismic data. Science, 373(6553), pp.434-438.

Khan, A., Huang, D., Durán, C., Sossi, P.A., Giardini, D. and Murakami, M., 2023. Evidence for a liquid silicate layer atop the Martian core. Nature, 622(7984), pp.718-723.

Khan, A., Sossi, P.A., Liebske, C., Rivoldini, A. and Giardini, D., 2022. Geophysical and cosmochemical evidence for a volatile-rich Mars. Earth and Planetary Science Letters, 578, p.117330.

King, A., Guignot, N., Henry, L., Morard, G., Clark, A., Le Godec, Y., & Itié, J. P., 2022. Combined angular and energy dispersive diffraction: optimized data acquisition, normalization and reduction. Journal of Applied Crystallography, 55(2), 218-227.

Knapmeyer-Endrun, B., Panning, M.P., Bissig, F., Joshi, R., Khan, A., Kim, D., Lekić, V., Tauzin, B., Tharimena, S., Plasman, M. and Compaire, N., 2021. Thickness and structure of the Martian crust from InSight seismic data. Science, 373(6553), pp.438-443.

Ko, B., Greenberg, E., Prakapenka, V., Alp, E.E., Bi, W., Meng, Y., Zhang, D. and Shim, S.H., 2022. Calcium dissolution in bridgmanite in the Earth’s deep mantle. Nature, 611(7934), pp.88-92.

Koch-Müller, M., Fei, Y., Wirth, R. and Bertka, C.M., 2002, March. Characterization of high-pressure iron-sulfur compounds. In Lunar and planetary science conference (p. 1424).

Kokubo, E. and Ida, S., 1998. Oligarchic growth of protoplanets. Icarus, 131(1), pp.171-178.

Kokubo, E. and Ida, S., 2000. Formation of protoplanets from planetesimals in the solar nebula. Icarus, 143(1), pp.15-27.

Koppers, A.A., Becker, T.W., Jackson, M.G., Konrad, K., Müller, R.D., Romanowicz, B., Steinberger, B. and Whittaker, J.M., 2021. Mantle plumes and their role in Earth processes. Nature Reviews Earth & Environment, 2(6), pp.382-401.

Krogh-Moe, J., 1956. A method for converting experimental X-ray intensities to an absolute scale. Acta Crystallographica, 9(11), 951-953.

Kunimoto, T., Irifune, T., Tange, Y., & Wada, K., 2016. Pressure generation to 50 GPa in Kawai-type multianvil apparatus using newly developed tungsten carbide anvils. High Pressure Research, 36(2), 97-104.

Kupenko, I., Dubrovinsky, L., Dubrovinskaia, N., McCammon, C., Glazyrin, K., Bykova, E., ... & Merlini, M., 2012. Portable double-sided laser-heating system for Mössbauer spectroscopy and X-ray diffraction experiments at synchrotron facilities with diamond anvil cells. Review of Scientific Instruments, 83(12).

Kurnosov, A., Marquardt, H., Frost, D.J., Ballaran, T.B. and Ziberna, L., 2017. Evidence for a $Fe^{3+}$-rich pyrolitic lower mantle from (Al, Fe)-bearing bridgmanite elasticity data. Nature, 543(7646), pp.543-546.

Lambrechts, M. and Johansen, A., 2012. Rapid growth of gas-giant cores by pebble accretion. Astronomy & Astrophysics, 544, p.A32.

Levison, H.F., Kretke, K.A. and Duncan, M.J., 2015a. Growing the gas-giant planets by the gradual accumulation of pebbles. Nature, 524(7565), pp.322-324.

Levison, H.F., Kretke, K.A., Walsh, K.J. and Bottke, W.F., 2015b. Growing the terrestrial planets from the gradual accumulation of submeter-sized objects. Proceedings of the National Academy of Sciences, 112(46), pp.14180-14185.

Liu, Z., Nishi, M., Ishii, T., Fei, H., Miyajima, N., Ballaran, T. B., ... & Katsura, T., 2017. Phase relations in the system $MgSiO_3$-$Al_2O_3$ up to 2300 K at lower mantle pressures. Journal of Geophysical Research: Solid Earth, 122(10), 7775-7788.

Mashino, I., Murakami, M., Miyajima, N. and Petitgirard, S., 2020. Experimental evidence for silica-enriched Earth's lower mantle with ferrous iron dominant bridgmanite. Proceedings of the National Academy of Sciences, 117(45), pp.27899-27905.

McDonough, W.F. and Sun, S.S., 1995. The composition of the Earth. Chemical geology, 120(3-4), pp.223-253.

McDonough, W.F. and Yoshizaki, T., 2021. Terrestrial planet compositions controlled by accretion disk magnetic field. Progress in Earth and Planetary Science, 8, pp.1-12.

Ming, L. C., & Bassett, W. A., 1974. Laser heating in the diamond anvil press up to 2000 °C sustained and 3000 °C pulsed at pressures up to 260 kilobars. Review of Scientific Instruments, 45(9), 1115-1118.

Morard, G., Garbarino, G., Antonangeli, D., Andrault, D., Guignot, N., Siebert, J., ... & Petitgirard, S., 2014. Density measurements and structural properties of liquid and amorphous metals under high pressure. High Pressure Research, 34(1), 9-21.

Morard, G., Hernandez, J. A., Guarguaglini, M., Bolis, R., Benuzzi-Mounaix, A., Vinci, T., ... & Ravasio, A., 2020. In situ X-ray diffraction of silicate liquids and glasses under dynamic and static compression to megabar pressures. Proceedings of the National Academy of Sciences, 117(22), 11981-11986.

Morbidelli, A., Kleine, T. and Nimmo, F., 2025. Did the terrestrial planets of the solar system form by pebble accretion?. Earth and Planetary Science Letters, 650, p.119120.

Morbidelli, A., Lunine, J.I., O'Brien, D.P., Raymond, S.N. and Walsh, K.J., 2012. Building terrestrial planets. Annual Review of Earth and Planetary Sciences, 40(1), pp.251-275.

Murakami, M., Hirose, K., Kawamura, K., Sata, N. and Ohishi, Y., 2004. Post-perovskite phase transition in $MgSiO_3$. Science, 304(5672), pp.855-858.

Murakami, M., Khan, A., Sossi, P.A., Ballmer, M.D. and Saha, P., 2024. The Composition of Earth's Lower Mantle. Annual Review of Earth and Planetary Sciences, 52(1), pp.605-638.

Murakami, M., Ohishi, Y., Hirao, N. and Hirose, K., 2012. A perovskitic lower mantle inferred from high-pressure, high-temperature sound velocity data. Nature, 485(7396), pp.90-94.

Neri, A., Man, L., Chantel, J., Farla, R., Bauer, G., Linhardt, S., ... & Frost, D. J., 2024. The development of internal pressure standards for in-house elastic wave velocity measurements in multi-anvil presses. Review of Scientific Instruments, 95(1).

Norman, N., 1957. The Fourier transform method for normalizing intensities. Acta Crystallographica, 10(5), 370-373.

O'Neill, H.S.C. and Palme, H., 2008. Collisional erosion and the non-chondritic composition of the terrestrial planets. Philosophical Transactions of the Royal Society A: Mathematical, Physical and Engineering Sciences, 366(1883), pp.4205-4238.

O'Neill, H.S.C., 1998. Composition of the silicate Earth: implications for accretion and core formation. The Earth's mantle: Composition, structure, and evolution, pp.3-126.

Oganov, A.R. and Ono, S., 2004. Theoretical and experimental evidence for a post-perovskite phase of $MgSiO_3$ in Earth's D" layer. Nature, 430(6998), pp.445-448.

Olson, P.L., Sharp, Z.D. and Garai, S., 2024. Pebble accretion and siderophile element partitioning between Earth's mantle and core. Physics of the Earth and Planetary Interiors, p.107295.

Ormel, C.W. and Klahr, H.H., 2010. The effect of gas drag on the growth of protoplanets-analytical expressions for the accretion of small bodies in laminar disks. Astronomy & Astrophysics, 520, p.A43.

Palme, H., O'Neill, H.S.C., Holland, H.D. and Turekian, K.K., 2014. Treatise on geochemistry. Chapter 2.1, cosmochemical estimates of mantle composition, pp.1-39.

Papadakis, E. P., 1972. Absolute Accuracy of the Pulse-Echo Overlap Method and the Pulse-Superposition Method for Ultrasonic Velocity. The Journal of the Acoustical Society of America, 52(3B), 843-846.

Prakapenka, V. B., Kubo, A., Kuznetsov, A., Laskin, A., Shkurikhin, O., Dera, P., ... & Sutton, S. R., 2008. Advanced flat top laser heating system for high pressure research at GSECARS: application to the melting behavior of germanium. High Pressure Research, 28(3), 225-235.

Ricolleau, A., Fei, Y., Cottrell, E., Watson, H., Deng, L., Zhang, L., Fiquet, G., Auzende, A.L., Roskosz, M., Morard, G. and Prakapenka, V., 2009. Density profile of pyrolite under the lower mantle conditions. Geophysical Research Letters, 36(6).

Rigden, S. M., Jackson, I., Niesler, H., Ringwood, A. E., & Liebermann, R. C., 1988. Pressure dependence of the elastic wave velocities for $Mg_2GeO_4$ spinel to 3 GPa. Geophysical Research Letters, 15(6), 605-608.

Righter, K. and O'Brien, D.P., 2011. Terrestrial planet formation. Proceedings of the National Academy of Sciences, 108(48), pp.19165-19170.

Ringwood, A.E., 1975. Composition and Petrology of the Earth's Mantle. MacGraw-Hill, 618.

Ringwood, A.E., 1991. Phase transformations and their bearing on the constitution and dynamics of the mantle. Geochimica et Cosmochimica Acta, 55(8), pp.2083-2110.

Rose-Weston, L., Brenan, J.M., Fei, Y., Secco, R.A. and Frost, D.J., 2009. Effect of pressure, temperature, and oxygen fugacity on the metal-silicate partitioning of Te, Se, and S: Implications for earth differentiation. Geochimica et Cosmochimica Acta, 73(15), pp.4598-4615.

Sakamaki, T., 2017. Density of hydrous magma. Chemical Geology, 475, 135-139.

Salamat, A., Fischer, R. A., Briggs, R., McMahon, M. I., & Petitgirard, S., 2014. In situ synchrotron X-ray diffraction in the laser-heated diamond anvil cell: Melting phenomena and synthesis of new materials. Coordination Chemistry Reviews, 277, 15-30.

Samuel, H., Drilleau, M., Rivoldini, A., Xu, Z., Huang, Q., Garcia, R.F., Lekić, V., Irving, J.C., Badro, J., Lognonné, P.H. and Connolly, J.A., 2023. Geophysical evidence for an enriched molten silicate layer above Mars's core. Nature, 622(7984), pp.712-717.

Sanloup, C., Guyot, F., Gillet, P., Fiquet, G., Mezouar, M., & Martinez, I., 2000. Density measurements of liquid Fe-S alloys at high-pressure. Geophysical Research Letters, 27(6), 811-814.

Sanloup, C., Jambon, A. and Gillet, P., 1999. A simple chondritic model of Mars. Physics of the Earth and Planetary Interiors, 112(1-2), pp.43-54.

Schmidt, S., 2014. GrainSpotter: a fast and robust polycrystalline indexing algorithm. Journal of Applied Crystallography, 47(1), 276-284.

Schwinger, J., 1949. On the classical radiation of accelerated electrons. Physical review, 75(12), 1912.

Shatskiy, A., Yamazaki, D., Morard, G., Cooray, T., Matsuzaki, T., Higo, Y., ... & Katsura, T., 2009. Boron-doped diamond heater and its application to large-volume, high-pressure, and high-temperature experiments. Review of Scientific Instruments, 80(2).

Shen, G., & Mao, H. K., 2016. High-pressure studies with x-rays using diamond anvil cells. Reports on progress in Physics, 80(1), 016101.

Shen, G., & Wang, Y., 2014. High-pressure apparatus integrated with synchrotron radiation. Reviews in Mineralogy and Geochemistry, 78(1), 745-777.

Shim, S.H., Duffy, T.S., Jeanloz, R. and Shen, G., 2004. Stability and crystal structure of MgSiO3 perovskite to the core-mantle boundary. Geophysical Research Letters, 31(10).

Singh, S., Coleman, A. L., Zhang, S., Coppari, F., Gorman, M. G., Smith, R. F., ... & Fratanduono, D. E., 2022. Quantitative analysis of diffraction by liquids using a pink-spectrum X-ray source. Journal of Synchrotron Radiation, 29(4), 1033-1042.

Sinmyo, R., & Hirose, K., 2010. The Soret diffusion in laser-heated diamond-anvil cell. Physics of the Earth and Planetary Interiors, 180(3-4), 172-178.

Sørensen, H. O., Schmidt, S., Wright, J. P., Vaughan, G. B., Techert, S., Garman, E. F., ... & Poulsen, H. F., 2012. Multigrain crystallography.

Stähler, S.C., Khan, A., Banerdt, W.B., Lognonné, P., Giardini, D., Ceylan, S., Drilleau, M., Duran, A.C., Garcia, R.F., Huang, Q. and Kim, D., 2021. Seismic detection of the martian core. Science, 373(6553), pp.443-448.

Steenstra, E.S. and van Westrenen, W., 2018. A synthesis of geochemical constraints on the inventory of light elements in the core of Mars. Icarus, 315, pp.69-78.

Stewart, A.J., Schmidt, M.W., Van Westrenen, W. and Liebske, C., 2007. Mars: A new core-crystallization regime. Science, 316(5829), pp.1323-1325.

Stixrude, L. and Lithgow-Bertelloni, C., 2022. Thermal expansivity, heat capacity and bulk modulus of the mantle. Geophysical Journal International, 228(2), pp.1119-1149.

Suer, T.A., Siebert, J., Remusat, L., Menguy, N. and Fiquet, G., 2017. A sulfur-poor terrestrial core inferred from metal–silicate partitioning experiments. Earth and Planetary Science Letters, 469, pp.84-97.

Taylor, G.J., 2013. The bulk composition of Mars. Geochemistry, 73(4), pp.401-420.

Tian, H., Zhang, T., Jia, Y., Peng, S. and Yan, C., 2021. Zhurong: Features and mission of China’s first Mars rover. The Innovation, 2(3).

van Keken, P.E. and Wilson, C.R., 2023. An introductory review of the thermal structure of subduction zones: I—motivation and selected examples. Progress in Earth and Planetary Science, 10(1), p.42.

Wagle, F. and Steinle-Neumann, G., 2019. Liquid iron equation of state to the terapascal regime from ab initio simulations. Journal of Geophysical Research: Solid Earth, 124(4), pp.3350-3364.

Walder, P. and Pelton, A.D., 2005. Thermodynamic modeling of the Fe-S system. Journal of phase equilibria and diffusion, 26, pp.23-38.

Walter, M.J., Thomson, A.R. and Smith, E.M., 2022. Geochemistry of silicate and oxide inclusions in sublithospheric diamonds. Reviews in Mineralogy and Geochemistry, 88(1), pp.393-450.

Wang, Y., & Shen, G., 2014. High-pressure experimental studies on geo-liquids using synchrotron radiation at the Advanced Photon Source. Journal of Earth Science, 25, 939-958.

Wang, Y., Rivers, M., Sutton, S., Nishiyama, N., Uchida, T., & Sanehira, T., 2009. The large-volume high-pressure facility at GSECARS: A “Swiss-army-knife” approach to synchrotron-based experimental studies. Physics of the Earth and Planetary Interiors, 174(1-4), 270-281.

Wang, Y., Uchida, T., Von Dreele, R., Rivers, M. L., Nishiyama, N., Funakoshi, K. I., ... & Kaneko, H., 2004. A new technique for angle-dispersive powder diffraction using an energy-dispersive setup and synchrotron radiation. Journal of applied crystallography, 37(6), 947-956.

Wänke, H. and Dreibus, G., 1994. Chemistry and accretion history of Mars. Philosophical Transactions of the Royal Society of London. Series A: Physical and Engineering Sciences, 349(1690), pp.285-293.

Wasson, J.T. and Kallemeyn, G.W., 1988. Compositions of chondrites. Philosophical Transactions of the Royal Society of London. Series A, Mathematical and Physical Sciences, 325(1587), pp.535-544.

Weidenschilling, S.J., 1977. Aerodynamics of solid bodies in the solar nebula. Monthly Notices of the Royal Astronomical Society, 180(2), pp.57-70.

Williams, J.P. and Cieza, L.A., 2011. Protoplanetary disks and their evolution. Annual Review of Astronomy and Astrophysics, 49(1), pp.67-117.

Xie, L., Yoneda, A., Liu, Z., Nishida, K., & Katsura, T., 2020. Boron-doped diamond synthesized by chemical vapor deposition as a heating element in a multi-anvil apparatus. High Pressure Research, 40(3), 369-378.

Yamazaki, D., Ito, E., Yoshino, T., Tsujino, N., Yoneda, A., Gomi, H., ... & Tange, Y., 2019. High-pressure generation in the Kawai-type multianvil apparatus equipped with tungsten-carbide anvils and sintered-diamond anvils, and X-ray observation on $CaSnO_3$ and $(Mg,Fe)SiO_3$. Comptes Rendus. Géoscience, 351(2-3), 253-259.

Yoshizaki, T. and McDonough, W.F., 2020. The composition of Mars. Geochimica et Cosmochimica Acta, 273, pp.137-162.

Zurkowski, C.C., Lavina, B., Case, A., Swadba, K., Chariton, S., Prakapenka, V. and Campbell, A.J., 2022a. $Fe_5S_2$ identified as a host of sulfur in Earth and planetary cores. Earth and Planetary Science Letters, 593, p.117650.

Zurkowski, C.C., Lavina, B., Chariton, S., Prakapenka, V. and Campbell, A.J., 2022b. Stability of $Fe_2S$ and $Fe_{12}S_7$ to 125 GPa; implications for S-rich planetary cores. Geochemical Perspectives Letters, 21.

# 4 Alumina solubility in periclase determined to lower mantle conditions and implications for ferropericlase inclusions in diamonds

**Lianjie Man**[1,*], Hongzhan Fei[1,2], Eun Jeong Kim[1], Adrien Néri[1], Longjian Xie[1,3], and Daniel. J. Frost[1]

[1]Bayerisches Geoinstitut, Universität Bayreuth, Bayreuth, Germany.
[2]Key Laboratory of Geoscience Big Data and Deep Resource of Zhejiang Province, School of Earth Sciences, Zhejiang University, Hangzhou, China
[3]Department of Earth Sciences, University College London, London WC1E6BS, UK
[*]Corresponding author.
E-mail address: lianjie.man@uni-bayreuth.de (L. Man).

This chapter has been published as: Man, L., Fei, H., Kim, E.J., Néri, A., Xie, L. and Frost, D.J., 2024. Alumina solubility in periclase determined to lower mantle conditions and implications for ferropericlase inclusions in diamonds. Geochimica et Cosmochimica Acta, 375, pp.36-49. DOI: https://doi.org/10.1016/j.gca.2024.05.002

## Author contributions

Lianjie Man: Conceptualization, Methodology, Formal analysis, Investigation, Data Curation, Visualization, Writing - Original Draft. Hongzhan Fei: Conceptualization, Investigation, Writing - Review & Editing. Eun Jeong Kim: Investigation, Writing - Review & Editing. Adrien Néri: Investigation, Writing - Review & Editing. Longjian Xie: Investigation, Writing - Review & Editing. Daniel J. Frost: Conceptualization, Formal analysis, Writing - Review & Editing, Methodology, Visualization, Funding acquisition.

## Abstract

A series of high-pressure multi-anvil experiments were conducted in the MgO-$Al_2O_3$ system between 15 and 50 GPa and at temperatures up to 2623 K, to determine the solubility of $Al_2O_3$ in periclase in the stability fields of coexisting spinel, corundum, the $Mg_2Al_2O_5$ modified ludwigite phase, the $MgAl_2O_4$ calcium ferrite phase, and the $MgAl_2O_4$ calcium titanate phase. The $Al_2O_3$ solubility in periclase is strongly temperature-dependent over the conditions investigated. Conversely, periclase $Al_2O_3$ solubility exhibits a negative relationship with pressure. Experiments with up to 40 mol.% FeO in ferropericlase show $Al_2O_3$ solubilities that are near identical to those of periclase, within experimental uncertainties. A simple thermodynamic model incorporating significant literature on ambient pressure measurements is able to describe periclase $Al_2O_3$ solubility up to 40 GPa. This model is used to investigate the $Al_2O_3$ contents of ferropericlase inclusions observed in natural diamonds, which vary up to 0.35 mol. %. Pressure-temperature curves along which particular inclusions formed can be produced if equilibrium can be assumed with Al-bearing minerals found in the same diamond. Alternatively, the maximum possible $Al_2O_3$ content in ferropericlase can be determined for a certain pressure-temperature profile and inclusions with $Al_2O_3$ contents that exceed this curve can be excluded from those conditions. To obtain such solubility curves, calculations are performed for periclase coexisting with the Al-rich phases spinel, garnet, bridgmanite and the $MgAl_2O_4$ calcium ferrite phase. The calculations indicate that periclase, and by inference ferropericlase, $Al_2O_3$-contents cannot be greater than 0.5 mol.% under present day adiabatic mantle temperatures and go through a minimum at mantle transition zone conditions. This excludes a number of Al-rich ferropericlase inclusions found in natural diamonds from being formed in the transition zone, unless temperatures were super-adiabatic. This subset of inclusions likely formed either at the base of the upper mantle or the top of the lower mantle, but must have formed at near adiabatic temperatures. The majority of ferropericlase inclusions have $Al_2O_3$ contents that would be consistent with formation in the transition zone at near slab temperatures, but could still have been formed at higher temperatures if $Al_2O_3$ activities were low.

**Keywords:** periclase alumina solubility; lower mantle; diamond inclusions; mantle temperature

## 4.1 Introduction

Determining the formation conditions of sublithospheric diamonds is important as they provide evidence for the mobility of carbon-bearing fluids or melts in the Earth's deep convecting interior (Stachel, 2001; Walter et al., 2011). The inclusions captured inside diamonds can potentially provide information on these formation conditions and possibly on the nature of the mobile carbon-bearing medium from which they formed (Anzolini et al., 2019; Thomson et al., 2016). Ferropericlase, (Mg,Fe)O, is apparently the most common type of inclusion found in proposed sublithospheric diamonds, and is often used to identify them as originating from the lower mantle (Harte et al., 1999; Hayman et al., 2005). Ferropericlase is, most likely, the second most abundant phase in the bulk of the lower mantle (Irifune and Tsuchiya, 2007). The high molar Fe/(Fe+Mg) ratios of some ferropericlase inclusions, which extend to values > 0.8, have also been attributed to an origin in the deep lower mantle due to either a pressure dependent shift in interphase Fe-Mg partitioning, or interaction between the mantle and core (Hayman et al., 2005; Kaminsky, 2012). Other studies have pointed out that ferropericlase could also form as a result of either decarbonation, or more likely reduction of carbonate melts (Liu, 2002; Brey et al., 2004; Thomson et al., 2016; Bulatov et al., 2019), at potentially any depth in the mantle. Diverse origins of ferropericlase inclusions are in fact supported by recent studies (Nimis et al., 2018; Lorenzon et al., 2023), that determined crystallographic orientation relationships (CORs) between inclusions and their diamond hosts. Specific CORs were observed only for Fe-rich ferropericlase inclusions, potentially implying a distinct syngenetic origin, versus a protogenetic origin for inclusions with lower Fe-contents that display random CORs.

By utilizing elastic geobarometry, where residual pressures are measured for inclusions still trapped in diamonds, it has been possible to determine that some ferropericlase inclusions have formation pressures ranging to at least 22.1 GPa (Anzolini et al., 2019; Nestola et al., 2023a). Such a technique provides a pressure-temperature (P-T) curve along which entrapment likely occurred (Angel et al., 2022; Kohn et al., 2023), but requires a complementary method in order to pinpoint both P and T conditions, as in traditional thermobarometry-thermometry assessments (e.g., Nimis, 2022).

In addition to FeO and MgO, there are a number of minor elements in natural ferropericlase inclusions, the concentration of which might reveal information on the formation conditions. For instance, the $Fe^{3+}/\Sigma Fe$ ratio of ferropericlase diamond inclusions has been used as an indicator of the redox conditions at which the diamonds formed (e.g., Wirth et al., 2014; Kaminsky et al., 2015; Kiseeva et al., 2022; Nestola et al., 2023b). One possibility is that the incorporation of $Al_2O_3$ into the structure of ferropericlase, which occurs via the component $(Al_{2/3},Va_{1/3})O$, where Va is a cation vacancy (Hallstedt, 1992), might reveal information on the P or T conditions of equilibrium. The effects of changing conditions on $Al_2O_3$ incorporation may also be of broader interest because $Al_2O_3$ has already been shown to have a marked effect on ferropericlase transport properties, such as electrical conductivity and diffusivity (e.g., Sempolinski and Kingery, 1980; Van Orman et al., 2003, 2009; Ammann et al., 2012; Riet et al., 2020). For example, the presence of just 0.1 mol.% $Al_2O_3$ raises the rate of Mg self-diffusion in periclase by 1 to 2 orders of magnitude at 25 GPa (Van Orman et al., 2003).

Ferropericlase inclusions found in natural diamonds have $Al_2O_3$ concentrations that range up to 0.35 mol. %, although the majority of samples have concentrations that are an order of magnitude lower than this (Walter et al., 2022). The variability in the $Al_2O_3$ concentration may provide information on the P, T, or $Al_2O_3$ activity at which the inclusions formed. Although it is difficult to independently assess the $Al_2O_3$ activity during formation, a maximum limit can be determined by assuming saturation with a mantle $Al_2O_3$-bearing phase, such as spinel or garnet. Knowledge of the P-T dependency of ferropericlase $Al_2O_3$ solubility should allow formation conditions to be excluded under which particular ferropericlase inclusions would have $Al_2O_3$ concentrations that exceed this upper limit. Alternatively, it may be possible to independently determine $Al_2O_3$ activity from the presence of proposed co-forming phases, such as garnet, in the same growth zone of the diamond.

Phase relations in the $MgO$-$Al_2O_3$ system have been intensively studied at ambient pressure under varying temperatures (e.g., Alper et al., 1962; Stubican and Roy, 1965; Mori, 1982; Zienert and Fabrichnaya, 2013). Periclase forms a limited solid solution with $Al_2O_3$, which is T dependent. At saturation with coexisting $MgAl_2O_4$ spinel, the periclase $Al_2O_3$ content reaches a value of approximately 9 mol % at 2500 K (Zienert and Fabrichnaya, 2013). However, currently the mixing behaviour of MgO and $Al_2O_3$ in periclase remains unexplored at high P and T. In addition to spinel, a series of $Al_2O_3$-rich phases which can coexist with periclase have been identified in the $MgO$-$Al_2O_3$ system under high P and T conditions, including $Al_2O_3$ corundum (Liu, 1975; Akaogi et al., 1999; Irifune et al., 2002; Kojitani et al., 2010), a calcium ferrite-structured $MgAl_2O_4$ (CF) phase (Irifune et al., 1991; Akaogi et al., 1999; Irifune et al., 2002), an $Mg_2Al_2O_5$ phase with a modified ludwigite (ldw) structure (Enomoto et al., 2009; Kojitani et al., 2010), and an $MgAl_2O_4$ calcium ferrite (CT) phase (Ono et al., 2005, 2006). The formation of various high-pressure $Al_2O_3$-rich phases will alter the $Al_2O_3$ activity within the system adding further complexity to the experimental study of the solubility behaviour.

In this study, we have performed a series of high-P and high-T multi-anvil experiments within the MgO-$Al_2O_3$ system, reaching pressures up to 50 GPa, to investigate the solubility of $Al_2O_3$ in periclase to lower mantle conditions. Complementary experiments were conducted in the FeO-MgO-$Al_2O_3$ system at 21 GPa and up to 2300 K to evaluate the potential influence of FeO on the solubility of $Al_2O_3$ in natural ferropericlase. Based on the experimental results, we evaluate the factors affecting the $Al_2O_3$ concentration in ferropericlase in the sublithospheric mantle and discuss the P-T formation conditions of ferropericlase inclusions found in natural diamonds.

## 4.2 Materials and Methods

For experiments conducted in the MgO-$Al_2O_3$ system, mixtures of reagent-grade MgO and $Al_2O_3$ powders with grain sizes of ~ 1 μm were used as starting materials. Powders with MgO:$Al_2O_3$ molar ratios of 6:1 and 12:1 were ground with ethanol in an agate mortar for around 1 hour to ensure the mixtures were homogenous. The mixtures were then dried overnight and stored in an oven at 125 °C before being loaded into high-pressure multi-anvil assemblies. For complementary experiments investigating the effect of FeO on the $Al_2O_3$ solubility in ferropericlase, (Mg,Fe)O pellets containing 20 mol.% (Fp80) and 40 mol.% (Fp60) FeO were synthesized from dried mixtures of reagent-grade $Fe_2O_3$ and MgO in a CO-$CO_2$ gas mixing furnace at 1100°C and an oxygen fugacity two log units below the fayalite-magnetite-quartz oxygen buffer. The recovered Fp80 and Fp60 pellets were ground and then mixed with $Al_2O_3$ in a molar ratio of 6:1. An Fp90 composition was produced from powders of Fp80 and MgO, and also mixed 6:1 with $Al_2O_3$. Approximately 5 wt.% metallic iron with a grain size < 10 μm was mixed with the resulting starting materials to control the oxygen fugacity.

We used multi-anvil presses with either a split-sphere guide block (Hymag) or an Osugi-type guide block (IRIS-15) at the Bayerisches Geoinstitut (BGI), for experiments between 15 - 23 GPa and 27 - 50 GPa, respectively. The methodologies and pressure calibrations for the Hymag press are described by Keppler and Frost (2005), and by Ishii et al. (2016; 2019) for the IRIS-15. A $Cr_2O_3$-doped MgO octahedron with a 10 mm edge length (OEL = 10 mm) was used with eight tungsten carbide cubic anvils with 4 mm truncation edge lengths (TEL = 4 mm, Ha06 cubes from Hawedia) for experiments between 15 and 23 GPa and cell assemblies with OEL/ TEL = 7 mm/3 mm and 5.7 mm/1.5 mm (F05 cubes from Fuji Die Co. Ltd.) for experiments at 27 GPa and 33 GPa, respectively. For an experiment at 50 GPa, a 5.7 mm/1.5 mm cell assembly was used with eight ultrahard 1°-tapered TJS01 tungsten carbide anvils (Fuji Die Co. Ltd), as calibrated by Ishii et al. (2019).

In each experiment in the $MgO-Al_2O_3$ system, except runs I1193 and H5299, the starting material was placed as a thin layer (≤ 100 μm) next to the hot junction of a type-D thermocouple (TC), to minimize the differences between TC readings and the sample temperatures, given the large temperature gradients in the higher pressure assemblies (e.g., van Westrenen et al., 2003). No correction was applied to the thermocouple emf to account for a possible pressure effect. Another sample capsule was usually placed adjacent to the $MgO-Al_2O_3$ mixture for a separate purpose, unrelated to the current study. As shown in Fig. 4.1a, the materials surrounding the $MgO-Al_2O_3$ samples were the MgO and $Al_2O_3$ ceramic components of the high-P assembly, which do not, therefore, introduce contamination into the samples. For run I1193, the TC was directly in contact with the centre of the rhenium furnace, and the temperature reading is therefore the temperature of the furnace. In run H5299, a semi-sintered MgO tube with 1.8 outer diameter and 1.2 inner diameter was filled with the sample and then placed into the cylindrical $LaCrO_3$ furnace. In this case only the sample composition within 100 μm of the TC junction is reported. For experiments in the $FeO-MgO-Al_2O_3$ system, the capsules were made of four-hole dense polycrystalline $Al_2O_3$ tubes, with 0.2 mm diameter holes. $MgO-Al_2O_3$, $Fp90-A_{l2}O_3$, $Fp80-Al_2O_3$, and $Fp60-Al_2O_3$ starting materials were placed in each of the holes. Thermocouples were not used in the experiments in the $FeO-MgO-Al_2O_3$ system as a comparison is made with the solubility in the $MgO-Al_2O_3$ sample.

After compression to the target load, a $LaCrO_3$ or rhenium furnace was used to heat the sample to the desired temperatures (1773 – 2623 K). Samples were heated for between 1 to 1200 min, depending on the P-T conditions, before quenching to room temperature by switching off the heating power and decompressing. After recovery, the assemblies were embedded in epoxy resin and then ground and polished with sandpaper and polishing cloths, utilizing increasingly finer diamond sprays (1 μm, 0.5 μm, and 0.25 μm). The experimental phase assemblages were characterized using a scanning electron microscope (SEM, LEO1530) and a micro-focused powder X-ray diffractometer (Brucker AXS D8 Discover) equipped with a two-dimensional solid-state detector, using a Co-Kα radiation source operated at 40 kV and 500 μA. The chemical compositions of the run products were then quantified using a JEOL JXA-8200 electron probe microanalyzer (EPMA) operating at 15 kV and 15 nA. Periclase, corundum, and iron metal were used as standards. Analyses were performed with a focused beam of approximately 1 μm diameter. Simulations on the influence of secondary fluorescence from the adjacent $Al_2O_3$-rich phase on the Al concentration in periclase were performed using the PENEPMA computer program (Llovet and Salvat, 2017). The effect is found to be negligible, as it contributes < 0.016 wt.% to the periclase analysis when the probe beam is 2 μm away from the grain boundary of an $Al_2O_3$-rich phase, see supplementary Fig. 4.S1.

**Table 4.1** Experimental Conditions and Results

| Run No. | Pressure (GPa) | Temperature (K) | Duration (min) | Coexisting phases[a] | EPMA Measurements on Periclase (wt.%) [b] | | | | | Normalized compositions (mol.%) | | |
|---|---|---|---|---|---|---|---|---|---|---|---|---|
| | | | | | MgO | FeO | $Al_2O_3$ | Total | N | MgO | FeO | $Al_2O_3$ |
| H5431b | 15 | 1773 (50) | 760 | Per, Sp | 99.8 (5) | n. d. | 0.9 (2) | 100.8 (3) | 11 | 99.63 (10) | 0.00 (0) | 0.37 (10) |
| H5424b | 15 | 2073 (50) | 30 | Per, Sp | 96.1 (3) | 0.5 (1) | 3.4 (2) | 100.0 (2) | 5 | 98.33 (14) | 0.30 (8) | 1.37 (8) |
| H5482b | 19 | 1773 (50) | 20 | Per, Cor | 99.1 (3) | 0.0 (0) | 0.5 (1) | 99.6 (3) | 6 | 99.79 (4) | 0.01 (1) | 0.21 (4) |
| H5490b | 19 | 1773 (50) | 10 | Per, Cor | 99.7 (8) | 0.0 (0) | 0.6 (1) | 100.3 (8) | 6 | 99.78 (3) | 0.01 (0) | 0.22 (3) |
| H5492b | 19 | 2073 (50) | 20 | Per, Cor | 97.5 (5) | 0.0 (0) | 2.5 (2) | 100.0 (3) | 7 | 98.98 (2) | 0.02 (2) | 1.00 (8) |
| H5495 | 19 | 2273 (50) | 5 | Per, Cor | 93.4 (8) | 0.0 (0) | 7.1 (7) | 100.6 (5) | 11 | 97.06 (29) | 0.01 (1) | 2.93 (29) |
| H5310b | 23 | 1923 (50) | 360 | Per, Cor | 99.9 (5) | 0.0 (0) | 1.1 (1) | 101.0 (5) | 14 | 99.55 (4) | 0.01 (1) | 0.45 (4) |
| H5306 | 23 | 2073 (50) | 180 | Per, Cor | 98.2 (7) | 0.0 (0) | 2.5 (1) | 100.7 (6) | 5 | 99.01 (3) | 0.01 (0) | 0.98 (4) |
| H5299[c] | 23 | 2273 (50) | 120 | Per, Cor, (Ldw) | 94.7 (5) | 0.0 (0) | 5.4 (2) | 100.1 (5) | 3 | 97.79 (9) | 0.02 (1) | 2.19 (9) |
| I1421c | 27 | 1973 (50) | 10 | Per, Cor | 99.2 (3) | 0.0 (0) | 0.9 (1) | 100.1 (3) | 12 | 99.64 (4) | 0.01 (1) | 0.34 (4) |
| H5420b | 23 | 2373 (50) | 15 | Per, Ldw | 93.0 (7) | 0.9 (7) | 6.6 (4) | 100.6 (4) | 9 | 96.72 (53) | 0.55 (39) | 2.73 (15) |
| H5435b | 23 | 2400 (50) | 5 | Per, Ldw | 90.1 (6) | 0.1 (0) | 8.3 (3) | 98.5 (7) | 15 | 96.42 (13) | 0.06 (2) | 3.52 (12) |
| H5317b | 23 | 2623 (50) | 3 | Per, Ldw | 84.7 (6) | 0.4 (1) | 15.6 (7) | 100.7 (6) | 9 | 92.97 (31) | 0.27 (6) | 6.76 (32) |
| H5359b | 23 | 2623 (50) | 1 | Per, Ldw | 85.4 (6) | 0.0 (0) | 15.0 (7) | 100.4 (4) | 9 | 93.48 (31) | 0.01 (1) | 6.51 (31) |
| H5345b | 23 | 2623 (50) | 1 | Per, Ldw | 86.9 (6) | 0.0 (0) | 14.1 (6) | 101.0 (6) | 13 | 93.97 (25) | 0.01 (1) | 6.02 (25) |
| I1401b | 27 | 1973 (50) | 10 | Per, CF | 100.5 (3) | 0.0 (0) | 0.8 (1) | 101.2 (2) | 11 | 99.70 (4) | 0.01 (1) | 0.29 (4) |
| I1412c | 27 | 2123 (50) | 5 | Per, CF | 99.6 (4) | 0.0 (0) | 1.1 (1) | 100.7 (3) | 16 | 99.54 (5) | 0.01 (1) | 0.45 (4) |
| I1255 | 27 | 2200 (50) | 120 | Per, CF | 97.9 (7) | n. d. | 2.6 (1) | 100.5 (6) | 16 | 98.96 (6) | 0.00 (0) | 1.04 (6) |
| I1193 | 33 | 2000 (50) | 1200 | Per, CF | 96.6 (4) | 0.0 (0) | 0.4 (1) | 97.0 (13) | 9 | 99.81 (6) | 0.02 (3) | 0.17 (4) |
| I1415 | 33 | 2300 (50) | 10 | Per, CF | 98.1 (5) | 0.1 (2) | 1.8 (1) | 100.0 (5) | 11 | 99.23 (13) | 0.06 (2) | 0.71 (4) |
| I1420 | 50 | 2000 (50) | 20 | Per, CT | 100.4 (4) | 0.0 (0) | 0.4 (0) | 100.8 (3) | 13 | 99.85 (2) | 0.01 (0) | 0.15 (4) |

Notes. [a] Abbreviations: Per, periclase; Sp, spinel; Cor, corundum; Ldw, $Mg_2Al_2O_5$ phase with a modified ludwigite structure; CF, calcium ferrite phase of $MgAl_2O_4$; CT, calcium titanate phase of $MgAl_2O_4$. [b] The numbers in parentheses are one standard deviation in terms of least units cited and n. d. is not detectable. N is the number of EPMA-analyses. [c] In run H5299, the TC broke at 2223 K, and the final temperature (2273 K) is extrapolated from the power-temperature relation of the same run. The coexisting phases are Per and Sp near the TC, but the Ldw phase, indicated in the brackets, appears in the hotter region of the assembly.

## 4.3 Results

### 4.3.1 *Phase assemblages identified in the $MgO$-$Al_2O_3$ system experiments*

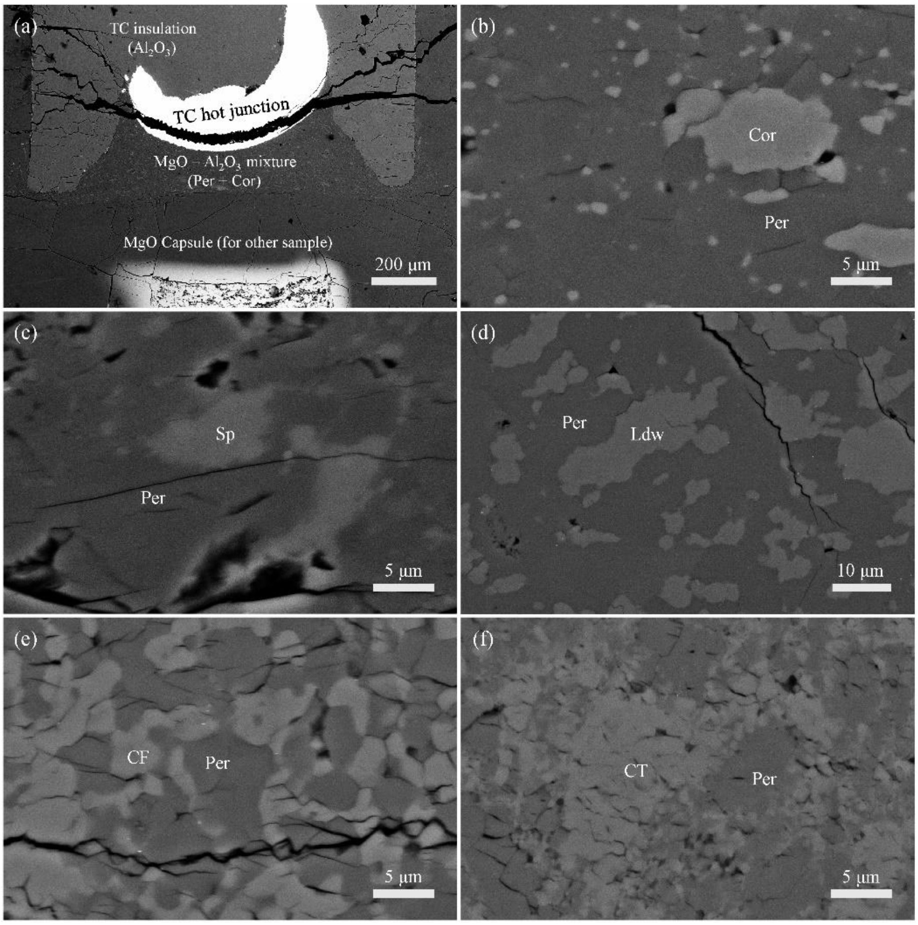

**Figure 4.1.** Backscattering electron images of recovered samples. a) An example where a $MgO$-$Al_2O_3$ mixture was placed around the thermocouple (TC) junction of a high-pressure assembly. The assembly was recovered from 23 GPa and 1923 K (H5310b). (b) An enlarged portion of the $MgO$-$Al_2O_3$ mixture located directly under the TC hot junction shown in (a) containing the assemblage periclase (Per) and corundum (Cor). (c) Coexisting periclase (Per) and spinel (Sp) recovered from 15 GPa and 1773 K (H5431b). (d) Coexisting periclase and $Mg_2Al_2O_5$ phase with a modified ludwigite structure (Ldw) recovered from 23 GPa and 2623 K (H5359b). (e) Coexisting periclase and calcium ferrite phase (CF) of $MgAl2O_4$ recovered from 27 GPa and 2200 K (I1255). (f) Coexisting periclase and calcium titanate (CT) phase of $MgAl_2O_4$ recovered from 50 GPa and 2000 K (I1420).

The experimental conditions and run products are listed in Table 4.1 and images of typical experimental samples are shown in Fig. 4.1. Diffusion and reaction of MgO or $Al_2O_3$ from the surrounding assembly into the samples was found to be minimal and all runs contained periclase coexisting with an $Al_2O_3$-rich phase, which therefore fixed the $Al_2O_3$ activity. As stated, in most of the experiments the MgO-$Al_2O_3$ sample was placed around the TC junction and a secondary sample was often placed below this, which was used for another purpose. This secondary sample was in some instances FeO-bearing and diffusion of FeO resulted in minor amounts of FeO in the MgO-$Al_2O_3$ samples, which reached values in the range 0.1-0.5 wt % in four samples and 0.9 wt % in one sample (Table 4.1). As explained later, FeO appears to have very little effect on the $Al_2O_3$ solubility in periclase, especially at these very low concentrations.

The average grain size of periclase in different runs ranged from approximately 5 μm to a little larger than 10 μm, depending on the temperature and heating duration. The chemical composition of periclase is homogenous within single periclase grains and does not show significant chemical zoning. The diffusion coefficients of Al in periclase are expected to be larger than 10-13 $m^2$/s under the pressure and temperature conditions in the present experiments (Van Orman et al., 2009). The diffusion length scale of Al in periclase should, therefore, be larger than the typical grain size of 5 μm within 1 min, implying that chemical equilibrium should be rapidly achieved. As the grain size of the starting materials is ~1 μm, the rapid grain growth, even in experiments run for only 10 min at 1773 K, also indicates rapid diffusion of Mg and Al in periclase, therefore, also supporting the attainment of chemical equilibrium in the run products.

The experimental phase relations are plotted in Fig.4.2 and compared with the previous estimates of these boundaries. The breakdown of $MgAl_2O_4$ spinel to MgO and $Al_2O_3$ was found to occur between 15 GPa and 19 GPa at temperatures between 1773 K and 2273 K, which agrees well with the phase boundaries established in the experiments of Akaogi et al. (1999) and Kojitani et al. (2010). At temperatures higher than 2273 K at 23 GPa, corundum and periclase recombined to form a $Mg_2Al_2O_5$ modified ludwigite (Ldw) structured phase, which is also consistent with previous studies (Enomoto et al., 2009 and Kojitani et al., 2010). The $MgAl_2O_4$ calcium ferrite (CF) structured phase was found at pressures of 27 GPa and 33 GPa, consistent with the transition boundary determined by Kojitani et al. (2010). A low-density calcium ferrite phase (LD-CF) identified by Ishii et al. (2021) at 27 GPa and 2773 K and a $MgAl_2O_4$ phase of unknown structure (unknown phase, UP) stable above 26 GPa and 2473 K found by Kojitani et al (2010) were out of the investigated pressure and temperature range of this study. At 50 GPa and 2000 K (I1420), a $MgAl_2O_4$ calcium titanate (CT) phase was identified by powder XRD (Supplementary Fig. 4.S2).

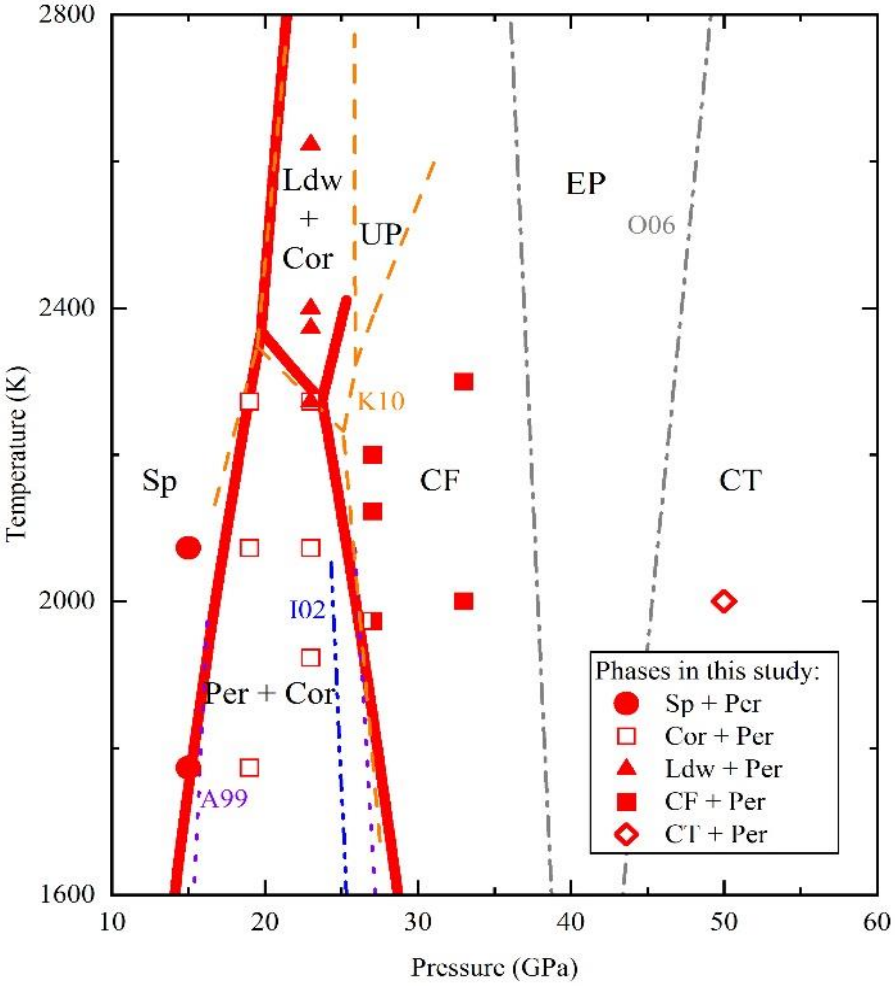

**Figure 4.2.** Phase relations in the MgO-Al$_2$O$_3$ system and the phase assemblages observed at different P-T conditions in this study. Abbreviations are Per, periclase; Sp, spinel; Cor, corundum; Ldw, Mg$_2$Al$_2$O$_5$ phase with a modified ludwigite structure; CF, calcium ferrite phase of MgAl$_2$O$_4$; CT, calcium titanate phase of MgAl$_2$O$_4$. UP is the MgAl$_2$O$_4$ phase with an unknown structure discovered by Kojitani et al. (2010) and EP is the ε-type MgAl$_2$O$_4$ phase found by Liu (1978) and confirmed by Ono et al. (2006). Thick red lines show the phase boundaries calculated from the thermodynamic model described in section 3.3, where the UP, EP, and CT phases were not considered. The violet dotted lines (A99) indicate the Sp = Per + Cor and Per + Cor = CF phase from Akaogi et al. (1999). The blue dash dotted line (I02) is the phase boundary Per + Cor = CF phase from Irifune et al. (2002). The orange dashed lines (K10) are phase boundaries between Sp, Per + Cor, CF, Ldw + Cor, and UP from Kojitani et al. (2010). The grey dash lines (O06) are the phase boundaries between CF/EP and EP/CT determined by Ono et al. (2006).

The chemical compositions of the coexisting phases can be found in Table 4.S1. The spinel and CF phase are slightly enriched in MgO, exhibiting an Al/Mg ratio ranging between 1.92 and 1.98. Coexisting corundum contains up to 2.5 mol.% MgO. The composition of the modified ludwigite phase closely aligns with $Mg_2Al_2O_5$ stoichiometry, within the margins of analytical uncertainty. In contrast, the $MgAl_2O_4$ CT phase synthesized at 50 GPa and 2000 K is markedly non-stoichiometric, with an Al/Mg ratio of 1.85.

### 4.3.2 *Solubility of $Al_2O_3$ in periclase*

Table 4.1 and Fig. 4.3 show the $Al_2O_3$ concentration in periclase coexisting with different Al-rich phases at various P-T conditions. Following the same non-linear trend as the ambient pressure data (e.g., Alper et al., 1962; Stubican and Roy, 1965; Mori, 1982; Zienert and Fabrichnaya, 2013), the solubility of $Al_2O_3$ in periclase increases strongly with temperature. For example, at 23 GPa it increases from 0.45 mol.% at 1923 K to higher than 6.8 mol % at 2623 K. The transition of the coexisting $Al_2O_3$-rich phase from corundum to the $Mg_2Al_2O_5$ ludwigite phase has a near negligible influence on the $Al_2O_3$ solubility in periclase, as the temperature dependence follows an almost identical trend before and after the phase transition at 23 GPa. Overall, pressure suppresses the solubility of $Al_2O_3$ in periclase and decreases its rate of change, i.e., sensitivity, with temperature. For example, an increase in temperature of 100 K at 1 bar and 2000 K raises the solubility by approximately 1.1 mol %, whereas the solubility drops by approximately the same amount if the pressure is increased to 15 GPa, where the temperature sensitivity, i.e., the increase in the periclase $Al_2O_3$ solubility for the same temperature increase, is approximately halved. By 33 GPa the experimentally determined solubilities are < 1 mol % even at the highest temperature investigated, and by 50 GPa the solubility is approximately one order of magnitude lower (0.15 mol.%) than the ambient pressure value at 2000 K. This pressure dependency is due to the positive volume change that occurs as Al enters periclase from a coexisting phase, which is compounded by the high-pressure phase transitions to increasingly denser phases. As periclase goes through no phase transition at mantle conditions, its $Al_2O_3$ solubility will likely decrease throughout the entire mantle, i.e. up to 135 GPa.

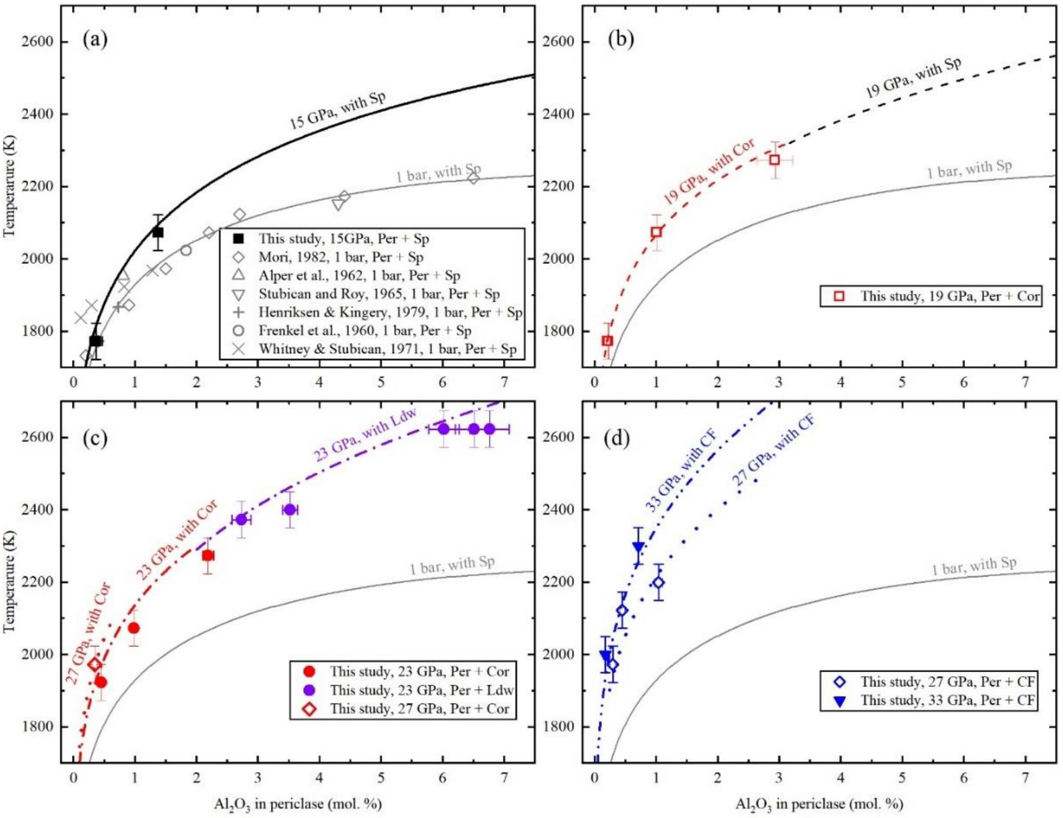

**Figure 4.3.** The solubility of $Al_2O_3$ in periclase as a function of pressure and temperature. Experimental results at 15 GPa (a), 19 GPa (b), 23 to 27 GPa (c), and 27 to 33 GPa are compared with a thermodynamic model that is fit to the entire dataset, as described in section 3.3. Results at ambient pressure from the literature (Frenkel et al., 1960; Alper et al., 1962; Stubicam and Roy, 1965; Whitney and Stubicam, 1971; Henriksen and Kingery, 1979; Mori, 1982) are also plotted for comparison. All curves are calculated considering the indicated coexisting phases at the denoted pressures using the thermodynamic model. The abbreviations are as described for Fig. 4.2.

### *4.3.3 Thermodynamic modeling of the MgO-$Al_2O_3$ System*

A series of equilibria involving a periclase $AlO_{1.5}$ component are used to fit the experimental data in the MgO-$Al_2O_3$ system over different pressure ranges, depending on the stability of the coexisting $Al_2O_3$-rich phase. In this fitting process thermodynamic terms for the standard state of the $AlO_{1.5}$ component and periclase non-ideal mixing terms are refined. The use of an $AlO_{1.5}$ component is consistent with previous 1 bar treatments (Hallstedt 1992; Zienert and Fabrichnaya, 2013) and with the models that use an $FeO_{1.5}$ component in wüstite and ferropericlase (Jung et al. 2004; Hidayat et al., 2017). For the thermodynamic properties of coexisting corundum and spinel, which are all treated as single component phases, the database of Holland and Powell (2011) is used. For the $Mg_2Al_2O_5$ modified ludwigite phase, the standard state properties were fitted using the phase relations (Kojitani et al., 2010), employing properties from the Holland and Powell (2011) database for all other phases, with the heat capacity estimated from a summation of values for periclase and corundum. For the CF phase an existing thermodynamic treatment was used (Kojitani et al., 2012). The phase boundaries calculated using these data are shown as the solid curves in Fig. 4.2 and are in good agreement with phase boundaries bracketed by Kojitani et al. (2010). As the phase boundaries with the CT phase are poorly known, the data point obtained at 50 GPa was not used in the model. To fit the phase equilibria data of Akaogi et al. (1999) and Kojitani et al. (2010) for the breakdown of spinel to periclase and corundum it was necessary to add a $\Delta V$ of disordering to the spinel Bragg-Williams treatment in the Holland and Powell (2011) database. These two previous studies on the phase relations are inconsistent with each other, which is assumed to be caused by metastable persistence of spinel at temperatures <1500°C in the experiments of Akaogi et al. (1999).

Several studies have examined the Al-content of periclase in equilibrium with spinel at 1 bar (Alper et al., 1962; Stubican and Roy, 1965; Mori, 1982). From the equilibrium

$$\underset{\text{spinel}}{\mathrm{MgAl_2O_4}} <=> \underset{\text{periclase}}{\mathrm{2AlO_{1.5} + MgO}} \tag{4.1}$$

the condition for equilibrium can be rearranged to give

$$-\Delta G^{\mathrm{o}}_{(1)} = RTln\left(X^{\mathrm{Per}}_{\mathrm{MgO}}\right) + 2RTln\left(X^{\mathrm{Per}}_{\mathrm{AlO_{1.5}}}\right) + W^{\mathrm{Per}}_{\mathrm{MgO-AlO_{1.5}}}\left[1 - 2X^{\mathrm{Per}}_{\mathrm{MgO}} + 3\left(X^{\mathrm{Per}}_{\mathrm{MgO}}\right)^2\right] \tag{4.2}$$

where $\Delta G^{\mathrm{o}}_{(1)}$ is the standard state Gibbs free energy of equilibrium (6.1), R is the gas constant, $X^{\mathrm{Per}}_{\mathrm{AlO_{1.5}}}$ is the mole fraction of $AlO_{1.5}$ in periclase, and $W^{\mathrm{Per}}_{\mathrm{MgO-AlO_{1.5}}}$ is a symmetric Margules interaction parameter that describes the non-ideality of mixing between MgO and $AlO_{1.5}$ in periclase. $W^{\mathrm{Per}}_{\mathrm{MgO-AlO_{1.5}}}$ is a function of temperature and pressure i.e.,

$$W^{\mathrm{Per}}_{\mathrm{MgO-AlO_{1.5}}} = W_H - TW_S + PW_V \tag{4.3}.$$

$\Delta G^{\mathrm{o}}_{(1)}$ is determined using the Holland and Powell (2011) database except for the $AlO_{1.5}$ component of periclase which is calculated at 1 bar and the temperature of interest from,

$$\Delta_f G^{o\,\mathrm{Per}}_{\mathrm{AlO_{1.5}(1bar,T)}} = 0.5\left[\Delta_f G^{o\,\mathrm{Cor}}_{\mathrm{Al_2O_3(1bar,T)}} + A + B\mathrm{T}\right] \tag{4.4}$$

where $\Delta_f G^{o\,Cor}_{Al_2O_3(\mathrm{1bar,T})}$ is the Gibbs free energy of formation of corundum, calculated from the Holland and Powell (2011) database, and A and B are constants. The terms A, B, $W_H$, and $W_S$ were refined by fitting 1 bar measurements of the Al- content of periclase in equilibrium with spinel (Frenkel et al., 1960; Alper et al., 1962; Stubican and Roy, 1965; Whitney and Stubican, 1971; Henriksen and Kingery, 1979; Mori, 1982) to equation (6.2). The non-stoichiometric higher MgO content of spinel observed at 1 bar with increasing temperature was ignored as it is relatively small (~5 mol %) and is not observed in the high-pressure data (see supplementary Table 4.S1). Using a series of equilibria similar to equation (6.2), data from experiments where periclase coexists with spinel, corundum, the $Mg_2Al_2O_5$ ludwigite phase and the $MgAl_2O_4$ CF phase, were fitted simultaneously in a weighted least squares procedure by refining the $W_V$ term of the periclase interaction parameter and the volume and bulk modulus of the periclase $AlO_{1.5}$ component. Refinement of the thermal expansion term resulted in unfeasibly high values and it was, therefore, fixed at the value for periclase. The resulting terms are reported in supplementary Table 4.S2-4.S4 and a comparison between the model and the experimental data is shown in Fig. 4.3. The model well describes both the ambient pressure data from the literature (Frenkel et al., 1960; Alper et al., 1962; Stubicam and Roy, 1965; Whitney and Stubicam, 1971; Henriksen and Kingery, 1979; Mori, 1982) and the high-pressure data from this study. The discrepancy in temperature between data points and the model are generally within 2%. The major uncertainty in the experimental data is caused by the temperature gradient in the sample region, even though we chose grains for microprobe analysis that were as close to the thermocouple hot junction as possible. As the hot junction generally extends over at least 0.5 mm in the radial direction and 0.2 mm axially (Fig. 4.1a), thermocouple readings are likely to be still averages over these regions, even though the high thermal conductivity of the thermocouple wires should alleviate this to some extent. Nevertheless, the difference in temperature between thermocouple readings and actual temperatures of the EPMA analysed region may be up to 50 K. Furthermore, no correction was applied to the thermocouple emf to take account of a potential pressure effect. Although such an effect has been measured for type-D thermocouple (Nishihara et al., 2020), the conditions at which it has been determined are at lower pressures and temperatures than examined here and cannot be safely extrapolated. Any pressure corrections on temperature measurements using type-D thermocouples determined in the future at conditions closer to the experiments performed here, would, therefore, have to be added on to the temperatures determined using $Al_2O_3$ solubility analyses.

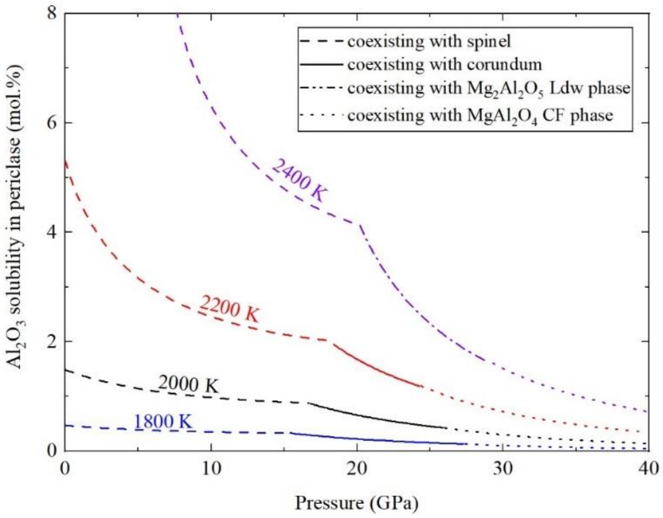

**Figure 4.4.** $Al_2O_3$ solubility in periclase as a function of pressure in the $MgO$-$Al_2O_3$ system calculated using the derived thermodynamic model. The coexisting phases are indicated by the type of dashed and solid lines. The abbreviations are as described for Fig. 4.2.

The experiment at 50 GPa, where the $MgAl_2O_4$ structured CT phase coexisted with periclase, was not included in the modelling as there are insufficient observations to obtain thermodynamic properties for the CT phase. As shown in Fig. 4.S3, an extrapolation of the model assuming equilibrium with the lower pressure CF phase underestimates the periclase $Al_2O_3$ content at 2000°C by approximately 0.07 mol %, which is outside of the analytical uncertainty of 0.04 mol %. Although the model is probably consistent once temperature uncertainties are also considered, it is unexpected that fixing the $Al_2O_3$ activity with the CF phase underestimates values in the CT phase stability field, as the latter has a smaller volume and we would, therefore, expect the model to overestimate it (Ono et al., 2006). It is possible that this discrepancy may be explained once reliable data to determine the thermodynamic properties from the phase boundaries becomes available.

Fig. 4.4 shows the results of the thermodynamic model with the $Al_2O_3$ content of periclase calculated at four different temperatures between ambient pressure and 40 GPa. The sensitivity of the $Al_2O_3$ solubility to temperature is high above 1800 K and increases with temperature, which can be attributed to the effect of the configurational entropy on the $Al_2O_3$ solubility and also due to a decrease in the Margules interaction term. However, the solubility also decreases with pressure, with a steepening in slope occurring upon the phase transformation of spinel to higher-pressure phases. This is an effect of the volume change of the governing equilibrium and is most likely caused by a change in site occupancy of Al, from partial tetrahedral occupancy in spinel to complete octahedral occupancy in corundum and the ludwigite structure. Periclase $Al_2O_3$ solubility could be applied as a thermometer and/or barometer in high pressure multi-anvil experiments, or in other high-pressure equipment. This might be useful, for example, in experiments where the thermocouple has broken, perhaps during studies of high-pressure melting phase relations. Very small amounts of $MgO$-$Al_2O_3$ mixtures could be added to the high-pressure assembly and then analysed afterwards to extract the temperature. At 2100 K and 15 GPa, for example, a 0.1 mol % difference in $Al_2O_3$ content, which is easily measurable, equates to a temperature difference of only 20 K. Whereas if the pressure at these conditions was uncertain by 2 GPa, this equates to a change in solubility of only 0.05 mol %, i.e., a 10 K uncertainty on the absolute temperature determination. The accuracy of such absolute temperature determinations increases with temperature but decreases with pressure and would become inaccurate above 27 GPa, where the solubility becomes low and small changes equate to large temperature changes. On the other hand, if the temperature were to be measured using a thermocouple, then at temperatures above 2200 K the solubility could be used to provide a quite accurate pressure determination, also with a practical limit of approximately 27 GPa, although potentially higher for experiments performed at the volatile-free silicate solidus.

### *4.3.4 Further experiments on the effect of FeO on ferropericlase $Al_2O_3$ solubility*

Two experiments (H5874, H5875) were conducted in the FeO-MgO-$Al_2O_3$ system at 21 GPa and temperatures of approximately 2000 and 2200 K respectively. As these experiments were performed to examine the effect of FeO on ferropericlase $Al_2O_3$ solubility at the same temperatures, no thermocouple was employed and temperatures are simply compared to those obtained from the MgO-$Al_2O_3$ sample in the same experiment. The run products of the four compositions in both experiments are periclase or ferropericlase coexisting with corundum (see Fig. 4.5 and Fig. 4.S4). Grains of metallic iron remained in all recovered samples from the FeO-bearing starting compositions, ensuring minimal ferric iron. The FeO concentrations in the ferropericlase samples are a few mole percent higher than in the starting materials (see Fig. 4.5 and Table 4.2), due to oxidation of metallic iron, most likely, by absorbed water in the starting materials and ceramic assembly components. The capsule containing the four samples was ground and exposed perpendicular to the axial direction of the furnace, close to the upper surface (end). As each sample is located at an approximately symmetric position, they should each have experienced the same temperature. Run H5875 was then ground down a second time by a further 0.3 mm to expose the four samples closer to the center of the capsule in the axial direction, which experienced a higher temperature (center) than at the end of the capsule. As shown in Fig. 4a, compared to the FeO-free end-member, the presence of up to 44 mol.% FeO in ferropericlase results in only a minor variation in ferropericlase $Al_2O_3$ solubility. In run H5874, for which the end-member periclase $Al_2O_3$ solubility gives a T of 2124±20 K, with the uncertainty propagated only from the compositional variation, the ferropericlase samples have identical $Al_2O_3$ solubilities within the analytical uncertainty (~0.1 mol.%). For the end of the sample in run H5875, the periclase solubility gives a T of 2235±13 K, whereas the more FeO-rich samples have slightly lower solubilites. Nevertheless, the T calculated for the ferropericlase samples are still at most only 42 K lower. At the center of the same sample the T is 2299±11 K, and the FeO-samples again record temperatures that are only 45 K lower. Given that the apparent effect of FeO on the ferropericlase $Al_2O_3$ solubility only seems to appear once the temperature is raised above approximately 2100 K, is seems more plausible that the FeO-samples at these higher temperatures are indeed recoding small radial temperature variations in the assembly, rather than an effect of FeO on the $Al_2O_3$

solubility. Even if there were an effect of FeO it appears to be insignificant at temperatures below 2100 K and at higher temperatures would cause differences in temperature of < 50 K for FeO contents up to 44 mol.% FeO. We consider, therefore, that for most practical applications the effect of FeO on the $Al_2O_3$ solubility in ferropericlase can be ignored.

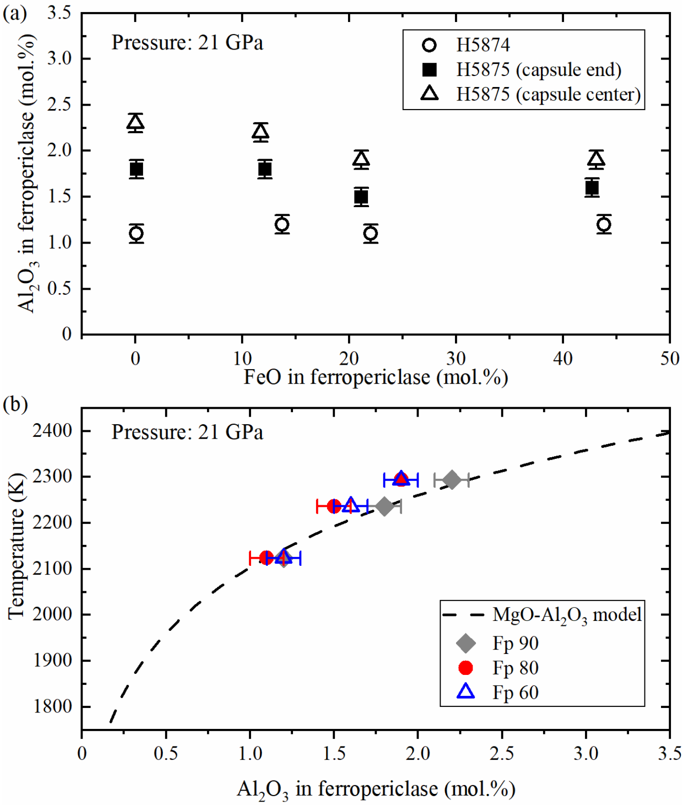

**Figure 4.5.** The solubility of $Al_2O_3$ in ferropericlase at 21 GPa. (a) The $Al_2O_3$ solubility is plotted as a function of the FeO content in ferropericlase. (b) The $Al_2O_3$ solubilities are plotted as a function of temperature determined from the periclase sample, assuming that all four samples in each capsule experienced the same temperature.

**Table 4.2.** Chemical Compositions of Periclase and Ferropericlase in Runs H5874 and H5875

| Run No. a | P (GPa) | Starting materials b | EPMA Measurements (wt.%) c | | | | Normalized compositions (mol.%) | | | |
|---|---|---|---|---|---|---|---|---|---|---|
| | | | MgO | FeO | $Al_2O_3$ | Total | N | MgO | FeO | $Al_2O_3$ |
| H5874a | 21 | Fp100 + $Al_2O_3$ | 94.9 (3) | 0.2 (0) | 2.7 (1) | 97.8 (2) | 8 | 98.8 (5) | 0.1 (0) | 1.1 (1) |
| H5874b | 21 | Fp90 + $Al_2O_3$ + Fe | 74.9 (3) | 21.5 (2) | 2.6 (1) | 99.0 (2) | 9 | 85.1 (1) | 13.7 (1) | 1.2 (0) |
| H5874c | 21 | Fp80 + $Al_2O_3$ + Fe | 64.5 (3) | 32.9 (3) | 2.4 (1) | 99.8 (3) | 9 | 76.8 (2) | 22.0 (2) | 1.1 (0) |
| H5874d | 21 | Fp60 + $Al_2O_3$ + Fe | 40.8 (3) | 57.8 (4) | 2.2 (1) | 100.8 (4) | 8 | 55.0 (3) | 43.8 (3) | 1.2 (1) |
| H5875a (end) | 21 | Fp100 + $Al_2O_3$ | 93.0 (3) | 0.2 (0) | 4.2 (1) | 97.5 (3) | 8 | 98.1 (1) | 0.1 (0) | 1.8 (1) |
| H5875b (end) | 21 | Fp90 + $Al_2O_3$ + Fe | 76.2 (4) | 19.1 (5) | 3.9 (2) | 99.3 (3) | 9 | 86.2 (3) | 12.1 (3) | 1.8 (1) |
| H5875c (end) | 21 | Fp80 + $Al_2O_3$ + Fe | 65.2 (2) | 31.7 (2) | 3.3 (1) | 100.1 (3) | 11 | 77.4 (1) | 21.1 (1) | 1.5 (1) |
| H5875d (end) | 21 | Fp60 + $Al_2O_3$ + Fe | 41.3 (1) | 56.4 (3) | 3.0 (1) | 100.6 (4) | 9 | 55.7 (1) | 42.7 (1) | 1.6 (1) |
| H5875a (center) | 21 | Fp100 + $Al_2O_3$ | 92.0 (2) | 0.1 (0) | 5.5 (2) | 97.5 (2) | 10 | 97.7 (1) | 0.0(0) | 2.3 (1) |
| H5875b (center) | 21 | Fp90 + $Al_2O_3$ + Fe | 75.8 (3) | 18.3 (3) | 4.8 (2) | 98.9 (3) | 15 | 86.2 (1) | 11.7 (2) | 2.2 (1) |
| H5875c (center) | 21 | Fp80 + $Al_2O_3$ + Fe | 64.4 (3) | 31.4 (3) | 4.0 (2) | 99.8 (4) | 17 | 77.0 (1) | 21.1 (2) | 1.9 (1) |
| H5875d (center) | 21 | Fp60 + $Al_2O_3$ + Fe | 40.5 (2) | 56.4 (4) | 3.5 (1) | 100.4 (3) | 18 | 55.1 (2) | 43.1 (3) | 1.9 (1) |

[a] “end” and “center” indicate the measured surfaces that were close to the end or the center of the capsule perpendicular to the axial direction.

[b] Fp is ferropericlase, with Fp90 indicating, for example, 90 mol % MgO.

[c] The numbers in parentheses are one standard deviation and N is the number of analyses.

## 4.4 Discussion

### *4.4.1 Maximum $Al_2O_3$ contents in ferropericlase in the mantle*

Before examining ferropericlase $Al_2O_3$ contents in natural systems, it is important to consider whether the presence of other components may influence the $Al_2O_3$ solubilities. The only component present in sufficient proportions to affect $Al_2O_3$ solubility in natural diamond inclusions is FeO, and even this effect appears to be relatively minor, as previously discussed. $Cr_2O_3$ shows the second highest concentrations that can reach values of ~2 wt. %, but the $Al_2O_3$-$Cr_2O_3$ interaction parameters would have to be extremely large for such concentrations to influence the $Al_2O_3$ content and this seems not to be the case for other solid solutions such as spinel or garnet (O'Neill and Wall 1987; Luth et al., 1990). The same argument can be used to discount the effects of other minor components. The $Fe^{3+}/\sum Fe$ ratios in ferropericlase inclusions found in natural diamonds are typically lower than 0.12, and less than 0.05 $Fe^{3+}$ per 1 oxygen formula unit and are therefore unlikely to have any influence (McCammon et al., 1997; McCammon et al., 2004; Kaminsky et al., 2015; Kiseeva et al., 2022). It might be considered that Na could influence the Al content through a charge balanced substitution. However, the Na contents of natural ferropericlase inclusions in diamonds are at most ~1 wt. % and as a result the Na-Al interaction parameter would have to be extremely large for an effect on $Al_2O_3$ solubility to be produced. Such a substitution is also clearly not required for large amounts of Al to be accommodated in the periclase and ferropericlase structures.

To determine how periclase $Al_2O_3$ solubility would change within assemblages that might form in the mantle, we have to consider which Al-rich phases will coexist with periclase in the $MgO$-$Al_2O_3$-$SiO_2$ system, as they will fix the $Al_2O_3$ activity. In Fig. 4a, solubilities are calculated for both the $MgO$-$Al_2O_3$ and $MgO$-$Al_2O_3$-$SiO_2$ systems at temperatures along a typical mantle adiabat (Katsura, 2022). The latent heat effect of the phase transitions has been smoothed out in this profile (see supplementary Fig. 4.S5). For the $MgO$-$Al_2O_3$ system the effects of pressure and temperature result in a maximum $Al_2O_3$ solubility of approximately 0.5 mol % being reached at the spinel to corundum transition near 16 GPa. At this point the strongly temperature dependent solubility in the spinel field gives way to the stronger pressure dependence in the corundum field. If a solubility of this magnitude were found in a ferropericlase inclusion in a diamond, this would imply either adiabatic conditions near the top of the transitions zone, assuming the $Al_2O_3$ activity were set by equilibrium with corundum or pure spinel, or super-adiabatic conditions over a broader depth interval, if we assume that the $Al_2O_3$ activity was actually lower than this. This maximum will only exist in an SiO2-free system however. In the $MgO$-$Al_2O_3$-$SiO_2$ system, thermodynamic calculation shows that spinel is in equilibrium with periclase only to approximately 10 GPa, where it transforms to pyrope through the reaction:

$$\underset{\text{spinel}}{\mathrm{MgAl_2O_4}} + \underset{\text{forsterite}}{\mathrm{3Mg_2SiO_4}} = \underset{\text{periclase}}{\mathrm{4MgO}} + \underset{\text{pyrope}}{\mathrm{Mg_3Al_2Si_3O_{12}}} \tag{4.5}$$

It is interesting to note that in the presence of periclase, the transformation to produce pyrope is displaced to much higher pressures than in peridotite mantle. In peridotite mantle the pyrope-forming reaction involves enstatite and occurs at approximately 1.5 GPa, but in the presence of excess periclase, enstatite is unstable with respect to forsterite. In the presence of pyrope the $Al_2O_3$ activity drops sharply with pressure, as calculated from the equilibrium,

$$\underset{\text{periclase}}{\mathrm{3MgO}} + \underset{\text{pyrope}}{\mathrm{Mg_3Al_2Si_3O_{12}}} <=> \underset{\text{forsterite}}{\mathrm{3Mg_2SiO_4}} + \underset{\text{periclase}}{\mathrm{Al_2O_3}} \tag{4.6}$$

and at higher pressures from similar equilibria involving wadsleyite and ringwoodite (high pressure polymorphs of forsterite). The presence of periclase means that there is no majoritic component in garnet at transition zone conditions because there is no $MgSiO_3$ component as it reacts with periclase to produce an $Mg_2SiO_4$ polymorph. This is actually consistent with analyses of garnet inclusions in natural diamonds that are considered to be co-occurring with ferropericlase inclusions and which indeed show no majorite component (Walter et al., 2022; Hutchinson, 1997).

As ringwoodite breaks down to periclase and bridgmanite at high pressure, the periclase Al-content is calculated to rise very rapidly due to the volume change of the equilibrium. We can again calculate the maximum plausible Al-content in periclase by using the pyrope end-member in the calculations:

$$\mathrm{Mg_3Al_2Si_3O_{12}} <=> \mathrm{3MgSiO_3} + \mathrm{Al_2O_3} \qquad (4.7)$$

pyrope bridgmanite periclase

At approximately 26 GPa pyrope will then break down (Ishii et al., 2023) and the CF-$MgAl_2O_4$ phase will become the most $Al_2O_3$-rich phase that can coexist with ferropericlase in the lower mantle. In a peridotite composition the bridgmanite $Al_2O_3$ content would fix the activity of $Al_2O_3$, but this would result in periclase $Al_2O_3$ solubilities lower than those indicated for coexistence with the CF phase. Although higher pressure $MgAl_2O_4$ polymorphs including the CT-phase are not considered in the model, as they are increasingly denser, they should lead to even lower ferropericlase $Al_2O_3$ contents compared to the CF phase field. The results on the CT phase discussed in section 3.3 are in general agreement with this, even if they do not agree perfectly with the extrapolation of the CF model. Therefore, the CF curve in Fig. 4.6a still provides a conservative maximum plausible ferropericlase $Al_2O_3$ content along a mantle adiabat.

The $Al_2O_3$ concentrations in periclase coexisting with bridgmanite in the MgO-$SiO_2$-$Al_2O_3$ system reported by Liu et al. (2019a, 2019b) at 27 GPa are in good agreement with our calculated values. As discussed previously, the effect of FeO and other components should be minimal on the ferropericlase $Al_2O_3$ contents and in fact experimentally determined values reported for ferropericlase coexisting with garnet and bridgmanite are in good agreement with those predicted in Fig. 4.6a (Frost and Langenhorst, 2002; Huang et al., 2021). Data from Irifune (1994) and Irifune et al. (2010) are also in good agreement with our calculations and document a sharp increase in ferropericalse $Al_2O_3$ concentration at the top of the lower mantle, as calculated in the model. However, some of the reported ferropericlase compositions have $SiO_2$ contents ≥ 1 wt.%, which correlate with higher $Al_2O_3$ contents and likely arise from beam overlap with silicate phases.

Our thermodynamic calculations reveal that, under current adiabatic mantle temperatures, the $Al_2O_3$ content in mantle ferropericlase cannot exceed 0.5 mol.%, when uncertainties are considered. While such a minor impurity content will not noticeably affect the thermodynamic or thermoelastic properties of ferropericlase, it could conceivably influence transport properties. As the self-diffusion of Mg in periclase is sensitive to its $Al_2O_3$ content (e.g., Van Orman et al., 2003, 2009; Ammann et al., 2012; Riet et al., 2020), the influence of $Al_2O_3$ on the rate of chemical diffusion in lower mantle ferropericlase may have implications for other transport properties, such as rheology. Furthermore, as the $Al_2O_3$-content in ferropericlase diminishes with increasing depth in the lower mantle, as shown in Fig. 4.6a, this may, therefore, suppress cation diffusion in periclase in the deep lower mantle. In conjunction with the negative pressure dependence of self-diffusion coefficients in pure periclase (e.g., Ita and Cohen, 1998), bulk chemical transport in the deep lower mantle may be substantially slower compared to the uppermost parts of the lower mantle, with the exception of the core-mantle boundary, where elevated temperatures could accelerate this transport.

### *4.4.2 Interpreting the $Al_2O_3$ contents of ferropericlase inclusions in natural diamonds*

Fig. 4.6b plots the $Al_2O_3$ compositional distribution of natural ferropericlase inclusions in diamonds from the recent review of Walter et al., (2022), and a few other studies (Seitz et al., 2018; Nimis et al., 2019; Gu et al., 2022; Kisseeva et al., 2022; Lorenzon et al., 2023). The $Al_2O_3$ concentration of the inclusions varies between 0 and approximately 0.35 mol.% (0.5 wt.%), with an average value close to 0.04 mol.% (0.1 wt. %). As discussed previously it is unlikely that the FeO content of ferropericlase has a significant effect on the $Al_2O_3$ solubility so we assume solubilities are the same as for periclase. In this scenario, the concentration of $Al_2O_3$ is a sensor for $Al_2O_3$ activity, temperature, and pressure, with differing sensitivities under different conditions. It can, in principle, be used to constrain any of these three factors if the other two are known, and would, therefore, be more powerful in combination with other methods. If the $Al_2O_3$ activity could be isolated, independently, for example, at a particular pressure and temperature this would provide important information on the chemical environment in which the inclusion formed. Even in the absence of other methods, however, some conclusions can be made on natural samples by making certain reasonable assumptions. Two approaches can be taken, firstly for estimating the conditions of ferropericlase formation and secondly for excluding certain conditions for high-$Al_2O_3$ bearing inclusions. Before employing compositions of natural samples, it should be pointed out that probably none of the available analyses were performed to specifically determine the ferropericlase $Al_2O_3$-content and in some studies, it was not even analysed. Furthermore, in most studies the uncertainties are not reported, and neither can it be clarified that the reported Al-contents originate from ferropericlase and not from other inclusions. In fact, one value reported by Burnham et al (2016) of 8.38 wt. % $Al_2O_3$, (with a similar level of $SiO_2$), can most likely be excluded on these grounds. There is also evidence for Al-spinel exsolution from ferropericlase (Wirth et al., 2014), and if such exsolution annealed up after entrapment it might result in misleading or inhomogeneous $Al_2O_3$ contents.

Nonetheless, taking the analyses at face value and employing the first approach, we can examine inclusions that are reported to co-occur with $Al_2O_3$-rich phases and calculate a temperature assuming equilibrium with these phases. Hutchison (1997), for example, reports that ferropericlase inclusion BZ243B co-occurs with pyrope-rich garnet and olivine. Assuming the olivine has not back transformed from a higher-pressure polymorph, then the formation pressure would have been between 10 and 14 GPa. As shown in Fig. 4.6a, the $Al_2O_3$ solubility changes strongly with pressure under these conditions resulting in formation conditions that vary along a curve extending from 1447 K at 10 GPa to 1680 K at 14 GPa. Hutchison et al. (2004), intriguingly, report a corundum inclusion which is proposed to be associated with ferropericlase (BZ241A). If these phases were indeed in equilibrium then this implies equilibration conditions between 1507 K at 16 GPa and 1597 K at 26 GPa. Harte et al. (1999) on the other hand report that ferropericlase BZ207B co-occurs with proposed bridgmanite, which back-transformed on decompression, and jeffbenite, which may be back-transformed from pyrope (Nestola et al., 2023c). The low Al-content of the proposed bridgmanite limits the pressure to the top of the lower mantle and if we assume pressures of 24-25 GPa, and that jeffbenite was indeed back-transformed from pyrope, we obtain temperatures of between 1800 and 1664 K respectively. As these examples show, to narrow the determined temperatures it would be necessary to obtain an independent measure of the pressure.

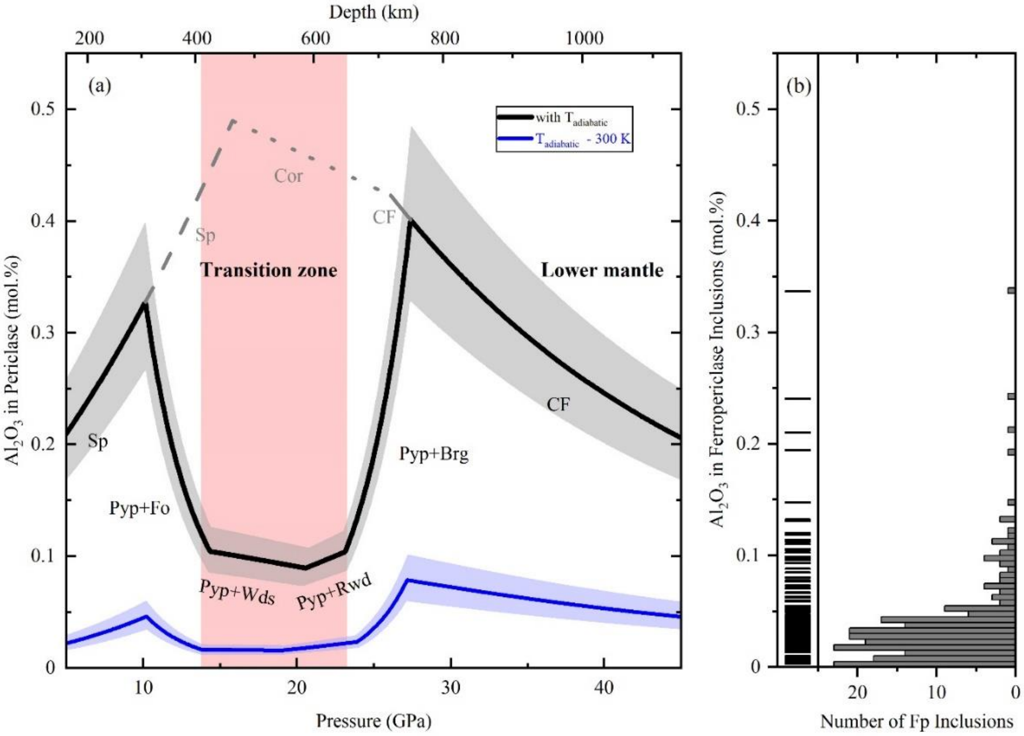

**Figure 4.6.** (a) $Al_2O_3$ solubility in periclase in the MgO-$SiO_2$-$Al_2O_3$ and MgO-$Al_2O_3$ systems calculated from the thermodynamic model. The black solid curve shows the calculated periclase $Al_2O_3$ concentration in the MgO-$SiO_2$-$Al_2O_3$ system coexisting with an Al-bearing mineral stable in the mantle at different depths, i.e., spinel (Sp), pyrope (Pyp), or $MgAl_2O_4$ CF phase, along a typical adiabatic mantle temperature (Katsura, 2022). Fo, Wds, and Rwd indicate the polymorphs of $Mg_2SiO_4$, forsterite, wadsleyite, and ringwoodite, respectively. Brg stands for the bridgmanite $MgSiO_3$ endmember. The dashed, dot, and solid grey curves show the maximum $Al_2O_3$ in periclase in the MgO-$Al_2O_3$ system, coexisting with Sp, corundum (Cor), and CF phase, respectively along the same adiabat. The solid blue line shows the periclase $Al_2O_3$ solubility in the MgO-$SiO_2$-$Al_2O_3$ system when the temperatures are 300 K lower than the mantle adiabat. The shaded regions indicate the uncertainties propagated from that of the adiabatic temperature. (b) The compositional distribution of $Al_2O_3$ contents in ferropericlase inclusions in diamonds, from Walter et al. (2022), Seitz et al., (2018), Nimis et al., (2019), Gu et al., (2022), Kisseeva et al., (2022) and Lorenzon et al., (2023).

Recently, Gu et al. (2022) reported an inclusion assemblage containing touching grains of ringwoodite, ferropericlase, and enstatite, where the enstatite grain was proposed to have been originally trapped as bridgmanite. Based on the Fe-Mg partitioning between ferropericlase and proposed bridgmanite, conditions of ~24 GPa and 1928±200 K were obtained. Nestola et al. (2023a) investigated a ferropericlase inclusion inside the same diamond using elastic geobarometry and obtained a quite consistent formation pressure of at least 22.1 (±2.1) GPa. We can make a temperature estimate for the inclusion reported by Gu et al. (2022) using the $Al_2O_3$ contents of the ferropericlase and the coexisting former bridgmanite inclusion, by equating the Gibbs free energies of the $Al_2O_3$ components in the two phases. In the particular inclusion, the bridgmanite FeO and $Al_2O_3$ contents are quite low, approximately 4.5 and 1.2 wt. % respectively and a coupled substitution of Al onto the two bridgmanite cation sites is, therefore, plausible (Huang et al., 2021). Using thermodynamic data for the bridgmanite $Al_2O_3$ component and an interaction parameter for bridgmanite $MgSiO_3$-$Al_2O_3$ mixing (reported in supplementary Table 4.S2 and 4.S3) derived by fitting coexisting compositions of bridgmanite and corundum determined by Liu et al (2017), we calculate a formation temperature of between 1987 K and 2099 K for pressures of 22.1 and 24 GPa respectively, which is in quite good agreement with the estimates of Gu et al. (2022). To give some idea of the uncertainty, the same calculation using the thermodynamic data of Stixrude and Lithgow-Bertelloni (2022) for the bridgmanite $Al_2O_3$ component gives temperatures that are approximately 150 K lower. If ideal mixing is assumed, all temperature estimates increase by 100 K. This is an interesting result because it not only indicates temperatures which are near or even possibly above a typical mantle adiabat at the top of the lower mantle, but the bridgmanite composition indicates $Al_2O_3$ activities that are relatively low, i.e. lower than those expected for typical mantle peridotite assemblages. As the bulk of ferropericlase inclusions have $Al_2O_3$ contents close to this low level (Fig. 4.6b) this might imply that they are in general formed at low $Al_2O_3$ activity rather than low temperatures. What is not clear, however, is why the assemblage reported by Gu et al. (2022) did not chemically reequilibrate during the journey to the lithosphere and then surface.

In the second approach, however, we can exclude conditions of formation of some inclusions where their $Al_2O_3$ contents would be higher than the calculated solubility in the MgO-$SiO_2$-$Al_2O_3$ system at those conditions. This of course works mainly for the highest $Al_2O_3$ bearing samples. The solubility calculated in the MgO-$SiO_2$-$Al_2O_3$ system in Fig. 4.6a should reflect the highest $Al_2O_3$ activity that can be obtained at any particular pressure and temperature. It is quite plausible that ferropericlase inclusions formed in the mantle under conditions where $Al_2O_3$-activities were lower than those implied by the coexistence of Al-rich phases. In some instances, for example, ferropericlase inclusions appear to co-occur with low-Al bearing chromite spinel (e.g. Kaminsky et al., 2001) that would impose $Al_2O_3$ activities much lower than implied by the curves in Fig. 4.6a. Similarly, the bridgmanite discussed in the last paragraph had an Al-content much lower than expected for a peridotite bulk composition. Therefore, even low ferropericlase $Al_2O_3$ contents could still equate to high temperatures of formation. However, ferropericlase $Al_2O_3$ contents cannot be higher than the calculated curves in Fig. 4.6a at any given pressure, unless temperatures were super adiabatic. Furthermore, the addition of FeO to the system has been shown to have an insignificant effect on $Al_2O_3$ solubility and further components such as CaO are hardly soluble in ferropericlase and will only serve to further lower the $Al_2O_3$ activity of the co-existing phase.

As shown in Fig. 4.6a, periclase $Al_2O_3$ solubility drops significantly in the mantle transition zone. This means that approximately eight of the most Al-rich ferropericlase inclusions can be excluded from forming in the mantle transition zone, unless temperatures were significantly higher than a typical mantle adiabat. These inclusions most likely formed either within a narrow pressure range around 10 GPa or in the top region of the lower mantle. However, these inclusions cannot have formed at temperatures more than 100 K lower than adiabatic temperatures, regardless of where they were produced. This is, therefore, good evidence that at least some diamonds did not form at low temperatures associated with either thick cratonic lithosphere or subduction zones, but at temperatures very close to those of the convecting mantle.

Several studies have proposed that ferropericlase-bearing diamonds may form in the mid-transition zone as carbonate melts released from a subducting slab are reduced on entering the ultramafic mantle (Thomson et al., 2016; Walter et al., 2022). Fig. 4.6a also shows the same maximum periclase Al-content curves calculated for a temperature profile 300 K below an adiabatic gradient, in order to approximate temperatures close to a subducting slab. The majority of ferropericlase inclusions have $Al_2O_3$-contents that would be quite consistent with such conditions in the transition zone, if they formed in equilibrium with garnet.

They could of course, however, have formed at higher temperatures, if $Al_2O_3$ activities were lower.

The $Al_2O_3$ content of ferropericlase inclusions can, therefore, be used to eliminate certain conditions for a subset of higher-Al bearing inclusions but the concentration on its own cannot provide a definitive answer regarding specific formation conditions. A more reliable approach is to use coexisting Al-bearing phases to constrain the $Al_2O_3$ activity and this can then be used to obtain temperatures through the use of an independent method to determine pressure, such as elastic thermobarometry (Anzolini et al., 2019; Kohn et al., 2023). It is also possible that other minor elements in ferropericlase inclusions can yield information on the formation conditions, using a similar type of calibration as performed here. The $SiO_2$ concentration, for example, is generally of a similar magnitude in natural ferropericlase inclusions (Walter et al., 2022) to the $Al_2O_3$ content. Such analyses are important as they provide one of the only mechanisms through which to determine temperatures in the sub-lithospheric mantle.

## 4.5 Conclusions

In this study, we have investigated the solubility of $Al_2O_3$ in periclase coexisting with a series of $Al_2O_3$-rich phases formed by high pressure and temperature phase transitions of $MgAl_2O_4$ spinel in the $MgO$-$Al_2O_3$ system. Experiments were performed at pressures up to 50 GPa and temperatures to 2623 K. The solubility of $Al_2O_3$ in periclase is temperature dependent with the sensitivity to $Al_2O_3$ content increasing with temperature but also decreasing with pressure. A thermodynamic model for periclase $Al_2O_3$ solubility uses the known phase transformation boundaries for $Al_2O_3$-rich phases in the system to determine their thermodynamic properties. This only works to conditions of the CF-structured $MgAl_2O_4$ phase at approximately 40 GPa as phase boundaries of higher-pressure polymorphs are not well constrained. The $Al_2O_3$ solubility in FeO-bearing ferropericlase appears to be almost identical to that of periclase, implying that FeO has little effect. Further thermodynamic calculations in a more representative mantle system ($MgO$-$SiO_2$-$Al_2O_3$) indicate that, throughout the mantle, the ferropericlase $Al_2O_3$ content cannot exceed 0.5 mol.% under current adiabatic mantle temperatures. Such a small content of $Al_2O_3$ will not influence the thermoelastic properties of ferropericlase, but could still influence transport properties as such concentrations have been reported to affect Mg self-diffusion.

Ferropericlase inclusions in diamonds have $Al_2O_3$ contents that vary up to approximately 0.35 mol. %. If such inclusions could be reliably considered to have formed contemporaneously with other $Al_2O_3$-rich inclusions such as garnets in the same diamond, then the concentration can be used to determine the temperature of formation. However, for most inclusions the $Al_2O_3$ activity at formation will be unknown and our model can only be used to determine the maximum $Al_2O_3$ solubility assuming coexistence with a $Al_2O_3$-rich phase of the mantle. Using this solubility relationship, conditions in the mantle can be excluded at which some ferropericlase inclusions could have formed because their $Al_2O_3$ contents would be too high. Thermodynamic calculations show that the solubility of $Al_2O_3$ in ferropericlase at mantle adiabatic conditions goes through two maxima, at the base of the upper mantle and top of the lower mantle. By comparison, the solubility at transition zones conditions goes through a minimum throughout the garnet stability field. As a result, a few ferropericlase inclusions can be excluded from formation in the transition zone as their $Al_2O_3$ contents are higher than even super adiabatic conditions would produce. These high-$Al_2O_3$ content inclusions must have been formed, however, at temperatures within 100 K of a typical mantle adiabat, either at the base of the upper mantle or at the very top of the lower mantle.

### Acknowledgments

We thank H. Fischer and S. Übelhack for their technical assistance in the machining of multianvil assemblies and maintenance of the presses, and thank R. Njul and A. Rother for their help with sample preparation. We appreciate thoughtful discussions with A. Withers. This research was supported by DFG grant FR1555/11.

### Data Availability

Data are available through Zenodo at https://doi.org/10.5281/zenodo.10828212.

## References

Akaogi, M., Hamada, Y., Suzuki, T., Kobayashi, M. and Okada, M., 1999. High pressure transitions in the system $MgAl_2O_4$–$CaAl_2O_4$: a new hexagonal aluminous phase with implication for the lower mantle. Physics of the Earth and Planetary Interiors, 115(1), pp.67-77.

Alper, A. M., McNally, R. N., Ribbe, P. H., Doman, R. C., 1962. The system MgO–$MgAl_2O_4$. J. Am. Ceram. Soc., 45, pp.263-268.

Ammann, M.W., Brodholt, J.P., Dobson, D.P., 2012. Diffusion of aluminium in MgO from first principles. Phys. Chem. Miner., 39, pp.503-514.

Angel, R.J., Alvaro, M., Nestola, F., 2022. Crystallographic methods for non-destructive characterization of mineral inclusions in diamonds. Rev. Mineral. Geochem., 88, pp.257-305.

Anzolini, C., Nestola, F., Mazzucchelli, M.L., Alvaro, M., Nimis, P., Gianese, A., Morganti, S., Marone, F., Campione, M., Hutchison, M.T., Harris, J.W., 2019. Depth of diamond formation obtained from single periclase inclusions. Geology, pp.219-222.

Brey, G. P., Bulatov, V., Girnis, A., Harris, J. W., Stachel, T., 2004. Ferropericlase—a lower mantle phase in the upper mantle. Lithos, 77, pp.655-663.

Bulatov, V. K., Girnis, A. V., Brey, G. P., Woodland, A. B., Höfer, H. E., 2019. Ferropericlase crystallization under upper mantle conditions. Contrib. to Mineral. Petrol., 174, pp.1-14.

Burnham, A. D., Bulanova, G. P., Smith, C. B., Whitehead, S. C., Kohn, S. C., Gobbo, L., Walter, M. J., 2016. Diamonds from the Machado River alluvial deposit, Rondônia, Brazil, derived from both lithospheric and sublithospheric mantle. Lithos, 265, pp.199-213.

Enomoto, A., Kojitani, H., Akaogi, M., Miura, H., Yusa, H., 2009. High-pressure transitions in $MgAl_2O_4$ and a new high-pressure phase of $Mg_2Al_2O_5$. J. Solid State Chem., 182, pp.389-395.

Frenkel, A. S., Shmukler, K. M., Sukharevskij, B. Y., Gul'ko, N. V., 1960. On the Mechanism of Dissolution and Precipitation of Spinel in a Periclase Solid Solution. Dokl. Akad. Nauk, 130, pp.1095-1098.

Frost, D.J., Langenhorst, F., 2002. The effect of $Al_2O_3$ on Fe-Mg partitioning between magnesiowüstite and magnesium silicate perovskite. Earth Planet. Sci. Lett., 199, pp.227-241.

Hallstedt, B., 1992. Thermodynamic assessment of the system $MgO–Al_2O_3$. J. Am. Ceram. Soc., 75, pp.1497-1507.

Gu, T., Pamato, M.G., Novella, D., Alvaro, M., Fournelle, J., Brenker, F.E., Wang, W., Nestola, F., 2022. Hydrous peridotitic fragments of Earth's mantle 660 km discontinuity sampled by a diamond. Nat. Geosci., 15, pp.950-954.

Harte, B., 1999. Lower mantle mineral associations in diamonds from Sao Luiz, Brazil, in: Fei Y, Bertka C. M., Mysen B. O. (eds), Mantle petrology: Field observations and high-pressure experimentation: A tribute to Francis R. (Joe), Geochem Soc Spec Publ, 6, pp.pp.125-153.

Hayman, P.C., Kopylova, M.G., Kaminsky, F.V., 2005. Lower mantle diamonds from Rio Soriso (Juina area, Mato Grosso, Brazil). Contrib. Mineral. Petrol., 149, pp.430-445.

Henriksen, A. F., Kingery, W. D., 1979. Effects of strain energy on precipitate morphology in MgO. Ceram. Int., 5, pp.56-60.

Hidayat, T., Shishin, D., Decterov, S. A., Jak, E., 2017. Experimental Study and Thermodynamic Re-optimization of the $FeO-Fe_2O_3-SiO_2$ System. J. Ph. Equilibria Diffus., 38, pp.477-492.

Holland, T. J. B., Powell, R., 2011. An improved and extended internally consistent thermodynamic dataset for phases of petrological interest, involving a new equation of state for solids. J. Metamorph. Geol., 29, pp.333-383.

Huang, R., Ballaran, T. B., McCammon, C. A., Miyajima, N., Dolejš, D., Frost, D. J., 2021. The composition and redox state of bridgmanite in the lower mantle as a function of oxygen fugacity. Geochim. Cosmochim. Acta, 303, pp.110-136.

Hutchison, M. T., The Constitution of the Deep Transition Zone and Lower Mantle Shown by Diamonds and Their Inclusions, Ph.D. Thesis, University of Edinburgh, 1997.

Hutchison, M.T., Nixon, P.H., Harley, S.L., 2004. Corundum inclusions in diamonds—discriminatory criteria and a corundum compositional dataset. Lithos, 77, pp.273-286.

Irifune, T., 1994. Absence of an aluminous phase in the upper part of the Earth's lower mantle. Nature, 370, pp.131-133.

Irifune, T., Fujino, K., Ohtani, E., 1991. A new high-pressure form of $MgAl_2O_4$. Nature, 349, pp.409-411.

Irifune, T., Naka, H., Sanehira, T., Inoue, T., Funakoshi, K., 2002. In situ X-ray observations of phase transitions in $MgAl_2O_4$ spinel to 40 GPa using multianvil apparatus with sintered diamond anvils. Phys. Chem. Miner., 29, pp.645-654.

Irifune, T., Shinmei, T., McCammon, C. A., Miyajima, N., Rubie, D. C., Frost, D. J., 2010. Iron partitioning and density changes of pyrolite in Earth’s lower mantle. Science, 327, pp.193-195.

Irifune, T., Tsuchiya, T., 2007. Mineralogy of the Earth-Phase transitions and mineralogy of the lower mantle. Treatise on Geophysics, 2, pp.33-62.

Ishii, T., Frost, D.J., Kim, E.J., Chanyshev, A., Nishida, K., Wang, B., Ban, R., Xu, J., Liu, J., Su, X., Higo, Y., 2023. Buoyancy of slabs and plumes enhanced by curved post-garnet phase boundary. Nat. Geosci. 16, 828–832.

Ishii, T., Criniti, G., Bykova, E., Dubrovinsky, L., Katsura, T., Arii, H., Kojitani, H., Akaogi, M., 2021. High-pressure syntheses and crystal structure analyses of a new low-density $CaFe_2O_4$-related and $CaTi_2O_4$-type $MgAl_2O_4$ phases. Am. Mineral., 106, pp.1105-1112.

Ishii, T., Liu, Z., Katsura, T., 2019. A breakthrough in pressure generation by a Kawai-type multi-anvil apparatus with tungsten carbide anvils. Engineering, 5, pp.434-440.

Ishii, T., Shi, L., Huang, R., Tsujino, N., Druzhbin, D., Myhill, R., Li, Y., Wang, L., Yamamoto, T., Miyajima, N., Kawazoe, T., 2016. Generation of pressures over 40 GPa using Kawai-type multi-anvil press with tungsten carbide anvils. Rev. Sci. Instrum., 8, 024501.

Ita, J., Cohen, R.E., 1998. Diffusion in MgO at high pressure: Implications for lower mantle rheology. Geophys. Res. Lett., 25, pp.1095-1098.

Jung, I. H., Decterov, S. A., Pelton, A. D., 2004. Critical thermodynamic evaluation and optimization of the $FeO$-$Fe_2O_3$-$MgO$-$SiO_2$ system. Metall. Mater. Trans. B., 35, pp.877-889.

Kaminsky, F., 2012. Mineralogy of the lower mantle: A review of 'super-deep'mineral inclusions in diamond. Earth-Sci. Rev., 110, pp.127-147.

Kaminsky, F., Zakharchenko, O., Davies, R., Griffin, W., Khachatryan-Blinova, G., Shiryaev, A., 2001. Superdeep diamonds from the Juina area, Mato Grosso state, Brazil. Contrib. Mineral. Petrol., 140, pp.734-753.

Kaminsky, F.V., Ryabchikov, I.D., McCammon, C.A., Longo, M., Abakumov, A.M., Turner, S., Heidari, H., 2015. Oxidation potential in the Earth's lower mantle as recorded by ferropericlase inclusions in diamond. Earth Planet. Sci. Lett., 417, pp.49-56.

Katsura, T., 2022. A revised adiabatic temperature profile for the mantle. J. Geophys. Res. Solid, 127, e2021JB023562.

Keppler, H., Frost, D. J., 2005. Introduction to minerals under extreme conditions. EMU Notes in Mineralogy, 7, pp.1-30

Kiseeva, E.S., Korolev, N., Koemets, I., Zedgenizov, D.A., Unitt, R., McCammon, C., Aslandukova, A., Khandarkhaeva, S., Fedotenko, T., Glazyrin, K., Bessas, D., 2022. Subduction-related oxidation of the sublithospheric mantle evidenced by ferropericlase and magnesiowüstite diamond inclusions. Nat. Commun., 13, 7517.

Kohn, M.J., Mazzucchelli, M.L., Alvaro, M., 2023. Elastic thermobarometry. Annu. Rev. Earth Planet. Sci., 51, pp.331-366.

Kojitani, H., Enomoto, A., Tsukamoto, S., Akaogi, M., Miura, H., Yusa, H., 2010. High-pressure high-temperature phase relations in $MgAl_2O_4$. J. Phys. Conf. Ser., 215, 012098.

Kojitani, H., Ishii, T., Akaogi, M., 2012. Thermodynamic investigation on phase equilibrium boundary between calcium ferrite-type $MgAl_2O_4$ and $MgO$+ $\alpha$-$Al_2O_3$. Phys.

Earth Planet. Inter., 212, pp.100-105.Liu, L. G., 1975. Disproportionation of $MgAl_2O_4$ spinel at high pressures and temperatures. Geophys. Res. Lett., 2, pp.9-11.

Liu, L. G., 1978. A new high-pressure phase of spinel. Earth Planet. Sci. Lett., 41, pp.398-404.

Liu, L.G., 2002. An alternative interpretation of lower mantle mineral associations in diamonds. Contrib. Mineral. Petrol., 144, pp.16-21.

Liu, Z., Nishi, M., Ishii, T., Fei, H., Miyajima, N., Ballaran, T.B., Ohfuji, H., Sakai, T., Wang, L., Shcheka, S., Arimoto, T., Tange, Y., Higo, Y., Irifune, T., Katsura, T.,2017. Phase relations in the system $MgSiO_3$-$Al_2O_3$ up to 2300 K at lower mantle pressures. J. Geophys. Res. Solid,, 122, 7775–7788.

Liu, Z., Akaogi, M., Katsura, T., 2019a. Increase of the oxygen vacancy component in bridgmanite with temperature. Earth Planet. Sci. Lett., 505, pp.141-151.

Liu, Z., Ballaran, T. B., Huang, R., Frost, D. J., Katsura, T. 2019b. Strong correlation of oxygen vacancies in bridgmanite with Mg/Si ratio. Earth Planet. Sci. Lett., 523, 115697.

Llovet, X., Francesc S., 2017. PENEPMA: A Monte Carlo program for the simulation of X-ray emission in electron probe microanalysis. Microsc Microanal, 23, pp.634-646.

Lorenzon, S., Wenz, M., Nimis, P., Jacobsen, S.D., Pasqualetto, L., Pamato, M.G., Novella, D., Zhang, D., Anzolini, C., Regier, M., Stachel, T., 2023. Dual origin of ferropericlase inclusions within super-deep diamonds. Earth Planet. Sci. Lett., 608, 118081.

Luth, R.W., Virgo, D., Boyd, F.R., Wood, B.J., 1990. Ferric iron in mantle-derived garnets: Implications for thermobarometry and for the oxidation state of the mantle. Contrib. to Mineral. Petrol., 104, pp.56-72.

McCammon, C., Hutchison, M., Harris, J., 1997. Ferric iron content of mineral inclusions in diamonds from Sao Luiz: A view into the lower mantle. Science, 278, pp.434-436.

McCammon, C.A., Stachel, T., Harris, J.W., 2004. Iron oxidation state in lower mantle mineral assemblages: II. Inclusions in diamonds from Kankan, Guinea. Earth Planet. Sci. Lett., 222, pp.423-434.

Mori, T., 1982. Solubility of $Al_2O_3$ in MgO. Yogyo-Kyokai-Shi, 90, pp.551-552.

Nestola, F., Pamato, M.G., Novella, D., Wang, Y., Qu, K., Smith, E.M., 2023a. Elastic geobarometry yielding a faithful sublithospheric depth for a ferropericlase inclusion in diamond. Lithos, 454–455, 107265.

Nestola, F., Regier, M.E., Luth, R.W., Pearson, D.G., Stachel, T., McCammon, C., Wenz, M.D., Jacobsen, S.D., Anzolini, C., Bindi, L., Harris, J.W., 2023b. Extreme redox variations in a superdeep diamond from a subducted slab. Nature, 613, pp.85-89.

Nestola, F., Prencipe, M. and Belmonte, D., 2023c. $Mg_3Al_2Si_3O_{12}$ jeffbenite inclusion in super-deep diamonds is thermodynamically stable at very shallow Earth’s depths. Sci. Rep., 13, 83.

Nimis, P., 2022. Pressure and temperature data for diamonds. Rev. Mineral. Geochem., 88, pp.533-565.

Nimis, P., Nestola, F., Schiazza, M., Reali, R., Agrosì, G., Mele, D., Tempesta, G., Howell, D., Hutchison, M.T., Spiess, R., 2019. Fe-rich ferropericlase and magnesiowüstite inclusions reflecting diamond formation rather than ambient mantle. Geology, 47, pp.27-30.

Nishihara, Y., Doi, S., Kakizawa, S., Higo, Y., Tange, Y., 2020. Effect of pressure on temperature measurements using WRe thermocouple and its geophysical impact. Phys. Earth Planet. Inter., 298, 106348.

O'Neill, H.S.C., Wall, V.J., 1987. The Olivine-Orthopyroxene-Spinel oxygen geobarometer, the nickel precipitation curve, and the oxygen fugacity of the Earth's Upper Mantle. J. Petrol., 28, pp.1169-1191.

Ono, S., Kikegawa, T., Ohishi, Y., 2006. The stability and compressibility of $MgAl_2O_4$ high-pressure polymorphs. Phys. Chem. Miner., 33, pp.200-206.

Ono, S., Ohishi, Y., Isshiki, M., Watanuki, T., 2005. In situ X-ray observations of phase assemblages in peridotite and basalt compositions at lower mantle conditions: Implications for density of subducted oceanic plate. J. Geophys. Res. Solid, 110, B02208.

Riet, A.A., Van Orman, J.A., Lacks, D.J., 2020. Molecular dynamics simulation of vacancy-solute binding free energy in periclase. Phys. Chem. Miner., 47, 38.

Seitz, H.M., Brey, G.P., Harris, J.W., Durali-Müller, S., Ludwig, T., Höfer, H.E., 2018. Ferropericlase inclusions in ultradeep diamonds from Sao Luiz (Brazil): high Li abundances and diverse Li-isotope and trace element compositions suggest an origin from a subduction mélange. Mineral Petrol, 112, pp.291-300.

Sempolinski, D.R., Kingery, W.D., 1980. Ionic conductivity and magnesium vacancy mobility in magnesium oxide. J. Am. Ceram. Soc., 63, pp.664-669.

Stachel, T., 2001. Diamonds from the asthenosphere and the transition zone. Eur. J. Mineral., 13, pp.883-892.

Stixrude, L., Lithgow-Bertelloni, C., 2022. Thermal expansivity, heat capacity and bulk modulus of the mantle. Geophys. J. Int. 228, 1119–1149.

Stubican, V. S., Roy, R., 1965. Mechanism of the precipitation of the spinel from MgO-$Al_2O_3$ solid solutions. J. Phys. Chem. Solids., 26, pp.1293-1297.

Thomson, A. R., Walter, M. J., Kohn, S. C., Brooker, R. A., 2016. Slab melting as a barrier to deep carbon subduction. Nature, 529, pp.76-79.

Van Orman, J.A., Fei, Y., Hauri, E.H., Wang, J., 2003. Diffusion in MgO at high pressures: Constraints on deformation mechanisms and chemical transport at the core-mantle boundary. Geophys. Res. Lett., 30, 1056.

Van Orman, J.A., Li, C., Crispin, K.L., 2009. Aluminum diffusion and Al-vacancy association in periclase. Phys. Earth Planet. Inter., 172, pp.34-42.

Walter, M. J., Thomson, A. R., Smith, E. M., 2022. Geochemistry of silicate and oxide inclusions in sublithospheric diamonds. Rev. Mineral. Geochem., 88, pp.393-450.

Walter, M.J., Kohn, S.C., Araujo, D., Bulanova, G.P., Smith, C.B., Gaillou, E., Wang, J., Steele, A., Shirey, S.B., 2011. Deep mantle cycling of oceanic crust: evidence from diamonds and their mineral inclusions. Science, 334, pp.54-57.

van Westrenen W., van Orman J. A., Watson H., Fei Y. and Watson E. B., 2003. Assessment of temperature gradients in multianvil assemblies using spinel layer growth kinetics. Geochem. Geophys. Geosyst. 4, 474.

Whitney II, W. P., Stubican, V. S., 1971. Interdiffusion studies in the system MgO-$Al_2O_3$. J. Phys. Chem. Solids, 32, pp.305-312.

Wirth, R., Dobrzhinetskaya, L., Harte, B., Schreiber, A., Green, H.W., 2014. High-Fe (Mg,Fe)O inclusion in diamond apparently from the lowermost mantle. Earth Planet. Sci. Lett., 404, pp.365-375.

Zienert, T., Fabrichnaya, O., 2013. Thermodynamic assessment and experiments in the system MgO–$Al_2O_3$. Calphad, 40, pp.1-9.

# Appendix A. Supplementary Material for

## Alumina solubility in periclase determined to lower mantle conditions and implications for ferropericlase inclusions in diamonds

This document contains additional figures and tables referred to in the paper. Figure 4.S1 shows modelling of EPMA secondary fluorescence. Figure 4.S2 shows X-ray diffraction patterns of CF and CT phases. Figure 4.S3 is a comparison between the thermodynamic model and the experimental data between 25 and 55 GPa at different temperatures. Figure 4.S4 is an image of an experimental sample containing ferropericlase and periclase sample. Figure 4.S5 shows the adiabatic temperature profile used in this study. Tables report the chemical composition of the $Al_2O_3$-rich phases coexisting with periclase (Table 4.S1), and the parameters used for thermodynamic modelling in this study (Tables 4.S2 to 4.S3).

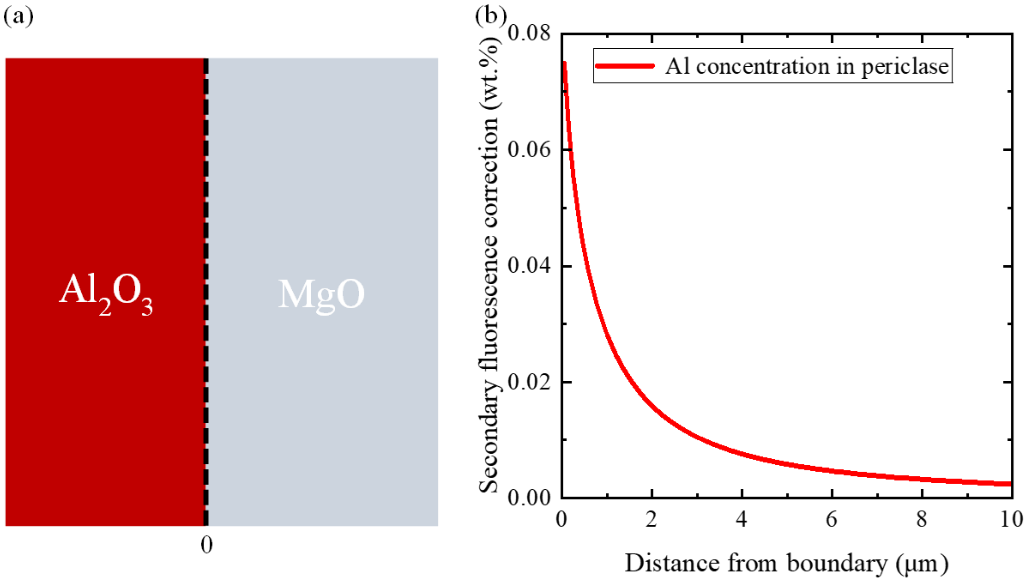

**Figure 4.S1.** Assessment of the secondary fluorescence effect on the EPMA-analyses of the Al concentration in periclase. (a) Schematic diagram of the geometry of the simulation of adjacent $Al_2O_3$ corundum and MgO periclase grains. (b) The contribution from secondary fluorescence of the adjacent $Al_2O_3$ grain on the measured $Al_2O_3$ concentration in periclase as a function of distance from the grain boundary. The simulations were performed using the computer program PENEPMA (Llovet and Salvat, 2017).

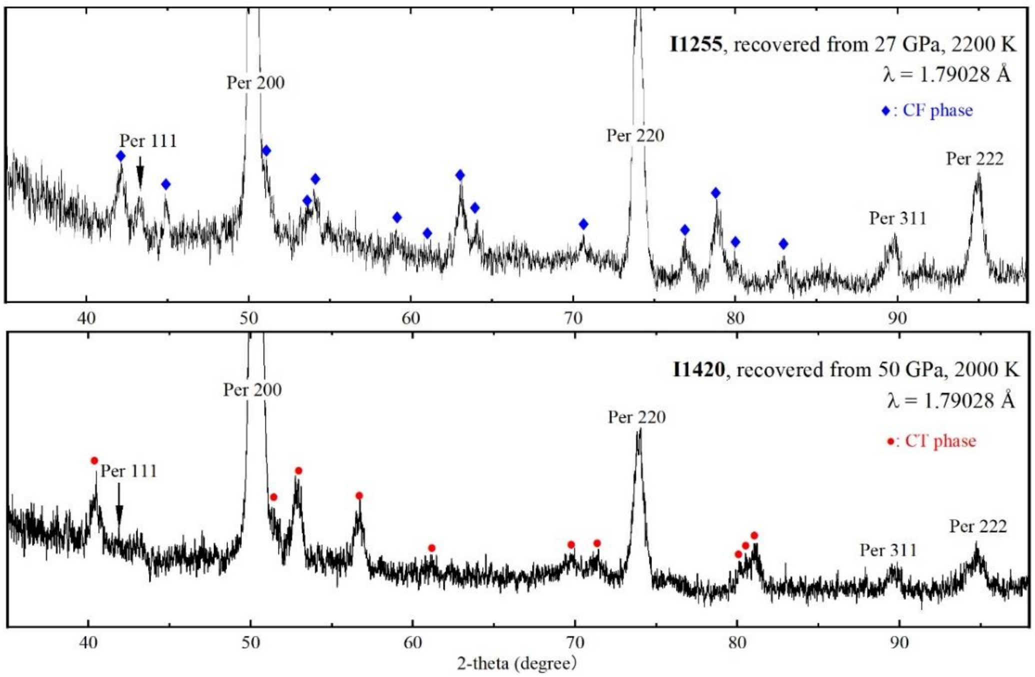

**Figure 4.S2.** Power XRD patterns of the recovered samples. (a) The coexistence of the CF phase and periclase in a sample recovered from conditions of 27 GPa and 2200 K. (b) The coexistence of the CT phase and periclase in a sample recovered from conditions of 50 GPa and 2000 K.

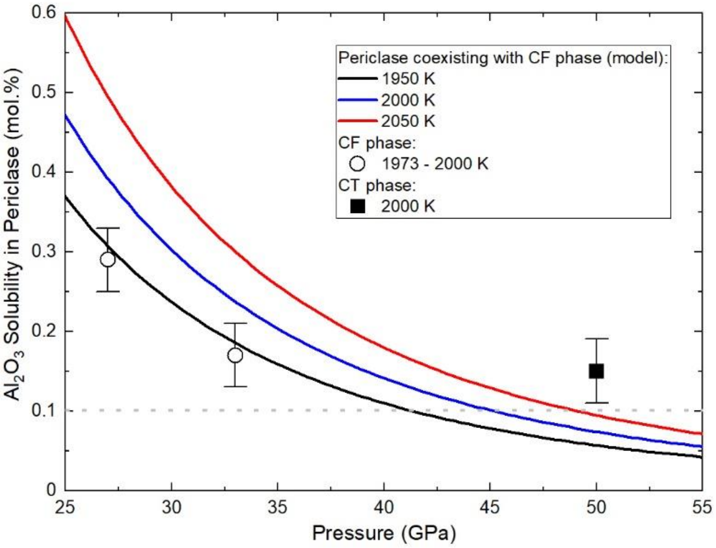

**Figure 4.S3.** The effect of pressure on the solubility of $Al_2O_3$ in periclase. The black, blue, and red curves show the solubility of $Al_2O_3$ in periclase coexisting with the CF phase calculated from the thermodynamic model established in this study at 1950 K, 2000 K, and 2050 K, respectively. The circle and square symbols are the experimental data on periclase coexisting with the CF and CT phases, respectively at approximately 2000 K.

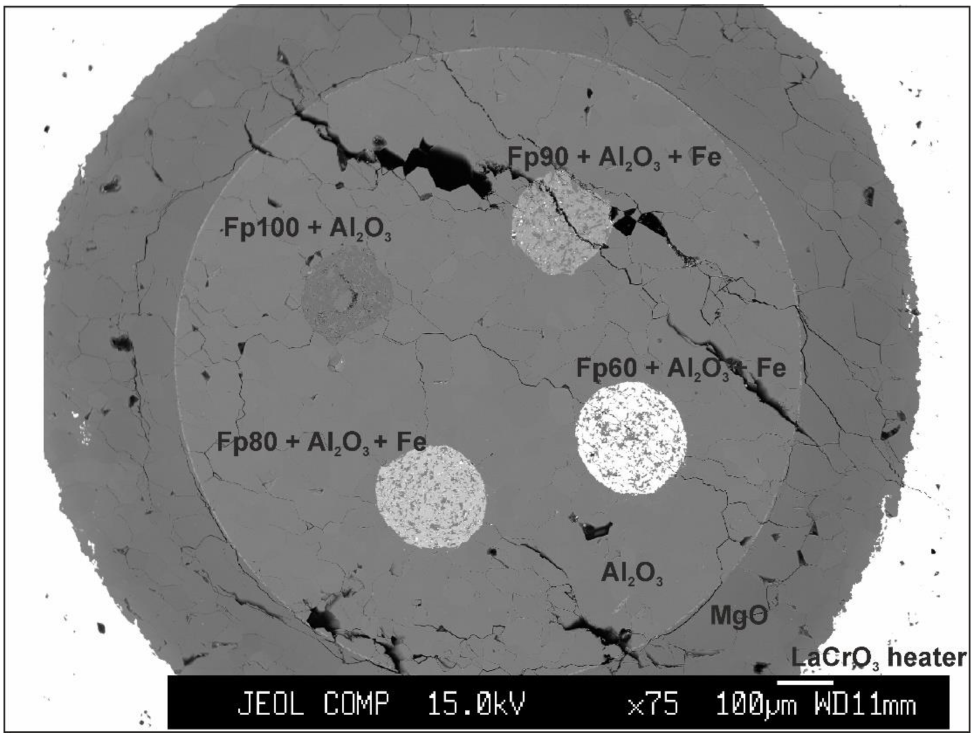

**Figure 4.S4.** A backscattered electron image of the recovered capsule and surrounding assembly from run H5875, sectioned perpendicular to the furnace direction. Samples with four different starting compositions were filled in each of the isolated holes of the capsule, which was a four-hole corundum thermocouple tube.

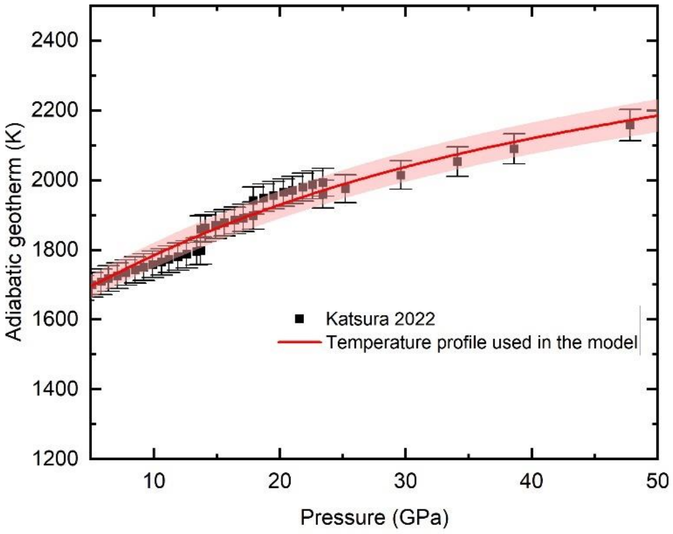

**Figure 4.S5.** A mantle adiabatic temperature profile, based on that of Katsura (2022), that is used in the model depicted in Fig. 4.4. The effect of latent heat due to phase transitions on the mantle adiabat is not accounted for to simplify the parameterization. The red solid curve was generated by refitting the adiabatic geotherm from Katsura (2022) using a 4th order polynomial. The shaded region shows the uncertainty of the geotherm, which is considered in the model presented in Fig. 4.6a.

**Table 4.S1.** Chemical Compositions of the Phases Coexisting with Periclase

| Run No. | P (GPa) | T (K) | Phase | EPMA Measurements (wt.%) b | | | | Normalized compositions (mol.%) | | | |
|---|---|---|---|---|---|---|---|---|---|---|---|
| | | | | MgO | FeO | $Al_2O_3$ | Total | N | MgO | FeO | $Al_2O_3$ |
| H5431b | 15 | 1773 (50) | Sp | 28.5 (2) | 0.0 (0) | 70.9 (6) | 99.4 (4) | 9 | 50.4 (4) | 0.0 (0) | 49.6 (3) |
| H5424b | 15 | 2073 (50) | Sp | 28.5 (1) | 0.2 (1) | 71.0 (3) | 99.6 (3) | 4 | 50.2 (1) | 0.2 (1) | 49.6 (2) |
| H5482b | 19 | 1773 (50) | Cor | 0.7 (3) | 0.0 (1) | 99.2 (1) | 100.0 (2) | 4 | 1.8 (8) | 0.1 (1) | 98.1 (7) |
| H5490b | 19 | 1773 (50) | Cor | 0.4 (1) | 0.0 (0) | 99.8 (3) | 100.2 (4) | 5 | 1.1 (2) | 0.0 (0) | 98.9 (2) |
| H5492b | 19 | 2073 (50) | Cor | 0.6 (2) | 0.0 (0) | 99.2 (3) | 99.8 (2) | 6 | 1.6 (4) | 0.0 (0) | 98.4 (4) |
| H5495 | 19 | 2273 (50) | Cor | 0.9 (2) | 0.0 (0) | 100.0 (2) | 100.9 (1) | 6 | 2.2 (5) | 0.0 (0) | 97.8 (5) |
| H5310b | 23 | 1923 (50) | Cor | 0.3 | 0.0 | 99.0 | 99.3 | 1 | 0.9 | 0.0 | 99.1 |
| H5306 | 23 | 2073 (50) | Cor | 0.5 (2) | 0.0 (0) | 99.4 (4) | 99.9 (3) | 8 | 1.2 (4) | 0.0 (0) | 98.8 (4) |
| H5299 | 23 | 2273 (50) | Cor | 0.5 (2) | 0.0 (0) | 96.9 (5) | 97.4 (7) | 3 | 1.4 (5) | 0.0 (0) | 98.6 (5) |
| I1421c | 27 | 1973 (50) | Cor | 1.0 (2) | 0.0 (0) | 98.0 (0) | 99.0 (3) | 2 | 2.4 (5) | 0.0 (0) | 97.6 (5) |
| H5420b | 23 | 2373 (50) | Ldw | 43.9 (4) | 0.3 (2) | 55.5 (4) | 98.8 (8) | 4 | 66.5 (2) | 0.3 (2) | 33.2 (1) |
| H5435b | 23 | 2400 (50) | Ldw | 43.8 (3) | 0.0 (0) | 55.4 (5) | 99.3 (5) | 8 | 66.6 (3) | 0.0 (0) | 33.3 (3) |
| H5317b | 23 | 2623 (50) | Ldw | 44.6 (2) | 0.2 (1) | 56.9 (4) | 101.7 (4) | 5 | 66.4 (2) | 0.1 (1) | 33.5 (2) |
| H5359b | 23 | 2623 (50) | Ldw | 44.4 (1) | 0.0 (0) | 56.0 (3) | 100.4 (3) | 4 | 66.7(1) | 0.0 (0) | 33.3 (1) |
| H5345b | 23 | 2623 (50) | Ldw | 44.6 (2) | 0.0 (0) | 56.0 (3) | 100.6 (3) | 5 | 66.9 (1) | 0.0 (0) | 33.1 (1) |
| I1401b | 27 | 1973 (50) | CF | 28.8 | 0.0 | 70.9 | 99.7 | 1 | 50.7 | 0.0 | 49.3 |
| I1412c | 27 | 2123 (50) | CF | 29.0 (7) | 0.0 (0) | 70.6 (9) | 99.6 (4) | 6 | 51.0 (9) | 0.0 (0) | 49.0 (9) |
| I1255 | 27 | 2200 (50) | CF | 28.8 (1) | n.d. | 70.9 (3) | 99.7 (4) | 9 | 50.7 (1) | 0.0 (0) | 49.3 (1) |
| I1193 | 33 | 2000 (50) | CF | 28.7 (3) | 0.0 (0) | 72.1 (4) | 100.8 (3) | 9 | 50.2 (3) | 0.0 (0) | 49.8 (3) |
| I1415 | 33 | 2300 (50) | CF | 29.1 (13) | 0.0 (0) | 70.2 (12) | 99.4 (12) | 10 | 51.1 (14) | 0.0 (0) | 48.8 (14) |
| I1420 | 50 | 2000 (50) | CT | 29.7 (4) | 0.0 (0) | 69.4 (4) | 99.2 (4) | 6 | 52.0 (4) | 0.0 (0) | 48.0 (4) |

**Table 4.S2.** Standard state thermodynamic parameters

| | **ΔfH kJ/mol** | **S $JK^{-1}mol^{-1}$** | **a** | **b ($x10^5$)** | **c** | **d** | **$V_0$ J/bar** | **$\alpha_0$ ($x10^5$) $K^{-1}$** | **$K_{T0}$ GPa** | **K′** |
|---|---|---|---|---|---|---|---|---|---|---|
| Periclase ($MgO$) | -601.55 | 26.5 | 0.0605 | 0.0362 | -535.8 | -0.2992 | 1.125 | 3.11 | 160 | 3.95 |
| Periclase ($Al_2O_3$) | | | | | | | *2.890* | *3.5* | *163.5* | *4* |
| Corundum | -1675.33 | 50.9 | 0.1395 | 0.589 | -2460.6 | -0.5892 | 2.558 | 1.8 | 254 | 4.34 |
| Spinel | -2301.26 | 82.0 | 0.2229 | 0.6127 | -1686.0 | -1.551 | 3.978 | 1.93 | 192.2 | 4.04 |
| $Mg_2Al_2O_5$ | *-2831.98* | *116.52* | *0.2347* | *1.1587* | *-4843.9* | *-0.506* | *4.803* | *2.0* | *200* | *4* |
| CF-$MgAl_2O_4$ | -2245.65 | 86.5 | 0.1510 | 1.918 | -652.58 | 0.3539 | 3.614 | 2.41 | 205 | 4.1 |
| Bridgmanite $Al_2O_3$ | -1637.767 | 51.8 | 0.1395 | 0.589 | -2460.6 | -0.5892 | 2.54 | 1.8 | 203 | 4 |

Note. $Cp = a + bT + cT^{-2} + dT^{-0.5}$ ($kJK^{-1}mol^{-1}$). Data for CF-$MgAl_2O_4$ from Kojitani et al., (2012). V0 of $Mg_2Al_2O_5$ is from Kojitani et al. (2010). Values in italic were refined in this study as described in the text. All other values are from Holland and Powell (2011).

**Table 4.S3.** Fitting Terms for the Standard State Gibbs Free Energy of the Periclase $Al_2O_3$ End Member and Margules Parameters for Periclase and $Al_2O_3$ Bridgmanite

| | **A**<br>kJ/mol | **B**<br>J $K^{-1}$ $mol^{-1}$ | **$W_H$**<br>kJ/mol | **$W_S$**<br>J $K^{-1}$ $mol^{-1}$ | **$W_V$**<br>J $GPa^{-1}$ $mol^{-1}$ |
|---|---|---|---|---|---|
| Periclase ($Al_2O_3$) | -34.27 | -14 | 156.381 | 41.917 | -362 |
| Bridgmanite ($Al_2O_3$) | | | 12 | | |

# 5 The Influence of Sulfur on the Elastic Properties of the Martian Core

**Lianjie Man**[1, *], Adrien Néri[1,2], Julien Chantel[2], Tiziana Boffa Ballaran[1], Robert Farla[3], Liang Yuan[1], Nicolas Guignot[4], Laura Henry[4], Jonathan Dolinschi[1], Fei Wang[1], Rémy Pierru[1], Hu Tang[1], Andrew King[4], Tony Yu[5], Man Xu[5], Yanbin Wang[5], Daniel J. Frost[1]

[1]Bayerisches Geoinstitut, Universität Bayreuth, Bayreuth, Germany.
[2] Univ. Lille, CNRS, INRAE, Centrale Lille, UMR 8207 - UMET - Unité Matériaux et Transformations, F-59000 Lille, France.
[3]Deutsches Elektronen-Synchrotron DESY, Notkestr. 85, 22607 Hamburg, Germany.
[4]Synchrotron SOLEIL, L'Orme de Merisiers, Saint Aubin-BP48, 91192 Gif-sur-Yvette, France
[5]Center for Advanced Radiation Sources, The University of Chicago, Chicago, IL, 60637 USA
***Corresponding author.**

Email address: lianjie.man@uni-bayreuth.de (L. Man).

This chapter has been submitted to ***Earth and Planetary Science Letters***

**Author contributions**

**Lianjie Man**: Conceptualization, Data curation, Formal analysis, Investigation, Methodology, Validation, Visualization, and Writing – original draft. **Adrien Néri**: Conceptualization, Investigation, Methodology, Validation, and Writing – review and editing. **Julien Chantel**: Investigation, Methodology, Validation, and Writing – review and editing. **Tiziana Boffa Ballaran**: Data curation, Formal analysis, Investigation, Methodology, Validation, and Writing – review and editing. **Robert Farla**: Investigation, Methodology, Validation, and Writing – review and editing. **Liang Yuan**: Investigation, and Methodology, Validation. **Nicolas Guignot:** Investigation, Methodology, and Writing – review and editing. **Laura Henry**: Investigation, Methodology, and Writing – review and editing. **Jonathan Dolinschi**: Investigation, Methodology. **Fei Wang**:

Investigation. **Rémy Pierru**: Investigation, Methodology. **Hu Tang**: Investigation. **Andrew King:** Methodology and Software. **Tony Yu**: Investigation, Methodology, and Writing – review and editing. **Man Xu**: Investigation, Methodology, and Writing – review and editing. **Yanbin Wang**: Investigation, Methodology, and Writing – review and editing. **Daniel J. Frost**: Conceptualization, Formal analysis, Investigation, Methodology, Validation, and Writing – review and editing.

### Abstract

Understanding the influence of light elements on the elastic properties of liquid iron under high pressure and temperature conditions is crucial for characterizing the composition of planetary cores. In this study, a series of P-wave velocity and density measurements on Fe and Fe-S liquids were conducted at pressures up to 17.8 GPa and temperatures up to 2273 K, using ultrasonic interferometry, the Beer-Lambert method, and a combination of angular and energy-dispersive X-ray diffraction techniques. The melting curve of Fe and the density of solid FeS were also experimentally constrained to facilitate thermodynamic modeling. By integrating these results with literature data on thermodynamic properties at ambient pressure and the melting curves of Fe and FeS, a self-consistent thermodynamic model for the Fe-FeS system was developed under conditions relevant to the Martian core. Our results indicate that sulfur lowers both the density and P-wave velocity of liquid Fe under Martian core conditions. To account for the observed density deficit in the Martian core, at least 20 wt.% sulfur would be required. However, such high sulfur concentrations would lower the P-wave velocity of liquid Fe, most significantly at the top of the Martian core, which conflicts with seismic observations from the InSight mission. This indicates that significant proportions of other light elements, such as carbon or hydrogen, are most likely required alongside sulfur to explain the large density deficit while maintaining the apparent high P-wave velocity in the Martian core.

**Keywords:** Fe-S liquid alloys; Elastic property; Thermodynamic modeling; Martian core

## 5.1 Introduction

Sulfur is generally considered to be a dominant light alloying element in the Martian core, with cosmochemical models estimating its content to be between 6.6 and 21.4 wt.% (Wänke and Dreibus, 1994; Lodders and Fegley, 1997; Sanloup et al., 1999; Taylor, 2013; Yoshizaki and McDonough, 2020). The enrichment of S in the Martian core is primarily supported by the observation of sulfur depletion in the Martian mantle, the fact that Mars appears more enriched in moderately volatile elements compared to Earth (e.g., Wänke, 1991), and sulfur's highly siderophile behavior at the moderate high pressure and temperature conditions likely to have prevailed during core-mantle differentiation of Mars (e.g., Rose-Weston et al., 2009; Suer et al., 2017; Steenstra and van Westrenen, 2018). Martian core-mantle fractionation most likely did not occur at sufficiently reducing conditions or at sufficiently high temperatures for either silicon or oxygen to have become major light alloying elements in the core (Yoshizaki et al., 2020; Rubie et al., 2004). Recent geophysical observations, particularly seismic data from the InSight mission, have revealed the size of the Martian core (Stähler et al., 2021) and provided direct constraints on the P-wave velocity at the top part of the liquid core (Irving et al., 2023). Geophysical models based on seismic observations indicate that the density of the Martian core is significantly lower than that of pure liquid Fe under the same pressure and temperature conditions (Stähler et al., 2021; Irving et al., 2023; Samuel et al., 2023; Khan et al., 2023). Depending on whether a basal magma layer (BML) is considered, the most recent geophysical models imply that the Martian core may contain 9–22 wt.% light elements (Irving et al., 2023; Samuel et al., 2023; Khan et al., 2023). However, the constrained P-wave velocity at the top of the Martian core remains comparable to that of pure liquid Fe (Irving et al., 2023; Samuel et al., 2023; Khan et al., 2023). If the effects of light elements, including sulfur, on the density and P-wave velocity of liquid iron under high pressures and temperatures (HP-HT) are systematically constrained by experimental and theoretical studies, seismic observations of the Martian core can provide strong evidence for the core's composition and for the nature of early differentiation processes.

Experimental measurements of the elastic properties of liquids under HP-HT conditions remain highly challenging and are generally associated with significant uncertainties and notable discrepancies between studies reported in the literature. For instance, under only modest pressures (<7 GPa), discrepancies in the reported densities of FeS liquids are as large as ~1 g/cm³, i.e. >20%, (Nishida et al., 2008; Nishida et al., 2011; Chen et al., 2014; Morard et al., 2018a; Xu et al., 2021). Furthermore, at 10 GPa, the maximum excess volumes of mixing between Fe and FeS liquids have been modeled as -0.94 cm³/mol (Morard et al., 2018a), -0.86 cm³/mol (Terasaki et al., 2019), and -0.49 cm³/mol in (Xu et al., 2021), with each study showing different trends as pressure increases. As a result, elastic models of Fe-S liquids, based on the sparse and inconsistent data, show even greater discrepancies when extrapolated to higher pressures and temperatures, complicating the interpretation of seismic observations.

On the other hand, theoretical calculations also encounter challenges when modeling liquid Fe alloys under the P-T conditions of the Martian core. This is primarily because ab initio calculations tend to largely overestimate the density of Fe-rich alloys at lower pressures, despite showing good agreement with experimental observations at the HP-HT conditions relevant to Earth's core (e.g., Dewaele et al., 2008; Wagle and Steinle-Neumann, 2019). For instance, a recent ab initio study on pure liquid Fe at pressures of 19 GPa and 35 GPa required a pressure correction of 16.6 GPa to match experimental data (Huang et al., 2023). Consequently, different calculation methods and correction schemes can lead to significant variations in the computed elastic properties (Kuskov and Belashchenko, 2016; Morard et al., 2018a; Wagle and Steinle-Neumann, 2019; Huang et al., 2023; Li et al., 2024). Moreover, the large discrepancies in experimental data for Fe-S alloys further complicate the application of reliable correction schemes, especially beyond pure liquid Fe.

Due to the large uncertainties inherent in liquid property measurements, even at ambient pressures, rigorous constraints can only be obtained by combining different types of measurements into a model capable of self-consistently describing the various thermodynamic, equations of state and phase equilibria observations (e.g. Dorogokupets et al., 2017). The model then needs to be evaluated against the widest possible dataset. In this study, we have used ultrasonic interferometry and several *in situ* X-ray methods, independently and simultaneously, to determine the elastic properties of pure Fe and Fe-S liquids under HP-HT, including density and P-wave velocity ($V_P$). By combining experimental constraints on solid phase density and melting curves, along with end-member thermodynamic data at ambient pressure and melting curves from the literature, we have developed a new self-consistent thermodynamic model for the Fe-FeS system applicable to the conditions of the Martian core.

## 5.2Experiments

### 5.2.1 *Starting materials*

The starting materials for the high-pressure *in-situ* synchrotron X-ray experiments consisted of regular cylinders of Fe or Fe-FeS mixtures with parallel polished bases. Samples for the ultrasonic experiments had diameters of 1.0 mm and were 0.6 mm high, while samples for X-ray absorption experiments had diameters of 0.6 mm and were 0.4 mm high. The pure Fe cylinders were made from Fe wires with 1 mm diameter and 99.99% purity. The Fe-FeS blocks were synthesized at 0.5–0.7 GPa and 1000 K using a piston-cylinder press and subsequently machined into the desired cylindrical shape. Details of the starting material for synthesis using the piston-cylinder press are provided in Supplementary Text 5.S1.

The resulting cylinders were homogeneous mixtures of Fe and FeS, confirmed by scanning electron microscope (SEM) analysis. SEM images of the recovered samples are shown in Fig. 5.S1. The pre-synthesis and machining steps are critical to ensure the quality of the subsequent in-situ synchrotron X-ray experiments, as they minimize porosity in the sample and reduce irregular deformation during compression steps.

### 5.2.2 *HP-HT multi-anvil experiments at synchrotron beamlines*

*In situ* multi-anvil experiments using synchrotron-based X-ray techniques were performed at beamline P61B at PETRA III (Farla et al., 2022), beamline PSICHE at SOLEIL (Henry et al., 2022), and beamline 13IDD at the APS (Wang et al., 2009). High pressures were achieved by compressing the sample assemblies using eight tungsten carbide (WC) cubes (F05, Fujilloy) with 26 mm edge lengths, truncated to 4 mm or 5 mm at the corners (truncated edge length, TEL). A $Cr_2O_3$-MgO octahedron with a 10 mm edge length (OEL) was used as the pressure medium with pyrophyllite gaskets, while boron-epoxy X-ray windows within gaskets were employed in experiments involving combined angle- and energy-dispersive structural analysis and refinement (CAESAR) and Beer-Lambert absorption measurements (see Sections 2.3 and 2.4). After reaching the target press load, high temperatures were generated using a tubular boron-doped diamond furnace (CVD-BDD) synthesized via chemical vapor deposition methods (Changsha 3-Better Ultra-Hard Materials Co., Ltd). The BDD furnace provides stable heating performance, while preserving the X-ray transparency of the assembly (Shatskiy et al., 2009; Xie et al., 2020) and helps minimize irregular deformation of the sample under HP-HT. The designs of the high-pressure assemblies are shown in Fig. 5.S2 and 5.S3. Energy-dispersive X-ray diffraction (ED-XRD) measurements of the samples and pressure markers under HP-HT conditions were collected using a Ge detector fixed at 2θ angles of either 6 or 8 degrees. Temperatures were monitored with a type-D thermocouple, while pressures were determined using the equation of state (EOS) of the pressure standards. Considering the temperature gradient within the sample, temperature fluctuations during the experiment, the fitting error of the pressure marker's unit cell volume, and the accuracy of the pressure marker, the experimental uncertainties in temperature and pressure are estimated to be 50 K and 0.5 GPa, respectively.

### *5.2.3 P-wave velocity measurements using ultrasonic interferometry*

A 36°-Y cut $LiNbO_3$ transducer was attached to the backside of the WC anvils to generate longitudinal waves that travelled parallel to the cylindrical axis of the samples. The transducers were fabricated into 2.5 mm or 3 mm diameter disks from 3-inch diameter and 60 µm thick $LiNbO_3$ wafers (Yamaju Ceramics) using a picosecond pulsed laser cutter. The transducer was electrically connected to an arbitrary waveform generator and digital oscilloscope through coaxial cables.

During the measurements, pulses with frequencies from 45 to 75 MHz were sent from the arbitrary waveform generator and transmitted to the sample through the WC anvil and buffer rod (BR). The reflections of the acoustic waves at each interface—including the BR-sample interface and the sample-backing plate (BP) interface—were recorded by the digital oscilloscope. The travel time through the sample was analyzed using the Pulse-echo overlap method (Papadakis et al., 1972) with the Echofinder software (Néri et al., 2024). The length of the samples under HP-HT conditions was measured using X-ray imaging, utilizing the absorption contrast between the Fe-rich samples and the BP and BR, which were made from $Al_2O_3$. An example of a liquid longitudinal wave velocity measurement is illustrated in Fig 5.1. The ultrasonic interferometry system installed at P61B is described in detail by Néri et al. (2024). For the ultrasonic experiments at the PSICHE beamline, we brought a similar system from the Bayerisches

Geoinstitut (BGI), which is also detailed in Néri et al. (2024). Further information about the ultrasonic interferometry system at 13IDD can be found in Jing et al. (2020).

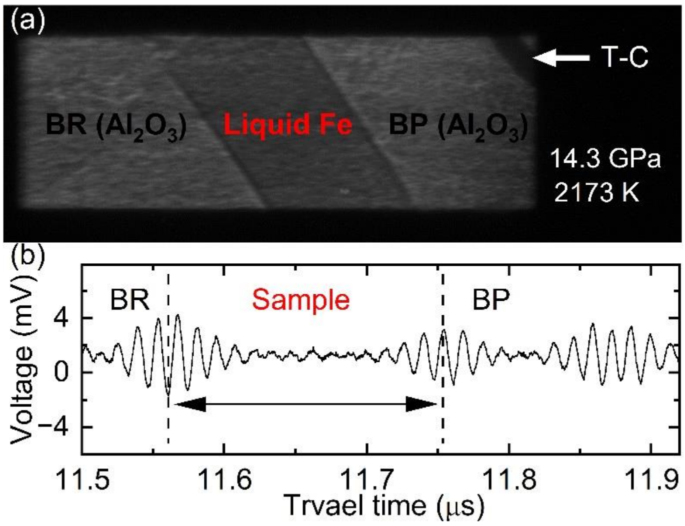

**Figure 5.1.** P-wave velocity measurements of liquid Fe at 14.3 GPa and 2173 K (BT657). (a) X-ray image of the sample. "BR" refers to the buffer rod, "BP" to the backing plate, and "T-C" to the thermocouple. The Fe sample is 0.46 mm thick. (b) Ultrasonic interferometry signal of the liquid sample at 75 MHz. The two-way travel time of the acoustic wave through the sample is indicated by the black arrow.

The samples were enclosed by a tube made from either single crystal MgO or polycrystalline $Al_2O_3$ (OD/ID = 1.6 mm/ 1.0 mm), and sealed at the top and bottom with a BP and a BR, both made from dense polycrystalline $Al_2O_3$, as shown in Fig 5.S2. The melting of the samples was monitored using multiple indicators, including the appearance of a diffuse scattering signal, the disappearance of sharp XRD peaks from the solid phases, and, most importantly, the disappearance of solid phases in the X-ray images (see Fig. 5.2). Additionally, significant changes in the acoustic signal through the sample provided further evidence of melting (Chantel et al., 2018; Xu et al., 2018). We have measured the $V_P$ of liquid Fe, liquid Fe with 6 wt.% S, and liquid Fe with 15 wt.% S at pressures up to 17.8 GPa and temperatures to 2273 K.

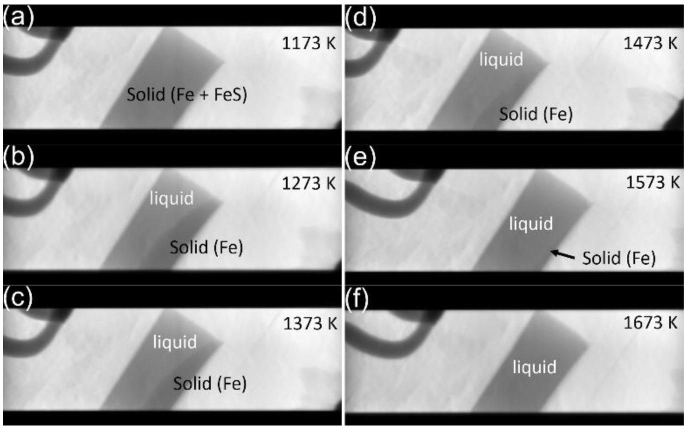

**Figure 5.2.** Representative X-ray radiographic images of Fe-S samples (MA229) during melting at approximately 8 GPa. The starting material was a mixture of metallic Fe and troilite (FeS), with a composition corresponding to Fe-15 wt.% S. The sample was in a subsolidus state at 1173 K, and exhibited coexisting solid Fe and liquid Fe-S between 1273 K and 1573 K. At 1673 K, the sample was fully molten, consisting of a single liquid phase.

### *5.2.4 Density measurements using the Beer-Lambert method*

We used the Beer-Lambert absorption method to evaluate the density of liquid Fe-15 wt.% S at high pressure and high temperature in a multi-anvil press at the PSICHE beamline. An $Al_2O_3$ disk, 1.2 mm in diameter and 0.25 mm thick, was used as the lid of the capsule and served as a density standard (Fig. 5.S3). Following the methodology described by Henry et al. (2022), a polychromator (rutile in this case) was placed in the beam path after the sample, and a series of absorption profiles spanning energies from 20 keV to 80 keV were collected simultaneously by scanning the sample perpendicularly across the beam with a 25 µm (horizontal) ×15 µm (vertical) spot size. The density of the molten sample was determined from its X-ray absorption profiles using the Beer-Lambert Law:

$$I(x) = I_0 \exp[-\mu_s \rho_s l_s(x) - \mu_{en} \rho_{en} l_{en}(x)] \tag{5.1}$$

where $x$ is the position along the absorption profile, $I_0$ and $I$ are the incident and transmitted beam intensities, respectively, $\mu$ is the mass absorption coefficient, $\rho$ is the density, and $l$ is the length of the beam path. The subscripts $s$ and $en$ indicate the sample and the surrounding assembly environment, respectively. Since the sample is cylindrical, the length of the beam path across the sample can be expressed as:

$$l_s(x) = 2\sqrt{r^2 - (x - x_0)^2} \tag{5.2}$$

where $r$ is the radius of the sample, and $x_0$ is the center of an absorption profile.

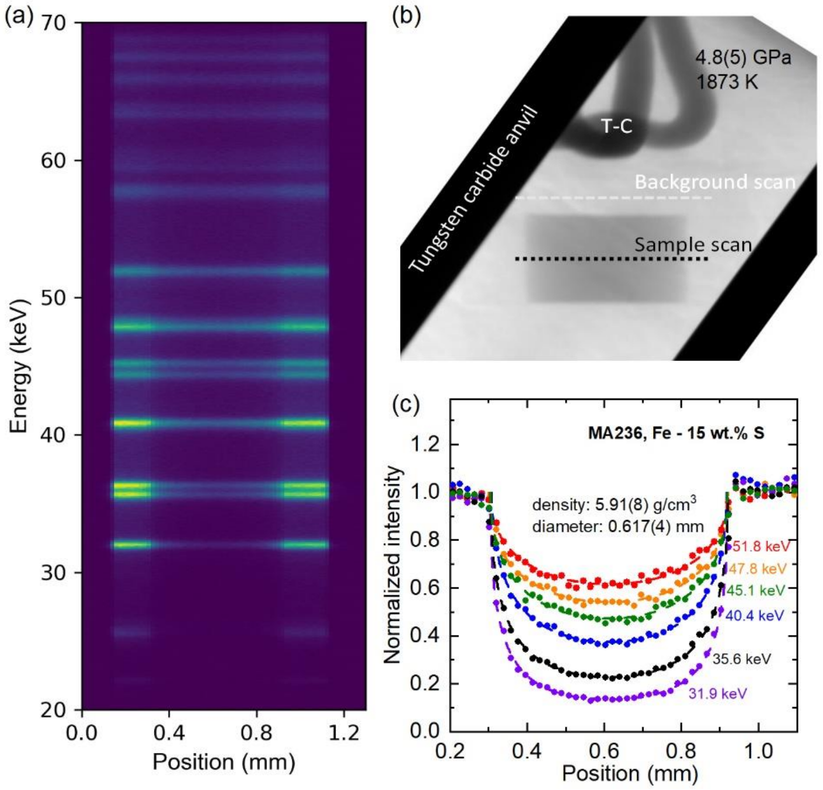

**Figure 5.3.** Density measurements of Fe-S liquids under high pressure obtained using the Beer-Lambert method. (a) X-ray absorption profile of the liquid sample at various energies. The pixel brightness indicates the transmitted beam intensity. (b) X-ray image of the liquid sample at 4.8 GPa and 1873 K. "T-C" indicates the thermocouple. The diameter of the sample is 0.617 mm. (c) Fitting of the X-ray absorption profiles of the liquid sample with X-ray energies ranging from 31.9 keV to 51.8 keV. The solid circles indicate the projected absorption profiles shown in (a), and the dashed curves are the fitted profiles at the corresponding energies, labeled beside each curve.

The absorption profiles of the $Al_2O_3$ lid were collected to subtract the assembly environment's contribution from the sample's absorption profile. The parameters $\mu_s$, $\rho_s$ and $r$ were obtained by fitting the absorption profile at a given energy. The mass absorption coefficient $\mu_s$ of the sample was assumed to be the same in both the solid and liquid states at the same X-ray energy. The $\mu_s$ values at different energies were determined by fitting the pre-melting absorption profiles of the sample, with the density calculated from the unit cell volumes obtained by XRD and the bulk composition of the sample. Absorption profiles centered at 31.9, 35.6, 36.3, 40.4, 44.3, 45.1, 47.8, and 51.8

keV, which have sufficient signal-to-noise ratio, were selected for density determination (Fig. 5.3).

### 5.2.5 CAESAR measurements on liquids

For the ultrasonic interferometry and X-ray absorption measurements of Fe-S liquids conducted at PSICHE, XRD data on the molten sample were simultaneously collected using the CAESAR technique (Wang et al., 2004; King et al., 2022), allowing both $V_P$ and density measurements on liquids. A series of ED-XRD spectra were collected at a 2θ ranging from 2.5° to 22.1° with a step size of 0.2°, obtained by moving the position of the Ge detector. The CAESAR method can provide XRD data with a large Q-range despite the limited opening angle of the multi-anvil press, while also generating a highly redundant dataset that facilitates efficient background subtraction and data reduction (Wang et al., 2004; King et al., 2022).

The scattering intensity spectra, $I(Q)$, were obtained from the 2-dimensional Energy-Angle-Intensity data using the conversion and correction procedures described in King et al. (2022). The diffraction peaks from the $Al_2O_3$ capsules in the $I(Q)$ profile were removed using the software RPS (Boccato et al., 2022). The structure factor $S(Q)$, distribution function $F(\mathrm{r})$, and radial distribution function $g(\mathrm{r})$ were calculated using the Amorpheus software package (Boccato et al., 2022). The liquid density estimation from the XRD data follows the methodology of Morard et al. (2014), which assumes that no atoms are located at distances shorter than the first coordination shell, where $F(\mathrm{r}) = -4\pi r\rho_0$ and $g(\mathrm{r}) = 0$, for $0 < \mathrm{r} < \mathrm{r_{min}}$, with $\mathrm{r_{min}}$ being the cutoff radius. During the conversion from $I(Q)$ to $F(\mathrm{r})$ in Amorpheus, an iterative procedure is applied to minimize oscillations in the low-$r$ region to satisfy the condition $F(\mathrm{r}) = -4\pi r\rho_0$. The atomic density $\rho_0$ is determined when $F(\mathrm{r})$ shows minimal oscillations.

### 5.2.6 Chemical analysis of the recovered samples

After the HP-HT measurements, the assemblies were recovered to ambient conditions and embedded in epoxy for polishing. The mounted samples, along with the pressure medium and BDD furnace, were first ground to a position near the center of the sample using a diamond polishing plate with 9 µm diamond grains. Subsequently, the samples were polished using polishing cloths with progressively finer diamond sprays (1 µm, 0.5 µm, and 0.25 µm).

The chemical compositions of the run products were quantified using a JEOL JXA-8200 electron probe microanalyzer (EPMA) operated at 15 kV and 15 nA. A defocused beam with a diameter of 20-30 μm was used for analyzing the quenched melt. Metallic Fe, pyrite ($FeS_2$), and periclase (MgO) were employed as standards for the quantification of Fe, S, and O, respectively.

## 5.3 Results

### *5.3.1 Elastic properties of Fe-S liquids under high pressure*

The measured densities and $V_P$ of liquid Fe and Fe-S alloys are summarized in Table 5.1. The uncertainties in the determined $V_P$ are estimated to range between 2% and 4%, primarily due to uncertainties in the sample length, as the samples tend to undergo slight deformation after melting (as shown in Fig. 5.1). In the pressure range investigated in this study (up to 17.8 GPa), the addition of sulfur decreases the P-wave velocities of liquid Fe, with this effect diminishing as pressure increases (Fig. 5.4). The influence of temperature on the $V_P$ of liquid Fe and Fe-S alloys is negligible within the experimental temperature range and falls within the measurement uncertainties. The $V_P$ of pure liquid Fe measured up to 14.3 GPa in this study are consistent, within uncertainty, with previous ultrasonic interferometry studies (Jing et al., 2014; Nishida et al., 2016; Nishida et al., 2020) and inelastic X-ray scattering (IXS) measurements (Kuwayama et al., 2020). The literature data on liquid Fe-S alloys show significant discrepancies, and a comparison with the results of this study parameterized through thermodynamic modeling, is discussed in Section 4.

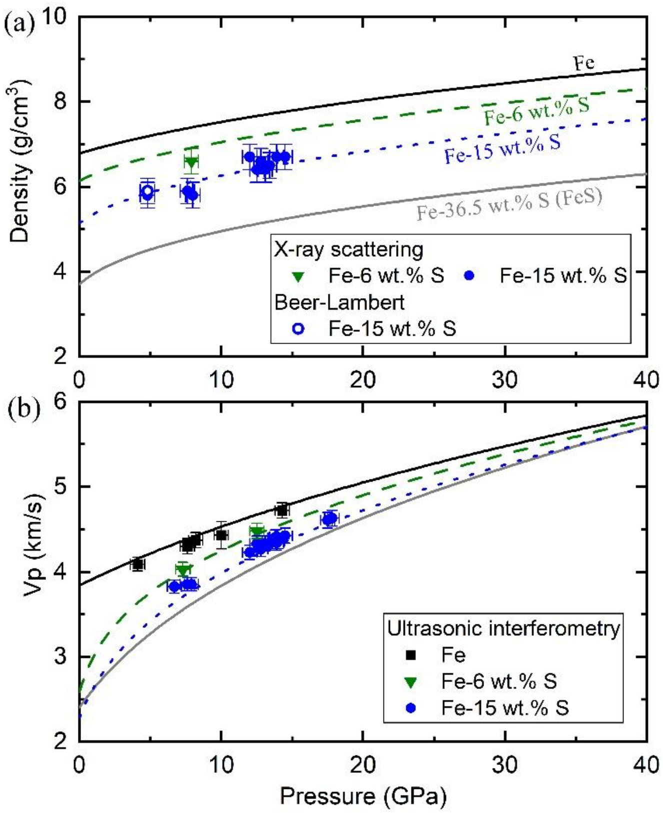

**Figure 5.4.** Densities (a) and P-wave velocities (b) of liquid Fe-FeS solutions. The black squares, green inverted triangles, and blue circles indicate experimental data from this study for Fe (1873–2273 K), Fe-6 wt.% S (1690–1873 K), and Fe-15 wt.% S (1473–2073 K), respectively. The curves in the figure are derived from the thermodynamic model determined in this study, plotted at 2150 K for Fe (black solid curves) and 1750 K for Fe-6 wt.% S (green dashed curves), Fe-15 wt.% S (blue dotted curves), and FeS (grey solid curves), respectively.

Structure factors $S(Q)$ and radial distribution functions $g(r)$ extracted from the XRD patterns of Fe-15 wt.% S liquid collected through the CAESAR method, are shown in Fig. 5.5. As shown in Fig. 5.S4 and Table 5.S1, the first sharp peak in the radial distribution function ($r_1$) of Fe-15 wt.% S liquid decreases from 2.51 nm at 4.8 GPa to 2.44 nm at the highest pressure investigated (14.5 GPa), indicating a progressively denser liquid structure. The $r_1$ positions and their pressure dependence are consistent with previous measurements for similar compositions (Morard et al., 2018a; Xu et al., 2021), as shown in Fig. 5.S4. The intrinsic uncertainty in the analysis of the XRD pattern for liquid alloys is approximately 3 atoms/nm$^3$ (Morard et al., 2014; Boccato et al., 2022), which corresponds to approximately 0.3 g/cm$^3$ for the measurements in this study, although the CAESAR method provides significantly better data quality compared to traditional methods (King et al., 2022; Xu et al., 2021). Nevertheless, in experiments where both CAESAR and Beer-Lambert measurements were performed (MA236), the resulting densities of Fe-15 wt.% S at 4.8 GPa and 1873 K are in good agreement, with densities of 5.8(3) g/cm³ from XRD measurements and 5.9(1) g/cm³ from the Beer-Lambert method. This consistency indicates that the accuracy of the XRD method is acceptable, even though its precision may not be as high. The measured densities of Fe-S liquids up to 14.5 GPa in this study align well with recent experimental data from Xu et al. (2021) at lower pressures (<7 GPa), within experimental uncertainties (Fig. 5.S5). Further comparisons with other experimental data and theoretical calculations are discussed later, following parameterization through thermodynamic modeling.

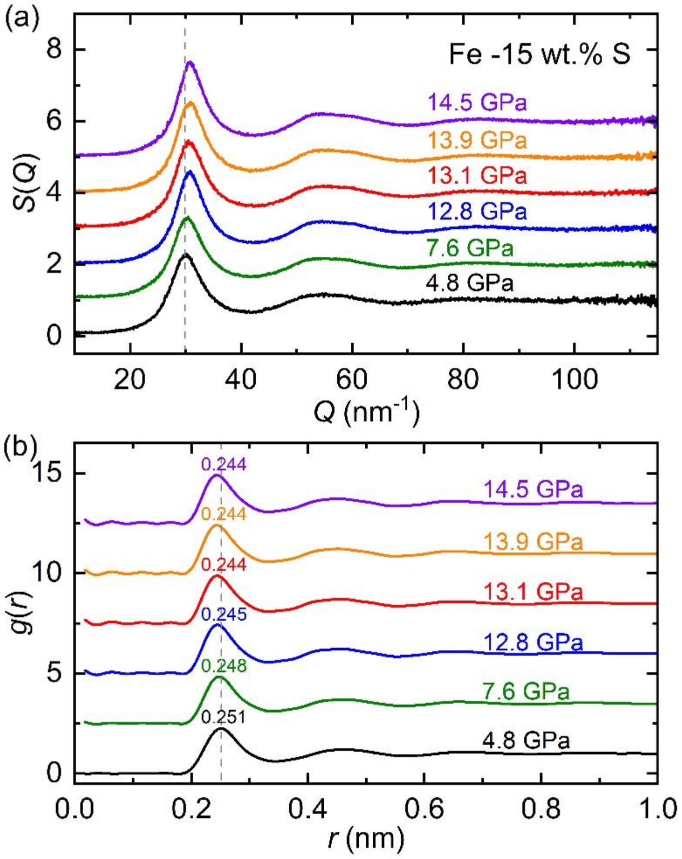

**Figure 5.5.** Structure factor $S(Q)$ (a) and radial distribution function $g(r)$ (b) of Fe-15 wt.% liquid from 4.8 to 14.5 GPa. The temperatures range from 1573 to 1773 K. The positions of the first sharp peak in the radial distribution functions are labeled on top of the peaks.

### 5.3.2 *Melting temperature of liquid Fe*

Melting temperatures of liquid Fe determined in this study, using ultrasonic interferometry and ED-XRD measurements, are closely aligned with the recently reported melting curves by Hou et al. (2021), Morard et al. (2018b), and Anzellini et al. (2013), as shown in Fig. 5.6a. Since the ultrasonic and ED-XRD measurements were conducted with temperature increments of approximately 50 K, the melting temperatures could be overestimated by up to 50 K. Even when accounting for these uncertainties, the melting temperatures determined in this study remain higher than those reported by Sinmyo et al. (2019) and Ezenwa and Fei (2023). Applying the extrapolation of the empirical polynomial from Nishihara et al. (2020) to correct for the pressure effect on the EMF of TC, the actual temperature for Fe melting at 14.3 GPa might be up to 81 K higher than the TC reading (see Table 5.1). However, since this empirical correction equation was developed based on experimental data below 1173 K, extrapolation to temperatures above 2000 K may not be reliable in the context of this study. Therefore, potential corrections for the pressure effect on the EMF are provided in Table 5.1 for reference but are not applied in the subsequent discussions.

### *5.3.3 Density of solid FeS phases under high pressure*

For sulfur-bearing samples, the P-V-T relationships of FeS IV and FeS V (Urakawa et al., 2004) were measured below the solidus temperatures. The volume data for the solid FeS phases are listed in Supplementary Tables 5.S2 and 5.S3 and plotted in Fig. 5.6d at selected temperatures, with further details shown in Fig. 5.S6. No detectable volume drops or jumps were observed during the phase transition between FeS IV and FeS V, consistent with previous studies that identify this transition as a second-order phase transition (Fei et al., 1995; Kusaba et al., 1998; Urakawa et al., 2004). The anomalous compression behavior in the pressure range of 4–12 GPa, previously proposed as a gradual spin transition of iron (Fei et al., 1995; Kusaba et al., 1998; Urakawa et al., 2004), was confirmed in our measurements (Fig. 5.6d and Fig. 5.S6). The P-V-T relations of FeS IV and FeS V are in good agreement with previous data and can, therefore, be combined into a comprehensive dataset for modeling the equations of state of solid FeS phases.

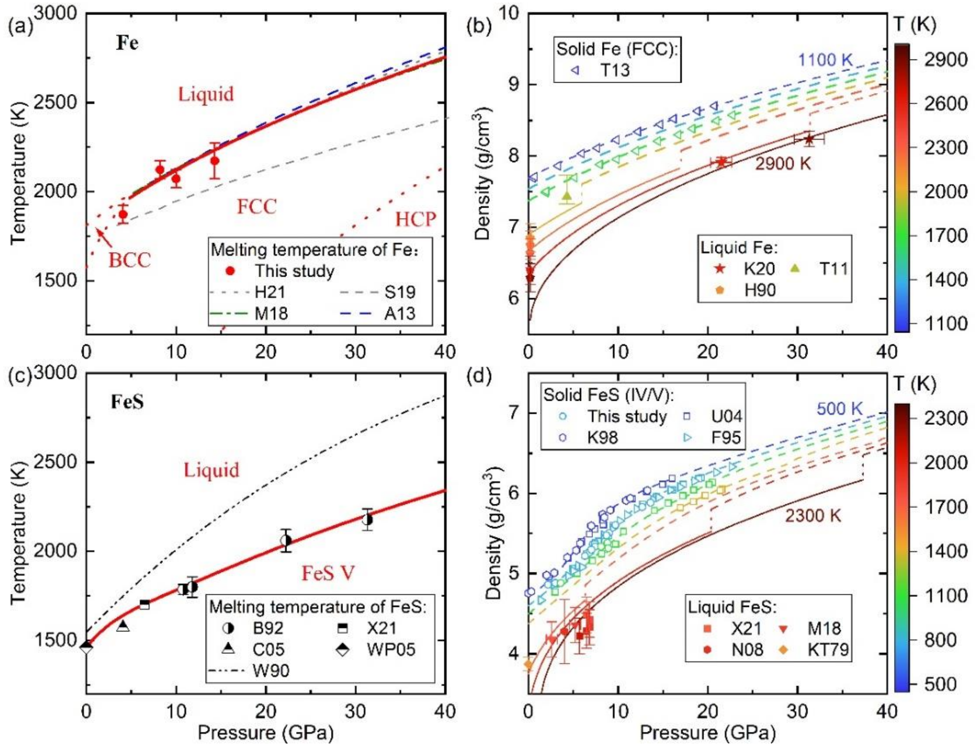

**Figure 5.6.** Melting curves and densities of Fe and FeS. (a, c) Melting curves of Fe and FeS. The red solid circles indicate the experimental data from this study, while the red curves are the melting curves derived from the thermodynamic models developed in this study. For Fe (panel a), melting curves from recent literature are shown for comparison: H21 (Hou et al., 2021), S19 (Sinmyo et al., 2019), M18 (Morard et al., 2018b), and A13 (Anzellini et al., 2013). BCC and HCP boundaries are from Dorogokupets et al. (2017). For FeS (panel c), the melting curve is compared with high-pressure data from B92 (Boehler, 1992) and ambient pressure data from WP05 (Waldner and Pelton, 2005). Upper limits of the melting temperature from X21 (Xu et al., 2021) and C05 (Chen et al., 2005) are shown, along with the W90 (Williams, 1990) melting curve. (b, d) Densities and derived equations of state for solid and liquid Fe and FeS. The solid and dashed lines indicate densities of liquid and solid phases from the thermodynamic model, plotted in 300 K increments. For Fe (panel b), experimental data for solid Fe (T13: Tsujino et al., 2013) and liquid Fe (K20: Kuwayama et al., 2020; T11: Tateyama et al., 2011; H90: Hixson et al., 1990) are shown. For FeS (panel d), experimental data for solid phases are from this study, as well as from U04 (Urakawa et al., 2004), K98 (Kusaba et al., 1998), and F95 (Fei et al., 1995). Liquid-phase data are from X21 (Xu et al., 2021), M18 (Morard et al., 2018a), N08 (Nishida et al., 2008), and KT70 (Kaiura and Toguri, 1979). The color bar indicates the temperatures of the symbols and curves.

### *5.3.4 Chemical compositions of the recovered samples*

The chemical compositions of the recovered samples are reported in Supplementary Table 5.S4, except for runs BT699 and MA234, where the melt escaped at the end of the measurements. In addition to Fe and S, less than 0.6 wt.% of O was detected in the recovered samples, probably due to slight oxidation of the starting Fe powers. This amount of O is not substantial and will be ignored in further discussion. The differences in the S concentrations between the measured values and the starting materials are less than 1 wt.%, which provides evidence that the measurements were performed in a nominally closed system, where the melts were effectively encapsulated during the in-situ measurements. We assume that the compositions of BT699 and MA234 were also the same as the starting material, i.e., pure Fe and Fe-6±1 wt.% S, respectively. Backscattered electron images of the successfully recovered samples are shown in Fig. 5.S7.

## 5.4 Thermodynamic modeling of Fe-FeS liquids

To systematically describe the effect of S on the elastic properties of Fe-rich liquids and reliably extrapolate the experimental results to the conditions covering the entire Martian core, we have developed a thermodynamic model based on the end members Fe and FeS. We combine constraints provided by density and elastic property measurements with data on the end-member melting curves to obtain a single self-consistent model. The P-T phase relations of a melting curve provide important constraints on both the densities and elastic properties of liquids once the properties of the corresponding solid phases are well known. We employ the equation of state framework developed by Stixrude and Lithgow-Bertelloni (2005, 2011, 2024), along with the references cited therein, as summarized in Supplementary Text 5.S2.

**Table 5.1** Experimental Conditions and Elastic Properties of Fe-S Liquids.

| Run No.[†] | P[¶] (GPa) | TC reading (K) | T correction[§] (K) | $V_p$ (km/s) | Density (g/cm$^3$) | Method[‡] |
|---|---|---|---|---|---|---|
| **Fe** | | | | | | |
| BT657 | 8.2(5) | 2123(50) | 53 | 4.37(9) | - | Ultrasonic |
| | 7.6(5) | 2223(50) | 55 | 4.30(9) | - | Ultrasonic |
| | 14.3(5) | 2173(100)[*] | 81 | 4.72(9) | - | Ultrasonic |
| | 14.3(5) | 2273(100)[*] | 88 | 4.74(9) | - | Ultrasonic |
| BT699 | 4.1(5) | 1873(50) | 25 | 4.09(8) | - | Ultrasonic |
| T2830 | 10.0(5) | 2073(50) | 59 | 4.43(16) | - | Ultrasonic |
| **$Fe_{94}S_6$** | | | | | | |
| MA234 | 12.5(5) | 1690(50) | 48 | 4.48(9) | - | Ultrasonic |
| MA235 | 7.3(5) | 1873(50) | 39 | 4.03(8) | 6.6(3) | Ultrasonic, XRD |
| **$Fe_{85}S_{15}$** | | | | | | |
| MA229 | 7.6(5) | 1673(50) | 33 | 3.85(8) | 5.9(3) | Ultrasonic, XRD |
| | 7.9(5) | 1873(50) | 41 | 3.85(8) | | Ultrasonic |
| | 8.0(5) | 1913(50) | 43 | | 5.8(3) | XRD |
| | 6.7(5) | 2023(50) | 42 | 3.82(16) | - | Ultrasonic |
| MA231 | 13.4(5) | 1490(50) | 40 | 4.34(9) | 6.5(3) | Ultrasonic, XRD |
| | 13.1(5) | 1573(50) | 43 | 4.33(9) | 6.4(3) | Ultrasonic, XRD |
| | 12.9(5) | 1773(50) | 53 | 4.33(9) | - | Ultrasonic |
| | 12.5(5) | 1523(50) | 40 | 4.33(9) | 6.4(3) | Ultrasonic, XRD |
| MA233 | 14.5(5) | 1600(50) | 50 | 4.42(9) | 6.7(3) | Ultrasonic, XRD |
| | 13.9(5) | 1680(50) | 50 | 4.41(9) | 6.7(3) | Ultrasonic, XRD |
| | 13.8(5) | 1773(50) | 55 | 4.40(9) | - | Ultrasonic |
| | 14.0(5) | 1873(50) | 61 | 4.36(9) | - | Ultrasonic |
| | 13.9(5) | 1973(50) | 67 | 4.34(9) | - | Ultrasonic |
| | 12.0(5) | 1480(50) | 37 | 4.23(8) | 6.7(3) | Ultrasonic, XRD |
| | 12.8(5) | 1573(50) | 43 | 4.26(9) | 6.6(3) | Ultrasonic, XRD |
| MA236 | 4.8(5) | 1773(50) | 26 | - | 5.8(3) | XRD |
| | 4.8(5) | 1873(50) | 28 | - | 5.8(3) | XRD |
| | 4.8(5) | 1873(50) | 28 | - | 5.9(1) | Beer-Lambert |
| T2833 | 17.8(5) | 1473(50) | 47 | 4.63(9) | - | Ultrasonic |
| | 17.5(5) | 1600(50) | 53 | 4.61(9) | - | Ultrasonic |

[†] Run numbers marked with BT, T, and MA refer to multi-anvil experiments conducted at beamline P61B (DESY), beamline 13IDD (APS), and beamline PSICHE (SOLEIL), respectively.

[¶] The reported pressures were calculated using the EOS of corundum from Shi et al. (2022). The differences between the pressures calculated using the EOS from Shi et al. (2022) and those from Néri et al. (2024) are within 0.2 GPa.

[§] Temperature corrections for the readings of type-D thermocouples at high pressures estimated based on the empirical polynomial extrapolation from Nishihara et al. (2020).

[*] TC failed and the temperatures were estimated based on the power-temperature relation established below 1773 K in the same heating cycle.

[‡] Vp values were measured using ultrasonic interferometry, while densities were determined via XRD or the Beer-Lambert method.

Numbers in parentheses indicate the uncertainties in the last digit.

### 5.4.1 *End member properties of Liquid Fe and FeS*

Thermodynamic models for Fe and FeS liquid endmembers are derived by fitting several key observations: (1) data on the thermal expansion of the liquid phases at ambient pressure, (2) the EOS of the solid endmembers and the melting curves at high pressures, and (3) $V_P$ measurements on liquid phases at both ambient and high pressures.

We compared a large set of literature data on the density of liquid Fe at ambient pressure, as shown in Fig. 5.7a. The fitted model lies in the middle of the wide range of experimental data (Kamiya et al., 2021; Le Maux et al., 2019; Watanabe et al., 2016; Drotning, 1981; Saito et al., 1969; Kirshenbaum and Cahill, 1962) but shows good agreement with recent high-temperature measurements up to 2320 K by Le Maux et al. (2019). In the case of liquid FeS, where limited literature data are available, the fitted model accurately captures the density measurements from Kaiura and Toguri (1979), though it deviates slightly from the results of Kucharski and Toguri (1994), being approximately 0.1 g/cm$^3$ higher (Fig. 5.7b).

Since the Gibbs free energies of the solid and liquid phases are equal along the melting curve, and the thermodynamic properties of the solid Fe and FeS phases can be well evaluated, the melting curves offer critical constraints on the Gibbs free energies of Fe and FeS liquids. Specifically, at the melting point, the Clausius–Clapeyron relation:

$$\frac{dT}{dP} = \frac{\Delta V}{\Delta S} \tag{5.3}$$

where $dT/dP$ is the slope of the melting curve, $\Delta S$ and $\Delta V$ are the entropy and volume change upon melting, respectively, highlighting that the shape of the melting curve is sensitive to $\Delta V$, providing important information on the volume and compressibility of the liquid phases using well-constrained properties of the solids. Thermodynamic models for solid Fe and FeS were fit to calorimetric data obtained at ambient pressure (Chase, 1998 for Fe, and Evans et al., 2010 and references therein for FeS) and thermoelastic measurements. For FCC Fe, the equation of state was fitted using data from Nishihara et al. (2012), Komabayashi et al. (2010), and Tsujino et al. (2013). For FeS IV and FeS V, data from Fei et al. (1995), Kusaba et al. (1998), and Urakawa et al. (2004), along with data collected in this study, were used. The transition between FeS IV and FeS V is described using a tricritical Landau model, and the gradual spin transition of Fe in FeS (Urakawa et al., 2004) is treated as the mixing of high-spin and low-spin FeS end members. More details on the thermodynamic model for solid FeS are provided in Supplementary Text 5.S3. While a spin transition of Fe may also occur in liquid FeS, the mixing of high-spin and low-spin states is expected to be significantly broadened at the high temperatures relevant to planetary core conditions, as seen in the model for the solid FeS phase (see Fig. 5.S8). Therefore, in this study, the liquid FeS end member is modeled as a single component. Properties of FeS liquid were then determined by fitting the melting curve of Boehler (1992) up to 43 GPa, which aligns with the melting data reported by Chen et al. (2005), Xu et al. (2021), and Edmund et al. (2024). Melting temperatures for Fe determined in this study, along with several recent Fe melting curves that show consistent results (e.g., Anzellini et al., 2013; Morard et al., 2018b; Hou et al., 2019), were used to constrain the properties of Fe liquid. The fitted parameters of the thermodynamic models for the solid and liquid phases are given in Table 5.2.

The $V_P$ of liquid Fe, measured at both ambient and high pressures, were incorporated into the fitting of the thermodynamic model for liquid Fe. This dataset includes results from this study as well as data from the literature (Nasch and Manghnani, 1998; Kuwayama et al., 2020; Nishida et al., 2020; Jing et al., 2014). In the case of FeS, however, limited $V_P$ data is available within the pressure range relevant to this study. The only applicable data is from Nishida et al. (2016), with $V_P$ of FeS liquid measured up to 6.4 GPa.

Comparisons between the model and experimental data for both solid and liquid Fe and FeS phases are shown in Fig. 5.6, with further details in Figs. 5.S6, 5.S9, and 5.S10. The density of FeS solid shows complexities both due to an Fe spin transition, which increases the density of FeS but can be seen to get broader in pressure with increasing temperature, and due to the second order transition of FeS IV to FeS V, which is temperature dependent. These effects are extremely well matched by the thermodynamic model, with the pressure and sharpness of the high-spin to low-spin transition of Fe in FeS at room temperature also matching the pressure and sharpness of the transition observed in Fe K $\beta$ emission line data collected by Rueff et al. (1999). Although the experimental densities of Fe and FeS liquids under high pressures were not included to fit the end-member models, the models show good agreement with the most recent experimental measurements. The density of liquid Fe from the present model closely matches the experimental data from Kuwayama et al. (2020) across the entire pressure range of the dataset (Fig. 5.6 and Fig. 5.S10). Under Martian core conditions, the differences in densities and P-wave velocities of liquid Fe derived from the current model, compared to other experimentally based models from the literature (Komabayashi et al., 2014; Dorogokupets et al., 2017), are within 0.2 $g/cm^3$ and 0.1 km/s, respectively, as shown in Fig. 5.S11. There is slightly less agreement with a recent model based on ab initio calculations (Wagle and Steinle-Neumann, 2019), most likely because it was developed for the TPa pressure range and has fewer constraints at the relatively low pressures relevant to this study.

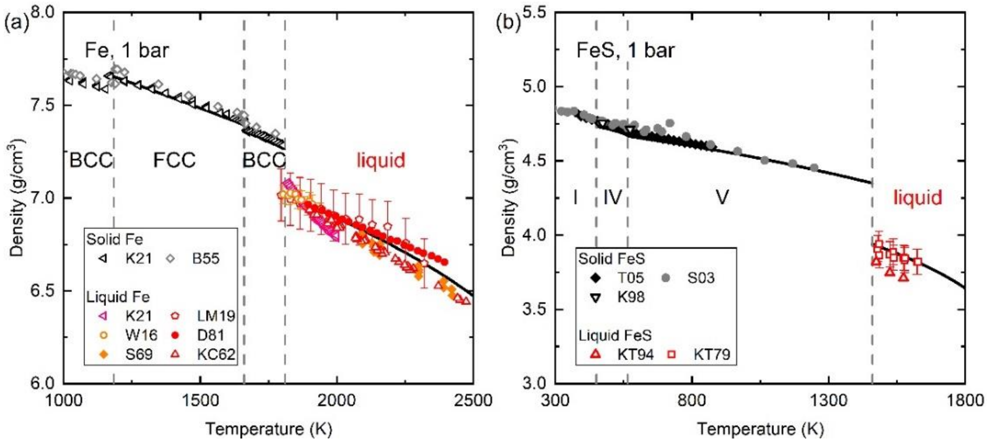

**Figure 5.7.** Densities of Fe (a) and FeS (b) under ambient pressure and elevated temperatures. The black solid curves depict the densities calculated using the thermodynamic model from this study. The symbols indicate data from literature for solid Fe (K21: Kamiya et al., 2021; B55: Basinski, et al., 1955), liquid Fe (LM19: K21: Kamiya et al., 2021; Le Maux et al., 2019; W16: Watanabe et al., 2016; D81: Drotning, 1981; S69: Saito et al., 1969; KC63: Kirshenbaum and Cahill, 1962), solid FeS (T05: Tenailleau et al., 2005; S03: Selivanov et al., 2003; K98: Kusaba et al., 1998), and liquid FeS (KT94: Kucharski and Toguri, 1994; KT79: Kaiura and Toguri, 1979). The densities of liquids in the super-cooled temperature regions are not included in the models.

As mentioned earlier, there is a significant discrepancy in the reported densities of liquid FeS under high pressure across the literature. Based on the systematic evaluation in this study, some of these values can be excluded. For example, the densities of liquid FeS reported by Nishida et al. (2011) and Chen et al. (2014) are even higher than those predicted at the same conditions for solid FeS by the EOS derived in this study, which is unlikely to be the case. In contrast, the current liquid FeS model agrees well with the experimental observations from Morard et al. (2018a) and Xu et al. (2021), falling within the experimental uncertainty (Fig. 5.6).

**Table 5.2.** Thermodynamic parameters of Fe and FeS phases refined in this study.

| **Phase** | $V_0$ **(cm$^3$ mol$^{-1}$)** | $K_{T0}$ **(GPa)** | $K'_T$ | $F_0$ **(KJ mol$^{-1}$)** | $\theta_0$ **(K)** | $\gamma_0$ | $q$ | $T_0$ **(K)** | $\beta_{el}$ **(J mol$^{-1}$ K$^{-2}$)** | $\gamma_{el}$ | $V_D$ **(cm$^3$ mol$^{-1}$)** | $S_D$ **(KJ mol$^{-1}$)** | $T_{c0}$ **(K)** |
|---|---|---|---|---|---|---|---|---|---|---|---|---|---|
| FeS V-HS | 18.58(3) | 85(1) | 4.7 | -117.6(3) | 249(2) | 2.35(2) | 0.50 | 300 | 0 | - | 0.325(6) | 11.2(2) | 565 |
| FeS V-LS | 16.23(6) | 104(2) | 4.0 | -106.7(3) | 288(3) | 1.73(5) | 1.60 | 300 | 0 | - | 0.325(6) | 11.2(2) | 565 |
| Liquid FeS | 22.31(6) | 19.4(3) | 6.5 | -271.6(3) | 98.5(4) | 1.45(2) | 1.80 | 1460 | 0 | - | - | - | - |
| FCC Fe | 6.93(1) | 150(2) | 5.5 | -2.6(0) | 279(2) | 2.16(4) | 0.50 | 300 | 0.0029(1) | 1.2(1) | - | - | - |
| Liquid Fe | 7.96(1) | 87(1) | 5.9 | -108.1(1) | 182(1) | 2.08(3) | 1.45 | 1811 | 0.0049(1) | 0.88(6) | - | - | - |

$V_0$: Volume at reference conditions; $K_{T0}$: Isothermal bulk modulus at reference conditions; $K'_T$: Pressure derivative of isothermal bulk modulus; $F_0$: Reference value of Helmholtz free energy; $\theta_0$: Debye temperature at reference state; $\gamma_0$: Grüneisen parameter at reference state; $q$: Volume dependency parameter for the Grüneisen parameter; $T_0$:Reference temperature; $\beta_{el}$: Parameter for thermal excitation of electrons; $\gamma_{el}$:Volume dependence of $\beta_{el}$; $V_D$: Maximum excess volume of Landau transition; $S_D$: Maximum excess entropy of Landau transition; $T_{c0}$: Critical temperature of Landau transition at ambient pressure. The equations for the thermodynamic expressions are summarized in Supplementary Text 5.S2.

### 5.4.2 *Elasticity of Fe-FeS solutions*

With the end-member thermodynamic models for liquid Fe and FeS established in this study, we can further examine the elastic properties of Fe-FeS liquid mixtures in detail. Based on the experimental results from this and previous studies, we find that within the experimental uncertainties, the densities and $V_P$ of Fe-S liquid mixtures can be accurately described by assuming ideal mixing of the Fe and FeS end members, without the need to introduce excess volume of mixing terms. The Gibbs free energy of the mixture is expressed as:

$$\begin{gathered} G(P,T,x_{FeS}) = (1-x_{FeS})G_{Fe_L}(P,T) + x_{FeS}G_{FeS_L}(P,T) \\ +(1-x_{FeS})RTln(1-x_{FeS}) + (x_{FeS})RTln(x_{FeS}) \end{gathered} \tag{5.4}$$

where $G_{Fe_L}(P,T)$ and $G_{FeS_L}(P,T)$ are the Gibbs free energy of pure liquid Fe and liquid FeS, respectively. Under a given P-T condition, the volume of the mixture is

$$V(x_{FeS}) = (1-x_{FeS})V_{Fe} + x_{FeS}V_{FeS_L} \tag{5.5}$$

but we can also calculate the volume using,

$$V(P,T,x_{FeS}) = \left(\frac{\partial G}{\partial P}\right)_T, \tag{5.6}$$

the isothermal bulk modulus from,

$$K_T(P,T) = -V\left(\frac{\partial P}{\partial V}\right)_T \tag{5.7}$$

and the adiabatic bulk modulus from,

$$K_S = -V\left(\frac{\partial P}{\partial V}\right)_S = \frac{C_P}{C_V}K_T \tag{5.8}$$

where $C_P$ is heat capacity at constant pressure, and $C_V$ is the heat capacity at constant volume. $C_P$, $C_V$ , entropy $S$ and thermal expansion $\alpha$, are calculated as follows:

$$C_P = T\left(\frac{\partial S}{\partial T}\right)_P \tag{5.9}$$

$$C_V = T\left(\frac{\partial S}{\partial T}\right)_V = C_P - TV\alpha^2 K_T \tag{5.10}$$

$$S = -\left(\frac{\partial G}{\partial T}\right)_P \tag{5.11}$$

$$\alpha = \frac{1}{V}\left(\frac{\partial V}{\partial T}\right)_P \tag{5.12}$$

The longitudinal velocity of the mixture is calculated from,

$$v_P = \sqrt{\frac{K_S}{\rho}} \tag{5.13}$$

Among the literature data on experimental measurements of Fe-S liquid densities, our model aligns well with recent multi-anvil experiments at pressures below 7 GPa from Xu et al. (2021), within experimental uncertainty across the full composition range (Fig. 5.S5). Additionally, density measurements from laser-heated diamond anvil cell (LH-DAC) experiments in the Fe(Ni)-S system by Morard et al. (2013) with 12 wt.% S and Kawaguchi et al. (2022) with 16 wt.% S also match our model (Fig. 5.S12). However, the data from Morard et al. (2013) begin to deviate at pressures above approximately 70 GPa, and densities from dynamic compression measurements at pressures above 100 GPa by Huang et al. (2018) show slight inconsistencies with our model. This discrepancy is likely because the FeS end-member model used in this study is constrained by melting curves up to only 43 GPa, making it potentially less applicable at much higher pressures. At pressures below 5 GPa, our model shows substantial inconsistencies with experimental measurements in the Fe-S and Fe(Ni)-S systems (Sanloup et al., 2000; Balog et al., 2003; Nishida et al., 2008; Morard et al., 2018a), which themselves show inconsistencies across the literature. This may be due to the complex mixing behavior caused by strong interactions between Fe-(Ni)-S at low pressures, while the system tends toward ideal mixing at higher pressures, as supported by the thermodynamic modeling in Xu et al. (2021), where the excess volume of mixing diminishes with increasing pressure.

There are also significant discrepancies in the reported effects of sulfur on the $V_P$ of liquid Fe alloys among experimental studies (Jing et al., 2014; Nishida et al., 2016; Nishida et al., 2020; Kawaguchi et al., 2017), though the reasons remain unclear. Our experiments and model show relatively good agreement with the results of Jing et al. (2014), whereas the trend of $V_P$ in Fe-S liquids rising rapidly to approach or exceed that of pure Fe at 10 GPa, as reported in Nishida et al. (2020) and Terasaki et al. (2019), is neither observed in our experiments nor supported by our model (see Fig. 5.S13).

The densities of Fe-S liquids from some recent ab initio calculations (Kuskov and Belashchenko, 2016; Huang et al., 2023) show good agreement with our experiments and thermodynamic models (Fig. 5.S14a). However, the $V_P$ from these studies do not match any experimental observations, including those from this study (Fig. 5.S14b). This seems to imply that simple pressure corrections to the calculation results may not adequately capture the second-order thermodynamic properties of Fe-rich liquids. In the case of another recent ab initio calculation on Fe-16 wt.% S liquid (Li et al., 2024), where no experimental corrections were applied, neither the density nor $V_P$ aligned closely with any experimental observations.

## 5.5 Implications on the composition of the Martian core

Using the newly derived thermodynamic model for the Fe-FeS system, we can place constraints on the composition of the Martian core based on its density and P-wave velocity that have been evaluated using data from the InSight lander (Stähler et al., 2021; Irving et al., 2023; Samuel et al., 2023; Khan et al., 2023). Comparisons of the density and P-wave velocity of liquid Fe-S alloys with estimates based on the InSight observations are illustrated in Fig. 5.8, along two hypothetical adiabatic temperature profiles: one that considers the presence of a basal magma layer (BML) and the other without

(Samuel et al., 2023). For the BML model comparison we have performed the calculation at the relatively high core-mantle boundary (CMB) temperature proposed in the BML model by Samuel et al., (2023). The gradient of the adiabatic temperature profile is calculated from the Fe-S thermodynamic model:

$$\frac{dT}{dP} = \frac{TV\alpha}{C_P} \tag{5.14}$$

Assuming sulfur is the only light element alloyed with Fe in the Martian core, approximately 30 wt.% S would be required to account for recently proposed core densities that consider no BML (Samuel et al., 2023; Irving et al., 2023). In contrast, either approximately 20 wt.% or 24 wt.% S would be needed to explain the density deficit in the Martian core models of Samuel et al. (2023) and Khan et al. (2023), respectively, where a BML is considered.

To put these possible core concentrations into context, they can be compared with cosmochemical estimates for the availability of S in the materials from which Mars is likely to have formed. Mars has often been considered to have a hereditary relationship to ordinary or enstatite chondrites, based on oxygen isotopes (Lodders and Fegley, 1997; Sanloup et al., 1999). If we assume that Mars formed only from ordinary chondrites (either H, L or LL) (Wasson and Kallemeyn, 1988), and all S partitioned into the core and none was lost due to volatility, then the core would contain approximately 10 wt. % S. If it were made from enstatite chondrites, on the other hand, the core would contain either 16 wt. % S (EL) or 27 wt. % S (EH), with the latter being comparable to that expected for CI chondrites. Consequently, models based on Mars being formed from mixtures of these meteorites propose core S contents in the range of 10 – 16 wt % (Lodders and Fegley, 1997; Sanloup et al., 1999). For concentrations of S in the Martian core to be more than 20 wt. % would require it to have formed mainly from EH or CI type materials and for virtually no S to have been lost due to incomplete condensation or evaporative processes. However, Mars is clearly depleted in elements with similar condensation temperatures to S but which remained lithophile, and a recent estimate based on the trends of such elements in SNC meteorites, concluded that there should be < 7 wt. % S in the core (Yoshizaki and McDonough, 2020). If Martian core sulfur contents are in the range of 20–30 wt.% then this would imply that the sulfur concentration of Mars is decoupled from other elements with similar condensation temperatures. This would also have important implications for the sulfur content of the Earth's core, which has in the past been constrained to be ≤ 1.7 wt. % based on the same type of reasoning (Dreibus and Palme, 1996).

However, a further argument against sulfur being the only light element is that a pure Fe-S Martian core cannot simultaneously match both the density and $V_P$ constraints from the InSight models, either with or without a BML. As shown in Fig. 5.8c and d, the high sulfur concentrations required to match the density of the core, decrease the P-wave velocity. This contradicts models based on InSight data that imply the P-wave velocity becomes higher than that of pure liquid Fe in the Martian core (Irving et al., 2023; Samuel et al., 2023; Khan et al., 2023). Although our thermodynamic model shows that the P-wave velocity of Fe-S liquid tends to converge with pure liquid Fe in the deeper Martian core, the velocity-lowering effect of sulfur remains significant, particularly in the upper part of the core. The comparison between the Fe-FeS thermodynamic model and the trends for the Martian core based on InSight measurements therefore highlights the need to consider additional light elements alongside sulfur, which could stiffen Fe-rich alloys and increase the P-wave velocity under Martian core conditions.

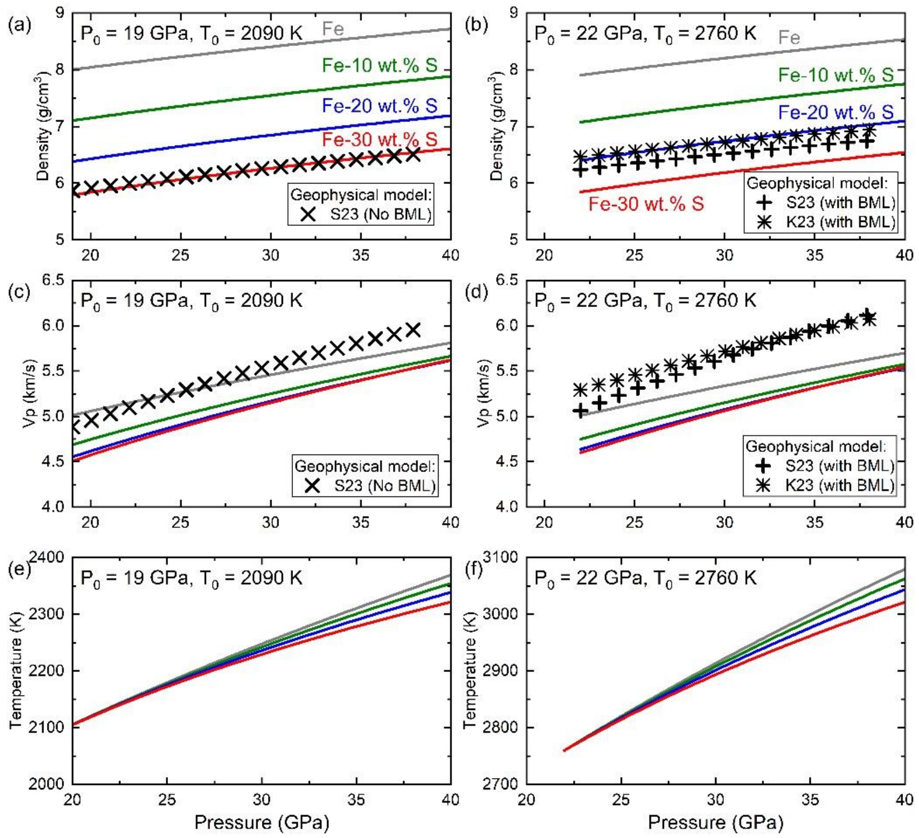

**Figure 5.8.** Comparison between the adiabatic properties of Fe-S liquids calculated from the thermodynamic model developed in this study (solid curves), with models for Martian core properties that are based on InSight measurements. Panels (a), (c), and (e) show density, longitudinal velocity, and temperature profiles calculated using a reference CMB temperature (T0) of 2090 K at 19 GPa (P0), compared with profiles that employ InSight measurements but assume no basal magma layer (BML) at the Martian core-mantle boundary (S23: Samuel et al., 2023). Panels (b), (d), and (f) are calculated at a reference CMB temperature of 2760 K at 22 GPa and are compared with profiles based on InSight measurements that assume the existence of a BML at the CMB of Mars (S23: Samuel et al., 2023; K23: Khan et al., 2023). The grey, green, blue, and red curves indicate compositions of pure Fe, Fe with 10 wt.% S, Fe with 20 wt.% S, and Fe with 30 wt.% S, respectively.

While the depletion of vanadium and chromium from the Earth's mantle has been used to argue for a reducing phase of terrestrial core formation that likely resulted in silicon entering the core (O'Neill, 1991), for Mars the same depletions do not seem to have occurred (Yoshizaki and McDonough, 2020). Oxygen, on the other hand, may dissolve into Fe-rich liquids in significant amounts if the temperature is sufficiently high (Tsuno et al., 2011). In the basal magma layer (BML) scenario proposed by Samuel et al. (2023), for example, the temperature at the Martian CMB is proposed to exceed 2700 K. Under such conditions approximately 10 mol.% oxygen could have dissolved into the Martian core, based on the model from Tsuno et al. (2011). However, as oxygen partitioned into the core, the FeO content of the BML would be lowered, most likely leading to the BML either crystallizing or becoming gravitationally unstable. A BML may, therefore, be inconsistent with CMB temperatures that are high enough for significant oxygen to enter the core. Conversely, in a "cold" CMB scenario, where a BML is absent or where it is not at the super-liquidus conditions proposed by Samuel et al. (2023), the solubility of oxygen in the core would be limited, as suggested by earlier models (e.g., Rubie et al., 2004). Thus, in both scenarios, the concentration of oxygen in the Martian core is likely to be limited.

Hydrogen and carbon have also been proposed as potential light elements in the Martian core (e.g., Gudkova and Zharkov, 2004; Yoshizaki and McDonough, 2020; Khan et al., 2022), although based on their volatility their concentrations in Mars should be much lower than sulfur. The effects of hydrogen on the elastic properties of liquid Fe at high pressures remain largely unknown due to experimental challenges. However, since the P-T melting curve of FeH is relatively flat at pressures below 20 GPa (Sakamaki et al., 2009), this implies that the densities and compressibilities of the solid and liquid FeH phases may be similar. We can then make a qualitative estimate of hydrogen's effect on liquid Fe using experimental results from $FeH_x$ solids. Using this approach, we would expect the addition of hydrogen to increase the P-wave velocity of solid Fe (e.g., Sakamaki et al., 2009; Thompson et al., 2018), while reducing its density. We estimate that approximately 0.3 wt. % H in the Martian core could lower the required amount of sulfur to within the range 10-15 wt. %, while maintaining a P-wave velocity that was broadly consistent with the Insight constraints. This core H content could form through reduction of approximately 0.7 wt % $H_2O$ from the silicate portion of the planet.

The incorporation of carbon (C) has also been shown to significantly increase the sound velocity of liquid Fe under Martian core conditions, as demonstrated in previous experiments (Nakajima et al., 2015). Therefore, the combined incorporation of S and C into the Martian core presents another promising solution for explaining seismic observations of the Martian core. However, the simultaneous incorporation of large amounts of H and C may be limited, as hydrogen reduces the solubility of carbon in liquid Fe (Hirose et al., 2019). Further systematic studies on the Fe-S-C and Fe-S-H ternary thermodynamic systems are necessary to explore these hypotheses and place more comprehensive constraints on the composition of the Martian core.

## Data statement

The data supporting the key findings of this study are provided in the main text and the supplementary materials. Additional data can be available on request.

## Acknowledgments

The authors thank S. Urakawa for kindly providing the original FeS volume data from Urakawa et al. (2004). We are grateful to R. Njul, A. Rother, S. Übelhack, and H. Fischer for their help with sample preparation. We thank D. Kraußе for assistance with EMPA measurements. We appreciate S. Linhardt and G. Bauer for maintaining the ultrasonic system at BGI. This research was supported by DFG grant FR1555/11. We acknowledge DESY (Hamburg, Germany), a member of the Helmholtz Association HGF, for the provision of experimental facilities. Parts of this research were carried out at PETRA III and we would like to thank S. Bhat, S. Ma, and S. Sonntag for assistance in using beamline P61B. Beamtime at P61B was allocated for proposals I-20211112 and I-20220375. We acknowledge the beamline PSICHE at SOLEIL for proving the beamtime and resources for the CAESAR, Beer-Lambert, and ultrasonic measurements.

The beamtime at PSICHE was allocated for proposals 20220713 and 20211352. Portions of this work were performed at GeoSoilEnviroCARS (The University of Chicago, Sector 13), Advanced Photon Source, Argonne National Laboratory. GeoSoilEnviroCARS is supported by the National Science Foundation – Earth Sciences via SEES: Synchrotron Earth and Environmental Science (EAR –2223273). This research used resources of the Advanced Photon Source, a U.S. Department of Energy (DOE) Office of Science User Facility operated for the DOE Office of Science by Argonne National Laboratory under Contract No. DE-AC02-06CH11357.

# References

Anzellini, S., Dewaele, A., Mezouar, M., Loubeyre, P. and Morard, G., 2013. Melting of iron at Earth's inner core boundary based on fast X-ray diffraction. Science, 340(6131), pp.464-466.

Balog, P.S., Secco, R.A., Rubie, D.C. and Frost, D.J., 2003. Equation of state of liquid Fe‐10 wt% S: Implications for the metallic cores of planetary bodies. Journal of Geophysical Research: Solid Earth, 108(B2).

Boccato, S., Garino, Y., Morard, G., Zhao, B., Xu, F., Sanloup, C., King, A., Guignot, N., Clark, A., Garbarino, G. and Morand, M., 2022. Amorpheus: a Python-based software for the treatment of X-ray scattering data of amorphous and liquid systems. High Pressure Research, 42(1), pp.69-93.

Boehler, R., 1992. Melting of the Fe-FeO and the Fe-FeS systems at high pressure: Constraints on core temperatures. Earth and Planetary Science Letters, 111(2-4), pp.217-227.

Chantel, J., Jing, Z., Xu, M., Yu, T. and Wang, Y., 2018. Pressure dependence of the liquidus and solidus temperatures in the Fe‐P binary system determined by in situ ultrasonics: Implications to the solidification of Fe‐P liquids in planetary cores. Journal of Geophysical Research: Planets, 123(5), pp.1113-1124.

Chase, M.W., 1998. NIST-JANAF Thermochemical Tables 4th ed. J. of Physical and Chemical Reffernce Data, pp.1529-1564.

Chen, J., Weidner, D.J., Wang, L., Vaughan, M.T. and Young, C.E., 2005. Density measurements of molten materials at high pressure using synchrotron X-ray radiography: Melting volume of FeS. In Advances in high-pressure technology for geophysical applications (pp. 185-194). Elsevier.

Chen, J., Yu, T., Huang, S., Girard, J. and Liu, X., 2014. Compressibility of liquid FeS measured using X-ray radiograph imaging. Physics of the Earth and Planetary Interiors, 228, pp.294-299.

Dewaele, A., Torrent, M., Loubeyre, P. and Mezouar, M., 2008. Compression curves of transition metals in the Mbar range: Experiments and projector augmented-wave calculations. Physical Review B—Condensed Matter and Materials Physics, 78(10), p.104102.

Dorogokupets, P.I., Dymshits, A.M., Litasov, K.D. and Sokolova, T.S., 2017. Thermodynamics and equations of state of iron to 350 GPa and 6000 K. Scientific reports, 7(1), p.41863.

Dreibus, G. and Palme, H., 1996. Cosmochemical constraints on the sulfur content in the Earth's core. Geochimica et Cosmochimica Acta, 60(7), pp.1125-1130.

Drotning, W.D., 1981. Thermal expansion of iron, cobalt, nickel, and copper at temperatures up to 600 K above melting.

Edmund, E., Bi, T., Geballe, Z.M., Brugman, K., Lin, J.F., Chariton, S., Prakapenka, V.B., Minár, J., Cohen, R.E. and Goncharov, A.F., 2024. Structure and transport properties of FeS at planetary core conditions. Earth and Planetary Science Letters, 646, p.118959.

Evans, K. A., R. Powell, and T. J. B. Holland, 2010. Internally consistent data for sulphur-bearing phases and application to the construction of pseudosections for mafic greenschist facies rocks in $Na_2O$–CaO–$K_2O$–FeO–MgO–$Al_2O_3$–$SiO_2$–$CO_2$–O–S–$H_2O$. Journal of Metamorphic Geology 28(6), pp.667-687.

Ezenwa, I.C. and Fei, Y., 2023. High pressure melting curve of Fe determined by intermetallic fast diffusion technique. Geophysical Research Letters, 50(6), p.e2022GL102006.

Farla, R., Bhat, S., Sonntag, S., Chanyshev, A., Ma, S., Ishii, T., Liu, Z., Néri, A., Nishiyama, N., Faria, G.A. and Wroblewski, T., 2022. Extreme conditions research using the large-volume press at the P61B endstation, PETRA III. Journal of synchrotron radiation, 29(2), pp.409-423.

Fei, Y., Prewitt, C.T., Mao, H.K. and Bertka, C.M., 1995. Structure and density of FeS at high pressure and high temperature and the internal structure of Mars. Science, 268(5219), pp.1892-1894.

Gudkova, T.V. and Zharkov, V.N., 2004. Mars: interior structure and excitation of free oscillations. Physics of the Earth and Planetary Interiors, 142(1-2), pp.1-22.

Henry, L., Guignot, N., King, A., Giovenco, E., Deslandes, J.P. and Itié, J.P., 2022. In situ characterization of liquids at high pressure combining X-ray tomography, X-ray diffraction and X-ray absorption using the white beam station at PSICHE. Journal of Synchrotron Radiation, 29(3), pp.853-861.

Hirose, K., Tagawa, S., Kuwayama, Y., Sinmyo, R., Morard, G., Ohishi, Y. and Genda, H., 2019. Hydrogen limits carbon in liquid iron. Geophysical Research Letters, 46(10), pp.5190-5197.

Hixson, R.S., Winkler, M.A. and Hodgdon, M.L., 1990. Sound speed and thermophysical properties of liquid iron and nickel. Physical Review B, 42(10), p.6485.

Hou, M., Liu, J., Zhang, Y., Du, X., Dong, H., Yan, L., Wang, J., Wang, L. and Chen, B., 2021. Melting of iron explored by electrical resistance jump up to 135 GPa. Geophysical Research Letters, 48(20), p.e2021GL095739.

Huang, D., Li, Y., Khan, A., Sossi, P., Giardini, D. and Murakami, M., 2023. Thermoelastic properties of liquid Fe-rich alloys under Martian core conditions. Geophysical Research Letters, 50(6), p.e2022GL102271.

Huang, H., Leng, C., Wang, Q., Yang, G., Hu, X., Wu, Y., Liu, X. and Fei, Y., 2018. Measurements of sound velocity of liquid Fe-11.8 wt% S up to 211.4 GPa and 6,150 K. Journal of Geophysical Research: Solid Earth, 123(6), pp.4730-4739.

Irving, J.C., Lekić, V., Durán, C., Drilleau, M., Kim, D., Rivoldini, A., Khan, A., Samuel, H., Antonangeli, D., Banerdt, W.B. and Beghein, C., 2023. First observations of core-transiting seismic phases on Mars. Proceedings of the National Academy of Sciences, 120(18).

Jing, Z., Wang, Y., Kono, Y., Yu, T., Sakamaki, T., Park, C., Rivers, M.L., Sutton, S.R. and Shen, G., 2014. Sound velocity of Fe–S liquids at high pressure: Implications for the Moon's molten outer core. Earth and Planetary Science Letters, 396, pp.78-87.

Jing, Z., Yu, T., Xu, M., Chantel, J. and Wang, Y., 2020. High-pressure sound velocity measurements of liquids using in situ ultrasonic techniques in a multianvil apparatus. Minerals, 10(2), p.126.

Kaiura, G.H. and Toguri, J.M., 1979. Densities of the molten FeS, FeS–$Cu_2S$ and Fe–S–O systems—utilizing a bottom-balance Archimedean technique. Canadian Metallurgical Quarterly, 18(2), pp.155-164.

Kamiya, A., Terasaki, H. and Kondo, T., 2021. Precise determination of the effect of temperature on the density of solid and liquid iron, nickel, and tin. American Mineralogist, 106(7), pp.1077-1082.

Kawaguchi, S.I., Morard, G., Kuwayama, Y., Hirose, K., Hirao, N. and Ohishi, Y., 2022. Density determination of liquid iron-nickel-sulfur at high pressure. American Mineralogist, 107(7), pp.1254-1261.

Kawaguchi, S.I., Nakajima, Y., Hirose, K., Komabayashi, T., Ozawa, H., Tateno, S., Kuwayama, Y., Tsutsui, S. and Baron, A.Q., 2017. Sound velocity of liquid Fe-

Ni‐S at high pressure. Journal of Geophysical Research: Solid Earth, 122(5), pp.3624-3634.

Khan, A., Huang, D., Durán, C., Sossi, P.A., Giardini, D. and Murakami, M., 2023. Evidence for a liquid silicate layer atop the Martian core. Nature, 622(7984), pp.718-723.

Khan, A., Sossi, P.A., Liebske, C., Rivoldini, A. and Giardini, D., 2022. Geophysical and cosmochemical evidence for a volatile-rich Mars. Earth and Planetary Science Letters, 578, p.117330.

King, A., Guignot, N., Henry, L., Morard, G., Clark, A., Le Godec, Y. and Itié, J.P., 2022. Combined angular and energy dispersive diffraction: optimized data acquisition, normalization and reduction. Journal of Applied Crystallography, 55(2), pp.218-227.

Kirshenbaum, A.D. and Cahill, J.A., 1962. The density of liquid iron from the melting point to 2500 K. Trans. Met. Soc. AIME, 224.

Komabayashi, T., 2014. Thermodynamics of melting relations in the system Fe‐FeO at high pressure: Implications for oxygen in the Earth's core. Journal of Geophysical Research: Solid Earth, 119(5), pp.4164-4177.

Kucharski, M., Ip, W. and Toguri, JM, 1994. The surface tension and density of $Cu_2S$, FeS, $Ni_3S_2$ and their mixtures. Canadian Metallurgical Quarterly , 33 (3), pp.197-203.

Kusaba, K., Syono, Y., Kikegawa, T. and Shimomura, O., 1998. High pressure and temperature behavior of FeS. Journal of Physics and Chemistry of Solids, 59(6-7), pp.945-950.

Kuskov, O.L. and Belashchenko, D.K., 2016. Thermodynamic properties of Fe-S alloys from molecular dynamics modeling: Implications for the lunar fluid core. Physics of the Earth and Planetary Interiors, 258, pp.43-50.

Kuwayama, Y., Morard, G., Nakajima, Y., Hirose, K., Baron, A.Q., Kawaguchi, S.I., Tsuchiya, T., Ishikawa, D., Hirao, N. and Ohishi, Y., 2020. Equation of state of liquid iron under extreme conditions. Physical Review Letters, 124(16), p.165701.

Le Maux, D., Courtois, M., Pierre, T., Lamien, B. and Le Masson, P., 2019. Density measurement of liquid 22MnB5 by aerodynamic levitation. Review of Scientific Instruments, 90(7).

Li, W.J., Li, Z., Ma, Z., Zhou, J., Wang, C. and Zhang, P., 2024. Thermoelastic properties and thermal evolution of the Martian core from ab initio calculated magnetic Fe‐S liquid. Journal of Geophysical Research: Planets, 129(4), p.e2023JE007874.

Lodders, K. and Fegley Jr, B., 1997. An oxygen isotope model for the composition of Mars. Icarus, 126(2), pp.373-394.

Morard, G., Boccato, S., Rosa, A.D., Anzellini, S., Miozzi, F., Henry, L., Garbarino, G., Mezouar, M., Harmand, M., Guyot, F. and Boulard, E., 2018b. Solving controversies on the iron phase diagram under high pressure. Geophysical Research Letters, 45(20), pp.11-074.

Morard, G., Bouchet, J., Rivoldini, A., Antonangeli, D., Roberge, M., Boulard, E., Denoeud, A. and Mezouar, M., 2018a. Liquid properties in the Fe-FeS system under moderate pressure: Tool box to model small planetary cores. American Mineralogist, 103(11), pp.1770-1779.

Morard, G., Garbarino, G., Antonangeli, D., Andrault, D., Guignot, N., Siebert, J., Roberge, M., Boulard, E., Lincot, A., Denoeud, A. and Petitgirard, S., 2014. Density measurements and structural properties of liquid and amorphous metals under high pressure. High Pressure Research, 34(1), pp.9-21.

Morard, G., Siebert, J., Andrault, D., Guignot, N., Garbarino, G., Guyot, F. and Antonangeli, D., 2013. The Earth's core composition from high pressure density measurements of liquid iron alloys. Earth and Planetary Science Letters, 373, pp.169-178.

Nakajima, Y., Imada, S., Hirose, K., Komabayashi, T., Ozawa, H., Tateno, S., Tsutsui, S., Kuwayama, Y. and Baron, A.Q., 2015. Carbon-depleted outer core revealed by sound velocity measurements of liquid iron–carbon alloy. Nature communications, 6(1), p.8942.

Nasch, P.M. and Manghnani, M.H., 1998. Molar volume, thermal expansion, and bulk modulus in liquid Fe-Ni alloys at 1 bar: Evidence for magnetic anomalies?. Geophysical Monograph Series, 101, pp.307-317.

Néri, A., Man, L., Chantel, J., Farla, R., Bauer, G., Linhardt, S., Boffa Ballaran, T. and Frost, D.J., 2024. The development of internal pressure standards for in-house elastic wave velocity measurements in multi-anvil presses. Review of Scientific Instruments, 95(1).

Nishida, K., Ohtani, E., Urakawa, S., Suzuki, A., Sakamaki, T., Terasaki, H. and Katayama, Y., 2011. Density measurement of liquid FeS at high pressures using synchrotron X-ray absorption. American Mineralogist, 96(5-6), pp.864-868.

Nishida, K., Suzuki, A., Terasaki, H., Shibazaki, Y., Higo, Y., Kuwabara, S., Shimoyama, Y., Sakurai, M., Ushioda, M., Takahashi, E. and Kikegawa, T., 2016. Towards a consensus on the pressure and composition dependence of sound velocity in the liquid Fe–S system. Physics of the Earth and Planetary Interiors, 257, pp.230-239.

Nishida, K., Terasaki, H., Ohtani, E. and Suzuki, A., 2008. The effect of sulfur content on density of the liquid Fe–S at high pressure. Physics and Chemistry of Minerals, 35, pp.417-423.

Nishida, K., Shibazaki, Y., Terasaki, H., Higo, Y., Suzuki, A., Funamori, N. and Hirose, K., 2020. Effect of sulfur on sound velocity of liquid iron under Martian core conditions. Nature communications, 11(1), p.1954.

Nishihara, Y., Doi, S., Kakizawa, S., Higo, Y. and Tange, Y., 2020. Effect of pressure on temperature measurements using WRe thermocouple and its geophysical impact. Physics of the Earth and Planetary Interiors, 298, p.106348.

Nishihara, Y., Nakajima, Y., Akashi, A., Tsujino, N., Takahashi, E., Funakoshi, K.I. and Higo, Y., 2012. Isothermal compression of face-centered cubic iron. American Mineralogist, 97(8-9), pp.1417-1420.

O'Neill, H.S.C., 1991. The origin of the Moon and the early history of the Earth—A chemical model. Part 2: The Earth. Geochimica et Cosmochimica Acta, 55(4), pp.1159-1172.

Papadakis, E.P., 1972. Absolute Accuracy of the Pulse-Echo Overlap Method and the Pulse-Superposition Method for Ultrasonic Velocity. The Journal of the Acoustical Society of America, 52(3B), pp.843-846.

Rose-Weston, L., Brenan, J.M., Fei, Y., Secco, R.A. and Frost, D.J., 2009. Effect of pressure, temperature, and oxygen fugacity on the metal-silicate partitioning of Te, Se, and S: Implications for earth differentiation. Geochimica et Cosmochimica Acta, 73(15), pp.4598-4615.

Rubie, D.C., Gessmann, C.K. and Frost, D.J., 2004. Partitioning of oxygen during core formation on the Earth and Mars. Nature, 429(6987), pp.58-61.

Rueff, J.P., Kao, C.C., Struzhkin, V.V., Badro, J., Shu, J.F., Hemley, R.J. and Mao, H.K., 1999. Pressure-induced high-spin to low-spin transition in FeS evidenced by X-ray emission spectroscopy. Physical Review Letters, 82(16), p.3284.

Saito, T., Shiraishi, Y. and Sakuma, Y., 1969. Density measurement of molten metals by levitation technique at temperatures between 1800 and 2200 °C. Trans Iron Steel Inst Japan, 9(2), pp.118-126.

Sakamaki, K., Takahashi, E., Nakajima, Y., Nishihara, Y., Funakoshi, K., Suzuki, T. and Fukai, Y., 2009. Melting phase relation of $FeH_x$ up to 20 GPa: Implication for the temperature of the Earth's core. Physics of the Earth and Planetary Interiors, 174(1-4), pp.192-201.

Samuel, H., Drilleau, M., Rivoldini, A., Xu, Z., Huang, Q., Garcia, R.F., Lekić, V., Irving, J.C., Badro, J., Lognonné, P.H. and Connolly, J.A., 2023. Geophysical evidence for an enriched molten silicate layer above Mars’s core. Nature, 622(7984), pp.712-717.

Sanloup, C., Guyot, F., Gillet, P., Fiquet, G., Mezouar, M. and Martinez, I., 2000. Density measurements of liquid Fe-S alloys at high-pressure. Geophysical Research Letters, 27(6), pp.811-814.

Sanloup, C., Jambon, A. and Gillet, P., 1999. A simple chondritic model of Mars. Physics of the Earth and Planetary Interiors, 112(1-2), pp.43-54.

Selivanov, E.N., Vershinin, A.D. and Gulyaeva, R.I., 2003. Thermal expansion of troilite and pyrrhotine in helium and air. Inorganic materials, 39, pp.1097-1102.

Shatskiy, A., Yamazaki, D., Morard, G., Cooray, T., Matsuzaki, T., Higo, Y., Funakoshi, K.I., Sumiya, H., Ito, E. and Katsura, T., 2009. Boron-doped diamond heater and its application to large-volume, high-pressure, and high-temperature experiments. Review of Scientific Instruments, 80(2).

Shi, W., Wei, W., Sun, N., Mao, Z., & Prakapenka, V. B. (2022). Thermal Equations of State of Corundum and Rh2O3 (II)-Type $Al_2O_3$ up to 153 GPa and 3400 K. Journal of Geophysical Research: Solid Earth, 127(4), e2021JB023805.

Sinmyo, R., Hirose, K. and Ohishi, Y., 2019. Melting curve of iron to 290 GPa determined in a resistance-heated diamond-anvil cell. Earth and Planetary Science Letters, 510, pp.45-52.

Stähler, S.C., Khan, A., Banerdt, W.B., Lognonné, P., Giardini, D., Ceylan, S., Drilleau, M., Duran, A.C., Garcia, R.F., Huang, Q. and Kim, D., 2021. Seismic detection of the martian core. Science, 373(6553), pp.443-448.

Steenstra, E.S. and van Westrenen, W., 2018. A synthesis of geochemical constraints on the inventory of light elements in the core of Mars. Icarus, 315, pp.69-78.

Stixrude, L. and Lithgow-Bertelloni, C., 2005. Thermodynamics of mantle minerals—I. Physical properties. Geophysical Journal International, 162(2), pp.610-632.

Stixrude, L. and Lithgow-Bertelloni, C., 2011. Thermodynamics of mantle minerals-II. Phase equilibria. Geophysical Journal International, 184(3), pp.1180-1213.

Stixrude, L. and Lithgow-Bertelloni, C., 2024. Thermodynamics of mantle minerals–III: the role of iron. Geophysical Journal International, 237(3), pp.1699-1733.

Suer, T.A., Siebert, J., Remusat, L., Menguy, N. and Fiquet, G., 2017. A sulfur-poor terrestrial core inferred from metal–silicate partitioning experiments. Earth and Planetary Science Letters, 469, pp.84-97.

Tateyama, R., Ohtani, E., Terasaki, H., Nishida, K., Shibazaki, Y., Suzuki, A. and Kikegawa, T., 2011. Density measurements of liquid Fe–Si alloys at high pressure using the sink–float method. Physics and Chemistry of Minerals, 38, pp.801-807.

Taylor, G.J., 2013. The bulk composition of Mars. Geochemistry, 73(4), pp.401-420.

Tenailleau, C., Etschmann, B., Wang, H., Pring, A., Grguric, B.A. and Studer, A., 2005. Thermal expansion of troilite and pyrrhotite determined by in situ cooling (873 to 373 K) neutron powder diffraction measurements. Mineralogical Magazine, 69(2), pp.205-216.

Terasaki, H., Rivoldini, A., Shimoyama, Y., Nishida, K., Urakawa, S., Maki, M., Kurokawa, F., Takubo, Y., Shibazaki, Y., Sakamaki, T. and Machida, A., 2019. Pressure and composition effects on sound velocity and density of core‐forming liquids: Implication to core compositions of terrestrial planets. Journal of Geophysical Research: Planets, 124(8), pp.2272-2293.

Thompson, E.C., Davis, A.H., Bi, W., Zhao, J., Alp, E.E., Zhang, D., Greenberg, E., Prakapenka, V.B. and Campbell, A.J., 2018. High‐pressure geophysical properties of Fcc phase FeHx. Geochemistry, Geophysics, Geosystems, 19(1), pp.305-314.

Tsujino, N., Nishihara, Y., Nakajima, Y., Takahashi, E., Funakoshi, K.I. and Higo, Y., 2013. Equation of state of γ-Fe: Reference density for planetary cores. Earth and Planetary Science Letters, 375, pp.244-253.

Urakawa, S., Someya, K., Terasaki, H., Katsura, T., Yokoshi, S., Funakoshi, K.I., Utsumi, W., Katayama, Y., Sueda, Y.I. and Irifune, T., 2004. Phase relationships and equations of state for FeS at high pressures and temperatures and implications for the internal structure of Mars. Physics of the Earth and Planetary Interiors, 143, pp.469-479.

Wagle, F. and Steinle‐Neumann, G., 2019. Liquid iron equation of state to the terapascal regime from *ab initio* simulations. Journal of Geophysical Research: Solid Earth, 124(4), pp.3350-3364.

Walder, P. and Pelton, A.D., 2005. Thermodynamic modeling of the Fe-S system. Journal of phase equilibria and diffusion, 26, pp.23-38.

Wang, Y., Rivers, M., Sutton, S., Nishiyama, N., Uchida, T. and Sanehira, T., 2009. The large-volume high-pressure facility at GSECARS: A “Swiss-army-knife” approach to synchrotron-based experimental studies. Physics of the Earth and Planetary Interiors, 174(1-4), pp.270-281.

Wang, Y., Uchida, T., Von Dreele, R., Rivers, M.L., Nishiyama, N., Funakoshi, K.I., Nozawa, A. and Kaneko, H., 2004. A new technique for angle-dispersive powder diffraction using an energy-dispersive setup and synchrotron radiation. Journal of applied crystallography, 37(6), pp.947-956.

Wänke, H. and Dreibus, G., 1994. Chemistry and accretion history of Mars. Philosophical Transactions of the Royal Society of London. Series A: Physical and Engineering Sciences, 349(1690), pp.285-293.

Wasson, J. T., and Kallemeyn, G. W., 1988 Compositions of Chondrites. Phil. Trans. R. Soc. Lond. A, 325

Watanabe, M., Adachi, M. and Fukuyama, H., 2016. Densities of Fe–Ni melts and thermodynamic correlations. Journal of materials science, 51, pp.3303-3310.

Williams, Q. and Jeanloz, R., 1990. Melting relations in the iron‐sulfur system at ultra‐high pressures: Implications for the thermal state of the Earth. Journal of Geophysical Research: Solid Earth, 95(B12), pp.19299-19310.

Xie, L., Yoneda, A., Liu, Z., Nishida, K. and Katsura, T., 2020. Boron-doped diamond synthesized by chemical vapor deposition as a heating element in a multi-anvil apparatus. High Pressure Research, 40(3), pp.369-378.

Xu, F., Morard, G., Guignot, N., Rivoldini, A., Manthilake, G., Chantel, J., Xie, L., Yoneda, A., King, A., Boulard, E. and Pandolfi, S., 2021. Thermal expansion of liquid Fe-S alloy at high pressure. Earth and Planetary Science Letters, 563, p.116884.

Xu, M., Jing, Z., Chantel, J., Jiang, P., Yu, T. and Wang, Y., 2018. Ultrasonic velocity of diopside liquid at high pressure and temperature: Constraints on velocity reduction in the upper mantle due to partial melts. Journal of Geophysical Research: Solid Earth, 123(10), pp.8676-8690.

Yoshizaki, T. and McDonough, W.F., 2020. The composition of Mars. Geochimica et Cosmochimica Acta, 273, pp.137-162.

# Appendix B. Supplementary Material for

## The Influence of Sulfur on the Elastic Properties of the Martian Core

### Supplementary Text 5.S1.

*Starting material syntheses using piston-cylinder press*

For the synthesis of Fe-FeS hot-pressed cylinders, Fe powder (<10 µm, 99.9%, Alfa-Aesar) and sulfur chips (99.995%, Chempur) were weighed and ground together in an agate mortar with ethanol for over 30 minutes to ensure homogeneity. The mixture was then dried in an oven at 70°C for more than 6 hours. The Fe-S powder was first loaded into corundum tubes with inner diameters (ID) of either 1.0 mm or 0.6 mm and approximately 1 mm in height. These corundum tubes, containing the Fe-S powder, were placed inside gold (Au) capsules with an outer diameter (OD) of 5 mm and an ID of 4.8 mm, and the surrounding space was filled with Fe-S powder of the same composition. Syntheses in the piston-cylinder (PC) press were conducted using the standard “3/4-inch” assemblies at the Bayerisches Geoinstitut (BGI), heating the samples at 0.5–0.7 GPa and 1000 K for over 6 hours. After cooling and decompression, the samples were recovered by breaking the corundum tubes. The sides of the resulting sintered samples were molded by the inner walls of the $Al_2O_3$ tube into cylindrical forms, although the top and bottom remained irregular. The samples were then double-side polished, resulting in regular cylinders with flat, parallel top and bottom surfaces perpendicular to the cylindrical sides.

**Supplementary Text 5.S2.**

*Summary of equations for thermodynamic modeling of end members*

The thermodynamic modeling of the endmember phases in this study is based on the equation of state framework established by Stixrude and Lithgow-Bertelloni (2005, 2011, 2024), along with the references cited therein.

The Helmholtz free energy, $F(V,T)$, is expressed as:

$$F(V,T) = F_0 + F_c(V) + [F_{th}(V,T) - F_{th}(V,T_0)] + [F_{el}(V,T) - F_{el}(V,T_0)] \qquad (5.S2.1)$$

where $F_0$ is the Helmholtz free energy of a reference state, and $F_c$, $F_{th}$, and $F_{el}$ are the contributions from cold compression, thermal lattice vibrations, and thermal excitation of electrons, respectively. The calculation of $F_c$ is based on Birch's finite strain theory:

$$F_c(V) = \frac{9}{2}K_{T0}V_0[f^2 + (K_T' - 4)f^3] \qquad (5.S2.2)$$

where $V_0$ is the volume at ambient pressure and reference temperature ($T_0$), $K_{T0}$ is the isothermal bulk modulus at the reference temperature ($T_0$), and $K_T'$ is its pressure derivative. The scalar part of the Eulerian finite strain, $f$, is expressed as:

$$f = \frac{1}{2}\left[\left(\frac{V_0}{V}\right)^{2/3} - 1\right] \qquad (5.S2.3)$$

The thermal contribution to the Helmholtz free energy $F_{th}(V,T)$ is expressed based on the Debye free energy function:

$$F_{th}(V,T) = 9nRT\left(\frac{\theta}{T}\right)^{-3}\int_0^{\theta/T} \ln[1 - exp(-x)]\, x^2 dx \qquad (5.S2.4)$$

where $n$ indicates the number of atoms in the chemical formula, $R$ is the ideal gas constant, and $\theta$ is the Debye temperature. $\theta$ varies with volume and is expressed as:

$$\theta^2 = \theta_0^2\left[1 + 6\gamma_0 f + \frac{1}{2}(-12\gamma_0 + 36\gamma_0{}^2 - 18q_0\gamma_0)f^2)\right] \quad (5.\mathrm{S}2.5)$$

where $\gamma_0$ and $q_0$ are the first and second logarithmic volume derivatives of the Debye temperature.

The electronic term $F_{el}$ is considered only for the metallic Fe phases (BCC, FCC, and liquid Fe) in this study,

$$F_{el}(V,T) = -\frac{1}{2}\beta_{el}(V)T^2 \quad (5.\mathrm{S}2.6)$$

with

$$\beta_{el}(V) = \beta_{el0}\left(\frac{V}{V_0}\right)^{\gamma_{el}} \quad (5.\mathrm{S}2.7)$$

Based on the established $F(V,T)$ expression, the P-V-T equation of state can be obtained by taking the partial derivative of $F$ with respect to volume.

$$P(V,T) = -\left(\frac{\partial F}{\partial V}\right)_T \quad (5.\mathrm{S}2.8)$$

The Gibbs free energy at a given P-T can then be obtained using the relation:

$$G(P,T) = F(V,T) + PV \quad (5.\mathrm{S}2.9)$$

Following Evans et al. (2010), the second-order phase transition from FeS IV to FeS V is treated using the tricritical Landau model. When the temperature is lower than the critical temperature ($T_c$), the contribution of the Landau transition to the Gibbs free energy $G_L$ and volume $V_{ex}$ are given by

$$G_L = S_D\left[(T - T_c)Q^2 + \frac{1}{3}T_{c0}Q^6\right] \quad (5.\mathrm{S}2.10)$$

$$V_{ex} = V_D(1 - Q^2) \quad (5.\mathrm{S}2.11)$$

where $V_D$ and $S_D$ are the maximum excess volume and maximum excess entropy, respectively. The macroscopic order parameter Q is expressed as

$$Q = \left(1 - \frac{T}{T_c}\right)^{1/4} \qquad (5.S2.12)$$

and

$$T_c = T_{c0} + \frac{V_D}{S_D} P \qquad (5.S2.13)$$

where $S_D$ is the maximum excess entropy. When $T \geq T_c$, $G_L = 0$ and $V_{ex} = V_D$.

Therefore, for the solid FeS phase, the Gibbs free energy is expressed as

$$G_{total}(P,T) = G(P,T) + G_L(P,T) \qquad (5.S2.14)$$

and the volume of the solid FeS phase is expressed as

$$V_{total} = V(P,T) + V_{ex}(P,T) \qquad (5.S2.15)$$

## Supplementary Text 5.S3.

## Thermodynamic modeling of the spin transition in solid FeS

In order to constrain properties of liquid FeS from its melting curve, we need a thermodynamic model for the solid FeS phases. In this study, the high-spin (HS) and low-spin (LS) states of NiAs-type FeS phases are treated as two separate end members each with their own equation of state properties. The gradual spin transition at high pressure and high temperature observed in experiments is modeled as a progressive change in the fraction of the LS component ($x_{LS}$) within the HS-LS FeS solid solution. The Gibbs free energy of the HS-LS FeS solid solution, $G_{FeS_S}$, is expressed as

$$G_{FeS_S}(P,T) = (1-x)G_{FeS_{HS}}(P,T) + xG_{FeS_{LS}}(P,T) + S_{conf}T + G_{XS}(T) \qquad (5.S3.1)$$

where $G_{FeS_{HS}}$ and $G_{FeS_{LS}}$ are the Gibbs free energy of HS and LS FeS, respectively. The configuration entropy of mixing, $S_{conf}$, is expressed as

$$S_{conf} = x_{LS}Rln(x_{LS}) + (1 - x_{LS})Rln(1 - x_{LS}) \tag{5.S3.2}$$

and the excess energy of mixing, $G_{XS}$, is modeled using a symmetrical Margules model

$$G_{XS}(T) = x(1 - x_{LS})W \tag{5.S3.3}$$

where $W$ is the Margules parameter, which is fitted to be 1.1 kJ/mol, and is assumed to remain constant across different pressures and temperatures.

Under thermodynamic equilibrium, the parameter $x_{LS}$ in $G_{FeS_S}(P,T)$ at a given P-T condition can be determined by minimizing $G_{FeS_S}(P,T)$ with $x_{LS}$. Once $x_{LS}$ is solved, the volume of the HS-LS FeS solid solution is calculated as

$$V_{FeS_S} = (1 - x)V_{FeS_{HS}} + xV_{FeS_{LS}} \tag{5.S3.4}$$

or

$$V_{FeS_S} = \left(\frac{\partial G_{FeS_S}}{\partial P}\right)_T \tag{5.S3.5}$$

Thermodynamic parameters for the solid FeS phases were evaluated in this study. The properties of the HS and LS FeS end members, along with the mixing parameters, were fitted simultaneously to match the thermochemical properties of FeS at ambient pressure (Evans et al., 2010 and references therein) and the experimentally measured volumes from this study and from the literature (Urakawa et al., 2004; Kusaba et al., 1998; Tenailleau et al., 2005; Selivanov et al., 2003). The resulting model, with parameters listed in Table 5.2, matches the experimental observations under ambient conditions and successfully describes the abnormal compression behavior observed at high pressure (Fig. 5.S6).

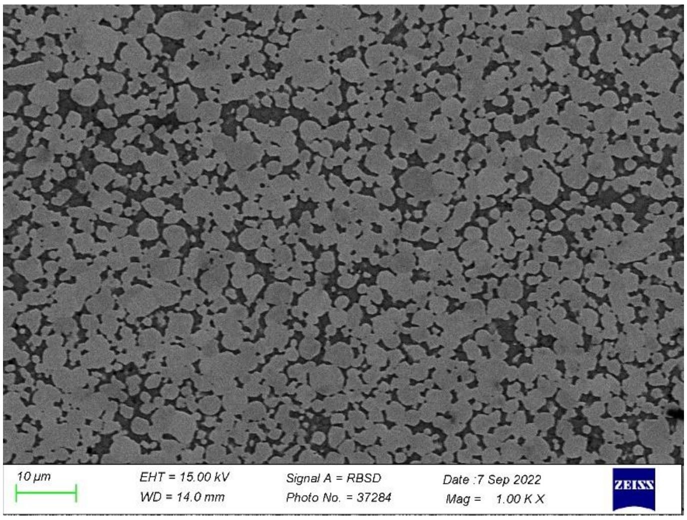

**Figure. 5.S1.** An example of the texture of the Fe-S starting material synthesized using a piston-cylinder press. The grey and black regions in the backscattered electron image are metallic Fe and troilite (FeS), respectively. The bulk composition is approximately Fe-6 wt.% S, used in runs MA234 and MA235.

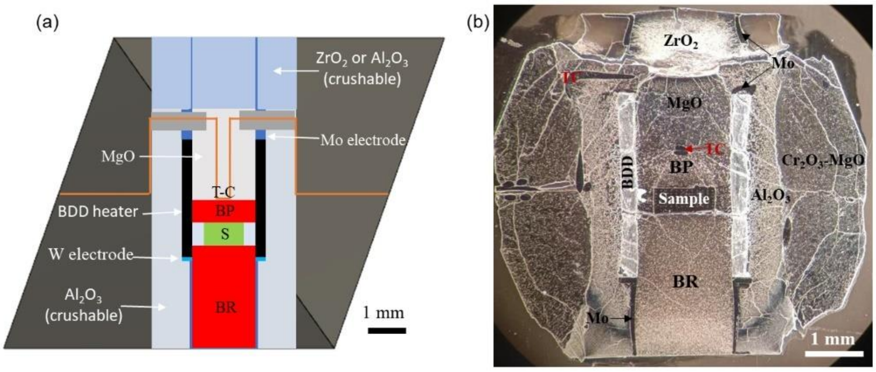

**Figure. 5.S2.** A schematic of the design (a) and an optical microscope reflected light image of the recovered high-pressure ultrasonic assembly. “BR” refers to the buffer rod, “BP” to the backing plate, “S” to the sample, “T-C” to the thermocouple, and “BDD” to boron-doped diamond.

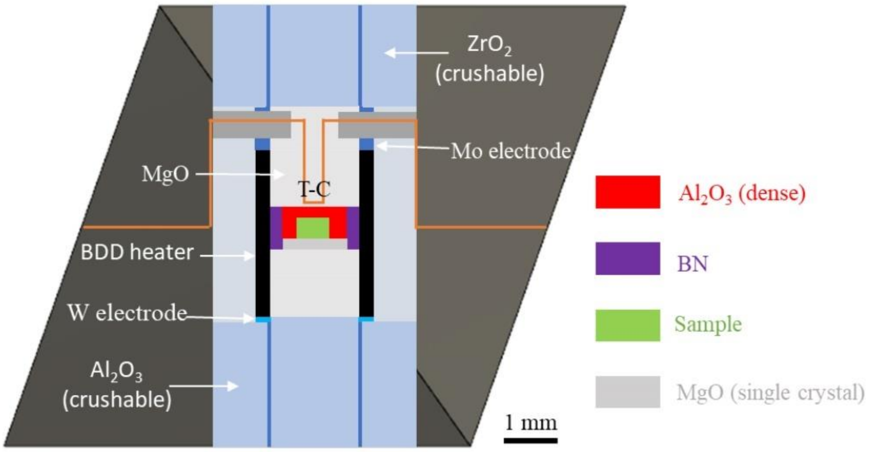

**Figure. 5.S3.** A schematic of the assembly for X-ray absorption measurements using the Beer-Lambert method. “T-C” refers to the thermocouple and “BDD” to boron-doped diamond.

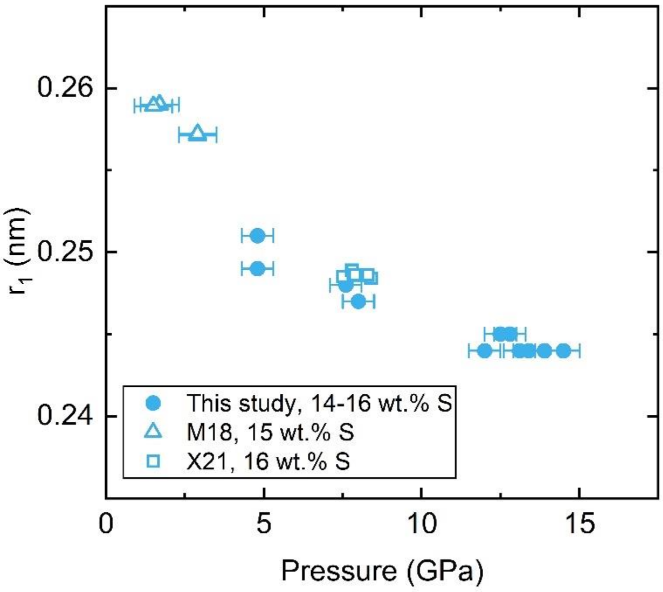

**Figure. 5.S4.** The change of positions of the first sharp peak in the radial distribution functions ($r_1$) with pressure. The compositions of the melts are Fe-S alloys with 14-16 wt.% S. The solid circles represent the results from this study. 'M18' refers to data from Morard et al. (2018), 'X21' to Xu et al. (2021).

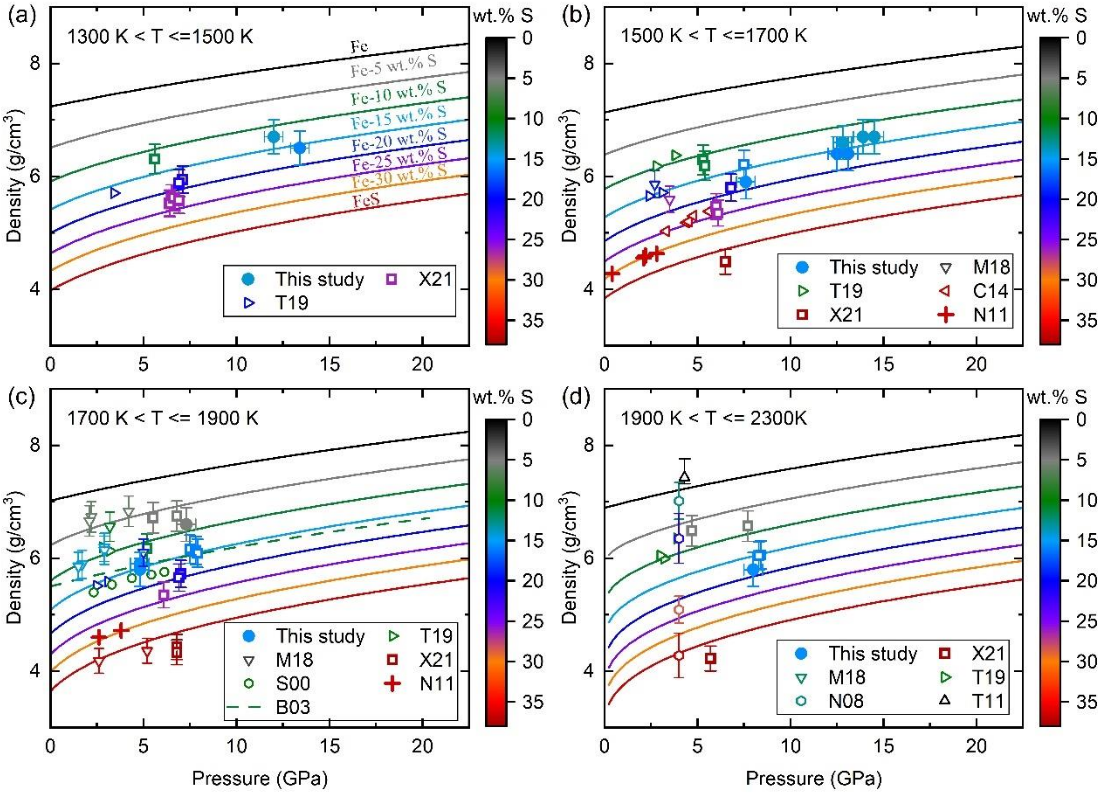

**Figure. 5.S5.** Comparison between model densities determined in this study with experimental results from various studies at temperatures between 1300 and 1500 K (a), 1500 and 1700 K (b), 1700 and 1900 K (c), and 1900 and 2300 K (d). The solid circles indicate experimental data from this study. 'X21' refers to data from Xu et al. (2021), 'T19' to Terasaki et al. (2019), 'M18' to Morard et al. (2018), 'C14' to Chen et al. (2014), 'N11' to Nishida et al. (2011), 'S00' to Sanloup et al. (2000), 'N08' to Nishida et al. (2008), and 'T11' to Tateyama et al. (2011). 'B03' indicates the equation of state for Fe-10 wt.% S from Balog et al. (2003). T19 provides experimental data from the Fe-Ni-S system, while the others report data from the Fe-S system. The solid curves in (a), (b), (c), and (d) are generated at 1400 K, 1600 K, 1800 K, and 2000 K, respectively, using the thermodynamic model from this study. Sulfur concentrations in the melt are indicated by the symbol colors, as shown in the color bar.

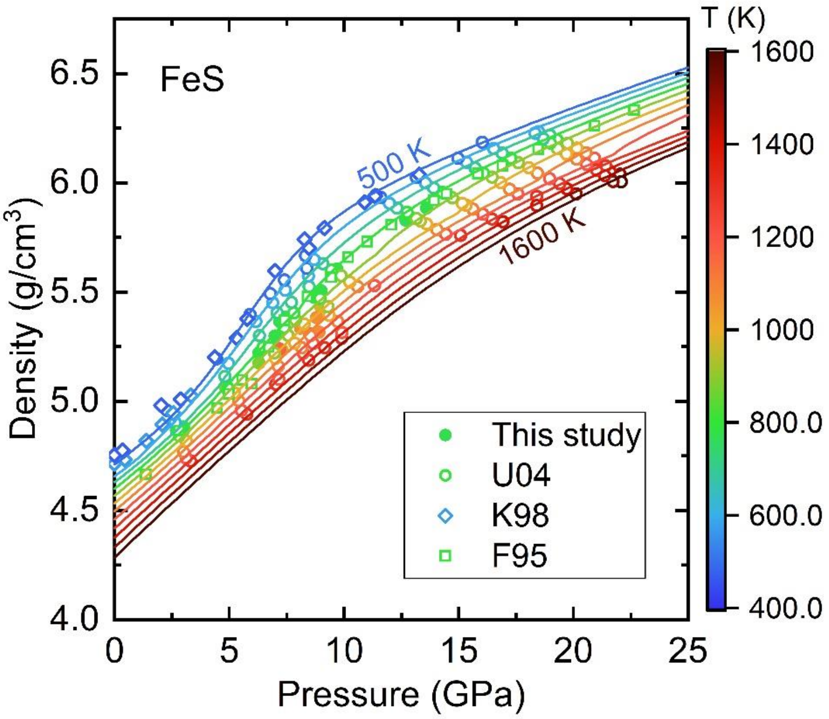

**Figure. 5.S6.** Equation of state of the solid FeS polymorphs, FeS IV and FeS V. The solid curves are generated using the thermodynamic model derived in this study. The solid circles show data from this study. 'U04' refers to data from Urakawa et al. (2004), 'K98' to Kusaba et al. (1998), 'F95' to Fei et al. (1995). Temperatures are indicated by the symbol colors, as shown in the color bar. The spin transition creates the strong curvature observed below 10 GPa, mainly at temperatures < 800 K because at higher temperatures the transformation occurs over a wide pressure range and is therefore less obvious. The Landau transition between IV and V phases can be observed as a kink in the isotherms visible mainly above 10 GPa.

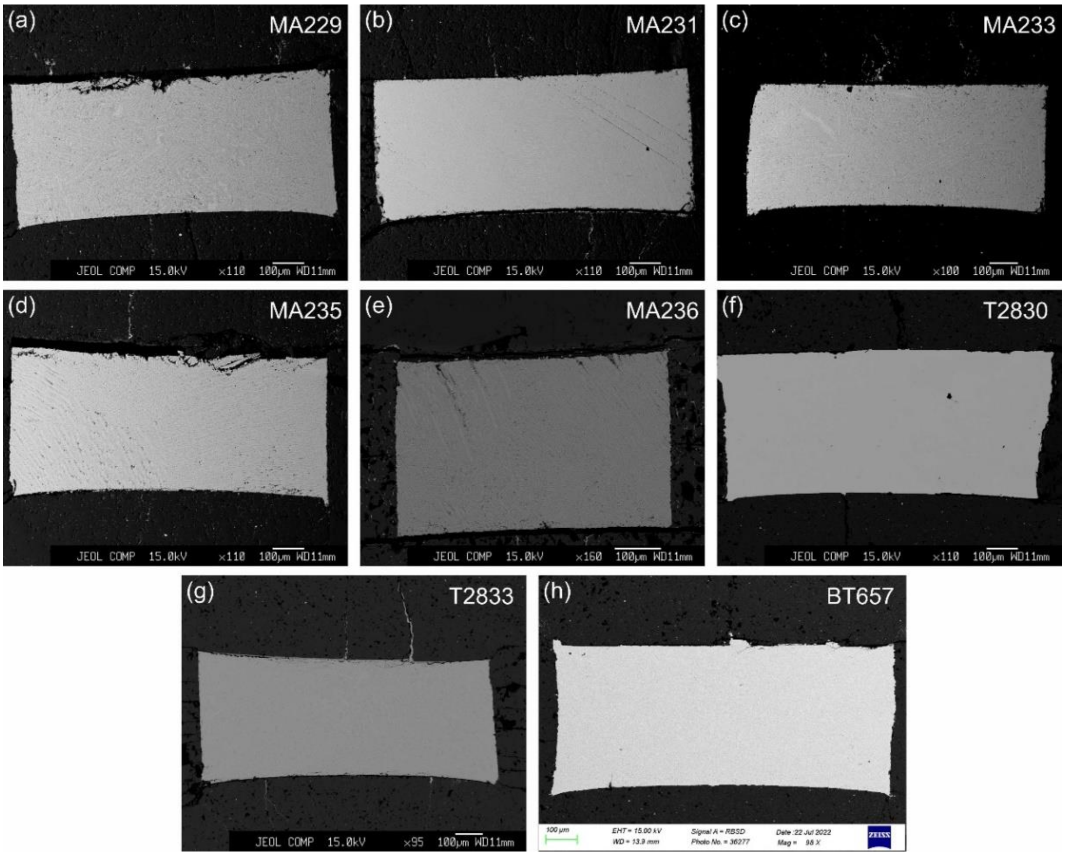

**Figure. 5.S7.** The back scattered electron images of the recovered samples of run MA229 (a), MA231 (b), MA233 (c), MA235 (d), MA236 (e), T2830 (f), T2883 (g), and BT657.

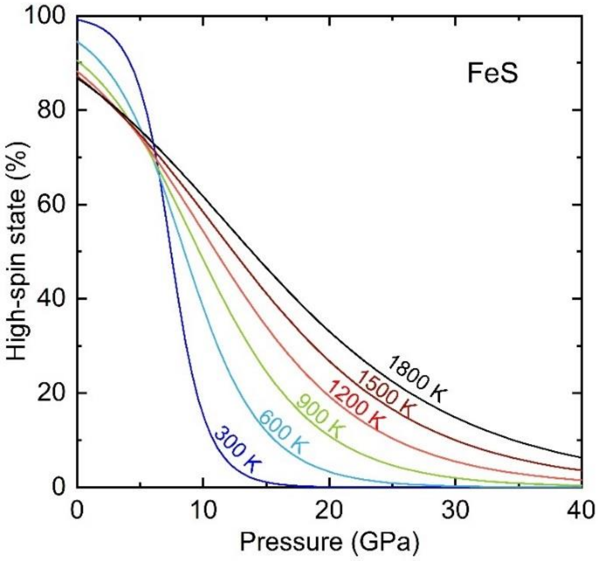

**Figure. 5.S8.** Spin transition of Fe in FeS IV and FeS V under high pressure. The curves are generated using the thermodynamic model developed in this study.

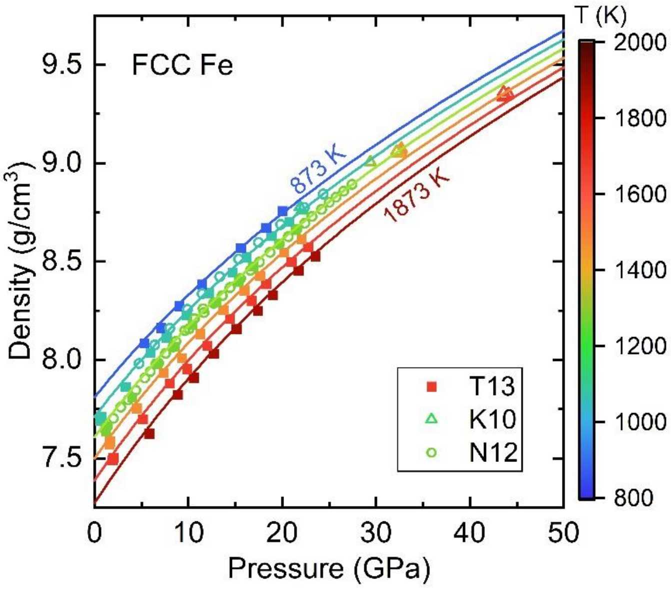

**Figure. 5.S9.** Equation of state of FCC Fe. The solid curves are generated using the thermodynamic model developed in this study. The data points from the literature (T13: Tsujino et al., 2013; K10: Komabayashi et al., 2010; N12: Nishihara et al., 2012) are plotted for comparison. Temperatures are indicated by the symbol colors, as shown in the color bar.

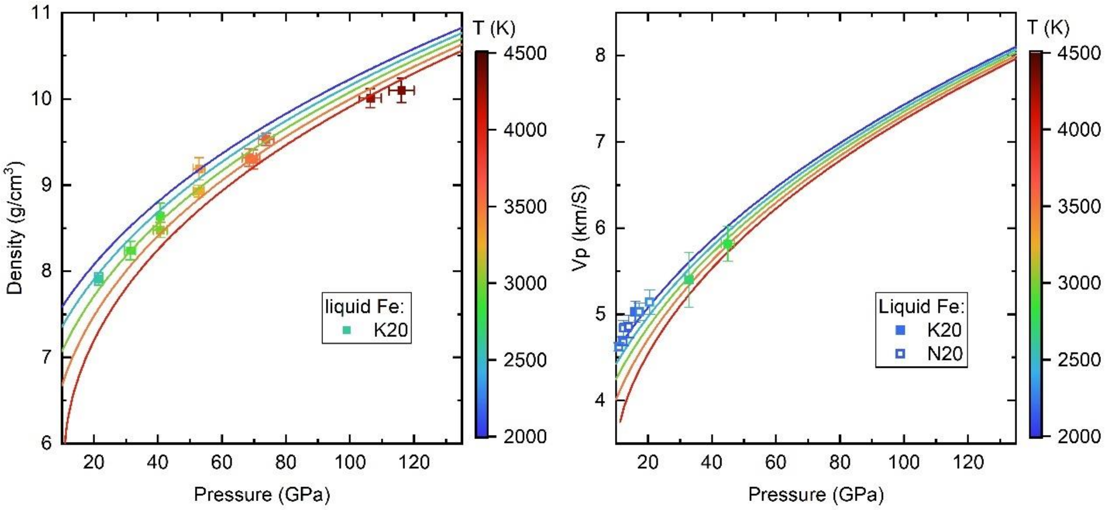

**Figure. 5.S10.** Comparison of the density (a) and longitudinal velocity (b) of liquid Fe derived from the thermodynamic model derived in this study (solid curves), compared with results from previous studies, up to 135 GPa. K20: Kuwayama et al., 2020; N20: Nishida et al., 2020.

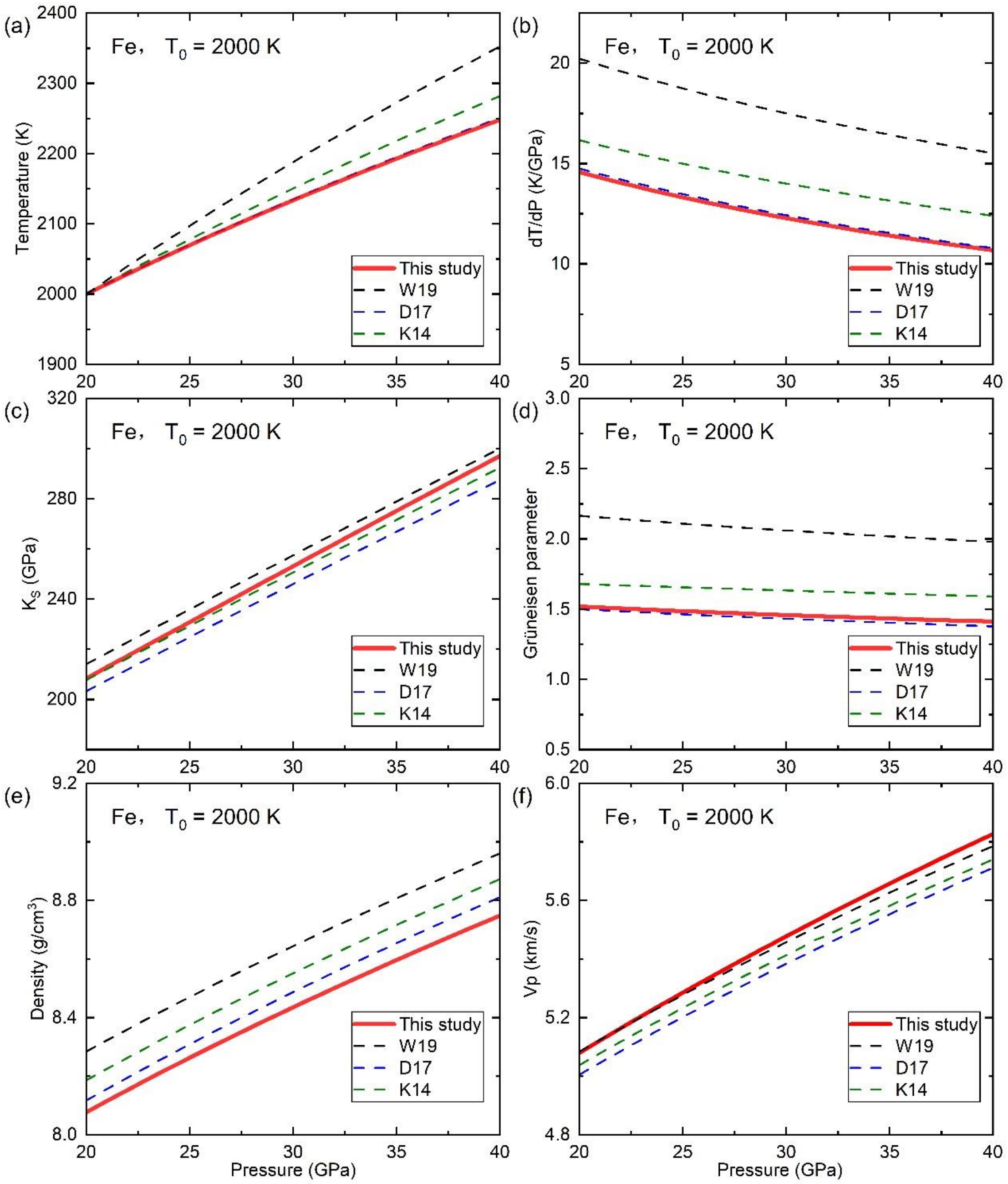

**Figure. 5.S11.** Comparison of the adiabatic properties of liquid Fe derived from the thermodynamic model (solid red curves) developed in this study with other models from the literature. W19: Wagle and Steinle-Neumann, 2019; D17: Dorogokupets et al., 2017; K14: Komabayashi, 2014. (a) Adiabatic temperature profiles of Fe with a reference temperature of 2000 K at 20 GPa. The slopes of the adiabatic temperature (b), adiabatic bulk moduli (c), Grüneisen parameters (d), densities (e), and sound velocities of liquid Fe are plotted along the temperature profiles shown in (a).

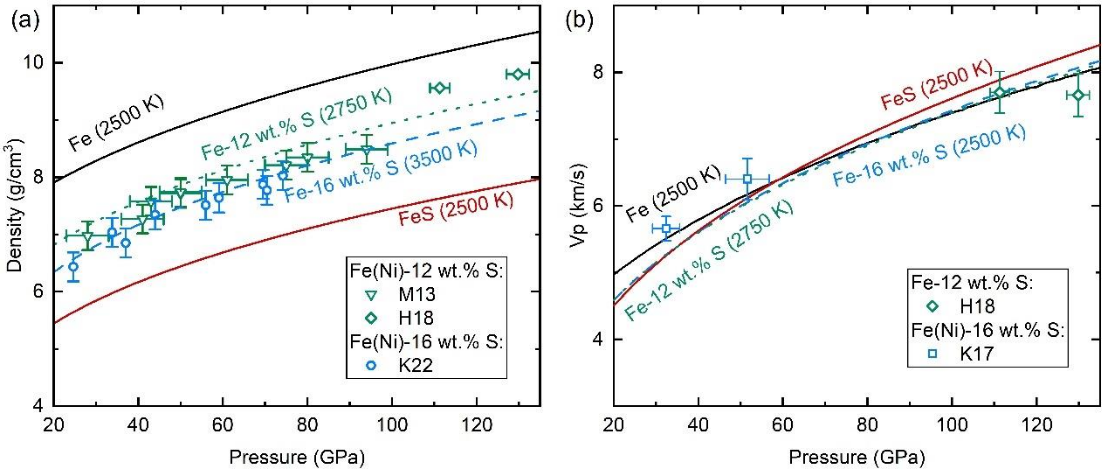

**Figure. 5.S12.** Comparisons of densities (a) and longitudinal velocities (b) of Fe-FeS melts calculated from the thermodynamic model with experimental data for the Fe(Ni)-S system from 20 to 135 GPa. The curves are generated from the model, with the corresponding temperatures and compositions labeled beside them. 'M13' refers to XRD results for Fe(Ni)-12 wt.% S from Morard et al. (2013) at temperatures between 2140 and 2830 K. 'H18' indicates dynamic compression results for Fe-11.8 wt.% S at temperatures from 2500 to 3130 K from Huang et al. (2018). 'K22' indicates XRD results for Fe(Ni)-16 wt.% S at temperatures from 3200 to 3700 K from Kawaguchi et al. (2022). 'K17' denotes IXS results for Fe(Ni)-16 wt.% S from Kawaguchi et al. (2017) at approximately 2500 K.

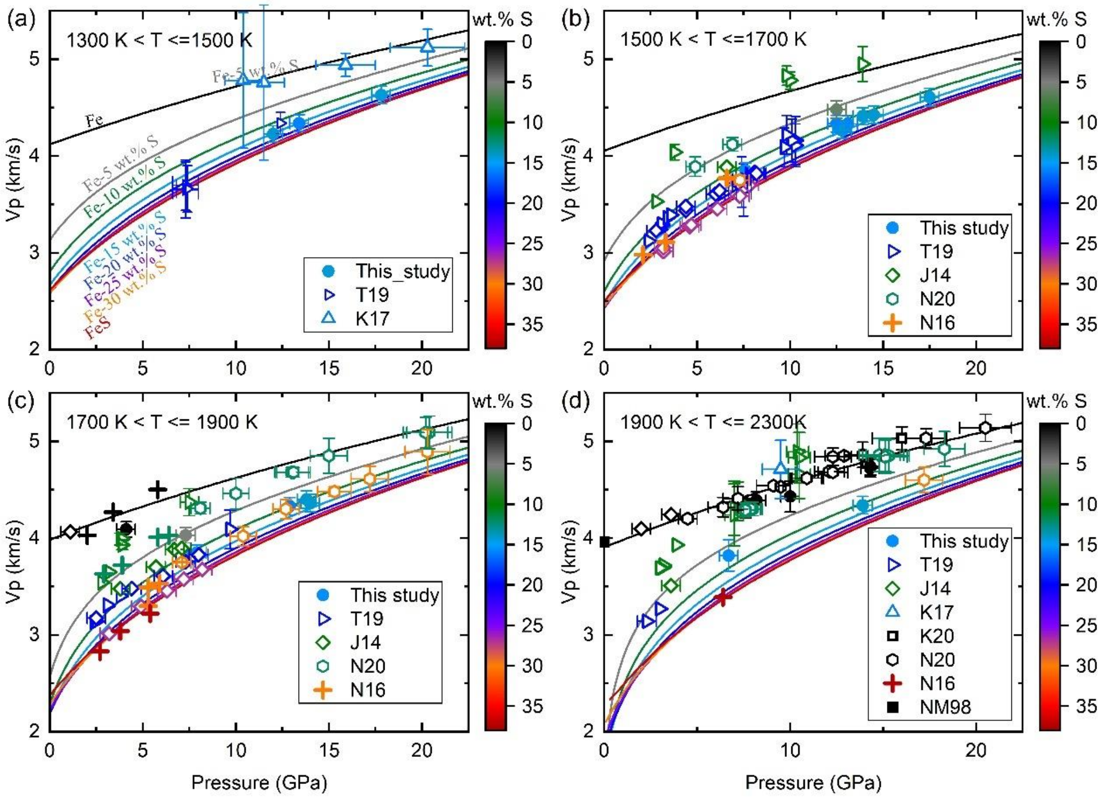

**Figure. 5.S13.** Comparison between longitudinal velocities for Fe-FeS melts calculated from the thermodynamic model with experimental results at temperatures of 1300–1500 K (a), 1500–1700 K (b), 1700–1900 K (c), and 1900–2300 K (d). Solid circles indicate experimental data from this study. 'T19' refers to Terasaki et al. (2019), 'K17' to Kawaguchi et al. (2017), 'J14' to Jing et al. (2014), 'N20' to Nishida et al. (2020), 'N16' to Nishida et al. (2016), 'K20' to Kuwayama et al. (2020), and 'NM98' to Nasch and Manghnani (1998). T19 and K17 provide experimental data from the Fe-Ni-S system, while the others report data from the Fe-S system. The solid curves in (a), (b), (c), and (d) were generated at 1400 K, 1600 K, 1800 K, and 2000 K, respectively, using the thermodynamic model from this study. Sulfur concentrations in the melt are indicated by the symbol colors, as shown in the color bar.

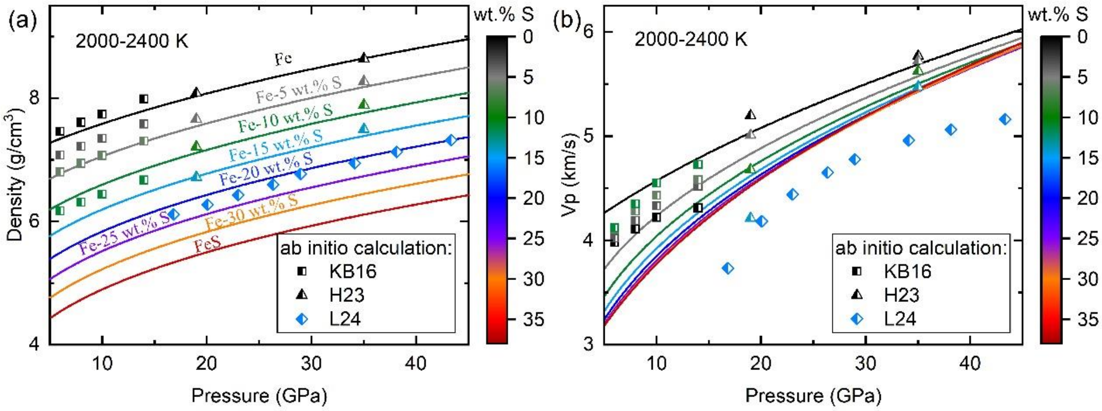

**Figure. 5.S14.** Comparison of densities (a) and longitudinal velocities (b) of Fe-FeS melts calculated from the thermodynamic model with results from ab initio calculations. 'KB16' refers to data at 2000 K from Kuskov and Belashchenko (2016), 'H23' to data at 2100 K and 2400 K from Huang et al. (2023), and 'L24' to data at 2000 K from Li et al. (2024). The solid curves were derived at 2000 K using the thermodynamic model from this study. Sulfur concentrations in the melt are indicated by the symbol colors, as shown in the color bar.

**Table 5.S1.** Chemical compositions, experimental conditions, and the fitting results of the XRD measurements on Fe-S liquids.

| **Run No.** | **Fe**[†] **(at. %)** | **S**[†] **(at. %)** | **P**[¶] **(GPa)** | **T**[¶] **(K)** | $r_1$[§] **(nm)** | **Density (atom/nm$^3$)** | **1 σ (atom/nm$^3$)** | **$\chi$2** |
|---|---|---|---|---|---|---|---|---|
| **MA229** | 75.8 | 24.2 | 7.6 | 1673 | 0.248 | 71.2 | 3 | 0.4 |
| | 75.8 | 24.2 | 8.0 | 1913 | 0.247 | 69.5 | 3 | 0.4 |
| **MA231** | 75.4 | 24.6 | 13.4 | 1490 | 0.244 | 78.1 | 3 | 0.6 |
| | 75.4 | 24.6 | 13.1 | 1573 | 0.244 | 76.6 | 3 | 1.9 |
| | 75.4 | 24.6 | 12.5 | 1523 | 0.245 | 76.8 | 3 | 1.7 |
| **MA233** | 77.6 | 22.4 | 14.5 | 1600 | 0.244 | 79.6 | 3 | 2.0 |
| | 77.6 | 22.4 | 13.9 | 1680 | 0.244 | 79.4 | 3 | 1.9 |
| | 77.6 | 22.4 | 12.0 | 1480 | 0.244 | 79.4 | 3 | 2.2 |
| | 77.6 | 22.4 | 12.8 | 1573 | 0.245 | 78.9 | 3 | 1.7 |
| **MA235** | 91.1 | 8.9 | 7.3 | 1873 | 0.249 | 73.6 | 3 | 0.4 |
| **MA236** | 75.8 | 24.2 | 4.8 | 1773 | 0.251 | 70.2 | 3 | 0.4 |
| | 75.8 | 24.2 | 4.8 | 1873 | 0.249 | 70.0 | 3 | 0.2 |

[†] The atomic percentages of Fe and S are normalized based on EPMA measurements from the recovered samples.

[¶] The overall uncertainties in pressure and temperature are estimated to be approximately 0.5 GPa and 50 K, respectively.

[§] $r_1$ represents the fitted position of the first sharp peak in the radial distribution function. The cutoff radius, $r_{min}$, was fixed at 0.192 nm for all fittings.

**Table 5.S2.** P-V-T relations of FeS IV

| No. | TC reading[†] (K) | T correction[†] (K) | Phase | $V_{Fe}$ (Å$^3$) | Pressure[¶] (GPa) | *a* (Å) | *c* (Å) | $V_{FeS}$ (Å$^3$) | $V_{FeS}$/Z[§] (Å$^3$) |
|---|---|---|---|---|---|---|---|---|---|
| MA229-08 | 773 | 9 | BCC, FeS IV | 22.97(1) | 7.4 | 6.725(2) | 5.538(2) | 216.9(2) | 27.11(3) |
| MA229-13 | 773 | 11 | FCC, FeS IV | 44.56(2) | 9.0 | 6.677(2) | 5.494(2) | 212.1(2) | 26.51(2) |
| MA231-05 | 773 | 9 | BCC, FeS IV | 22.99(1) | 7.2 | 6.732(2) | 5.545(2) | 217.7(2) | 27.21(2) |
| MA231-14 | 773 | 13 | HCP, FeS IV | 21.53(2) | 12.7 | 6.559(1) | 5.378(1) | 200.3(1) | 25.04(1) |
| MA233-05 | 773 | 9 | FCC, FeS IV | 44.97(1) | 7.4 | 6.732(1) | 5.542(1) | 217.5(1) | 27.19(1) |
| MA234-06 | 773 | 9 | FCC, FeS IV | 44.98(2) | 7.4 | 6.745(2) | 5.554(2) | 218.9(2) | 27.36(2) |
| MA234-16 | 773 | 14 | HCP, FeS IV | 21.44(5) | 13.6 | 6.535(3) | 5.366(2) | 198.4(2) | 24.81(3) |
| MA235-06 | 773 | 9 | FCC, FeS IV | 45.08(2) | 7.0 | 6.760(6) | 5.568(3) | 220.4(5) | 27.55(6) |
| MA235-11 | 773 | 10 | FCC, FeS IV | 44.65(2) | 8.7 | 6.688(1) | 5.505(1) | 213.2(1) | 26.66(1) |
| T2833-03 | 773 | 11 | FCC, FeS IV | 44.41(11) | 9.7 | 6.641(2) | 5.453(3) | 208.3(2) | 26.04(3) |

[†] Temperature corrections for the readings of type-D thermocouples at high pressures based on the empirical polynomial extrapolation from Nishihara et al. (2020).

[¶] Pressures were calculated using the equation of state of FCC Fe evaluated in this study or BCC and HCP Fe from Dorogokupets et al., 2017.

[§] The number of formula units per unit cell (Z) for FeS IV is 8.

**Table 5.S3.** P-V-T relations of FeS V

| **No.** | **TC reading**[†] **(K)** | **T correction**[†] **(K)** | **Phase** | $V_{Fe}$ **(Å$^3$)** | **Pressure**[¶] **(GPa)** | ***a*** **(Å)** | ***c*** **(Å)** | $V_{FeS}$ **(Å$^3$)** | $V_{FeS}/Z$[§] **(Å$^3$)** |
|---|---|---|---|---|---|---|---|---|---|
| MA229-16 | 973 | 15 | FCC, FeS V | 44.99(2) | 9.0 | 3.354(1) | 5.516(1) | 53.75(5) | 26.88(2) |
| MA229-17 | 1073 | 18 | FCC, FeS V | 45.27(2) | 8.8 | 3.363(1) | 5.536(1) | 54.23(4) | 27.12(2) |
| MA229-20 | 1173 | 20 | FCC, FeS V | 45.57(1) | 8.5 | 3.378(2) | 5.565(3) | 54.97(15) | 27.49(7) |
| MA230-12* | 773 | 4 | BCC, FeS V | 23.56(1) | 3.0 | 3.475(1) | 5.716(3) | 59.77(12) | 29.89(6) |
| MA230-17* | 773 | 8 | BCC, FeS V | 23.10(1) | 6.3 | 3.397(1) | 5.596(2) | 55.91(9) | 27.96(4) |
| MA230-19* | 873 | 10 | FCC, FeS V | 45.51(3) | 6.3 | 3.407(1) | 5.611(1) | 56.41(4) | 28.21(2) |
| MA230-20* | 973 | 13 | FCC, FeS V | 45.46(6) | 7.3 | 3.396(1) | 5.585(1) | 55.79(5) | 27.89(2) |
| MA230-21* | 1073 | 18 | FCC, FeS V | 45.25(7) | 8.9 | 3.377(1) | 5.561(2) | 54.92(6) | 27.46(3) |
| MA232-06 | 773 | 4 | BCC, FeS V | 23.60(1) | 2.7 | 3.476(2) | 5.732(3) | 59.98(15) | 29.99(7) |
| MA235-14 | 1073 | 17 | FCC, FeS V | 45.46(5) | 8.1 | 3.375(1) | 5.546(2) | 54.71(6) | 27.36(3) |
| MA235-15 | 1168 | 17 | FCC, FeS V | 45.94(10) | 7.2 | 3.393(3) | 5.587(10) | 55.71(32) | 27.86(16) |
| MA236-09 | 773 | 3 | BCC, FeS V | 23.67(4) | 2.2 | 3.477(3) | 5.732(5) | 60.03(20) | 30.01(10) |
| MA236-11 | 1023 | 7 | FCC, FeS V | 46.78(12) | 3.3 | 3.482(1) | 5.723(2) | 60.08(7) | 30.04(3) |
| MA236-15 | 1073 | 9 | FCC, FeS V | 46.81(17) | 3.6 | 3.475(1) | 5.719(2) | 59.82(7) | 29.91(3) |
| MA236-16 | 1173 | 10 | FCC, FeS V | 47.07(10) | 3.7 | 3.478(4) | 5.725(11) | 59.98(37) | 29.99(19) |

[†] Temperature corrections for the readings of type-D thermocouples at high pressures estimated based on the empirical polynomial extrapolation from Nishihara et al. (2020).

[¶] Pressures were calculated using the equation of state of FCC Fe evaluated in this study or BCC Fe from Dorogokupets et al.; 2017

[§] The number of formula units per unit cell (Z) for FeS V is 2.

[*] TC failed in run MA230, and the temperatures were estimated based on the power-temperature relation established in other experiments.

**Table 5.S4.** Chemical composition of the recovered samples

| Run No. | Fe (wt.%) | S (wt.%) | O (wt.%) | Total (wt.%) |
|---|---|---|---|---|
| MA229 | 83.3(4) | 15.3(2) | 0.6(1) | 99.2(5) |
| MA231 | 83.4(2) | 15.7(1) | 0.2(1) | 99.3(1) |
| MA233 | 84.6(2) | 14.0(1) | 0.5(1) | 99.1(1) |
| MA235 | 93.3(4) | 5.2(2) | 0.6(1) | 99.2(3) |
| MA236 | 83.1(3) | 15.2(2) | 0.4(1) | 98.7(1) |
| T2830 | 98.9(3) | 0.0(0) | 0.2(1) | 99.2(3) |
| T2833 | 84.5(1) | 14.1(1) | 0.6(1) | 99.2(1) |
| BT657 | 98.6(2) | 0.0(0) | 0.2(1) | 98.9(2) |

## Supplemental References

Balog, P.S., Secco, R.A., Rubie, D.C. and Frost, D.J., 2003. Equation of state of liquid Fe-10 wt% S: Implications for the metallic cores of planetary bodies. Journal of Geophysical Research: Solid Earth, 108(B2).

Chen, J., Yu, T., Huang, S., Girard, J. and Liu, X., 2014. Compressibility of liquid FeS measured using X-ray radiograph imaging. Physics of the Earth and Planetary Interiors, 228, pp.294-299.

Dorogokupets, P.I., Dymshits, A.M., Litasov, K.D. and Sokolova, T.S., 2017. Thermodynamics and equations of state of iron to 350 GPa and 6000 K. Scientific reports, 7(1), p.41863.

Evans, K. A., R. Powell, and T. J. B. Holland. "Internally consistent data for sulphur-bearing phases and application to the construction of pseudosections for mafic greenschist facies rocks in $Na_2O$–CaO–$K_2O$–FeO–MgO–$Al_2O_3$–$SiO_2$–$CO_2$–O–S–$H_2O$." Journal of Metamorphic Geology 28, no. 6 (2010): 667-687.

Fei, Y., Prewitt, C.T., Mao, H.K. and Bertka, C.M., 1995. Structure and density of FeS at high pressure and high temperature and the internal structure of Mars. Science, 268(5219), pp.1892-1894.

Huang, D., Li, Y., Khan, A., Sossi, P., Giardini, D. and Murakami, M., 2023. Thermoelastic properties of liquid Fe-rich alloys under Martian core conditions. Geophysical Research Letters, 50(6), p.e2022GL102271.

Huang, H., Leng, C., Wang, Q., Yang, G., Hu, X., Wu, Y., Liu, X. and Fei, Y., 2018. Measurements of sound velocity of liquid Fe-11.8 wt% S up to 211.4 GPa and 6150 K. Journal of Geophysical Research: Solid Earth, 123(6), pp.4730-4739.

Jing, Z., Wang, Y., Kono, Y., Yu, T., Sakamaki, T., Park, C., Rivers, M.L., Sutton, S.R. and Shen, G., 2014. Sound velocity of Fe–S liquids at high pressure: Implications for the Moon's molten outer core. Earth and Planetary Science Letters, 396, pp.78-87.

Kawaguchi, S.I., Morard, G., Kuwayama, Y., Hirose, K., Hirao, N. and Ohishi, Y., 2022. Density determination of liquid iron-nickel-sulfur at high pressure. American Mineralogist, 107(7), pp.1254-1261.

Kawaguchi, S.I., Nakajima, Y., Hirose, K., Komabayashi, T., Ozawa, H., Tateno, S., Kuwayama, Y., Tsutsui, S. and Baron, A.Q., 2017. Sound velocity of liquid Fe-Ni-S at high pressure. Journal of Geophysical Research: Solid Earth, 122(5), pp.3624-3634.

Komabayashi, T. and Fei, Y., 2010. Internally consistent thermodynamic database for iron to the Earth's core conditions. Journal of Geophysical Research: Solid Earth, 115(B3).

Komabayashi, T., 2014. Thermodynamics of melting relations in the system Fe-FeO at high pressure: Implications for oxygen in the Earth's core. Journal of Geophysical Research: Solid Earth, 119(5), pp.4164-4177.

Kusaba, K., Syono, Y., Kikegawa, T. and Shimomura, O., 1998. High pressure and temperature behavior of FeS. Journal of Physics and Chemistry of Solids, 59(6-7), pp.945-950.

Kuskov, O.L. and Belashchenko, D.K., 2016. Thermodynamic properties of Fe-S alloys from molecular dynamics modeling: Implications for the lunar fluid core. Physics of the Earth and Planetary Interiors, 258, pp.43-50.

Kuwayama, Y., Morard, G., Nakajima, Y., Hirose, K., Baron, A.Q., Kawaguchi, S.I., Tsuchiya, T., Ishikawa, D., Hirao, N. and Ohishi, Y., 2020. Equation of state of liquid iron under extreme conditions. Physical Review Letters, 124(16), p.165701.

Li, W.J., Li, Z., Ma, Z., Zhou, J., Wang, C. and Zhang, P., 2024. Thermoelastic properties and thermal evolution of the Martian core from ab initio calculated magnetic Fe-S liquid. Journal of Geophysical Research: Planets, 129(4), p.e2023JE007874.

Morard, G., Bouchet, J., Rivoldini, A., Antonangeli, D., Roberge, M., Boulard, E., Denoeud, A. and Mezouar, M., 2018. Liquid properties in the Fe-FeS system under moderate pressure: Tool box to model small planetary cores. American Mineralogist, 103(11), pp.1770-1779.

Morard, G., Siebert, J., Andrault, D., Guignot, N., Garbarino, G., Guyot, F. and Antonangeli, D., 2013. The Earth's core composition from high pressure density measurements of liquid iron alloys. Earth and Planetary Science Letters, 373, pp.169-178.

Nasch, P.M. and Manghnani, M.H., 1998. Molar volume, thermal expansion, and bulk modulus in liquid Fe-Ni alloys at 1 bar: Evidence for magnetic anomalies?. Geophysical Monograph Series, 101, pp.307-317.

Nishida, K., Ohtani, E., Urakawa, S., Suzuki, A., Sakamaki, T., Terasaki, H. and Katayama, Y., 2011. Density measurement of liquid FeS at high pressures using synchrotron X-ray absorption. American Mineralogist, 96(5-6), pp.864-868.

Nishida, K., Shibazaki, Y., Terasaki, H., Higo, Y., Suzuki, A., Funamori, N. and Hirose, K., 2020. Effect of sulfur on sound velocity of liquid iron under Martian core conditions. Nature communications, 11(1), p.1954.

Nishida, K., Suzuki, A., Terasaki, H., Shibazaki, Y., Higo, Y., Kuwabara, S., Shimoyama, Y., Sakurai, M., Ushioda, M., Takahashi, E. and Kikegawa, T., 2016. Towards a consensus on the pressure and composition dependence of sound velocity in the liquid Fe–S system. Physics of the Earth and Planetary Interiors, 257, pp.230-239.

Nishida, K., Terasaki, H., Ohtani, E. and Suzuki, A., 2008. The effect of sulfur content on density of the liquid Fe–S at high pressure. Physics and Chemistry of Minerals, 35, pp.417-423.

Nishihara, Y., Doi, S., Kakizawa, S., Higo, Y. and Tange, Y., 2020. Effect of pressure on temperature measurements using WRe thermocouple and its geophysical impact. Physics of the Earth and Planetary Interiors, 298, p.106348.

Nishihara, Y., Nakajima, Y., Akashi, A., Tsujino, N., Takahashi, E., Funakoshi, K.I. and Higo, Y., 2012. Isothermal compression of face-centered cubic iron. American Mineralogist, 97(8-9), pp.1417-1420.

Sanloup, C., Guyot, F., Gillet, P., Fiquet, G., Mezouar, M. and Martinez, I., 2000. Density measurements of liquid Fe-S alloys at high-pressure. Geophysical Research Letters, 27(6), pp.811-814.

Selivanov, E.N., Vershinin, A.D. and Gulyaeva, R.I., 2003. Thermal expansion of troilite and pyrrhotine in helium and air. Inorganic materials, 39, pp.1097-1102.

Stixrude, L. and Lithgow-Bertelloni, C., 2005. Thermodynamics of mantle minerals—I. Physical properties. Geophysical Journal International, 162(2), pp.610-632.

Stixrude, L. and Lithgow-Bertelloni, C., 2011. Thermodynamics of mantle minerals-II. Phase equilibria. Geophysical Journal International, 184(3), pp.1180-1213.

Stixrude, L. and Lithgow-Bertelloni, C., 2024. Thermodynamics of mantle minerals–III: the role of iron. Geophysical Journal International, 237(3), pp.1699-1733.

Tateyama, R., Ohtani, E., Terasaki, H., Nishida, K., Shibazaki, Y., Suzuki, A. and Kikegawa, T., 2011. Density measurements of liquid Fe–Si alloys at high pressure using the sink–float method. Physics and Chemistry of Minerals, 38, pp.801-807.

Tenailleau, C., Etschmann, B., Wang, H., Pring, A., Grguric, B.A. and Studer, A., 2005. Thermal expansion of troilite and pyrrhotite determined by in situ cooling (873 to 373 K) neutron powder diffraction measurements. Mineralogical Magazine, 69(2), pp.205-216.

Terasaki, H., Rivoldini, A., Shimoyama, Y., Nishida, K., Urakawa, S., Maki, M., Kurokawa, F., Takubo, Y., Shibazaki, Y., Sakamaki, T. and Machida, A., 2019. Pressure and composition effects on sound velocity and density of core-forming liquids: Implication to core compositions of terrestrial planets. Journal of Geophysical Research: Planets, 124(8), pp.2272-2293.

Tsujino, N., Nishihara, Y., Nakajima, Y., Takahashi, E., Funakoshi, K.I. and Higo, Y., 2013. Equation of state of γ-Fe: Reference density for planetary cores. Earth and Planetary Science Letters, 375, pp.244-253.

Urakawa, S., Someya, K., Terasaki, H., Katsura, T., Yokoshi, S., Funakoshi, K.I., Utsumi, W., Katayama, Y., Sueda, Y.I. and Irifune, T., 2004. Phase relationships and equations of state for FeS at high pressures and temperatures and implications for the internal structure of Mars. Physics of the Earth and Planetary Interiors, 143, pp.469-479.

Wagle, F. and Steinle-Neumann, G., 2019. Liquid iron equation of state to the terapascal regime from ab initio simulations. Journal of Geophysical Research: Solid Earth, 124(4), pp.3350-3364.

Xu, F., Morard, G., Guignot, N., Rivoldini, A., Manthilake, G., Chantel, J., Xie, L., Yoneda, A., King, A., Boulard, E. and Pandolfi, S., 2021. Thermal expansion of liquid Fe-S alloy at high pressure. Earth and Planetary Science Letters, 563, p.116884.

# 6 The structure and stability of $Fe_{4+x}S_3$ and its potential to form a Martian inner core

Lianjie Man[1] *, Xiang Li[2], Tiziana Boffa Ballaran[1], Wenju Zhou[3], Julien Chantel[4], Adrien Néri[1,4], Ilya Kupenko[2], Georgios Aprilis[2], Alexander Kurnosov[1], Olivier Namur[5], Michael Hanfland[2], Nicolas Guignot[6], Laura Henry[6], Leonid Dubrovinsky[1], Daniel. J. Frost[1]

[1]Bayerisches Geoinstitut, Universität Bayreuth, Bayreuth, Germany.

[2]ESRF-The European Synchrotron, Grenoble, France.

[3]Material Physics and Technology at Extreme Conditions, Laboratory of Crystallography, University of Bayreuth, Bayreuth, Germany.

[4]Univ. Lille, CNRS, INRAE, Centrale Lille, UMR 8207 - UMET - Unité Matériaux et Transformations, F-59000 Lille, France.

[5]Earth and Environmental Sciences, KU Leuven, 3001 Leuven, Belgium.

[6]Synchrotron SOLEIL, L'Orme de Merisiers, Saint Aubin-BP48, 91192 Gif-sur-Yvette, France.

***Corresponding author.**

E-mail address: lianjie.man@uni-bayreuth.de (L. Man).

This chapter has been published as: Man, L., Li, X., Boffa Ballaran, T., Zhou, W., Chantel, J., Néri, A., ... and Frost, D. J., 2025. The structure and stability of $Fe_{4+x}S_3$ and its potential to form a Martian inner core. Nature Communications, 16(1), 1710. DOI: https://doi.org/10.1038/s41467-025-56220-2

## Author contributions

L.M. conceived and designed this project. L.M., X.L., T.B.B., L.D., W.Z., J.C., A.N., I.K., G.A., A.K., M.H., N.G., L.H., and D.J.F. performed the experiments. W.Z., T.B.B., L.D., X.L., and L.M. analyzed the single-crystal X-ray diffraction data. L.M., D.J.F., X.L., A.N., O.N., I.K., and L.D. contributed to the interpretation of the results. L.M. and D.J.F. wrote the paper with contributions from all the authors.

## Abstract

Seismic, geodetic and cosmochemical evidence point to Mars having a sulfur-rich liquid core. Due to the similarity between estimates of the core's sulfur content and the iron - iron sulfide eutectic composition at core conditions, it has been concluded that temperatures are too high for Mars to have an inner core. Recent low density estimates for the core, however, appear consistent with sulfur contents that are higher than the eutectic composition, leading to the possibility that an inner core could form from a high-pressure iron sulfide phase. Here we report the crystal structure of a phase with the formula $Fe_{4+x}S_3$, the iron content of which increases with temperature, approaching the stoichiometry $Fe_5S_3$ under Martian inner core conditions. We show that $Fe_{4+x}S_3$ has a higher density than the liquid Martian core and that a $Fe_{4+x}S_3$ inner core would crystalize if temperatures fall below 1960 (±105) K at the center of Mars.

## 6.1 Introduction

Observations from NASA's InSight mission have revealed that the core of Mars is enriched in light elements, as its density appears to be substantially lower than that of Fe-Ni alloy (Stähler et al., 2021; Irving et al. 2023; Samuel et al., 2023; Khan et al., 2023). Based on seismic wave reflections at the apparent core-mantle boundary of Mars, models considering either the existence (Samuel et al., 2023; Khan et al., 2023) or absence (Stähler et al., 2021; Irving et al. 2023; Samuel et al., 2023) of a basal silicate magma layer indicate that the Martian core contains 9 to 20 wt.% or 20 to 25 wt.% of light elements, respectively. In either case, the abundance of light elements in the Martian core is significantly higher than in Earth's core (5 to 10 wt.%) (Hirose et al., 2013), implying considerable differences in accretion and differentiation processes during the early stages of planetary formation (Chambers et al., 2001). From cosmochemical perspectives and geochemical considerations, candidate light elements in the Martian core include S, O, C, and H (Wänke and Dreibus, 1994; Lodders and Fegley, 1997; Sanloup et al., 1999; Yoshizaki and McDonough, 2020). Sulfur, in particular, is often highlighted as a likely major light element in the Martian core, primarily due to it being the most prevalent moderately volatile element in the solar nebula (Palme et al., 2014), its siderophile ("iron-loving") behavior during core-mantle differentiation (Rose-Weston et al., 2009), and the fact that core formation on Mars was likely not a sufficiently reducing or high-temperature process for Si or O to be major light elements (Rubie et al., 2015). Assessments based on similarly volatile lithophile elements argue for < 7 wt. % S in the Martian core (Yoshizaki and McDonough, 2020) but this would most likely require significant proportions of C and H to explain the core's density deficit, which should, by the same arguments, be even more depleted in Mars than S. If similarly volatile elements are used to predict the S contents of ordinary and enstatite chondrites, the resulting concentrations for most of these meteorite sub-types are underestimated, raising the possibility that S contents of planetary bodies might vary independently of elements with similar condensation temperatures.

Seismic and lander radio science data from the InSight mission have confirmed that Mars has a liquid core (Stähler et al., 2021; Irving et al. 2023; Samuel et al., 2023; Khan et al., 2023; Le Maistre et al., 2023), but the presence of a solid inner core cannot be currently excluded on geophysical grounds (Stähler et al., 2021; Irving et al. 2023). If further geophysical observations were to verify the existence, size, and density of a Martian inner core, then combined with the appropriate mineral physical interpretation, this would provide essential constraints on the composition and temperature of the interior, as well as the possible mechanisms that initiated and terminated the magnetic field in early Mars (Breuer et al., 2015; Helffrich, 2017). In the scenario of a S-rich Martian core, the cooling and solidification processes of an initially fully molten Martian core are primarily governed by the melting phase relations of the Fe-FeS system under the high-pressure and high-temperature (HP-HT) conditions relevant to the Martian core. The eutectic composition in the Fe-FeS system shifts in the direction of the Fe-rich side with increasing pressure, from approximately 15.5 wt.% S at 21 GPa (Fei et al., 2000), i.e. the pressure at the top of the Martian core, to approximately 12 wt.% S at 40 GPa (Stewart et al., 2007; Mori et al., 2017; Morard et al., 2008), the pressure at the center of Mars. Within the possible compositional range of Mars' core, either Fe or Fe sulfides could be liquidus phases that might crystalize as an inner core (Helffrich, 2017; Stewart et al., 2007). Understanding the crystal structures and densities of these liquidus phases is, therefore, critical for determining their behavior during cooling of the Martian core.

In addition to the endmembers Fe and FeS, the solid phases reported under Martian core conditions in the Fe-FeS system include $Fe_2S$, $Fe_3S$, and $Fe_{3+x}S_2$ (Fei et al., 2000; Stewart et al., 2007). $Fe_2S$ is identified as a subsolidus phase in the Fe-FeS system at 21 GPa but is replaced by $Fe_3S$ or $Fe_{3+x}S_2$ when the temperature increases above the solidus temperature on the FeS-rich side of the eutectic (Fei et al., 2000). Whether $Fe_2S$ becomes a liquidus phase under higher pressures, corresponding to deeper Martian core conditions, remains unknown. $Fe_3S$ adopts a $Fe_3P$-type structure and has a S content (16 wt.%) close to the eutectic composition of the Fe-FeS system at Martian core pressures (Fei et al., 2000). During the cooling of the Martian core, if the sulfur concentration in the liquid core is above but close to the eutectic composition, $Fe_3S$ is expected to crystallize. $Fe_3S$ would be gravitationally stable at the center of the Martian core, as its density would be higher than that of the residual liquid (Stewart et al., 2007). However, if the bulk composition is more sulfur-enriched, for example, greater than 16 wt.% S at 21 GPa (Fei et al., 2000), the phase described as $Fe_{3+x}S_2$ would be the liquidus phase (Helffrich, 2017). $Fe_{3+x}S_2$ decomposes during decompression and cannot be recovered to ambient pressure (Fei et al., 1997; Zhao et al., 2024). Its crystal structure can, therefore, only be investigated in-situ, under high pressure conditions. The crystal system of $Fe_{3+x}S_2$ has been determined to be orthorhombic using powder X-ray diffraction (Zhao et al., 2024), but its structure remains undetermined. Consequently, the density and elastic properties of $Fe_{3+x}S_2$ remain largely unknown.

In order to determine the crystal structure and density relations of the elusive $Fe_{3+x}S_2$ phase, we conducted a series of HP-HT experiments within the Fe-FeS system, employing multiple in-situ and ex-situ characterization techniques. However, instead of $Fe_{3+x}S_2$, we obtained a crystal structure for an iron sulfide phase that is more accurately described, on the basis of its crystallography, as $Fe_{4+x}S_3$. This phase was synthesized within the P-T and compositional range where $Fe_{3+x}S_2$ has been previously reported, which almost certainly has the same structure. We have further investigated the composition, density and potential role of $Fe_{4+x}S_3$ in forming a Martian inner core.

## 6.2 **Results**

### ***6.2.1 Structural refinement of $Fe_{4+x}S_3$***

As the target $Fe_{3+x}S_2$ phase is known to decompose to nano-crystallites of a few different phases during decompression (Fei et al., 1997), we performed high-pressure single crystal structure analyses in the diamond anvil cell (DAC) following *in situ* syntheses through laser heating (LH) at pressures of approximately 15 GPa and 21 GPa. The starting material for the LH-DAC experiments comprised degraded "$Fe_{3+x}S_2$" crystals, which were initially synthesized at pressures ranging from 14 to 16 GPa in a multi-anvil (MA) press. Although these starting materials maintained a homogeneous composition on a scale of less than 100 nm, their crystal structure experienced degradation during the decompression process in the MA press, and therefore, cannot be directly used for structure determination. After syntheses in the LH-DAC, single crystal X-ray diffraction (SC-XRD) data were collected at room temperature and high pressures on the newly grown crystals in the reacted LH area. Using a micro-focused synchrotron X-ray beam (~1 μm * 1 μm) it was possible to index reflections from numerous sub-μm sized grains with different orientations in each sample. Structural solution of several of these grains led to the identification of a previously unknown structure exhibiting orthorhombic symmetry in the reacted areas of two experiments conducted at 15 GPa and 1150(±200) K (run LJFeS01) and 21 GPa and 1400(±200) K (run LD101). The reflections measured for all grains indicate clearly that the space group of this phase is Pnma. Structural refinement of two single crystals exhibiting the best discrepancy factors in each experiment (see more details in Supplementary Methods) indicates that the phase is characterized by five non-equivalent crystallographic sites for Fe and three non-equivalent sites for S.

As shown in Fig.6.1, there are four Fe sites that are five-fold coordinated, forming four edge-sharing Fe-S square pyramids; whereas the remaining iron site is four-fold coordinated, creating a Fe-S tetrahedron. The fundamental building blocks of the structure of $Fe_{4+x}S_3$ are consistent with the high pressure $Fe_{12}S_7$ phase (Zurkowski et al., 2022), stable above 100 GPa and the $Fe_2S$ phase stable above 21 GPa (Zurkowski et al., 2022; Oka et al., 2022). The tetrahedral site can be considered as an interstitial site between neighboring Fe-S square pyramids. If all the Fe and S sites are fully occupied, this would lead to a stoichiometry corresponding to $Fe_5S_3$. However, refinements of the SC-XRD data indicate that the Fe tetrahedral site is not fully occupied, leading to a chemical formula $Fe_{4+x}S_3$ (Supplementary Table 6.S1 and Table 6.1), where x is the Fe occupancy at the tetrahedral site. In experimental run LD101, the occupancy of the tetrahedral site in the $Fe_{4+x}S_3$ phase was found to be 0.77 (±0.01), which can be described with the more appropriate stoichiometry $Fe_{4.77}S_3$, or following the formula of Fei et al. (2000), $Fe_{3.18}S_2$. In another experimental run, LJFeS01, conducted under lower pressure-temperature (P-T) conditions than LD101, the tetrahedral site occupancy was refined to 0.11 (±0.01) Fe atoms. This results in the composition $Fe_{4.11}S_3$, or $Fe_{2.74}S_2$ when expressed in the $Fe_{3+x}S_2$ formula. Moreover, the unit cell volume of the $Fe_{4+x}S_3$ phase at 21 GPa and 300 K synthesized in run LD101 (331.2 $Å^3$) is notably larger than that at 15 GPa and 300 K synthesized in run LJFeS01 (324.0 $Å^3$). This is clearly due to the increased Fe occupancy of the tetrahedral site, which causes an increase in tetrahedral volume and, therefore, an increase in unit-cell volume (see Supplementary Discussion and Supplementary Fig. 6.S1). The details of the crystallographic parameters are presented in Table 1 and Supplementary Table 6.S2. The $Fe_{4.11}S_3$ crystal in run LJFeS01 was then further compressed up to 22.5 GPa at room temperature to examine its density and compressibility (Supplementary Table 6.S3). The compression curve of $Fe_{4.11}S_3$ at room temperature was then fitted using a second-order Birch-Murnaghan equation of state (Birch, 1947), resulting in $V_0 = 364.8(5)$ $Å^3$ and $K_0 = 97(2)$ GPa. After normalizing to the same pressure, for example, 21 GPa, the densities of $Fe_{4.11}S_3$ and $Fe_{4.77}S_3$ samples are 23.7% and 20.2% lower than hcp Fe (Fei et al., 2016), respectively. The non-stoichiometry, therefore, also affects the density, which increases with Fe content, in spite of the increase in the unit cell volume.

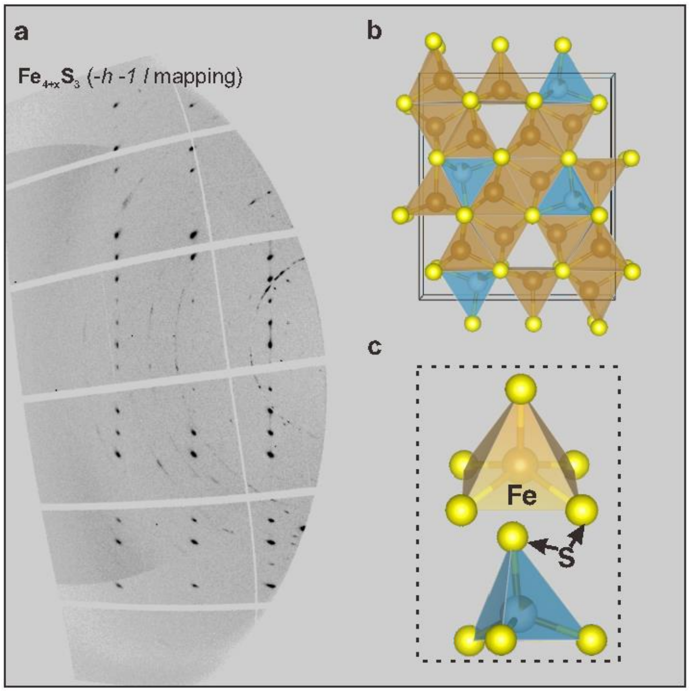

**Figure 6.1.** *In situ* single crystal structure determination of $Fe_{4+x}S_3$ under high pressure. (a) The diffraction mapping displays the reflections that satisfy the condition -h -1 l for $Fe_{4+x}S_3$ (space group: Pnma), which were collected at 14.9(1) GPa at room temperature following laser heating at 1150(±200) K (run LJFeS01). The data were acquired through a step-scan procedure spanning the range of ω from -30° to 30°. (b) The structural model of $Fe_{4+x}S_3$ as determined by SC-XRD. (c) Depiction of the building blocks, including the Fe-S pyramid and semi-occupied Fe-S tetrahedron, that constitute $Fe_{4+x}S_3$. The crystal structure models were visualized using the software Vesta (Momma and Izumi, 2011).

**Table 6.1.** Atomic coordinates and equivalent isotropic displacement parameters for $Fe_{4+x}S_3$

| | x | y | z | Occ. | $U_{iso}$ |
|---|---|---|---|---|---|
| $Fe_{4.11}S_3$, 14.9(1) GPa, V = 324.0(6) $Å^3$ | | | | | |
| a = 10.897(5) Å, b = 3.125(1) Å, c = 9.515(18) Å | | | | | |
| Fe1 | 0.5697 (2) | 0.25 | 0.5826 (3) | 1 | 0.029 (1) |
| Fe2 | 0.2731 (2) | 0.25 | 0.0687 (3) | 1 | 0.026 (2) |
| Fe3 | 0.2850 (2) | 0.25 | 0.7915 (4) | 1 | 0.027 (2) |
| Fe4 | 0.0246 (2) | 0.25 | 0.6208 (4) | 1 | 0.035 (1) |
| Fe5 | 0.0587 (14) | 0.25 | 0.215 (3) | 0.11(1) | 0.029 (5) |
| S1 | 0.3728 (3) | 0.25 | 0.5858 (5) | 1 | 0.031 (2) |
| S2 | 0.3758 (2) | 0.25 | 0.2651 (6) | 1 | 0.030 (2) |
| S3 | 0.1275 (3) | 0.25 | 0.4203 (5) | 1 | 0.032 (2) |
| $Fe_{4.77}S_3$, 21.1(5) GPa, V = 332.4 (2) $Å^3$ | | | | | |
| a = 11.073(3) Å, b = 3.182(1) Å, c = 9.435(4) Å | | | | | |
| Fe1 | 0.5724 (2) | 0.25 | 0.5745 (3) | 1 | 0.018 (1) |
| Fe2 | 0.2779 (2) | 0.25 | 0.0617 (3) | 1 | 0.019 (1) |
| Fe3 | 0.2723 (2) | 0.25 | 0.7840 (3) | 1 | 0.021 (1) |
| Fe4 | 0.0285 (2) | 0.25 | 0.6084 (4) | 1 | 0.028 (1) |
| Fe5 | 0.0640 (3) | 0.25 | 0.2102 (4) | 0.77 (1) | 0.016 (1) |
| S1 | 0.3688 (4) | 0.25 | 0.5784 (4) | 1 | 0.016 (1) |
| S2 | 0.3740 (4) | 0.25 | 0.2628 (5) | 1 | 0.016 (1) |
| S3 | 0.1340 (4) | 0.25 | 0.4178 (5) | 1 | 0.019 (1) |

The space group of $Fe_{4+x}S_3$ is Pnma. All the data was collected at room temperature.

To ascertain whether the $Fe_{4+x}S_3$ phase we identified at high pressure and room temperature is thermodynamically stable at the HP-HT conditions of synthesis, and to determine if a phase transition occurs during temperature quenching, we conducted *in situ* HP-HT XRD measurements using an Fe plus 15 wt. % S composition, in a multi-anvil press (MA) at the beamline PSICHE, SOLEIL (Supplementary Table 6.S4). A representative result (run MA233), as presented in Fig. 6.2, reveals a series of peaks emerging in the energy-dispersive (ED) XRD pattern when the temperature reached 800 K at a pressure of approximately 14 GPa. These peaks, which cannot be indexed as polymorphs of Fe and FeS (Urakawa et al., 2004), can all be indexed to the Pnma $Fe_{4+x}S_3$ phase identified in our study. This finding supports the conclusion that the Pnma $Fe_{4+x}S_3$ phase is indeed the thermodynamically stable phase under these HP-HT conditions. The unit cell expanded by around 6% as the temperature increased from 800 K to 1100 K. This degree of expansion is too large to be solely attributed to thermal expansion. This abnormal volume expansion confirms the results of our LH-DAC experiments that the $Fe_{4+x}S_3$ phase tends to incorporate more iron and becomes progressively denser with increasing temperature.

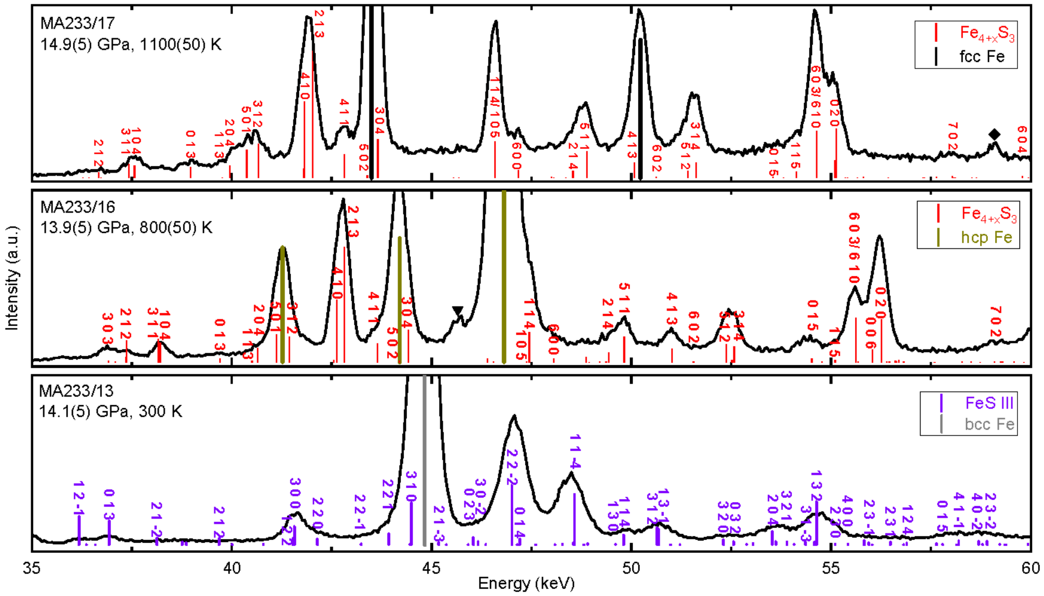

**Figure 6.2.** *In situ* ED-XRD patterns collected in a synchrotron MA experiment using an $Fe_{85}S_{15}$ starting material conducted at approximately 14 GPa and at the temperatures indicated. The Ge detector was positioned at an angle of 8.02 degrees 2θ. The grey, dark yellow, black, violet, and red sticks indicate bcc Fe, hcp Fe, fcc Fe, FeS III, and $Fe_{4+x}S_3$ reflections, respectively. The minor peaks marked with black reversed triangles appear to be residual from FeS IV and those marked by diamonds are from FeO.

The $Fe_{4+x}S_3$ phase discovered in this study is stable within the same P-T range reported for the $Fe_{3+x}S_2$ and $Fe_3S_2$ phases in the literature (Fei et al., 2000; Fei et al., 1997; Zhao et al., 2024; Zhang et al., 2008; Tsuno et al., 2009; Urakawa et al., 2018). The composition range and temperature-composition relations of $Fe_{4+x}S_3$ are consistent with that reported for both $Fe_{3+x}S_2$ and $Fe_3S_2$ (see Fig. 6.3a). Therefore, the $Fe_{3+x}S_2$ or $Fe_3S_2$ phase, whose crystal structure was previously unknown, is certain to be the same as the $Fe_{4+x}S_3$ phase identified in this study

### 6.2.2 P-V-T-x relations of $Fe_{4+x}S_3$

Chemical composition analyses of the quenched products from our in-house MA experiments further demonstrate the nonstoichiometric nature of the $Fe_{4+x}S_3$ phase, as well as its relationship with P, T, and sulfur activity. These experiments were carried out within the Fe-FeS system under a range of conditions: pressures from 14 to 27 GPa, temperatures from 918 to 1640 K, and varying bulk sulfur concentrations (Supplementary Table 6.S5). Representative images illustrating the phase assemblages and textures of the recovered samples can be found in the Supplementary Fig. 6.S2. Fig. 6.S3a illustrates that the Fe/(Fe+S) ratio, and consequently the value of x in $Fe_{4+x}S_3$, increases notably with increasing temperature. A large range of variation in the value of x in $Fe_{4+x}S_3$, from 0.09 to 0.80, was observed in this study that approaches the theoretical limits permissible within the crystallographic framework (i.e. 0 to 1). However, x also varies depending on the nature of the coexisting phase, i.e. the Fe activity, being approximately 0.2 higher when coexisting with metallic iron compared to FeS at 16 GPa, based on the results in this study. Although we cannot quantify the effect of pressure on the variation of x from the current dataset, x may increase with pressure at a given temperature. This possibility is implied by the deviation observed in the previous study by Fei et al. (2000), conducted at 21 GPa, where x values are higher and deviate from the trend observed at 16 GPa in this study.

With the established relationship between temperature and composition for $Fe_{4+x}S_3$, we can evaluate its P-V-T-x relations using the HP-HT data from this study and from the literature (Zhao et al., 2024). The experiments from Zhao et al. (2024) were conducted at pressures between 13 and 16 GPa, and contain metallic iron. Therefore, we can fit the temperature-composition relationship from our in-house multi-anvil (MA) experiments and literature (Urakawa et al., 2004; Tsuno et al., 2009) with $Fe_{4+x}S_3$ coexisting with metallic iron at approximately 16 GPa to constrain the compositional effects (i.e. influence of the x parameter) on volume. A linear fit of $\mathrm{x} = a \times (T - b)$ yields the result $a = 9.5 \pm 0.6 \times 10^{-4}\mathrm{K}^{-1}$ and $b = 750 \pm 50\ \mathrm{K}$, where T is in K. The composition-volume relation can be determined using the single crystal refinements collected in this study, from the volume difference between the $Fe_{4.11}S_3$ and $Fe_{4.77}S_3$ samples, after normalization to the same pressure. After correcting the effects of composition and compressibility on the volume of $Fe_{4+x}S_3$, we can estimate its thermal expansion. We assume that the thermal expansion coefficient of $Fe_{4+x}S_3$ does not vary significantly with x, and fit the P-V-T data of $Fe_{4+x}S_3$ from this study and the literature (Zhao et al., 2024) using the thermal expansion expression: $\alpha = 1/V\ (\partial V/\partial T)_P$, assuming $\alpha$ remains constant over the limited pressure (13 to 16 GPa) and temperature range (800 to 1100 K). The resulting thermal expansion coefficient is 5.3±2.0 × 10-5 K-1, which is comparable to that of the $Fe_3S$ phase (~3.6 × 10-5 K-1 at 1000 K and 15 GPa, Chen et al., 2007), but significantly smaller than that previously estimated for the "$Fe_3S_2$" phase (~26.58 × 10-5 K-1) in the same pressure and temperature range (Zhao et al., 2024). The significant overestimation of $\alpha$ in the previous study by Zhao et al. (2024) is due to the fact that the volume expansion resulting from compositional variation with temperature was not accounted for separately in the evaluation of thermal expansion. The P-V-T-x relations of $Fe_{4+x}S_3$ are shown in Fig. 6.3. These relations accurately describe the large volume changes observed in the experimental data, which are caused by both thermal expansion and compositional variation.

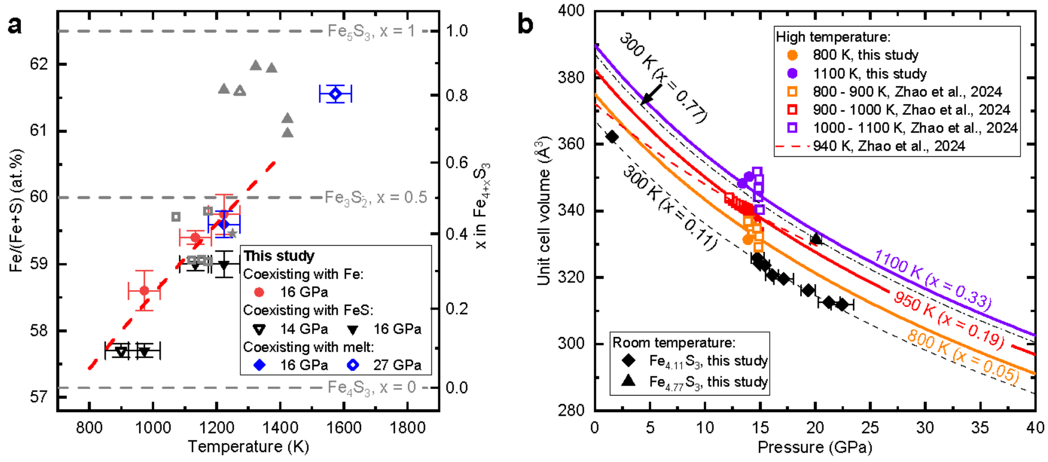

**Figure. 6.3.** P-V-T-x relations of $Fe_{4+x}S_3$. (a) Compositions of $Fe_{4+x}S_3$ obtained from quenched MA experiments. In the present study, the $Fe_{4+x}S_3$ samples coexist with metallic Fe (red-filled circles, 16 GPa), solid FeS (black open inverted triangles, 14 GPa; black solid inverted triangles, 16 GPa), or Fe-S melt (blue solid diamonds, 16 GPa; blue open diamonds, 27 GPa). The grey symbols indicate results from the literature: open squares (Tsuno et al., 2009), filled triangles (Fei et al., 2000), open triangles (Zhang et al., 2008), and the filled star (Urakawa et al., 2018). The red dashed line is a linear fit of the x-T relationship for samples coexisting with metallic iron at pressures of 15-16 GPa. (b) Compression curves of $Fe_{4+x}S_3$ for various compositions and temperatures. The black dashed line, orange solid line, red solid line, and violet solid line show values generated from the P-V-T-x model at 300 K, 800 K, 950 K, and 1100 K. The x values in high temperature curves follow the x-T relations indicated by the red dashed line in Fig. 6.3a. The black diamonds and triangles are data collected in a DAC at 300 K in this study. The solid circles are the HP-HT data in this study and the open squares are the HP-HT data from the literature, which were interpreted as $Fe_3S_2$ (Zhao et al., 2024). The red dashed line indicates the EOS of "$Fe_3S_2$" at 940 K, as reported by Zhao et al. (2024).

## 6.3 Discussion

Although there is currently no direct geophysical evidence confirming the existence of a Martian inner core, recent seismic and geodetic observations have provided important constraints on the state of the core as a whole (Stähler et al., 2021; Irving et al. 2023; Samuel et al., 2023; Khan et al., 2023; Le Maistre et al., 2023). Seismic measurements have detected the apparent core-mantle boundary of Mars, supplied decisive evidence that at least the upper region of Mars' core is in a liquid state and provided estimates for the core's average density (Stähler et al., 2021; Irving et al. 2023; Samuel et al., 2023; Khan et al., 2023) that range from 5.7 to 6.65 g/cm$^3$. The substantial variation in these density estimates stems from whether a basal magma layer is considered to exit, which in turn implies different thermal regimes for Mars' interior. While the innermost state of Mars' core has not yet been revealed by seismic observations, the detected liquid region of the core sets an upper limit to a potential inner core radius of < 750 km (Irving et al. 2023). Models based on geodesy also support the existence of a liquid core, though these observations are generally insensitive to an inner core unless it is sufficiently big (Defraigne et al., 2003). Based on the assumption that the sulfur content of Mars' core may be quite close to the Fe-FeS eutectic, previous models have proposed that temperatures are likely too high for an inner core to form (Stewart et al., 2007; Fei et al., 2005). However, the relatively low densities recently proposed for the core (Stähler et al., 2021; Irving et al. 2023; Samuel et al., 2023) raises the possibility that the composition may lie to the S-rich side of the eutectic at conditions approaching the center of Mars. To examine this possibility, we first determine whether an $Fe_{4+x}S_3$ inner core would be gravitationally stable and the temperature required for it to crystallize, then compare this with proposed Martian areotherms to assess the likely core crystallization regime.

If we extrapolate the obtained P-V-T-x relations for $Fe_{4+x}S_3$ to inner core conditions, the density will increase both due to compression and because x will approach 1, reaching a value of 7.5(±0.3) g/cm$^3$ at the center of Mars (40 GPa and 2000K). This is larger than the range estimated using recent seismic observations for the density at the center of a liquid Martian core (Stähler et al., 2021; Irving et al. 2023; Samuel et al., 2023; Khan et al., 2023), implying that an $Fe_{4+x}S_3$ inner core would be gravitationally stable in a bottom-up crystallization regime (Supplementary Fig. 6.S3). It is worth noting that in estimating the density of $Fe_{4+x}S_3$, the thermal expansion coefficient was assumed to be constant, which likely results in a slight underestimate of the inner core density. Even though this assumption does affect the conclusion of gravitational stability, further *in situ* HP-HT experiments would be required to establish a full thermodynamic model describing the P-V-T-x relations of $Fe_{4+x}S_3$, considering both the P-T effect on the variation of x and the effect of x on the thermoelastic properties of $Fe_{4+x}S_3$.

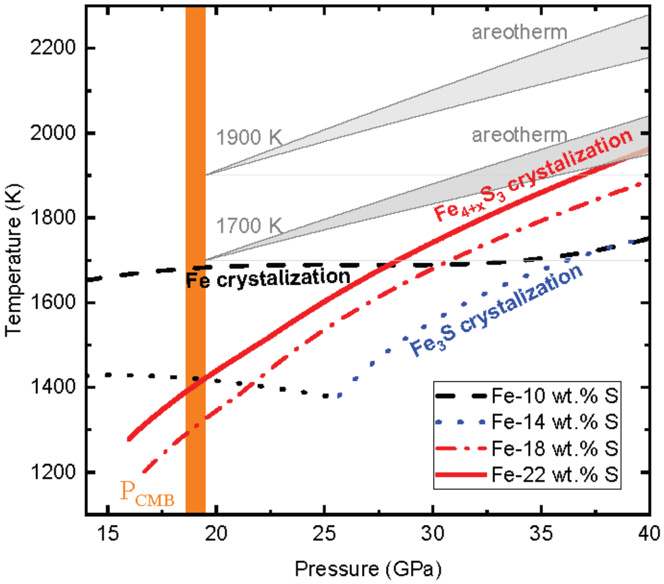

**Figure 6.4** Fe-S system liquidus curves as a function of pressure. Black dashed line: Fe-10 wt.% S liquid where Fe is the liquidus phase; blue dotted line: Fe-14 wt.% S where $Fe_3S$ is the liquidus phase; black dotted line: Fe-14 wt.% S where Fe is the liquidus phase < 25 GPa; red sold lines: Fe-18 wt.% S with $Fe_{4+x}S_3$ as the liquidus phase; red dash-dot line: Fe-22 wt.% S with $Fe_{4+x}S_3$ as the liquidus phase. The grey-shaded regions are estimated areotherm of the Martian core[16] with CMB temperatures at 1700 K and 1900 K.

Constraints on the temperature for inner core crystallization can be obtained by examining the thermal stability of $Fe_{4+x}S_3$, which increases quite significantly with pressure, from less than 1200 K at 14 GPa (Fei et al., 1997) to ~1500 K at 21 GPa (Fei et al., 2000). At higher temperatures, $Fe_{4+x}S_3$ will melt incongruently to form solid FeS and Fe-S liquid: $\mathrm{Fe}_{4+x}\mathrm{S}_3(\mathrm{solid}) = 2\mathrm{FeS}(\mathrm{solid}) + \mathrm{Fe}_{2+x}\mathrm{S}$ (liquid). The $Fe_{4+x}S_3$ synthesized in this study coexists with Fe-S liquid at 1640 K and 27 GPa, indicating a melting temperature higher than this. An extrapolation of the melting curve to the pressure at the center of the Martian core (~40 GPa), indicates that $Fe_{4+x}S_3$ is stable up to approximately 1970(±105) K (Supplementary Fig. 6.S4). This relatively refractory behavior of $Fe_{4+x}S_3$ underlines the potential for it to form planetary inner cores.

The solidification regime of the Martian core will depend on the core's composition and temperature. We have parameterized the melting phase relations in the Fe-FeS system up to 40 GPa considering the liquidus phases Fe, $Fe_3S$, $Fe_{4+x}S_3$, and FeS and using our results and those from the literature (Supplementary Fig. 6.S5). Since there is no experimental evidence to support the stability of $Fe_{12}S_7$ and $Fe_2S$ (Zurkowski et al., 2022; Fei et al., 2000) as liquidus phases under Martian core conditions, these phases were not considered in our model. Fig. 6.4 shows Fe-S liquidus curves for different amounts of S, compared with Martian areotherms, from which the core solidification regime can be inferred by considering potential points of intersection. As illustrated in Fig. 6.5., during the cooling of Mars, if the core contains ~7-12 wt.% S, Fe-metal snow will form at the top of the Martian core, as proposed previously (Stewart et al., 2007). The crystalized Fe will sink but will be dissolved again in the deeper core region where the liquidus temperature is then lower than the areotherm (see curve 10 wt.% S in Fig. 6.4). If the Martian core contains ~13-16 wt.% S, the liquidus curve will first decrease with pressure (see curve 14 wt.% S in Fig. 6.4), where Fe-metal is the liquidus phase. However, as the S content of the eutectic melt decreases with increasing pressure, $Fe_3S$ will replace Fe as the liquidus phase at higher pressures (21 to 32 GPa, depending on the exact S content), which will cause the liquidus temperature to increase with pressure. In this case, the areotherm could intersect the liquidus curve at both the top and bottom of the Martian core, which means that both iron snow and bottom-up growth of $Fe_3S$ could occur simultaneously. However, if the Martian core contains 17-25 wt.% S, which would be quite consistent with recent density estimates (Stähler et al., 2021; Irving et al. 2023; Samuel et al., 2023), $Fe_{4+x}S_3$ will be the liquidus phase over the entire pressure range of the Martian core, with a liquidus temperature that increases continuously with pressure (see curves 18 and 22 wt.% S in Fig. 6.4). This means that an $Fe_{4+x}S_3$ inner core will start to crystalize if the center of such a S-rich Martian core cools below approximately 1960 K.

Mars has no active global magnetic field, implying that there is no dynamo operating in the Martian core. Crystallization of Fe in the form of iron snow would cause chemical convection below the snow zone, although whether this convection would provide enough energy to run a dynamo is debated (Breuer et al., 2015; Helffrich et al., 2017; Hauck et al., 2006; Bland et al., 2008; Rückriemen et al., 2015), as it is dependent on the generation of a positive net buoyancy flux (Hemingway et al., 2021). In contrast, the crystallization of a sulfide inner core is consistent with the absence of an active dynamo, as the residual liquid would be richer in Fe and would, therefore, remain at the base of the outer core, inhibiting chemical convection (Breuer et al., 2015).

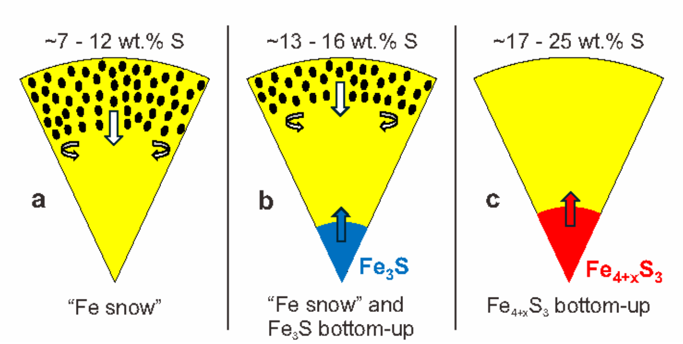

**Figure 6.5.** Solidification regimes of the Martian core for different bulk core sulfur concentrations. (a) Iron snow. (b) Simultaneous iron snow and $Fe_3S$ crystalizing from the center. (c) Bottom-up crystallization of $Fe_{4+x}S_3$.

The presence of an inner core composed of $Fe_{4+x}S_3$ would likely have a negligible impact on interpretations of geodetic observations. For instance, with a small inner core allowed by current seismic constraints (e.g., a radius of <600 km), the mass of an $Fe_{4+x}S_3$ inner core would constitute less than 5% of the total core mass, altering the moment of inertia by only ~0.1%. Additionally, according to numerical calculations, the nutation effects of an inner core with a radius of 600 km are expected to be insignificant (Defraigne et al., 2003). Thus, geodesy alone may be insufficient to constrain the existence of a relatively small inner core, and further seismic observations from future space missions, as well as additional analyses of InSight seismic data, are needed to provide more definitive evidence regarding the presence or absence of a Martian inner core. Further experimental measurements to enable seismic velocities of $Fe_{4+x}S_3$ to be determined would be also important for the interpretation of potential inner core-related seismic signals.

The temperature at the center of the Martian core would need to be lower than 1800 K to allow $Fe_3S$ to crystallize or for an 'iron snow' zone to reach the Martian center and form an inner core of Fe (Fig. 6.4). This corresponds to a temperature of approximately 1500–1600 K at the core-mantle boundary (CMB), which is lower than all current thermal models for Mars (Fei et al., 2005; Hauck and Phillips, 2002; Williams and Nimmo, 2004; Plesa et al., 2015; Samuel et al., 2021; Huang et al., 2022). Therefore, crystallization of an $Fe_3S$ or Fe inner core are likely to be only future scenarios, possible only after Mars has cooled further (Stewart et al., 2007). On the other hand, the crystallization temperature of $Fe_{4+x}S_3$ in a core containing, for example, 22 wt.% S—an amount that could satisfy the Martian core's density deficit (e.g., Irving et al. 2023)—would be approximately 1960 (±105) K. This approaches the lower limit of the estimated temperature of the Martian core in some thermal models (Hauck and Phillips, 2002; Williams and Nimmo, 2004; Plesa et al., 2015). The detection of a Martian inner core through further geophysical observations, along with an estimate of its density, would provide critical constraints on the chemical composition and temperature of the Martian core. Moreover, the existence of a Martian inner core would imply a relatively cool Martian interior, which would be incompatible with the presence of a basal magma layer on top of the CMB. Conversely, if an inner core is confirmed to be absent, the $Fe_{4+x}S_3$ melting temperature, i.e., 1960 (±105) K, would provide a lower limit for the temperature at the center of Mars.

It is worth noting that the addition of other light elements, such as O, C, and H, may impact the crystallization phase relations of the Fe-FeS system, though the effects remain largely unknown due to a lack of experimental studies in more complex systems. On the one hand, the addition of multiple light elements could further lower the eutectic temperature of the system making an inner core less likely. On the other hand, it is possible that elements such as H, that can be incorporated in high pressure sulfides in stoichiometric proportions (Abeykoon et al., 2023), might partition sub-equally between liquid and melt phases and have little effect on crystallization temperatures. While this study provides a preliminary estimation of the likelihood of $Fe_{4+x}S_3$ crystallization in the Martian core, further experiments involving relevant more complex chemical compositions are needed to test the hypotheses proposed here.

## 6.4 Methods

***Starting material.*** The initial mixtures were composed of metallic iron powder (99.9%, 10 µm particle size) and high-purity elemental sulfur (99.999%). The bulk compositions of the mixtures are listed in Supplementary Table 6.S5. The elements were mixed in an agate mortar under ethanol for about 45 minutes, followed by drying overnight in an oven at 340 K. For the in-house multi-anvil experiments, the mixed powder was directly used as the starting material, without any pre-treatment. For the synchrotron multi-anvil experiments, the powder mixtures underwent a pre-sintering process. This involved compressing the powders in a piston-cylinder press at 0.5 GPa and 1000 K for over 6 hours. Following sintering, the materials were machined into regular cylinders, each measuring approximately 1 mm in diameter and 0.6 mm in height. The sintered cylinders contained a mixture of metallic Fe and troilite (FeS). For the LH-DAC experiments, a pre-synthesized $Fe_{4+x}S_3$ crystal separated from a prior multi-anvil experiment was utilized. The degraded crystal was pre-compressed into a thin pallet, roughly 10 µm thick, to serve as the starting material.

***In-house multi-anvil experiments.*** 10 mm and 7 mm edge length octahedral assemblies were compressed using tungsten carbide cubic anvils with 5 mm and 3 mm truncation edge lengths (TEL), respectively. The 10/5 assembly was used for experiments targeting pressures between 14 to 16 GPa. The 7/3 assembly was utilized for the experiments at 27 GPa (Ishii et al., 2016; Liu et al., 2017). In these in-house multi-anvil experiments, the pressure uncertainties at high temperatures are estimated to be ±2 GPa. The starting materials were loaded into a gold capsule for run S7995, while MgO capsules were used in all other runs. After reaching the target loads, the samples were heated to high temperatures using $LaCrO_3$ heaters. Temperatures were monitored using a type D W-Re thermocouple, except for run S7995 and I1691a, where the temperature was estimated based on the power-temperature relation from previous experiments. The pressure effects on the electromotive force (EMF) of the thermocouple were corrected (Nishihara et al., 2020). These temperatures were maintained for durations ranging from 1 to 10 hours, followed by rapid quenching to room temperature by shutting down the power source.

***Synchrotron multi-anvil experiments.*** The experiments were conducted at the beamline PSICHE at the SOLEIL synchrotron (King et al., 2022). This assembly was equipped with a boron-doped diamond (BDD) heater, synthesized through the chemical vapor deposition (CVD) method (Nishida et al., 2020; Xie et al., 2020). The CVD-BDD heaters are notable for providing stable heating conditions and high X-ray transparency, which assists the collection of high quality XRD data. The assemblies were compressed to high pressures using tungsten carbide anvils with 5 mm TEL. The samples, which were placed in a corundum ($Al_2O_3$) capsule, were illuminated by the white X-ray beams, and the energy-dispersive XRD patterns of the samples were collected *in-situ* at high pressures and high temperatures. The unit cell parameters of the phases present in the samples were determined through Rietveld Le Bail fitting, using the GSAS-II software package (Toby et al., 2013). Temperatures were measured using a type D thermocouple, with corrections also applied for pressure effects on the EMF (Nishihara et al., 2020). Pressures were evaluated using the equation of state of corundum (Shi et al., 2022). The differences in pressure are less than 0.2 GPa when applying an alternative pressure standard for corundum (Néri et al., 2024).

***Single crystal syntheses in LH-DAC and high-pressure SC-XRD.*** We employed a BX90-type diamond anvil cell (Kantor et al., 2012), equipped with a pair of diamond anvils each having a culet diameter of 250 µm for the high-pressure single crystal synthesis and measurements. Pre-indented rhenium gaskets were employed. A thin platelet of $Fe_{4+x}S_3$ sample was sandwiched between two KCl layers and compressed to approximately 15 GPa in run LJFeS01. KCl provided both thermal insulation and the pressure marker (Dewaele et al., 2012) in the experiment. The sample was then heated from both sides using near-infrared lasers to a temperature of 1150 (200) K, employing a modified version of the portable double-sided laser of the ID14 beamline at ESRF (Kupenko et al., 2012; Aprilis et al., 2017). The temperature for LJFeS01 was estimated based on the melting phase relations in the high-pressure Fe-FeS system (Fei et al., 1997), as the $Fe_{4+x}S_3$ phase coexisted with Fe-S liquid (Supplementary Fig. 6.S6). For run LD101, helium was loaded at 1.2 kbar and served both as a pressure-transmitting medium and thermal insulator for laser heating. The sample was compressed to approximately 20 GPa and then heated to 1300 (200) K, employing the in-house laser-heating system at the Bayerisches Geoinstitut (Fedotenko et al., 2019), with temperatures estimated by fitting the radiation of the sample using a grey body approximation. The pressure of run LD101 was estimated based on a pressure calibration of the Raman shift of the diamond anvils (Akahama and Kawamura, 2006). For both runs, the samples were subjected to heating for durations ranging from 5 to 10 seconds before being rapidly quenched to room temperature.

High-pressure XRD measurements were conducted at the high-pressure diffraction beamline ID15B at the ESRF in Grenoble. We utilized a focused X-ray beam with a wavelength of 0.4100 Å, and a beam size of approximately 1 µm × 1 µm. Initially, a 2D-scan XRD map with a step size of 2 µm was constructed by scanning the sample stage (Hrubiak et al., 2019). This process was aimed at locating phases of interest within the samples, as illustrated in Supplementary Fig. 6.S6. Upon locating these phases, SC-XRD data collection was conducted over a range of -30 degrees to +30 degrees for LJFeS01, and -34 degrees to +34 degrees for LD101, with an increment step of 0.5 degrees. The Domain Auto Finder program (DAFi) (Aslandukov et al., 2022) was employed for the rapid identification of domains of $Fe_{4+x}S_3$ microcrystals within the complete SC-XRD dataset collected from the multiphase samples. Domains of $Fe_{4+x}S_3$ were primarily located in the region adjacent to the melt within the laser-heated spots. In the colder areas of the laser-heated spot, FeS III and several unidentified phases were indexed from the SC-XRD dataset. As this paper concentrates on the stability of liquidus phases, some further reflections for the unidentified subsolidus sulfide structures identified within the samples are outside of the scope of this discussion. Data reductions were performed using the CrysAlis Pro software package. The crystal structures of $Fe_{4+x}S_3$ from each run were subsequently solved and refined using the Olex2 software package (Dolomanov et al., 2009). Further details regarding the structure solution and refinement can be found in Supplementary Methods.

***Sample Recovery and Chemical Analysis.*** After the completion of the in-house multi-anvil experiments, the run products were carefully recovered to ambient conditions, mounted in epoxy resin and subsequently polished for chemical analyses. The samples were analyzed using a JEOL JXA-8200 electron probe microanalyzer (EPMA), which was operated at 15 kV and 15 nA. Calibration standards of metallic iron, pyrite, and periclase were employed for Fe, S, and O, respectively. The solid phases of the samples were analyzed with a focused beam, approximately 1 µm in diameter. The compositions of the quenched liquids were measured using a defocused beam with a diameter ranging from 10 to 30 µm, depending on the size of the quenched texture.

***Parameterization of liquidus temperature.*** The pressure and composition dependencies of the liquidus temperature are parameterized following a similar approach to previous models (Rivoldini et al., 2011; Helffrich, 2017), incorporating more experimental constraints from this study. The melting phase diagram at a given pressure is constructed using the melting temperatures of the liquidus phases (Fe, $Fe_3S$, $Fe_{4+x}S_3$, and FeS) and the eutectic temperature and composition as anchor points. It is assumed that the liquidus temperature has a linear dependence on sulfur concentration when Fe or FeS is the liquidus phase, and a parabolic dependence on sulfur concentration when $Fe_{4+x}S_3$ or $Fe_3S$ are the liquidus phases. Fe, $Fe_{4+x}S_3$, and FeS are liquidus phases at pressures from 14 to 21 GPa, while Fe, $Fe_3S$, $Fe_{4+x}S_3$, and FeS are liquidus phases at pressures above 21 GPa. We use the melting curves of Fe (Dorogokuoets et al., 2017) and FeS (Boehler, 1992) from the literature and evaluate the eutectic compositions and temperatures at high pressures (Supplementary Fig. 6.S7), as well as the melting curves of $Fe_3S$ and $Fe_{4+x}S_3$ (Supplementary Fig. 6.S4), using data from this study and the literature (Fei et al., 1997; Fei et al., 2000; Thompson et al., 2022). The change in the peritectic composition from $Fe_{4+x}S_3$ plus liquid to FeS plus liquid as a function of pressure was estimated based on data from this study and the literature (Fei et al., 1997; Fei et al., 2000). The sulfur content is parameterized to increase with pressure until it reaches the composition of $Fe_5S_3$. Meanwhile, the peritectic composition at the point where $Fe_3S$ plus liquid reacts to $Fe_{4+x}S_3$ plus liquid is assumed to be the composition of $Fe_3S$ (16.1 wt.% S). The parameters describing the model are listed in Supplementary Table 6.S6. The melting phase relations at 15 GPa, 21 GPa, 27 GPa, and 40 GPa, generated using this model, are plotted in Supplementary Fig. 6.S5 and compared with literature data to demonstrate consistency.

## Data Availability

The data supporting the main findings of this work are available in the main text and the supplementary materials. Additional data can be available from the corresponding author upon request.

## Acknowledgments

The authors thank L. Yuan, R. Pierru, and E. Kubik for insightful discussions. We appreciate assistance from D. Krauße, A. Potzel, and D. Wiesner in chemical characterization using electron microscopy. R. Njul, A. Rother, H. Fischer, and S. Übelhack are acknowledged for their help with sample preparation and the maintenance of the large volume presses at BGI. This research was supported by DFG grant FR1555/11. We acknowledge the European Synchrotron Radiation Facility (ESRF) for provision of experiment time at the ID15 beamline and offline laser-heating facilities of the ID14 beamline. IK acknowledges funding provided by the European Union (ERC, LECOR, project number 101042572). Views and opinions expressed are, however, those of the authors only and do not necessarily reflect those of the European Union or the European Research Council. Neither the European Union nor the granting authority can be held responsible for them.

# References

Abeykoon, S., Howard, C., Dominijanni, S., Eberhard, L., Kurnosov, A., Frost, D.J., Boffa Ballaran, T., Terasaki, H., Sakamaki, T., Suzuki, A. and Ohtani, E., 2023. Deuterium content and site occupancy in iron sulfide at high pressure and temperature determined using in situ neutron diffraction measurements. Journal of Geophysical Research: Solid Earth, 128, e2023JB026710.

Akahama, Y. and Kawamura, H., 2006. Pressure calibration of diamond anvil Raman gauge to 310 GPa. Journal of Applied Physics, 100, 043516.

Aprilis, G., Strohm, C., Kupenko, I., Linhardt, S., Laskin, A., Vasiukov, D.M., Cerantola, V., Koemets, E.G., McCammon, C., Kurnosov, A. and Chumakov, A.I., 2017. Portable double-sided pulsed laser heating system for time-resolved geoscience and materials science applications. Review of Scientific Instruments, 88, 084501.

Aslandukov, A., Aslandukov, M., Dubrovinskaia, N. and Dubrovinsky, L., 2022. Domain Auto Finder (DAFi) program: the analysis of single-crystal X-ray diffraction data from polycrystalline samples. Journal of Applied Crystallography, 55, pp.1383–1391.

Birch, F., 1947. Finite elastic strain of cubic crystals. Physical Review, 71, pp.809–823.

Bland, M.T., Showman, A.P. and Tobie, G., 2008. The production of Ganymede's magnetic field. Icarus, 198, pp.384–399.

Boehler, R., 1992. Melting of the Fe-FeO and the Fe-FeS systems at high pressure: Constraints on core temperatures. Earth and Planetary Science Letters, 111, pp.217–227.

Breuer, D., Rueckriemen, T. and Spohn, T., 2015. Iron snow, crystal floats, and inner-core growth: modes of core solidification and implications for dynamos in terrestrial planets and moons. Progress in Earth and Planetary Science, 2, pp.1–26.

Chambers, J.E. and Wetherill, G.W., 2001. Planets in the asteroid belt. Meteoritics & Planetary Science, 36, pp.381–399.

Chen, B., Gao, L., Funakoshi, K.I. and Li, J., 2007. Thermal expansion of iron-rich alloys and implications for the Earth's core. Proceedings of the National Academy of Sciences of the United States of America, 104, pp.9162–9167.

Chudinovskikh, L. and Boehler, R., 2007. Eutectic melting in the system Fe–S to 44 GPa. Earth and Planetary Science Letters, 257, pp.97–103.

Defraigne, P., Rivoldini, A., Van Hoolst, T. and Dehant, V., 2003. Mars nutation resonance due to free inner core nutation. Journal of Geophysical Research: Planets, 108, E12.

Dewaele, A., Belonoshko, A.B., Garbarino, G., Occelli, F., Bouvier, P., Hanfland, M. and Mezouar, M., 2012. High-pressure–high-temperature equation of state of KCl and KBr. Physical Review B, 85, 214105.

Dolomanov, O.V., Bourhis, L.J., Gildea, R.J., Howard, J.A. and Puschmann, H., 2009. OLEX2: a complete structure solution, refinement and analysis program. Journal of Applied Crystallography, 42, pp.339–341.

Dorogokupets, P.I., Dymshits, A.M., Litasov, K.D. and Sokolova, T.S., 2017. Thermodynamics and equations of state of iron to 350 GPa and 6000 K. Scientific Reports, 7, 41863.

Fedotenko, T., Dubrovinsky, L., Aprilis, G., Koemets, E., Snigirev, A., Snigireva, I., Barannikov, A., Ershov, P., Cova, F., Hanfland, M. and Dubrovinskaia, N., 2019. Laser heating setup for diamond anvil cells for in situ synchrotron and in-house high and ultra-high pressure studies. Review of Scientific Instruments, 90, 104501.

Fei, Y. and Bertka, C., 2005. The interior of Mars. Science, 308, pp.1120–1121.

Fei, Y., Bertka, C.M. and Finger, L.W., 1997. High-pressure iron-sulfur compound, $Fe_3S_2$, and melting relations in the Fe-FeS system. Science, 275, pp.1621–1623.

Fei, Y., Li, J., Bertka, C.M. and Prewitt, C.T., 2000. Structure type and bulk modulus of $Fe_3S$, a new iron-sulfur compound. American Mineralogist, 85, pp.1830–1833.

Fei, Y., Murphy, C., Shibazaki, Y., Shahar, A. and Huang, H., 2016. Thermal equation of state of hcp-iron: Constraint on the density deficit of Earth's solid inner core. Geophysical Research Letters, 43, pp.6837–6843.

Hauck, S.A. and Phillips, R.J., 2002. Thermal and crustal evolution of Mars. Journal of Geophysical Research: Planets, 107, pp.6-1–6-19.

Hauck, S.A., Aurnou, J.M. and Dombard, A.J., 2006. Sulfur's impact on core evolution and magnetic field generation on Ganymede. Journal of Geophysical Research: Planets, 111, E9.

Helffrich, G., 2017. Mars core structure—concise review and anticipated insights from InSight. Progress in Earth and Planetary Science, 4, pp.1–14.

Hemingway, D.J. and Driscoll, P.E., 2021. History and future of the Martian dynamo and implications of a hypothetical solid inner core. Journal of Geophysical Research: Planets, 126, e2020JE006663.

Hirose, K., Labrosse, S. and Hernlund, J., 2013. Composition and state of the core. Annual Review of Earth and Planetary Sciences, 41, pp.657–691.

Hrubiak, R., Smith, J.S. and Shen, G., 2019. Multimode scanning X-ray diffraction microscopy for diamond anvil cell experiments. Review of Scientific Instruments, 90, 025109.

Huang, Q., Schmerr, N.C., King, S.D., Kim, D., Rivoldini, A., Plesa, A.C., Samuel, H., Maguire, R.R., Karakostas, F., Lekić, V. and Charalambous, C., 2022. Seismic detection of a deep mantle discontinuity within Mars by InSight. Proceedings of the National Academy of Sciences of the United States of America, 119, e2204474119.

Irving, J.C., Lekić, V., Durán, C., Drilleau, M., Kim, D., Rivoldini, A., Khan, A., Samuel, H., Antonangeli, D., Banerdt, W.B. and Beghein, C., 2023. First observations of core-transiting seismic phases on Mars. Proceedings of the National Academy of Sciences of the United States of America, 120, e2217090120.

Ishii, T., Shi, L., Huang, R., Tsujino, N., Druzhbin, D., Myhill, R., Li, Y., Wang, L., Yamamoto, T., Miyajima, N. and Kawazoe, T., 2016. Generation of pressures over 40 GPa using Kawai-type multi-anvil press with tungsten carbide anvils. Review of Scientific Instruments, 87, 024501.

Kantor, I., Prakapenka, V., Kantor, A., Dera, P., Kurnosov, A., Sinogeikin, S., Dubrovinskaia, N. and Dubrovinsky, L., 2012. BX90: A new diamond anvil cell design for X-ray diffraction and optical measurements. Review of Scientific Instruments, 83, 125102.

Khan, A., Huang, D., Durán, C., Sossi, P.A., Giardini, D. and Murakami, M., 2023. Evidence for a liquid silicate layer atop the Martian core. Nature, 622, pp.718–723.

King, A., Guignot, N., Henry, L., Morard, G., Clark, A., Le Godec, Y. and Itié, J.P., 2022. Combined angular and energy dispersive diffraction: optimized data acquisition, normalization and reduction. Journal of Applied Crystallography, 55, pp.218–227.

Kupenko, I., Dubrovinsky, L., Dubrovinskaia, N., McCammon, C., Glazyrin, K., Bykova, E., Ballaran, T.B., Sinmyo, R., Chumakov, A.I., Potapkin, V. and Kantor, A., 2012. Portable double-sided laser-heating system for Mössbauer spectroscopy and X-ray diffraction experiments at synchrotron facilities with diamond anvil cells. Review of Scientific Instruments, 83, 124501.

Le Maistre, S., Rivoldini, A., Caldiero, A., Yseboodt, M., Baland, R.M., Beuthe, M., Van Hoolst, T., Dehant, V., Folkner, W.M., Buccino, D. and Kahan, D., 2023. Spin state and deep interior structure of Mars from InSight radio tracking. Nature, 619, pp.733–737.

Liu, Z., Nishi, M., Ishii, T., Fei, H., Miyajima, N., Boffa Ballaran, T., Ohfuji, H., Sakai, T., Wang, L., Shcheka, S. and Arimoto, T., 2017. Phase relations in the system $MgSiO_3$-$Al_2O_3$ up to 2300 K at lower mantle pressures. Journal of Geophysical Research: Solid Earth, 122, pp.7775–7788.

Lodders, K. and Fegley Jr, B., 1997. An oxygen isotope model for the composition of Mars. Icarus, 126, pp.373–394.

Momma, K. and Izumi, F., 2011. VESTA 3 for three-dimensional visualization of crystal, volumetric and morphology data. Journal of Applied Crystallography, 44, pp.1272–1276.

Morard, G., Andrault, D., Guignot, N., Sanloup, C., Mezouar, M., Petitgirard, S. and Fiquet, G., 2008. In situ determination of Fe–$Fe_3S$ phase diagram and liquid structural properties up to 65 GPa. Earth and Planetary Science Letters, 272, pp.620–626.

Mori, Y., Ozawa, H., Hirose, K., Sinmyo, R., Tateno, S., Morard, G. and Ohishi, Y., 2017. Melting experiments on Fe–$Fe_3S$ system to 254 GPa. Earth and Planetary Science Letters, 464, pp.135–141.

Néri, A., Man, L., Chantel, J., Farla, R., Bauer, G., Linhardt, S., Boffa Ballaran, T. and Frost, D.J., 2024. The development of internal pressure standards for in-house elastic wave velocity measurements in multi-anvil presses. Review of Scientific Instruments, 95, 013902.

Nishida, K., Xie, L., Kim, E.J. and Katsura, T., 2020. A strip-type boron-doped diamond heater synthesized by chemical vapor deposition for large-volume presses. Review of Scientific Instruments, 91, 095108.

Nishihara, Y., Doi, S., Kakizawa, S., Higo, Y. and Tange, Y., 2020. Effect of pressure on temperature measurements using WRe thermocouple and its geophysical impact. Physics of the Earth and Planetary Interiors, 298, 106348.

Oka, K., Tateno, S., Kuwayama, Y., Hirose, K., Nakajima, Y., Umemoto, K., Tsujino, N. and Kawaguchi, S.I., 2022. A cotunnite-type new high-pressure phase of $Fe_2S$. American Mineralogist, 107, pp.1249–1253.

Palme, H., Lodders, K. and Jones, A., 2014. Solar system abundances of the elements. In: Treatise on Geochemistry, 2nd ed., Elsevier, pp.1–27.

Plesa, A.C., Tosi, N., Grott, M. and Breuer, D., 2015. Thermal evolution and Urey ratio of Mars. Journal of Geophysical Research: Planets, 120, pp.995–1010.

Rivoldini, A., Van Hoolst, T., Verhoeven, O., Mocquet, A. and Dehant, V., 2011. Geodesy constraints on the interior structure and composition of Mars. Icarus, 213, pp.451–472.

Rose-Weston, L., Brenan, J.M., Fei, Y., Secco, R.A. and Frost, D.J., 2009. Effect of pressure, temperature, and oxygen fugacity on the metal-silicate partitioning of Te, Se, and S: Implications for earth differentiation. Geochimica et Cosmochimica Acta, 73, pp.4598–4615.

Rubie, D.C., Jacobson, S.A., Morbidelli, A., O'Brien, D.P., Young, E.D., de Vries, J., Nimmo, F., Palme, H. and Frost, D.J., 2015. Accretion and differentiation of the terrestrial planets with implications for the compositions of early-formed Solar System bodies and accretion of water. Icarus, 248, pp.89–108.

Rückriemen, T., Breuer, D. and Spohn, T., 2015. The Fe snow regime in Ganymede's core: A deep-seated dynamo below a stable snow zone. Journal of Geophysical Research: Planets, 120, pp.1095–1118.

Samuel, H., Ballmer, M.D., Padovan, S., Tosi, N., Rivoldini, A. and Plesa, A.C., 2021. The thermo-chemical evolution of Mars with a strongly stratified mantle. Journal of Geophysical Research: Planets, 126, e2020JE006613.

Samuel, H., Drilleau, M., Rivoldini, A., Xu, Z., Huang, Q., Garcia, R.F., Lekić, V., Irving, J.C., Badro, J., Lognonné, P.H. and Connolly, J.A., 2023. Geophysical evidence for an enriched molten silicate layer above Mars's core. Nature, 622, pp.712–717.

Sanloup, C., Jambon, A. and Gillet, P., 1999. A simple chondritic model of Mars. Physics of the Earth and Planetary Interiors, 112, pp.43–54.

Shi, W., Wei, W., Sun, N., Mao, Z. and Prakapenka, V.B., 2022. Thermal Equations of State of Corundum and $Rh_2O_3$ (II)-Type $Al_2O_3$ up to 153 GPa and 3400 K. Journal of Geophysical Research: Solid Earth, 127, e2021JB023805.

Stähler, S.C., Khan, A., Banerdt, W.B., Lognonné, P., Giardini, D., Ceylan, S., Drilleau, M., Duran, A.C., Garcia, R.F., Huang, Q. and Kim, D., 2021. Seismic detection of the martian core. Science, 373, pp.443–448.

Stewart, A.J., Schmidt, M.W., Van Westrenen, W. and Liebske, C., 2007. Mars: A new core-crystallization regime. Science, 316, pp.1323–1325.

Thompson, S., Sugimura-Komabayashi, E., Komabayashi, T., McGuire, C., Breton, H., Suehiro, S. and Ohishi, Y., 2022. High-pressure melting experiments of $Fe_3S$ and a thermodynamic model of the Fe–S liquids for the Earth's core. Journal of Physics: Condensed Matter, 34, 394003.

Toby, B.H. and Von Dreele, R.B., 2013. GSAS-II: the genesis of a modern open-source all-purpose crystallography software package. Journal of Applied Crystallography, 46, pp.544–549.

Tsuno, K. and Ohtani, E., 2009. Eutectic temperatures and melting relations in the Fe–O–S system at high pressures and temperatures. Physics and Chemistry of Minerals, 36, pp.9–17.

Urakawa, S., Kamuro, R., Suzuki, A. and Kikegawa, T., 2018. Phase relationships of the system Fe-Ni-S and structure of the high-pressure phase of $(Fe_{1-x}Ni_x)_3S_2$. Physics of the Earth and Planetary Interiors, 277, pp.30–37.

Urakawa, S., Someya, K., Terasaki, H., Katsura, T., Yokoshi, S., Funakoshi, K.I., Utsumi, W., Katayama, Y., Sueda, Y.I. and Irifune, T., 2004. Phase relationships and equations of state for FeS at high pressures and temperatures and implications for the internal structure of Mars. Physics of the Earth and Planetary Interiors, 143, pp.469–479.

Wänke, H. and Dreibus, G., 1994. Chemistry and accretion history of Mars. Philosophical Transactions of the Royal Society A: Physical and Engineering Sciences, 349, pp.285–293.

Williams, J.P. and Nimmo, F., 2004. Thermal evolution of the Martian core: Implications for an early dynamo. Geology, 32, pp.97–100.

Xie, L., Yoneda, A., Liu, Z., Nishida, K. and Katsura, T., 2020. Boron-doped diamond synthesized by chemical vapor deposition as a heating element in a multi-anvil apparatus. High Pressure Research, 40, pp.369–378.

Yoshizaki, T. and McDonough, W.F., 2020. The composition of Mars. Geochimica et Cosmochimica Acta, 273, pp.137–162.

Zhang, L. and Fei, Y., 2008. Effect of Ni on Fe–FeS phase relations at high pressure and high temperature. Earth and Planetary Science Letters, 268, pp.212–218.

Zhao, B., Morard, G., Boccato, S., Mezouar, M. and Antonangeli, D., 2024. Phase diagram and thermo-elastic properties of Fe-S compounds up to 15 GPa: Thermodynamic constraints on the core of medium-sized telluric planets. Earth and Planetary Science Letters, 634, 118676.

Zurkowski, C.C., Lavina, B., Chariton, S., Prakapenka, V. and Campbell, A.J., 2022. Stability of $Fe_2S$ and $Fe_{12}S_7$ to 125 GPa; implications for S-rich planetary cores. Geochemical Perspectives Letters, 21, pp.1–10.

# Appendix C. Supplementary Material for

## The structure and stability of $Fe_{4+x}S_3$ and its potential to form a Martian inner core

### Supplementary Methods

***Single crystal structure solution and refinement of $Fe_{4+x}S_3$.*** We utilized the Olex2 software package (Dolomanov et al., 2009) to solve and refine the single-crystal data after data reduction. Atomic scattering factors were used for the Fe and S atoms. In a preliminary model the structural solution identified four Fe positions (Fe1-Fe4) and three S positions (S1-S3), which form edge-sharing Fe-S square pyramids. All these atomic positions were refined anisotropically. However, significant electron density was observed in the interstitial sites among the square pyramids. The electron cloud intensity was insufficient to be identified as an Fe atom, and if identified as an S atom, the S-S bond length would be unrealistically short. We used the Platon software within the Olex2 package to search unsuccessfully for twin laws, confirming that the abnormal electron density in the interstitial site was not due to twinning. Based on the known compositional information of this phase, we propose that the interstitial site is occupied only partially by Fe (Fe5). Since the occupancies for Fe1, Fe2, Fe3, Fe4, S1, S2, and S3 were 0.98, 1.00, 0.98, 0.98, 1.00, 0.99, and 1.03, respectively, these positions can be considered fully occupied within the measurement error range. Therefore, we fixed these positions to full occupancy and refined the occupancy of the Fe5 position which was refined isotropically.

## Supplementary Discussion

***Single-crystal structure-chemistry relationship.*** The two single-crystal samples analyzed in this study have different compositions due to the presence of a different amount of Fe in the tetrahedral interstitial site (Fe5). As the amount of Fe increases at the Fe5 site the tetrahedral volume also increases. Such changes cannot be compared directly, since the pressure at which the two samples have been measured is different, however, since the change in the tetrahedral volume between sample LJFeS01 (4.54(1) Å$^3$, x=0.11) and sample LD101 (4.85(1) Å$^3$, x = 0.77) is 7%, we can expect a much larger difference when compared at a same pressure. The polyhedral volumes of sites Fe1, Fe2, Fe3 and Fe4 also increase due to the opening of the S atoms sub-lattice caused by the increase in amount of Fe at the Fe5 site. Such changes are not uniform because they depend on which S atom belongs to the coordination sphere, and are less than 3% for Fe1, Fe2 and Fe3 but are 7% for Fe4. The effect of composition on the unit-cell volume is shown in Supplementary Fig. 6.S1 where the compression of sample LJFeS01 (x = 0.11) is compared with the unit-cell volume of sample LD101 (x = 0.77), which is approximately 6% larger due to the presence of more Fe into the Fe5 site.

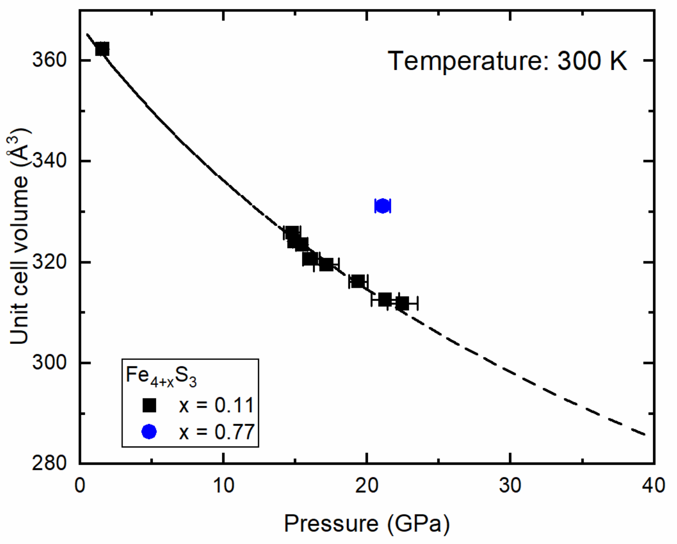

**Figure. 6.S1.** P-V-T-x relations of $Fe_{4+x}S_3$ under high pressure and room temperature.

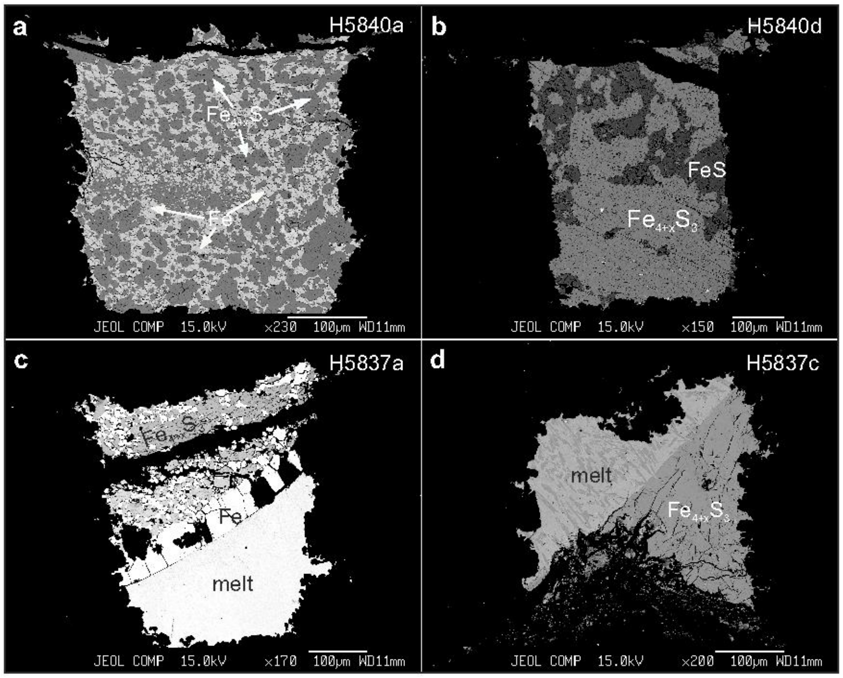

**Figure. 6.S2.** Backscattered electron images depicting $Fe_{4+x}S_3$ and associated phases from multi-anvil experiments, all encapsulated in MgO capsules. (a) $Fe_{4+x}S_3$ alongside metallic Fe, obtained at 16 GPa and 998 K. (b) $Fe_{4+x}S_3$ with FeS, also from 16 GPa and 998 K. (c) $Fe_{4+x}S_3$ in the presence of metallic iron and a melt phase, recovered from 16 GPa and 1266 K. (d) $Fe_{4+x}S_3$ with a melt phase, recovered from 16 GPa and 1266 K.

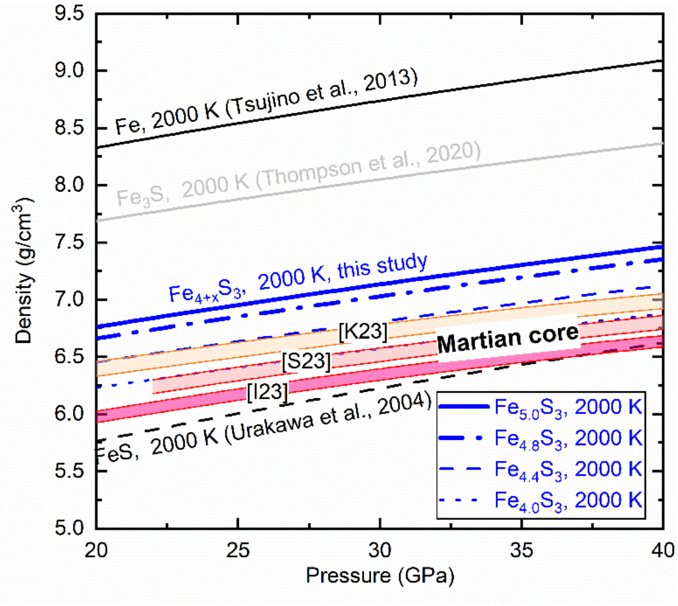

**Figure. 6.S3**. Comparison between the densities of Fe, $Fe_3S$, $Fe_{4+x}S_3$, and FeS under Martian core conditions and at 2000 K. The blue curves are for $Fe_{4+x}S_3$ determined in this study for x = 0, 0.4, 0.8, and 1. The black solid curve, light grey solid curve, and black dash curves are the density of fcc iron (Tsujino et al., 2013), $Fe_3S$ (Thompson et al., 2020), and FeS (Urakawa et al., 2004). Density estimates for the liquid Martian core (S23: Samuel et al. (2023); I23: Irving et al. (2023); K23: Khan et al. (2023)) are plotted for comparison.

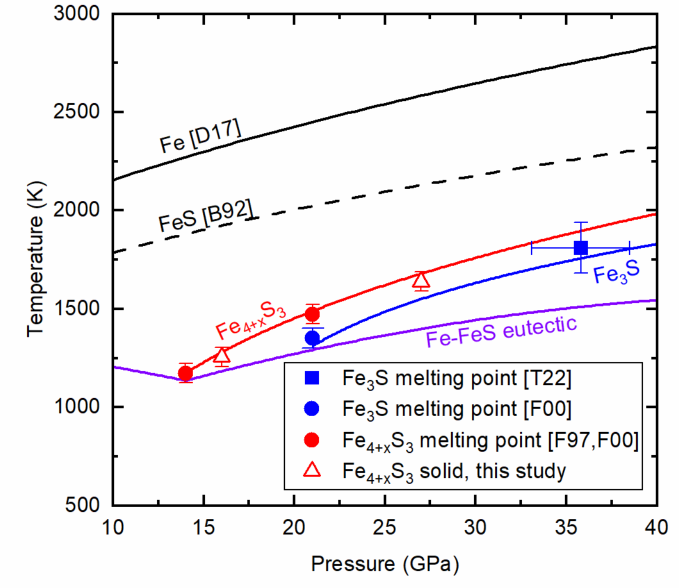

**Figure. 6.S4.** The melting curves of $Fe_{4+x}S_3$ and $Fe_3S$ under Martian core conditions evaluated in this study. The red solid curve indicates the melting temperature of $Fe_{4+x}S_3$, constrained by data from this study (red open triangles) and the literature (red circles, Fei et al., 1997; Fei et al., 2000) where the liquidus phase was originally reported as $Fe_3S_2$ or $Fe_{3+x}S_2$. The red open triangles indicate the temperature at which $Fe_{4+x}S_3$ coexists with Fe-S liquids, which constrains the lower limit of $Fe_{4+x}S_3$ melting. The blue solid curves indicate the melting curves of $Fe_3S$ used in the model in this study. The blue circle (Fei et al., 2000) and blue square (Thompson et al., 2022) denote the reported melting temperatures of $Fe_3S$ from the literature. For comparison, the melting curves of Fe (Dorogokupets et al., 2017), FeS (Boeher, 1992), and the Fe-FeS eutectic temperatures evaluated in this study are also plotted.

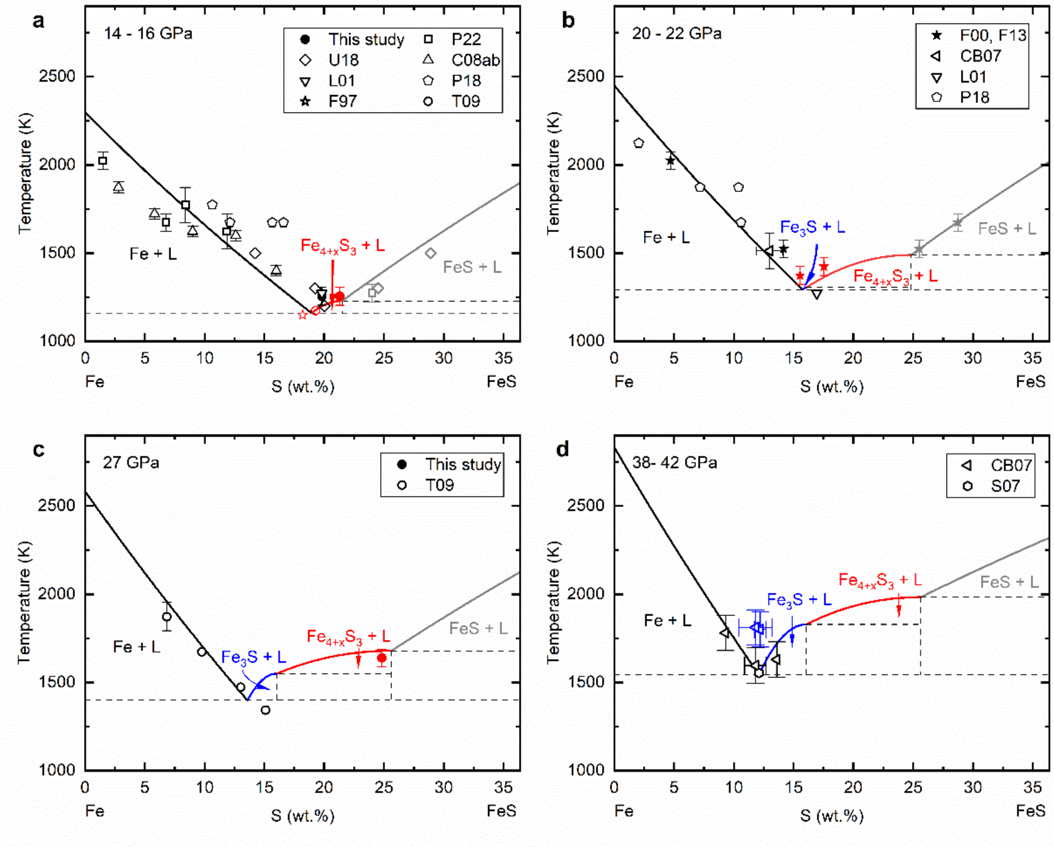

**Figure. 6.S5.** Melting phase diagrams of the Fe-FeS system at 15 GPa (a), 21 GPa (b), 27 GPa (c), and 40 GPa (d). The curves are generated from the model derived in this study, with the colors indicating liquidus curves where particular phases are on the liquidus, black for Fe, blue for Fe$_3$S, red for Fe$_{4+x}$S$_3$, and grey for FeS. The liquidus curves where Fe and FeS are liquidus phases are assumed to vary linearly with sulfur concentration, while those with Fe$_3$S and Fe$_{4+x}$S$_3$ as the liquidus phases are assumed to follow a parabolic relationship. The solid circles are the experimental data from this study. The symbols P22 (Pease and Li, 2022), U18 (Urakawa et al., 2018), C08ab (Chen et al., 2008a, b), L01 (Li et al., 2001), P18 (Pommier et al., 2018), F97 (Fei et al., 1997), T09 (Tsuno et al., 2009), F00 (Fei et al., 2000), F13 (Fei et al., 2013), CB07 (Chudinovskikh and Boehler, 2007), and S07 (Stewart et al., 2007) represent the experimental data reported in the literature.

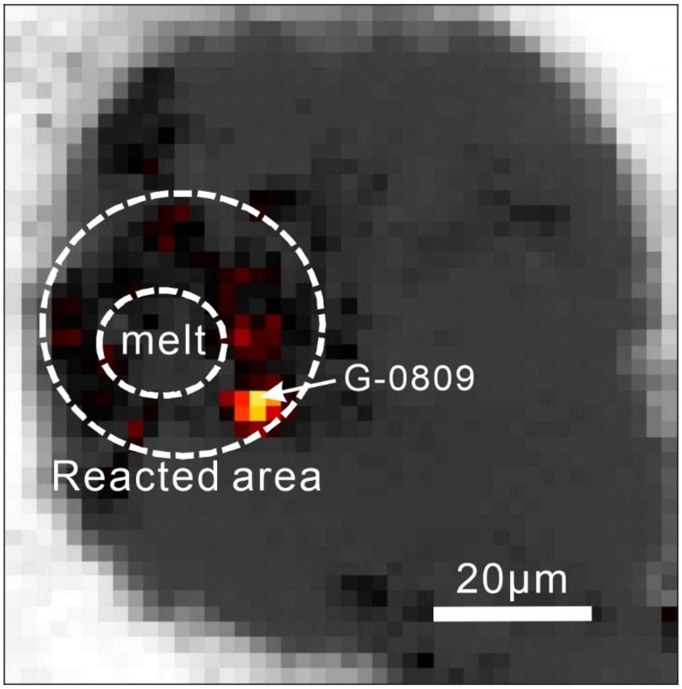

**Figure. 6.S6.** Two-dimensional mapping of the (2 1 3) Peak of $Fe_{4+x}S_3$ in Experiment LJFeS01. This diffraction map was created by systematically moving the sample stage in 2 μm increments. The specific location chosen for the single XRD measurement is highlighted in the image and labeled as G-0809.

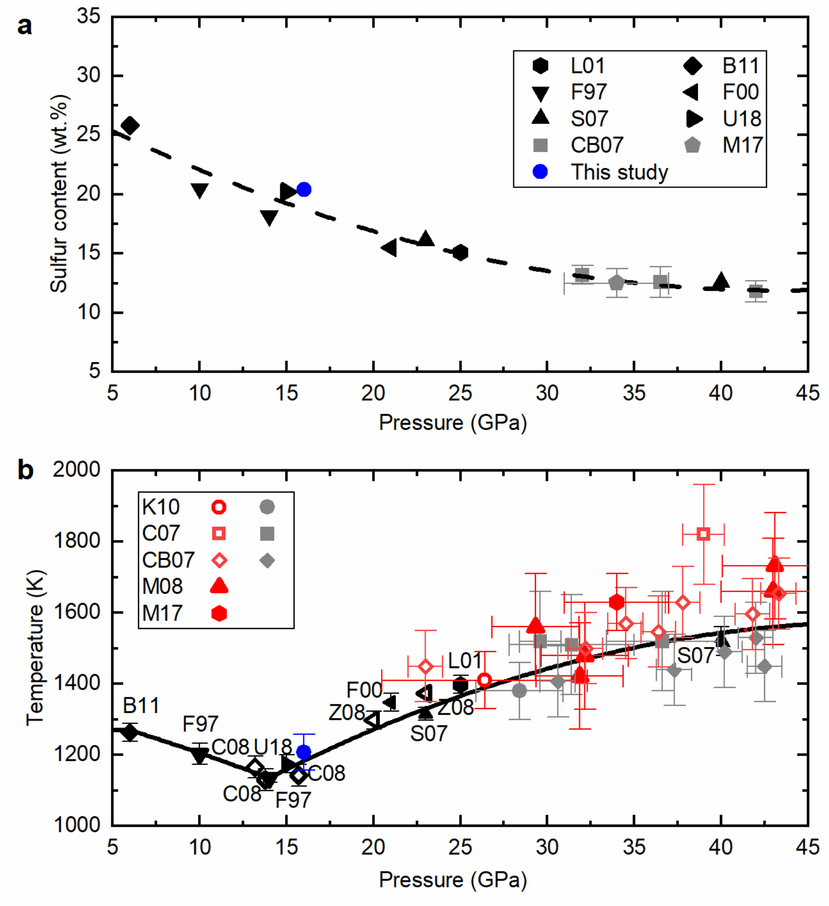

**Figure. 6.S7.** Eutectic compositions (a) and eutectic temperatures (b) of Fe-FeS system under high pressure. The blue circles represent the data from this study. Data points denoted L01 (Li et al., 2001), S07 (Stewart et al., 2007), F07 (Fei et al., 2007), B11 (Buono and Walker, 2011), F00 (Fei et al., 2000), CB07 (Chudinovskikh and Boehler, 2007), K10 (Kamada et al., 2010), C07 (Campbell et al., 2007), M08 (Morard et al., 2008), and M17 (Mori et al., 2017) are taken from the literature. In (b), black and blue symbols represent the eutectic temperatures, while red and grey symbols represent the temperatures where melts and solids are detected, respectively.

**Table 6.S1.** Experimental Conditions and Identified $Fe_{3+x}S_2$ in LH-DAC Runs.

| ***Run No.*** | *Starting Material* | *Pressure Medium* | *P (GPa)** | *T (K)†* | *Unit Cell Volume at 300 K* | *x‡* |
|---|---|---|---|---|---|---|
| **LJFeS01** | $Fe_{4+x}S_3$ (S7995) | KCl | 14.9(1) | 1150(200) | 324.0(6) | 0.11(1) |
| **LD101** | $Fe_{4+x}S_3$ (I1570a) | He | 21.1(5) | 1400(200) | 331.2(2) | 0.77(1) |

*The pressures are measured at room temperature after laser heating. KCl was used as a pressure standard (Dewaele et al., 2012) in run LJFeS01. The Raman shifts of diamond culets (Akahama and Kawamura, 2006) was used to estimate the pressure of LD101 at room temperature.

†In run LJFeS01, the temperatures were not directly measured but estimated based on the phase relations and compositions of the run products. For run LD101, the temperature was determined by fitting the collected thermal radiation spectrum with the Planck radiation function, following the gray-body approximation.

‡The x values in $Fe_{4+x}S_3$ were estimated by single crystal XRD refinements.

**Table 6.S2.** Crystallographic data and structure refinement details for $Fe_{4+x}S_3$

| | $Fe_{4.11}S_3$ | $Fe_{4.77}S_3$ |
|---|---|---|
| Formula weight | 325.72 | 362.58 |
| Pressure | 14.9(1) GPa | 21.5(5) GPa |
| Temperature | 298(2) K | 298(2) K |
| Wavelength | 0.410 Å | 0.410 Å |
| Crystal system | Orthorhombic | Orthorhombic |
| Space group | Pnma | Pnma |
| Unit cell dimensions | $a$ = 10.897(5) Å $\alpha$ = 90° | $a$ = 11.073(3) Å $\alpha$ = 90° |
| | $b$ = 3.1252(6) Å $\beta$ = 90° | $b$ = 3.1820(6) Å $\beta$ = 90° |
| | $c$ = 9.515(18) Å $\gamma$ = 90° | $c$ = 9.435(4) Å $\gamma$ = 90° |
| Volume | 324.0(6) Å$^3$ | 332.43(17) Å$^3$ |
| Z | 4 | 4 |
| Density (calculated) | 6.671 g/cm$^3$ | 7.245 g/cm$^3$ |
| Absorption coefficient | 4.18 mm$^{-1}$ | 4.67 mm$^{-1}$ |
| F(000) | 619 | 688 |
| Crystal size | 0.015 x 0.013 x 0.013 mm$^3$ | 0.003 x 0.002 x 0.002 mm$^3$ |
| θ range for data collection | 3.96 to 21.00° | 1.64 to 15.40° |
| Index ranges | -14<=h<=14, -4<=k<=4, -6<=l<=7 | -13<=h<=11, -4<=k<=3, -9<=l<=8 |
| Reflections collected | 259 | 252 |
| Independent reflections | 204 [R(int) = 0.020] | 178 [R(int) = 0.042] |
| Coverage of independent reflections | 39.4% | 58.1% |
| Refinement method | Full-matrix least-squares on F$^2$ | Full-matrix least-squares on F$^2$ |
| Data / restraints / parameters | 204 / 6 / 47 | 178 / 0 / 46 |
| Goodness-of-fit | 1.157 | 1.017 |
| Final R indices [>2σ(I)] | $R_{obs}$ = 0.058, $wR_{obs}$ = 0.157 | Robs = 0.055, $wR_{obs}$ = 0.138 |
| R indices [all data] | $R_{all}$ = 0.073, $wR_{all}$ = 0.192 | Rall = 0.075, $wR_{all}$ = 0.152 |
| Largest diff. peak and hole | 0.86 and -1.02 e·Å$^{-3}$ | 1.87 and -1.25 e·Å$^{-3}$ |

**Table 6.S3.** Unit Cell Parameters of $Fe_{4+x}S_3$ at High Pressures and 300 K measured in DAC.

| Pressure (GPa)* | *a* (Å) | *b* (Å) | *c* (Å) | *V* (Å$^3$) |
|---|---|---|---|---|
| **LJFeS01, x = 0.11** | | | | |
| 1.6(1) | 11.466(2) | 3.245(4) | 9.737(1) | 362.3(6) |
| 14.8(6) | 10.929(1) | 3.165(1) | 9.420(7) | 325.9(3) |
| 14.9(1) | 10.897(5) | 3.125(1) | 9.515(2) | 324.2(3) |
| 15.4(4) | 10.991(7) | 3.160(3) | 9.319(1) | 323.6(6) |
| 16.1(6) | 10.944(8) | 3.159(3) | 9.279(1) | 320.7(4) |
| 17.1(9) | 10.953(8) | 3.133(3) | 9.316(1) | 319.6(6) |
| 19.4(7) | 10.812(1) | 3.138(1) | 9.304(8) | 316.2(3) |
| 21.3(10) | 10.787(3) | 3.129(3) | 9.261(2) | 312.6(6) |
| 22.5(11) | 10.766(2) | 3.120(1) | 9.284(8) | 311.8(3) |
| **LD101, x = 0.77** | | | | |
| 20.1(5) | 11.054(3) | 3.178(7) | 9.428(5) | 331.2(2) |

*The pressures in LJFeS01 were determined based on the KCl pressure scale (Dewaele et al., 2012) and the pressure in LD101 was estimated by the Raman shift of diamond anvils (Akahama and Kawamura, 2006).

**Table 6.S4.** Unit Cell Parameters of $Fe_{4+x}S_3$ from Synchrotron Multi-anvil Experiments.

| Run No./ File No. | S. M. (wt.%) | P (GPa) | T$^†$ (K) | Unit Cell Parameters of $Fe_{4+x}S_3$ *a* (Å) | *b* (Å) | *c* (Å) | *V* (Å$^3$) |
|---|---|---|---|---|---|---|---|
| PEISCHE, SOLEIL | | | | | | | |
| MA231/017 | $Fe_{85}S_{15}$ | 13.4(5) | 1100(50) | 11.278(3) | 3.217(1) | 9.597(3) | 348.2(1) |
| MA233/016 | $Fe_{85}S_{15}$ | 13.9(5) | 800(50) | 11.072(2) | 3.152(1) | 9.494(2) | 331.3(1) |
| MA233/017 | $Fe_{85}S_{15}$ | 14.9(5) | 1100(50) | 11.277(1) | 3.217(1) | 9.656(1) | 350.2(1) |

*The pressures are determined based on the $Al_2O_3$ pressure scale (Shi et al., 2022).

†Temperatures were measured using a type-D thermocouple, with the pressure effects on thermocouple EMF corrected (Nishihara et al., 2020).

S.M. is starting material

**Table 6.S5.** Chemical Compositions of Run Products in Multi-anvil Experiments.

| Run No. | P* (GPa) | T* (K) | Starting Material (wt.%) | Duration (min) | Phase | Compositions determined by EPMA[†] | | | | |
|---|---|---|---|---|---|---|---|---|---|---|
| | | | | | | Fe (wt.%) | S (wt.%) | O (wt.%) | Total (wt.%) | N |
| S7995 | 14 | 918 | $Fe_{72.3}S_{27.7}$ | 210 | $Fe_{4+x}S_3$ | 70.0(2) | 29.5(2) | 0.3(1) | 99.8(3) | 17 |
| | | | | | FeS | 62.9(1) | 36.3(1) | 0.2(0) | 99.3(2) | 6 |
| H5840a | 16 | 995 | $Fe_{87.5}S_{12.5}$ | 600 | $Fe_{4+x}S_3$ | 70.7(3) | 28.6(2) | 0.6(1) | 100.0(4) | 12 |
| | | | | | Fe | 99.3(3) | 0.1(0) | 0.4(1) | 99.8(3) | 8 |
| H5840b | 16 | 995 | $Fe_{80}S_{20}$ | 600 | $Fe_{4+x}S_3$ | 70.7(3) | 28.7(2) | 0.6(0) | 100.0(3) | 6 |
| | | | | | Fe | 99.2(2) | 0.1(0) | 0.3(1) | 99.5(2) | 7 |
| H5840c | 16 | 995 | $Fe_{75}S_{25}$ | 600 | $Fe_{4+x}S_3$ | 70.6(3) | 28.5(3) | 0.6(0) | 99.7(2) | 9 |
| | | | | | Fe | 99.4(2) | 0.1(1) | 0.3(0) | 99.7(2) | 5 |
| H5840d | 16 | 995 | $Fe_{70}S_{30}$ | 600 | $Fe_{4+x}S_3$ | 69.9(2) | 29.4(1) | 0.7(1) | 99.9(2) | 18 |
| | | | | | FeS | 62.8(1) | 35.9(2) | 0.2(1) | 98.9(2) | 9 |
| S8013a | 16 | 1161 | $Fe_{87.5}S_{12.5}$ | 210 | $Fe_{4+x}S_3$ | 71.4(2) | 28.0(2) | 0.6(1) | 99.9(2) | 10 |
| | | | | | Fe | 98.7(3) | 0.6(2) | 0.4(1) | 99.7(2) | 15 |
| S8013b | 16 | 1161 | $Fe_{80}S_{20}$ | 210 | $Fe_{4+x}S_3$ | 71.3(2) | 27.9(2) | 0.4(0) | 99.6(2) | 11 |
| | | | | | Fe | 98.7(3) | 0.3(2) | 0.2(0) | 99.3(2) | 9 |
| S8013c | 16 | 1161 | $Fe_{75}S_{25}$ | 210 | $Fe_{4+x}S_3$ | 71.2(2) | 27.8(2) | 0.4(0) | 99.5(2) | 9 |
| | | | | | Fe | 98.2(5) | 0.6(2) | 0.3(1) | 99.1(3) | 8 |
| S8013d | 16 | 1161 | $Fe_{70}S_{30}$ | 210 | $Fe_{4+x}S_3$ | 70.8(3) | 28.2(1) | 0.6(1) | 99.6(4) | 18 |
| | | | | | FeS | 62.9(2) | 35.9(1) | 0.3(0) | 99.1(3) | 9 |
| H5837a | 16 | 1266 | $Fe_{87.5}S_{12.5}$ | 180 | $Fe_{4+x}S_3$ | 71.5(3) | 27.6(2) | 0.5(1) | 99.5(3) | 12 |
| | | | | | Fe | 97.6(2) | 2.0(0) | 0.2(0) | 99.8(2) | 9 |
| | | | | | melt | 79.4(2) | 19.6(1) | 0.3(1) | 99.3(2) | 32 |
| H5837b | 16 | 1266 | $Fe_{80}S_{20}$ | 180 | $Fe_{4+x}S_3$ | 71.6(3) | 27.8(2) | 0.4(1) | 99.7(3) | 38 |
| | | | | | Fe | 97.3(3) | 1.7(1) | 0.2(0) | 99.2(2) | 7 |
| | | | | | melt | 79.1(2) | 19.6(1) | 0.4(1) | 99.1(2) | 15 |
| H5837c | 16 | 1266 | $Fe_{75}S_{25}$ | 180 | $Fe_{4+x}S_3$ | 71.4(2) | 27.8(2) | 0.4(1) | 99.6(3) | 26 |
| | | | | | melt | 77.9(2) | 21.2(2) | 0.4(0) | 99.4(1) | 24 |
| H5837d | 16 | 1266 | $Fe_{70}S_{30}$ | 180 | $Fe_{4+x}S_3$ | 71.0(2) | 28.3(2) | 0.4(1) | 99.8(2) | 12 |
| | | | | | FeS | 62.6(2) | 36.2(2) | 0.2(1) | 99.1(3) | 15 |
| | | | | | melt | 77.5(3) | 21.4(3) | 0.5(1) | 99.4(1) | 5 |
| I1691a | 27 | 1640 | $Fe_{75}S_{25}$ | 30 | $Fe_{4+x}S_3$ | 73.2(2) | 26.2(1) | 0.6(1) | 100.0(2) | 13 |
| | | | | | melt | 74.2(2) | 24.5(3) | 0.8(1) | 99.4(1) | 16 |

*The uncertainties of pressures and temperatures are estimated to be 2 GPa and 50 K, respectively. Temperatures were measured using a type-D thermocouple, with the pressure effects on thermocouple EMF corrected (Nishihara et al., 2020).

[†] The figures within the brackets represent the standard deviations, expressed in the smallest cited units, and 'N' denotes the number of analyses.

**Table 6.S6.** Parameters describing the melting phase diagram of the Fe-FeS system

| **Parameter** | **Expression/ Reference** |
|---|---|
| Melting temperature of Fe | Dorogokupets et al., 2017 |
| Melting temperature of FeS | Boehler, 1992 |
| Melting temperature of $Fe_3S$ (K)* | $T_0$ = 1305, $P_0$ = 21, a = 4.6(5), c = 4.8(5) |
| Melting temperature of $Fe_{4+x}S_3$ (K)* | $T_0$ = 1173, $P_0$ = 14, a = 6.5(5), c = 3.1(3) |
| Eutectic temperature (K) | $T_{eu} = 1135 + 26.6 \times (P - 14) - 0.44 \times (P - 14)^2$,<br>$\boldsymbol{P \geq 14}$ **GPa** |
| Eutectic composition (wt.% S) | $X_{eu} = 31.1 - 1.03 \times P + 0.014 \times P^2$ |
| Peritectic composition (wt.% S)<br>($Fe_3S$ to $Fe_{4+x}S_3$) | $X_{per1} = 16.1$ |
| Peritectic composition (wt.% S)<br>($Fe_{4+x}S_3$ to FeS) | $X_{per2} = \begin{cases} 0.55 \times (P - 14) + 21.0, \mathbf{14} \leq \boldsymbol{P} \leq \mathbf{22.4}\ \textbf{GPa} \\ 25.6, \boldsymbol{P} > \mathbf{22.4}\ \textbf{GPa} \end{cases}$ |

*The melting temperature of $Fe_3S$ and $Fe_{4+x}S_3$ are expressed using the Simon-Glatzel equation (Simon and Glatzel, 1929): $T_{met} = T_0 \left(\frac{P-P_0}{a}\right)^{1/c}$, where P and $P_0$ are in GPa and $T_0$ in K.

## Supplementary References

Akahama, Y., & Kawamura, H., 2006. Pressure calibration of diamond anvil Raman gauge to 310 GPa. Journal of Applied Physics, 100, 043516.

Boehler, R., 1992. Melting of the Fe-FeO and the Fe-FeS systems at high pressure: Constraints on core temperatures. Earth and Planetary Science Letters, 111, pp.217–227.

Buono, A. S., & Walker, D., 2011. The Fe-rich liquidus in the Fe–FeS system from 1 bar to 10 GPa. Geochimica et Cosmochimica Acta, 75, pp.2072–2087.

Campbell, A. J., Seagle, C. T., Heinz, D. L., Shen, G., & Prakapenka, V. B., 2007. Partial melting in the iron–sulfur system at high pressure: A synchrotron X-ray diffraction study. Physics of the Earth and Planetary Interiors, 162, pp.119–128.

Chen, B., Gao, L., Leinenweber, K., Wang, Y., Sanehira, T., & Li, J., 2008a. In situ investigation of high-pressure melting behavior in the Fe-S system using synchrotron X-ray radiography. High Pressure Research, 28, pp.315–326.

Chen, B., Li, J., & Hauck, S. A., 2008b. Non-ideal liquidus curve in the Fe-S system and Mercury's snowing core. Geophysical Research Letters, 35, L07201.

Chudinovskikh, L., & Boehler, R., 2007. Eutectic melting in the system Fe–S to 44 GPa. Earth and Planetary Science Letters, 257, pp.97–103.

Dewaele, A., Belonoshko, A. B., Garbarino, G., Occelli, F., Bouvier, P., Hanfland, M., & Mezouar, M., 2012. High-pressure–high-temperature equation of state of KCl and KBr. Physical Review B, 85, 214105.

Dolomanov, O. V., Bourhis, L. J., Gildea, R. J., Howard, J. A., & Puschmann, H., 2009. OLEX2: a complete structure solution, refinement and analysis program. Journal of Applied Crystallography, 42, pp.339–341.

Dorogokupets, P. I., Dymshits, A. M., Litasov, K. D., & Sokolova, T. S., 2017. Thermodynamics and equations of state of iron to 350 GPa and 6000 K. Scientific Reports, 7, 41863.

Fei, Y., 2013. Simulation of the planetary interior differentiation processes in the laboratory. Journal of Visualized Experiments, 81, e50778.

Fei, Y., Bertka, C. M., & Finger, L. W., 1997. High-pressure iron-sulfur compound, $Fe_3S_2$, and melting relations in the Fe-FeS system. Science, 275, pp.1621–1623.

Fei, Y., Li, J., Bertka, C. M., & Prewitt, C. T., 2000. Structure type and bulk modulus of $Fe_3S$, a new iron-sulfur compound. American Mineralogist, 85, pp.1830–1833.

Irving, J.C., Lekić, V., Durán, C., Drilleau, M., Kim, D., Rivoldini, A., Khan, A., Samuel, H., Antonangeli, D., Banerdt, W. B., & Beghein, C., 2023. First observations of core-transiting seismic phases on Mars. Proceedings of the National Academy of Sciences USA, 120, e2217090120.

Kamada, S., Terasaki, H., Ohtani, E., Sakai, T., Kikegawa, T., Ohishi, Y., Hirao, N., Sata, N., & Kondo, T., 2010. Phase relationships of the Fe–FeS system in conditions up to the Earth's outer core. Earth and Planetary Science Letters, 294, pp.94–100.

Khan, A., Huang, D., Durán, C., Sossi, P. A., Giardini, D., & Murakami, M., 2023. Evidence for a liquid silicate layer atop the Martian core. Nature, 622, pp.718–723.

Li, J., Fei, Y., Mao, H.K., Hirose, K., & Shieh, S. R., 2001. Sulfur in the Earth’s inner core. Earth and Planetary Science Letters, 193, pp.509–514.

Morard, G., Andrault, D., Guignot, N., Sanloup, C., Mezouar, M., Petitgirard, S., & Fiquet, G., 2008. In situ determination of Fe–$Fe_3S$ phase diagram and liquid structural properties up to 65 GPa. Earth and Planetary Science Letters, 272, pp.620–626.

Mori, Y., Ozawa, H., Hirose, K., Sinmyo, R., Tateno, S., Morard, G., & Ohishi, Y., 2017. Melting experiments on Fe–$Fe_3S$ system to 254 GPa. Earth and Planetary Science Letters, 464, pp.135–141.

Nishihara, Y., Doi, S., Kakizawa, S., Higo, Y., & Tange, Y., 2020. Effect of pressure on temperature measurements using WRe thermocouple and its geophysical impact. Physics of the Earth and Planetary Interiors, 298, 106348.

Pease, A., & Li, J., 2022. Liquidus determination of the Fe-S and (Fe, Ni)-S systems at 14 and 24 GPa: Implications for the Mercurian core. Earth and Planetary Science Letters, 599, 117865.

Pommier, A., Laurenz, V., Davies, C. J., & Frost, D. J., 2018. Melting phase relations in the Fe-S and Fe-S-O systems at core conditions in small terrestrial bodies. Icarus, 306, pp.150–162.

Samuel, H., Drilleau, M., Rivoldini, A., Xu, Z., Huang, Q., Garcia, R. F., Lekić, V., Irving, J. C., Badro, J., Lognonné, P. H., & Connolly, J. A., 2023. Geophysical evidence for an enriched molten silicate layer above Mars's core. Nature, 622, pp.712–717.

Shi, W., Wei, W., Sun, N., Mao, Z., & Prakapenka, V. B., 2022. Thermal Equations of State of Corundum and $Rh_2O_3$ (II)-Type $Al_2O_3$ up to 153 GPa and 3400 K. Journal of Geophysical Research: Solid Earth, 127, e2021JB023805.

Simon, F., & Glatzel, G., 1929. Bemerkungen zur schmelzdruckkurve. Zeitschrift für anorganische und allgemeine Chemie, 178, pp.309–316.

Stewart, A. J., Schmidt, M. W., Van Westrenen, W., & Liebske, C., 2007. Mars: A new core-crystallization regime. Science, 316, pp.1323–1325.

Thompson, S., Komabayashi, T., Breton, H., Suehiro, S., Glazyrin, K., Pakhomova, A., & Ohishi, Y., 2020. Compression experiments to 126 GPa and 2500 K and thermal equation of state of $Fe_3S$: Implications for sulphur in the Earth's core. Earth and Planetary Science Letters, 534, 116080.

Thompson, S., Sugimura-Komabayashi, E., Komabayashi, T., McGuire, C., Breton, H., Suehiro, S., & Ohishi, Y., 2022. High-pressure melting experiments of $Fe_3S$ and a thermodynamic model of the Fe–S liquids for the Earth's core. Journal of Physics: Condensed Matter, 34, 394003.

Tsujino, N., Nishihara, Y., Nakajima, Y., Takahashi, E., Funakoshi, K.I., & Higo, Y., 2013. Equation of state of $\gamma$-Fe: Reference density for planetary cores. Earth and Planetary Science Letters, 375, pp.244–253.

Tsuno, K., & Ohtani, E., 2009. Eutectic temperatures and melting relations in the Fe–O–S system at high pressures and temperatures. Physics and Chemistry of Minerals, 36, pp.9–17.

Urakawa, S., Kamuro, R., Suzuki, A., & Kikegawa, T., 2018. Phase relationships of the system Fe-Ni-S and structure of the high-pressure phase of $(Fe_{1-x}Ni_x)_3S_2$. Physics of the Earth and Planetary Interiors, 277, pp.30–37.

Urakawa, S., Someya, K., Terasaki, H., Katsura, T., Yokoshi, S., Funakoshi, K. I., Utsumi, W., Katayama, Y., Sueda, Y.I., & Irifune, T., 2004. Phase relationships and equations of state for FeS at high pressures and temperatures and implications for the internal structure of Mars. Physics of the Earth and Planetary Interiors, 143, pp.469–479.

# List of the author’s publications

(1) Yuan, H., **Man, L.**, Kim, D.Y., Popov, D., Meng, Y., Greenberg, E., Prakapenka, V. and Zhang, L., 2022. HP-$PdF_2$-type $FeCl_2$ as a potential Cl-carrier in the deep Earth. *American Mineralogist*, 107(2), pp.313-317. [Not included in the dissertation]
DOI: https://doi.org/10.2138/am-2022-8283

(2) Neri, A., **Man, L.**, Chantel, J., Farla, R., Bauer, G., Linhardt, S., Boffa Ballaran, T. and Frost, D.J., 2024. The development of internal pressure standards for in-house elastic wave velocity measurements in multi-anvil presses. *Review of Scientific Instruments*, *95*(1). P. 013902. [Not included in the dissertation]
DOI: https://doi.org/10.1063/5.0169260

(3) **Man, L.**, Fei, H., Kim, E.J., Néri, A., Xie, L. and Frost, D.J., 2024. Alumina solubility in periclase determined to lower mantle conditions and implications for ferropericlase inclusions in diamonds. *Geochimica et Cosmochimica Acta*, 375, pp.36-49.
DOI: https://doi.org/10.1016/j.gca.2024.05.002

(4) Su, X., Liu, J., Zhou, Y., **Man, L.**, & Hou, M., 2025. Inner core composition of the Moon and Ganymede constrained by thermal equation of state of $Fe_{0.99}C_{0.01}$. *Journal of Geophysical Research: Planets*, 130(1), e2024JE008612. [Not included in the dissertation]
DOI: https://doi.org/10.1029/2024je008612

(5) **Man, L.**, Li, X., Boffa Ballaran, T.,Zhou, W., Chantel, J., Néri, A., Kupenko, I., Aprilis, G., Kurnosov, A., Namur, O., Hanfland, M., Guignot, N., Henry, L., Dubrovinsky, L. and Frost, D.J., 2025. The structure and stability of $Fe_{4+x}S_3$ and its potential to form a Martian inner core. *Nature Communications*, 16, 1710.
DOI: https://doi.org/10.1038/s41467-025-56220-2

## (Eidesstattliche) Versicherungen und Erklärungen

(§ 9 Satz 2 Nr. 3 PromO BayNAT)

*Hiermit versichere ich eidesstattlich, dass ich die Arbeit selbstständig verfasst und keine anderen als die von mir angegebenen Quellen und Hilfsmittel benutzt habe (vgl. Art. 97 Abs. 1 Satz 8 BayHIG).*

(§ 9 Satz 2 Nr. 3 PromO BayNAT)

*Hiermit erkläre ich, dass ich die Dissertation nicht bereits zur Erlangung eines akademischen Grades eingereicht habe und dass ich nicht bereits diese oder eine gleichartige Doktorprüfung endgültig nicht bestanden habe.*

(§ 9 Satz 2 Nr. 4 PromO BayNAT)

*Hiermit erkläre ich, dass ich Hilfe von gewerblichen Promotionsberatern bzw. -vermittlern oder ähnlichen Dienstleistern weder bisher in Anspruch genommen habe noch künftig in Anspruch nehmen werde.*

(§ 9 Satz 2 Nr. 7 PromO BayNAT)

*Hiermit erkläre ich mein Einverständnis, dass die elektronische Fassung meiner Dissertation unter Wahrung meiner Urheberrechte und des Datenschutzes einer gesonderten Überprüfung unterzogen werden kann.*

(§ 9 Satz 2 Nr. 8 PromO BayNAT)

*Hiermit erkläre ich mein Einverständnis, dass bei Verdacht wissenschaftlichen Fehlverhaltens Ermittlungen durch universitätsinterne Organe der wissenschaftlichen Selbstkontrolle stattfinden können*

……………………………………………………………………………………….
Ort, Datum, Unterschrift